Gabriela Ferreira de Vasconcelos Martins

Mestre em Química

New devices to monitor oxidative stress biomarkers in *point-of-care*: a new tool for cancer prevention

Dissertação para obtenção do Grau de Doutor em

Nanotecnologias e Nanociências

Orientador: Maria Goreti Sales, Professor Adjunto, Instituto Superior de Engenharia do Porto, Instituto Politécnico do Porto
Co-orientador: Elvira Maria Correia Fortunato, Professor Catedrático, Faculdade de Ciências e Tecnologia, Universidade NOVA de Lisboa

Júri:

Presidente: Prof. Doutor Rodrigo Ferrão de Paiva Martins
Arguentes: Prof. Doutor Arben Merkoçi
Prof. Doutor Carlos Manuel de Melo Pereira
Vogais: Prof. Doutor Rodrigo Ferrão de Paiva Martins
Prof. Doutor Francisco Miguel Gama
Prof. Doutor Hugo Manuel Brito Águas
Prof. Doutora Maria Goreti Ferreira Sales
Prof. Doutor Bruno Costa-Silva

FACULDADE DE CIÊNCIAS E TECNOLOGIA
UNIVERSIDADE NOVA DE LISBOA

Dezembro de 2018

Gabriela Ferreira de Vasconcelos Martins

Mestre em Química

New devices to monitor oxidative stress biomarkers in *point-of-care*: a new tool for cancer prevention

Dissertação para obtenção do Grau de Doutor em

Nanotecnologias e Nanociências

Orientador: Maria Goreti Sales, Professor Adjunto, Instituto Superior de Engenharia do Porto, Instituto Politécnico do Porto

Co-orientador: Elvira Maria Correia Fortunato, Professor Catedrático, Faculdade de Ciências e Tecnologia, Universidade NOVA de Lisboa

FACULDADE DE CIÊNCIAS E TECNOLOGIA
UNIVERSIDADE NOVA DE LISBOA

Dezembro de 2018

New devices to monitor oxidative stress biomarkers in *point-of-care*: a new tool for cancer prevention

Acknowledgments

Like someone great said one day "Above all, do not fear difficult moments, the best comes from them..." (*Dra. Rita Levi-Montalcini*). This project and thesis is the outcome not only of my individual work, but also it is the reflection of all the important people that surrounded me and to whom I would like to thank.

Firstly, I want to acknowledge my supervisors, Prof. Goreti Sales and Prof. Elvira Fortunato for giving me the opportunity to develop this work, under their close guidance. They are both *role models* in science, and life, that had inspired me each day to never give up, searching with imagination a solution to every problem. To Prof. Goreti I deeply thank the daily encouragement, the trust in my choices, the scientific advices in our discussions and the constant enthusiasm that she always bring to our "science talks". I thank to Prof. Elvira sharing her scientific knowledge, rising important questions in our meetings, that in most cases ended with great achievements in our work. Also, I want to acknowledge Prof. Elvira the opportunity to develop scientific work in the CENIMAT facilities, whereas it was possible to explore and investigate extra scientific approaches. Thank you to both for the support, confidence and supervision along this work.

To Fundação para a Ciência e Tecnologia (FCT), the financial support that enabled the development of this scientific work.

To all my colleagues in the BioMark that, in some way, contributed to this work; specially, Ana Patrícia for our enthusiastic "electro-talks", Helena Gomes for her advices and good sense, Liliana Truta, Felismina Moreira, Alexandra Santos, Carolina Hora and Mariana Carneiro for their patience, support and kindness and all others colleagues.

To Ana Marques, from FCT-UNL, the help in the lab and the hospitality during my stay in Lisbon, as well as the scientific comments along my thesis work.

To Dr. Rui Fernandes (TEM analysis, *I3S*) and Dr. Rui Rocha (SEM analysis, *CEMUP*), all the constructive discussions related with the analysis of my samples.

To all my friends that have been my support, being always present and available when I need it (because science is full of *ups and downs*). To Esther Garcia, Ana Torres and Sofia Caridade thank you for continuing this crazy wonderful friendship that, despite the long distance, remains always with me.

To my family, for their presence in my life, their support in my decisions and their kindness in the right moments... Specially, to my parents for always trusting in me, knowing that I am a reflection of them; to my brother, for being there when I need it (even without knowing it); to my

grandmother Emília for being an inspiration in every day of my life, she is the true role model in my beliefs and she will always continue to be...

To my dear husband Ricarte, for truly believing in me when I couldn't, for being my constant support and most enthusiastic admirer. I wouldn't be here without you!

And finally, to my best achievement in life, to my dear incredible son Guilherme, that since the first day of life inspires me to be each day better and stronger... I hope that science will also inspire him one day!

Resumo

Segundo as recentes estatísticas da Organização Mundial de Saúde (OMS), a segunda principal causa de morte a nível mundial é o cancro, com uma taxa de mortes em 2018 de 9.6 milhões de pessoas. Em particular, as doenças relacionadas com cancro já originaram 26% do número total de mortes ocorridas em Portugal em 2016. Vários mecanismos estão associados ao desenvolvimento de cancro, sendo que o stress oxidativo parece exercer um papel crucial na origem desta doença. Assim, a deteção precoce de múltiplos biomarcadores do stress oxidativo constitui uma ferramenta essencial na prevenção do cancro e também na seleção das terapias mais eficazes.

A procura de metodologias para análise específica de biomarcadores do stress oxidativo *in loco* continua a ser um desafio para a investigação biomédica. Até ao momento, os métodos analíticos utilizados para o diagnóstico de cancro, que incluem um exame patológico, são insuficientes para deteção precoce da progressão do tumor. Assim, para ultrapassar esta necessidade, o principal objetivo deste projeto é desenvolver métodos de deteção rápidos, simples e precisos para quantificação de biomarcadores de stress oxidativo, com metodologias de recolha não-invasivas, de modo a conduzir a um diagnóstico rápido e de confiança numa fase inicial da doença.

Para este efeito, esta tese apresenta o fabrico de biomateriais com propriedades sensoriais integradas em substratos condutores inovadores, para deteção *in loco* de biomarcadores de stress oxidativo. De modo a obter processos de reconhecimento bioquímico de elevada seletividade e especificidade, foi utilizada uma tecnologia de impressão molecular, que permite criar locais artificiais de reconhecimento. No decorrer da fabricação das plataformas transdutoras eletroquímicas, o papel foi usado como material de suporte alternativo aos materiais convencionais geralmente incorporados nos sistemas de elétrodos.

Em suma, espera-se que os resultados deste plano possam contribuir, no futuro, para o desenvolvimento e aplicação de plataformas de multi-analitos para rápida e simultânea deteção de biomarcadores do stress oxidativo num contexto local.

Termos-chave: *Biosensor eletroquímico; Polímero de impressão molecular; Biomarcador do stress oxidativo; Deteção no local; Substrato de papel.*

Abstract

According to the most recent World Health Organization (WHO) data, cancer is the second leading cause of death worldwide, accounting for 9.6 million deaths in 2018. In particular, cancer diseases have caused 26% of the total deaths in Portugal in 2016. Among the complex mechanisms associated to cancer development, Oxidative Stress (OS) seems to play an important role at the origin of the disease. Thus, early diagnosis of multiple OS biomarkers may be a fundamental tool in cancer prevention and in more efficient therapeutic strategies.

Despite the development and the research efforts that are being made, accurate and early detection methods for cancer are still lacking. The demand for specific OS biomarker assays carried out in wide screening programs in point-of-care (POC) is undoubtedly a difficult but potentially useful challenge for biomedical research and health. So far, current methods for cancer diagnosis based upon pathological examination alone are insufficient for detecting early tumour progression.

Thus, to overcome this need, the present project aims the development of quick, simple and accurate detection of selected OS biomarkers, collected using minimally invasive methods, in order to allow rapid and reliable diagnosis at early stages of the disease. Under this scope, the design of sensitive biosensing materials integrated with novel conductive substrates for POC screening of OS biomarkers will be presented. In order to achieve a specific and highly selective bio-chemical recognition process, molecular imprinting strategy was used to create the artificial recognition sites. During the fabrication of electrochemical transduction platforms, paper was introduced as a novel alternative to the conventional support materials usually incorporated in electrode systems.

Overall, it is expected that the outcome of this plan will contribute, in the future, to the development and application of a multi-analyte platform for simultaneous fast screening of cancer biomarkers in POC context.

Keywords: *Electrochemical biosensor; Molecular imprinting polymer; Oxidative stress biomarker; Point-of-care sensing; Paper substrate.*

Table of Contents

List of Figures

List of Tables

List of Abbreviations

AFM	Atomic force microscopy
APTES	(3-Aminopropyl)triethoxysilane
ATR	Attenuated total reflectance
C	Capacitor
CE	Counter/auxiliary electrode
CNTs	Carbon nanotubes
CV	Cyclic voltammetry
DMF	Dimethylformamide
DNA	Deoxyribonucleic acid
DPV	Differential pulse voltammetry
EDS	Energy dispersive X-ray spectroscopy
EIS	Electrochemical impedance spectroscopy
ELISA	Enzyme-linked immunosorbent assay
Fe_2O_3	Magnemite
α-Fe_2O_3	Hematite
γ-Fe_2O_3	Maghemite
FET	Field-effect transistor
FITC	Fluorescein isothiocyanate
FRP	Free radical polymerization
FTIR	Fourier-transform infrared spectroscopy
GC-MS	Gas chromatography mass spectrometry
4-HNE	4-Hydroxynonenal
H_2O_2	Hydrogen peroxide
HPLC	High performance liquid chromatography
ISFET	Ion-selective field-effect transistor
L	Inductor
LC-MS	Liquid chromatography–mass spectrometry
LOD	Limit of detection
MB	Methylene blue
MDA	Malonaldehyde
MIP	Molecularly imprinted polymer
MNP	Magnetic nanoparticle
MRI	Magnetic resonance imaging
MWNT	Multi-walled nanotube
MWNT-COOH	Multi-walled nanotube, carboxylic acid functionalized
NIP	Non-molecularly imprinted polymer

NMR	Nuclear magnetic resonance
NO	Nitric oxide
NO_2	Nitronium group
3-NT	3-Nitrotyrosine
O_2	Oxygen
O_2^-	Superoxide anion
$O_2^{-\cdot}$	Superoxide radical
$OH^\cdot$	Hydroxyl radical
8-OHdG	8-Hydroxy-2'-deoxyguanosine
8-OHG	8-Hydroxyguanosine
$ONOO^-$	Peroxynitrite
OS	Oxidative stress
PBS	Phosphate buffered saline
PEDOT	Poly(3,4-ethylenedioxythiophene)
P3MT	Poly (3-methylthiophene)
POC	Point-of-care
PSA	Prostate specific antigen
PVC	Polyvinyl chloride
PVC-COOH	Polyvinyl chloride, carboxylated
QCM	Quartz crystal microbalance
R	Resistor
RE	Reference electrode
RNS	Reactive nitrogen species
ROS	Reactive oxygen species
RRS	Resonance Raman spectroscopy
RSD	Relative standard deviation
SDS	Sodium dodecyl sulphate
SEM	Scanning electron microscopy
SERS	Surface-enhanced Raman spectroscopy
SiO_2	Silicon dioxide
SnO_2	Tin(IV) oxide
SPE	Screen-printed electrode
SPR	Surface plasmon resonance
SWNT	Single-walled nanotube
SWV	Square wave voltammetry
TBARS	Thiobarbituric acid reactive substances
TGA	Thermogravimetric analysis
TEM	Transmission electron microscopy
TEOS	Tetraethyl orthosilicate
UV-Vis	Ultraviolet–visible spectroscopy

WE	Working electrode
WHO	World Health Organization

Symbols

$\mathbf{C_d}$	Double-layer capacitance
E	Applied potential
$\mathbf{E_0}$	Amplitude of the voltage signal at t = 0
$\mathbf{E_{pa}}$	Anodic peak potential
$\mathbf{E_{pc}}$	Cathodic peak potential
$\mathbf{\Delta E_p}$	Difference between the anodic and cathodic peak potentials
I	Current
$\mathbf{I_{pa}}$	Anodic peak current
$\mathbf{I_{pc}}$	Cathodic peak current
n	Number of electrons involved in the electrochemical reaction
t	Time
$\mathbf{R_{ct}}$	Charge-transfer resistance
$\mathbf{R_\Omega}$	Solution resistance
V	Potential
Z	Impedance of the system
$\mathbf{Z_W}$	Warburg impedance
θ	Phase shift
υ	Scan-rate
ω	Angular frequency

CHAPTER 1

1 Framework

1.1 MOTIVATION

Currently, about 26% of Portuguese people died of cancer every year, according to the most recent World Health Organization (WHO) data (*WHO, 2016*). As a leading cause of death worldwide, the most common types of cancer death includes lung, liver, colorectal, stomach and breast. Although there are some well-identified risk factors, such as, tobacco smoking, alcohol consumption, obesity, among others, aging is another important factor to take in account for the development of cancer. So, as the way a person grows older, the incidence of cancer rises dramatically due to a danger combination of the risks for specific cancers with a less efficient cellular repair mechanism [1][2].

In this context, cancer mortality can be substantially reduced if cases are detected and treated early. However, despite all the research efforts that have been made in the last decades, screening programmes for quick, low-cost and *in loco* diagnostic are still lacking. So, the application of biochemical markers for the diagnosis and management of patient's status has been a growing approach in recent years, while developments in molecular biology lead to a continuous discovery of new circulating biomarkers. In parallel, molecular epidemiological studies have evidenced a link between oxidative stress (OS) and carcinogenesis. Indeed, OS-based biomarkers have been proven essential in revealing how OS may mediate toxicity induced by many known carcinogenic environmental agents [3]. Looking closer to the sub-products originated by OS, the most used and promising biomarkers found until now include 8-hydroxy-2'-deoxyguanosine (8-OHdG), 3-nitrotyrosine (3-NT), malonaldehyde (MDA) and 4-hydroxynonenal (4-HNE).

Nevertheless, the current analytical strategies used for the detection, monitoring and diagnosis of cancer are still insufficient. Despite their high sensitivity and selective response, these hold some limitations, such as, long analysis time, complex operation and large volume samples. Alternatively, biosensors are miniaturized devices, portable, easy-to-use with a straightforward operation, that can track in real-time multiple biomarkers in clinically relevant samples. Under this purpose, a modified-transducer surface is fabricated herein and afterwards, functionalized and tailored with suitable bioreceptor elements. So, a biomimetic polymeric network can be

finely designed through specific interactions between the building blocks of a biocompatible matrix and the desired specific target [4], enabling in the end, a specific, simple, inexpensive biosensor device. Moreover, to accomplish a suitable performance regarding the selectivity and sensitivity parameters of the sensor device, suitable electrochemical platforms that include cellulose paper are designed and functionalized in order to fabricate facile *point-of-care* (POC) testing device.

1.2 OBJECTIVES

The study and development of biosensor devices and novel supporting materials have been the *core-pieces* of BioMark and CENIMAT research groups receiving this plan, including the detection of cancer and neurodegenerative diseases. Under this context, the main goals of this work are:

(*1*) Identification and selection of the OS biomarkers that are most relevant in cancer diseases;
(*2*) Design and integration of a bioreceptor material, especially using molecular imprinting technology, directly assembled on an electrochemical sensing platform;
(*3*) Fabrication of low cost paper-based innovative conductive substrates to be fully-integrated as biosensing platforms;
(4) And ultimately, the fabrication of nanostructured electrochemical labels to be incorporated, in the future, in the development of a suitable multi-analyte platform for a simultaneous screening in POC of relevant OS biomarkers;

1.3 THESIS OUTLINE

This thesis is organized in eight chapters.

Firstly, **Chapter 1** describes the motivation and the main objectives of this work, with a summary description of the structure of the thesis. The list of publications and communications (*oral and poster*) associated to this PhD thesis is also presented.
Chapter 2 provides some fundamental background regarding the design and principle of biosensor devices, emphasizing those with special relevance to the present project. A brief *state-of-the-art* applied to the selected biomarkers is also described. An overview of the most common used nanomaterials and their main applications is addressed herein.
Chapter 3 presents the main results concerning the development, characterization and application of a biomimetic biosensor for electrochemical detection of 8-OHdG biomarker. This oxidized base is the most widely used biomarker for sensing oxidative DNA damage. The assembly of a plastic antibody film on the surface of a commercial gold electrode enabled the detection down to picoMolar level. Herein, a conventional three-electrode system was chosen to study the electrochemical performance of the plastic antibody designed towards 8-OHdG

quantification. This configuration was suitable is terms of analytical features and sample analysis feasibility, but it was not compatible with POC analysis.

In order to overcome the limitations of the conventional commercially-available electrodes, **Chapter 4**, describes the design, fabrication and application of an innovative paper-based sensing device for assessing 8-OHdG. Under this scope, paper was employed as an environmental-friendly alternative to other electrode supports. Although the levels of detection were not comparable with the previous commercial approach, the proposed carbon-based electrochemical sensor hold special features, such as, the potential to be miniaturized into smaller portable size, being disposable and low-cost. Still, this configuration required however additional improvements in terms of production, as it was being produced solely by manual techniques, which hindered the reproducibility of the different electrodes.

Thus, more advanced techniques of microfabrication were introduced and, **Chapter 5** focused on the production, characterization and application of a wax-printed paper-based device enabling the integration of the 3 electrode in the same platform for the direct assessment of 3-NT biomarker. Besides the novelty of using a flexible paper-based printed electrode, herein 3-NT was chosen as the target molecule due to the known correlation between this product of protein oxidation and many acute and chronic diseases. Although it is the first paper-based electrochemical sensor to the detection of 3-NT molecule, the main limitation of this electrochemical sensing platform was that detection levels should be improved. This could be solved by employing a more favourable biorecognition approach.

In order to enhance both selectivity and sensitivity of the previous approach, a molecular imprinting technology for 3-NT is presented in **Chapter 6**. Herein, the incorporation of this strategy with the previous wax-printed paper-based electrode enabled to create specific sites of biorecognition towards the direct electrochemical detection of 3-NT molecule. In addition, the applicability of this biosensor was tested and validated through assays performed in urine samples.

Finally, it was important that a multi-analyte detection could be achieved to solve current POC needs. This could be achieved by having one electrode per analyte or trying to have a single electrode that enables a multi-analyte detection. This last option was selected, for being simpler. Thus, **Chapter 7** focused on the fabrication and characterization of core-shell magnetic nanoparticles modified with a redox-active probe. The use of magnetic nanoparticles meant a pre-concentration effect at the sensing surface and the modification of the redox-active probe signalled which biomarker was being targeted. Under this concept, a specific redox probe binds to a specific OS biomarker bound to a molecularly-imprinted support, and the electrical signal of the bound probe should identify the biomarker involved and its quantity. For this purpose, each redox probe to be read should be linked to a different OS biomarker. This concept was tested herein for a single redox probe, but it is important to highlight that it could be further extended to other compounds. First, the experimental conditions during the synthesis of the nanoparticles were studied and optimized, in order to tune the size and electrochemical performance of the

material. Next, the redox probe also needed special tuning to ensure that its electrochemical signal was the only signal generated at its redox potential range.
Finally, **Chapter 8** summarizes the main conclusions of this project and highlights potential applications for future research work.

1.4 LIST OF PUBLICATIONS

1.4.1 Papers published in international scientific journals

- Gabriela V. Martins, Ana C. Marques, Elvira Fortunato, M. Goreti F. Sales, "Electrochemical paper-based biosensor for label-free detection of 3-nitrotyrosine in human urine samples using molecular imprinted polymer", *submitted.*

- Gabriela V. Martins, Ana C. Marques, Elvira Fortunato, M. Goreti F. Sales, "Wax-printed paper-based device for direct electrochemical detection of 3-nitrotyrosine", *Electrochimica Acta* (2018), 284, 60-68.

- Gabriela V. Martins, Ana P. M. Tavares, Elvira Fortunato, M. Goreti F. Sales, "Paper-Based Sensing Device for Electrochemical Detection of Oxidative Stress Biomarker 8-Hydroxy-2′-deoxyguanosine (8-OHdG) in Point-of-Care", *Scientific Reports* (2017), 7, 14878-14887.

- Gabriela V. Martins, Ana C. Marques, Elvira Fortunato, M. Goreti F. Sales, "8-hydroxy-2′-deoxyguanosine (8-OHdG) biomarker detection down to picoMolar level on a plastic antibody film", *Biosensors and Bioelectronics* (2016), 86, 225-234.

1.4.2 Communications presented in national and international scientific conferences

- Gabriela V. Martins, Stefano Chiussi, Goreti F. Sales, "Fabrication of flexible sensing devices for application in cancer diagnosis", IV Jornada Científica de IBEROS, Lugo (Spain), 11 July 2018 (*oral presentation*)

- Gabriela V. Martins, Ana C. Marques, Elvira Fortunato, M. Goreti F. Sales, "Electrochemical paper-based sensor integrated with molecular imprinting towards point-of-care diagnosis", 6th World Congress and Expo on Nanotechnology and Material Science, Valencia (Spain), 16-18 April 2018 (*oral presentation*).

- Gabriela V. Martins, Ana C. Marques, Elvira Fortunato, M. Goreti F. Sales, "An imprinted paper-based biosensor designed towards point-of-care diagnosis", Graduate Student Symposium on Molecular Imprinting, Porto (Portugal), 8-9 June 2018 (*oral presentation*).

- Gabriela V. Martins, Ana C. Marques, Elvira Fortunato, Helena R. Fernandes, M. Goreti F. Sales, "Carbon-based electrodes on paper substrates for biosensing purposes", iBEM - International Biomedical Engineering Meeting, Porto (Portugal), 21 March 2018 (*poster presentation*).

- Gabriela V. Martins, Elvira Fortunato, Helena R. Fernandes, M. Goreti F. Sales, "Chip-on-Paper for sensoring 8-hydroxy-2'-deoxyguanosine (8-OHdG) oxidative stress biomarker in point-of-care", NanoPT2016 International Conference, Braga (Portugal), 16-19 February 2016 (*oral presentation*).

- Gabriela V. Martins, Elvira Fortunato, Helena R. Fernandes, M. Goreti F. Sales, "A molecularly imprinted sensor for sensitive detection of 8-hydroxy-2'-deoxyguanosine (8-OHdG) oxidative stress biomarker", Graduate Student Symposium on Molecular Imprinting, Kent (UK), 27-28 August 2015 (*poster presentation*).

- Gabriela V. Martins, Elvira Fortunato, Helena R. Fernandes3, M. Goreti F. Sales, "A biomimetic sensor for monitoring oxidative stress biomarker in point-of-care", 1st ASPIC International Congress, Lisbon (Portugal), 25-26 November 2014 (*poster presentation*).

CHAPTER 2

2 Introduction

Along this chapter, a brief background concerning the fundamental principles of biosensors, the importance of biomarkers and their application in the context biomedical devices is presented and discussed. In addition, the integration of novel electrode systems based on modified-conductive substrates is also explored, as a potential alternative in the design of low-cost, efficient and portable sensor platforms.

2.1 OXIDATIVE STRESS

An overview of the current literature highlights the diversity and, in some cases, divergent theories proposed to understand the aging process and their mean features. Generally, "aging" can be defined as the sum of all the mechanisms that can, direct or indirectly, modify the functions of a living being, by preventing it from maintaining physiological balance and, consequently, causing the death of the organism. One of the first theories proposed by Harman in the 1950s was the so-called "*free radical theory*" claiming that the production of free radicals among aerobic organisms was determinant for causing cellular damage [5]. Under this scope, the definition of "*free radicals*" comprises atoms and molecules composed by unpaired and highly reactive electrons in their outer orbits, making these radicals quite unstable and highly reactive [6].

Afterwards, it was found that reactive oxygen species (ROS) greatly contributed to the accumulation of oxidative damage to cell macromolecules, but this kind of molecules were not exclusively free radical species. So, ROS are metabolites of molecular oxygen (O_2) holding higher reactive behaviour than O_2 that includes superoxide radical (O_2^-), hydroxyl radical (OH^-) and hydrogen peroxide (H_2O_2), among others. Interestingly, in normal physiological conditions, ROS are continuously generated as by-product species during normal aerobic phenomena, as a response to stress stimuli, pathological conditions or even to external environment effects [3]. Furthermore, as a protective barrier against these harmful compounds, one can find a complex system of antioxidant and protecting species (see Figure 2.1), such as, superoxide dismutase, glutathione peroxidase, glutathione reductase, catalase, glutathione and vitamins C and D [7].

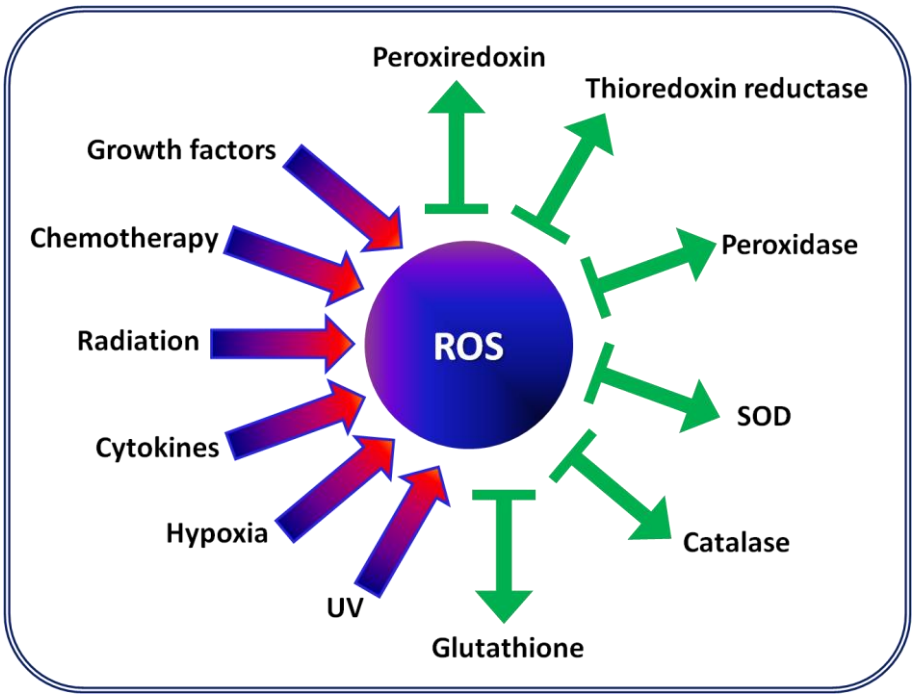

Figure 2.1: Adapted scheme highlighting the various activators and inhibitors factors associated to the production of ROS [7].

Nowadays, some believe that our cell metabolism may be the source of our aging process. This "*oxidative stress theory*" claims that high levels of ROS are directly linked to damage of macromolecules, like proteins, nucleic acids and lipids [8]. Although low levels of ROS enable cell signal transduction and immune response, a high accumulation of ROS in the organism can overload cellular macromolecules under OS circumstances, resulting in some human diseases, specially from cardiovascular and neurodegenerative origin. These include, Alzheimer, Parkinson and Huntington disease, and also some cancer pathologies [9][10]. In this regard, recent studies have shown that high concentrations of biological markers originated from OS occurrence can be associated with degenerative diseases, hypertension, type II diabetes and several types of cancer [11]. In parallel with ROS, reactive nitrogen species (RNS) can also occur, enabling analogous nitrosative effects.

Nevertheless, ROS also play a crucial role as signalling molecules in response to changes in intra- and extracellular environment, aiming to ensure the maintenance of physiological functions [7]. Currently, this is a controversial issue around ROS, besides their active part in the damage of relevant biomolecules, studies along the years have also confirmed their importance through the mechanisms involved in the antioxidant defence systems [12]. In addition, at the cellular level, ROS can be originated from both endogenous and exogenous sources [13][14], as seen in Figure 2.2. Although ROS produced by exogenous processes that includes, ozone, ultra-violet radiation and other environmental pollutants can cause OS, in most circumstances, the endogenous ROS-originated the main threat responsible for attacking cell molecules. Importantly, not all endogenous ROS production hold negative consequences, occurring some

controlled and relevant enzymatic reactions that are important for cellular maintenance function [3]. In particular, the endogenous antioxidant defences include a network of antioxidant enzymes, such as, superoxide dismutase, gluthathione peroxidase and catalase that are widely distributed in the cells holding the ability to counterbalance oxidative stimulus. Thus, on a normal and continuous basis, all living organism are exposed to ROS, in aerobic environment conditions.

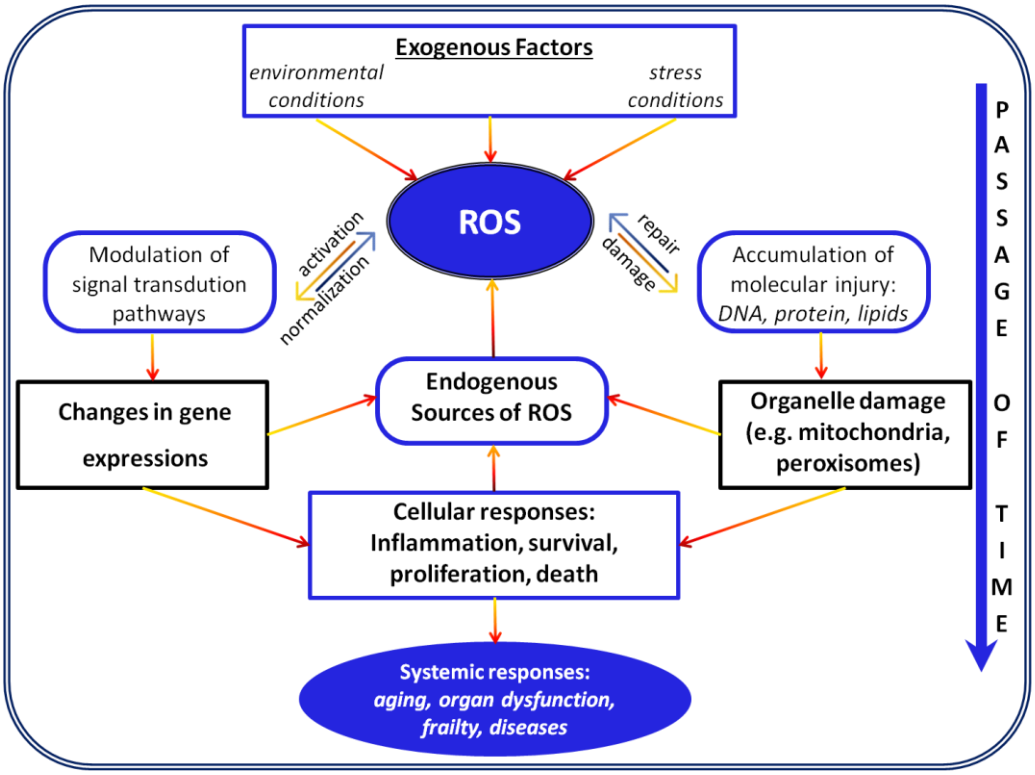

Figure 2.2: Adapted scheme showing the proposed mechanisms for ROS production and their contribution to the aging process [14].

Most cancer pathologies can be commonly defined by three main stages that are: initiation, promotion and progression [15]. Along all phases, OS plays a relevant role, specifically, during cancer initiation and progression. ROS can increase DNA mutations and also contribute to a growth in cell proliferation or a decrease in apoptosis of the initiated cell population. In addition, OS will also participate in the progression stage by introducing further DNA alterations to the initial cellular population [7]. Overall, a close but still not clear link has been commonly proposed by epidemiological and experimental data between the development and progression of cancer pathologies and OS phenomena. In this context, the physiological level of relevant biological markers presented in various biological tissues or fluids can be also influenced by external conditions, such as, age [16] and gender [17], for instance. Thereby, the importance of

establishing and understanding early biological markers has been a growing need in order to accomplish novel therapeutic approaches and, consequently, reduce disease's mortality.

2.1.1 Biomarkers of Oxidative Stress

In order to assess OS in biological matrices, two different approaches can be employed:
(i) the increase of the levels of ROS can be directly quantified or;
(ii) the damage resulted from OS can be measured.

There are some studies related to the direct detection and quantification of ROS in complex biological samples but their main limitations resulted from their low stability, high reactivity and short half-lives [18][19]. Therefore, the most common way is not measuring the level of ROS themselves, but quantify the damage originated from these, since in terms of consequences to the organism, it is the outcome of OS that matters rather than the total amount of ROS originated. As mentioned before, the radical species that are formed during OS phenomena will interact directly with the biomolecules present in the cells, such as, proteins, phospholipids and nucleic acids, causing cell degeneration and death [13][20]. In parallel, specific molecules are produced and their quantification can be used as OS biomarkers for different biological matrices [21]. Overall, biomarkers of OS can be designated as molecules that are modified by suffering interactions with ROS in a biological microenvironment.
According to IUPAC recommendations, "*biomarker*" is defined as a parameter that can be used to identify a toxic effect in an individual organism and can be applied in extrapolation between species, or as an indicator signalling an event or condition in a biological system or sample and giving a measure of exposure, effect, or susceptibility [22]. Moreover, a successful biomarker should have (1) high specificity for the effect of interest; (2) high sensitivity; (3) reflection of an early effect; (4) easy and inexpensive analysis; (5) low background level of the biomarker in the body fluid of interest; (6) a well-established relationship between the response of the biomarker and exposure, and (7) a well-established relationship between the response of the biomarker and the induced damage [10].
Under this scope, a relevant and global biological indicator of oxidative damage is not yet available, mainly because measuring OS is quite complex and a combination of different measurements may be required. Although the key issue to the assessment of oxidative status of an organism may be the analysis and quantification of different OS biomarkers, special care must be taken during the interpretation of the results [12]. Thus, the discovery and selection of robust biomarkers is crucial for screening, early diagnosis, and monitoring relevant diseases. Case-studies have investigated a possible correlation between the impact of environmental factors, like air pollution or smoke, and the occurrence of OS but results were not conclusive [23]. Moreover, the identification and validation of potential biomarkers may be hindered by their low levels in the biological fluids and the intrinsic variability among control and patient samples. Several studies related to neurodegenerative disease diagnostics and monitoring have been discussed in order to conclude that, by analysing the inflammatory profile in association with

disease-specific biomarkers, the diagnostic and prognostic could potentially be improved [24]. Thus, there is a need to work with a wide screen of possible biological markers. According to the origin of the biomolecule, OS biomarkers can be categorized in the following way (see Table 2.1):

Table 2.1: Summary of the most relevant OS biomarkers and their main categories.

MEASURE	Biological Marker	Reference
DNA oxidation	8-Hydroxy-2'-deoxyguanosine	[25–30]
	8-Hydroxyguanosine	[31,32]
Lipid peroxidation	Malondialdehyde	[33–38]
	4-Hydroxynonenal	[39,40]
	8-Isoprostane	[41]
	Acrolein	[42,43]
Protein oxidation	3-Nitrotyrosine	[44–48]
	3-Chlorotyrosine	[49]
	2-Pyrrolidone	[50]

Although most of the performed studies have assessed the presence of OS biomarkers in blood, serum, plasma or urine samples, other biological fluids such as, cerebrospinal fluid, nasal lavage fluid, joint fluid, breast milk, tissues or exhaled breath have been successfully used. So, the application of different analytical methodologies to a wide diversity of biological samples have improved the accuracy of the biomarker assays. Meanwhile, great efforts are still on-going in order to develop a suitable screening program targeted for POC assessment. Beyond prevention, early detection is the most crucial determinant for successful treatment and survival. So far, current methods for cancer diagnosis based upon pathological examination alone are insufficient for detecting early tumour progression. Under this scope, the potential of using OS biomarker assays for early detection purpose has been acknowledged as a determinant tool for successful cancer treatment, monitoring and survival.

2.1.1.1 8-Hydroxy-2'-deoxyguanosine

The most commonly studied biological markers of DNA damage obtained through the attack of nucleotides bases are 8-OHdG and 8-hydroxyguanosine (8-OHG). Both 8-OHdG and 8-OHG products constitute oxidation derivates of guanine, one of the four main nucleobases found in the nucleic acids DNA and RNA. In this context, the formation of 8-OHdG through DNA hydroxylation is an important mechanism of oxygen-radical induced mutagenesis [51] and has already been acknowledged as a suitable biomarker of OS [52]. For now, high-performance liquid chromatography (HPLC) has been the popular choice for determining the levels of this kind of biomarker. In addition, 8-OHdG is the most widely used fingerprint of DNA damage, yielding strong implications along carcinogenesis evolution. Two possible mechanisms can be presented concerning the formation of 8-OHdG, as can be seen in Figure 2.3:

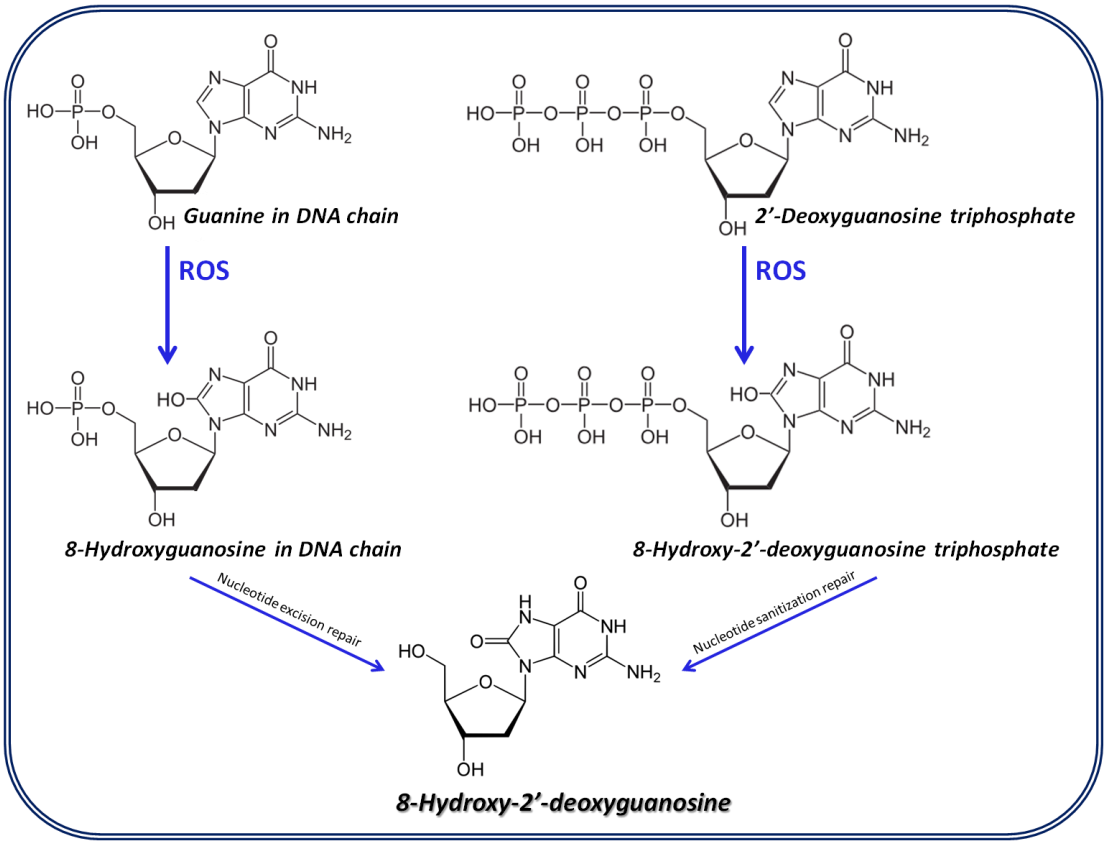

Figure 2.3: Adaptation of the proposed mechanism for the formation of 8-OHdG [16].

Different methodologies have been proposed to analyze 8-OHdG in biological samples, including Resonance Rayleigh Scattering (RRS) [53], Gas Chromatography - Mass Spectrometry (GC-MS) [54], Enzyme-Linked Immunosorbant assay (ELISA) [55] and HPLC [56]. Although these conventional detection techniques have reached good selectivity and suitable detection limits, they hold strong limitations, such as, time consuming and often require the use of sophisticated and laborious technologies, highly qualified personnel, and excessive

handling of biological samples. Specifically, biochemical methods such as ELISA can undertake cross-reactions, which can give false-negative or false-positive results. Furthermore, in most cases, GC-based methodologies operate with pre-treatment procedures prior to qualitative and quantitative analysis, originating long analysis periods. So, the development of fast, sensitive, easy-to-use and low cost approaches for 8-OHdG detection remains a continuous challenge.

Over the last years, 8-OHdG biomolecule has been quantified in various biological samples, such as, urine [57], saliva [58], blood [29] and tissue [59]. It was found that the average levels of 8-OHdG in healthy humans is around 20 ng/mL, a value that increases when OS rises [60]. Bolner *et al.* have demonstrated that 8-OHdG levels in Parkinson's disease patients can be 2-3 times higher than in healthy controls [29]. Therefore, highly sensitive (*nanomolar level*) methodologies are needed for the assessment of 8-OHdG.

Although the detection of oxidative damage is being widely applied in human research and clinical applications, we still need more data about the main factors that determine the basal levels of these biomarkers among general population. Meanwhile, some interesting studies have suggested that some variables, such as, age, sex, alcohol consumption, level of education, the time season of sample collection and exposure to heavy metals are implicated with 8-OHdG quantification [61][62]. Thus, special care must be taken during data analysis because the occurrence of this type of OS biomarker can be monitored not only in body fluids and tissues of patients, but also in healthy people in physiological (and variable) concentrations.

2.1.1.2 3-Nitrotyrosine

Looking more closely into the OS pathway, one finds nitric oxide (NO), a reactive nitrogen specie that plays an important role in many pathologies, such as, ischemia-reperfusion, septic shock, neurodegenerative and chronic inflammatory diseases [63]. The overproduction of this nitric oxide can generate a cytotoxic molecule called peroxynitrite ($ONOO^{\cdot}$) that is responsible for attacking protein residues [64]. As a consequence, 3-NT is obtained as a stable final-product and has been indicated as a biomarker for OS diagnosis [63]. Although peroxynitrite has been regularly correlated with increased oxidative reactions and DNA damage in inflamed tissues [63][64], it is not the only source of production of 3-NT marker.

Free 3-NT can be synthesized *in-vivo* by the direct reaction of tyrosine with nitrating oxidants (see Figure 2.4), which includes mainly three distinct biochemical processes [44]. Briefly, (i) the superoxide anion ($O_2^{\cdot -}$) is the product of the one-electron reduction of oxygen being the standard reduction potential for this conversion from molecular highly dependent on the nature of the medium; (ii) nitric oxide is an highly reactive free radical that is formed in mammalian cells during the oxidation of L-arginine to L-citrulline$^{\bullet -}$; and finally (iii) peroxynitrite that, contrary to nitric oxide and superoxide anion is not a free radical specie, but constitutes a strong oxidant and a nitrating agent that can originate the nitration of tyrosine residues in proteins. Thus, tyrosine nitration is the permanent addition of a nitronium group ($+NO_2$) at the *ortho*-position

resulting in free or protein-associated 3-NT. Consequently, the formation of nitro-aromatic compounds such as 3-NT can be directly associated with nitrosative stress [65].

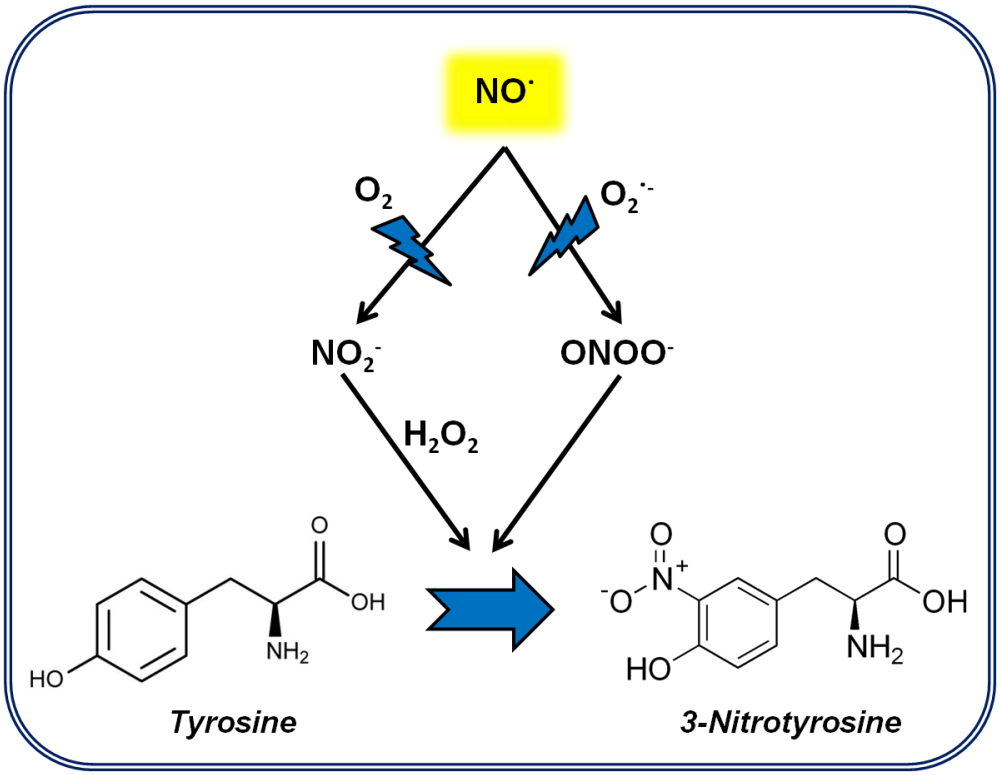

Figure 2.4: Adapted scheme showing the different pathways responsible for the nitration of tyrosine residues of proteins and consequent production of 3-NT [44].

Meanwhile, independently of the route of formation of 3-NT (*via* oxidation of nitric oxide, *via* peroxynitrite formation, etc.), the quantitative estimation of 3-NT, either free or bound to proteins, has been employed as a marker of oxidative damage in chronic inflammation [66], cardiovascular [67], atherosclerotic [68] and tobacco smoke–associated lung diseases [69]. Moreover, as mentioned before, the reactive species responsible for leading to tyrosine nitration usually have very short half-lives and, consequently, their direct measurement in biological environment is highly difficult.

In this context, 3-NT has been detected in several biological tissues and fluids, such as, plasma, serum, urine, cerebrospinal fluid, tissue samples, among others. Aiming for an accurate quantification, different methodologies have been proposed including immunoassays [48], GC-MS [70][71], liquid chromatography methods coupled with ultraviolet [72][73], fluorescence [74], mass spectrometry [65] and electrochemical detection [75]. Therefore, the application of the above techniques enabled very low limits of detection with high accuracy standards, but still involved complex and time-consuming sample preparation steps that are not compatible with routine *in-loco* analysis. Moreover, current detection methods are quite expensive and impractical for scaling up [76]. Since 3-NT was suggested as a biomarker of OS, a growing

effort has been made to implement portable, facile and rapid analysis of clinical samples in POC screening, as a way to improve the outcome of prevention and therapeutic approaches.

2.1.1.3 Malondialdeyde and Hydroxynonenal

As mentioned earlier, lipids are one of the major targets of oxidative attack and, the modification of these molecules can increase the risk of some degenerative diseases [77]. Once lipid peroxidation is initiated, the propagation of chain reactions will occur until a number of secondary, but highly damaging products are produced. Among others, the two most used end products of lipid peroxidation are MDA and 4-HNE (see Figure 2.5).

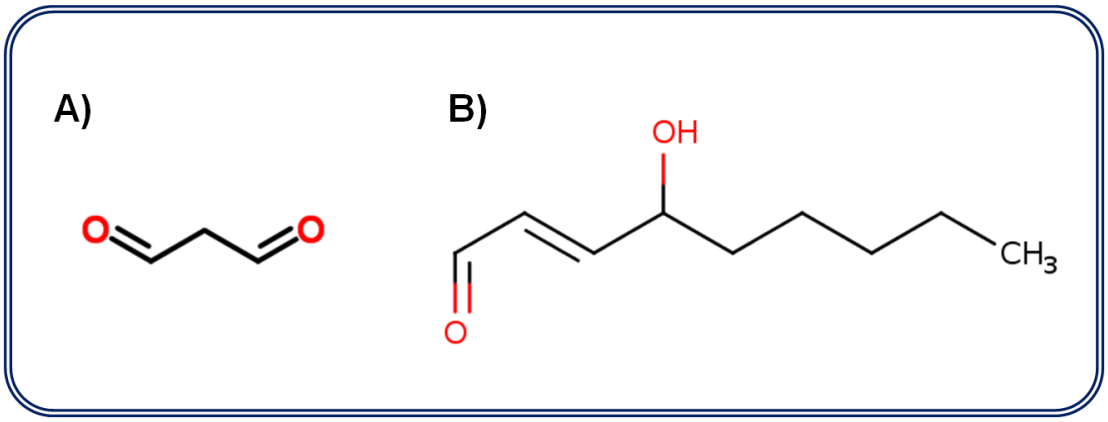

Figure 2.5: Chemical structure of A) malondialdehyde and B) 4-hydroxynonenal.

One of the most common techniques to quantify MDA levels is through the spectrophotometric thiobarbituric reactive specie (TBARS) assay. Although this methodology is quite easy and straightforward to be implemented, it is a non-specific test that can detect aldehydes other than MDA, with some artefact issues related to sample preparation [76]. Moreover, MDA data obtained through TBARS approach seem to be highly influenced by the smoking status, meaning that a wide variety of studies have found a significantly increased level of MDA in smokers in comparison with non-smokers [76].

MDA quantification as an OS biomarker has been used in various biological matrices, such as, saliva [37], urine [77], plasma [78], tissue [38], among others. Another technique also employed to assess MDA levels in biological samples is by using an HPLC approach [79]. Therein, a comparative study against the traditional TBARS assay have showed an overestimation of the MDA concentration found during the TBARS methodology. Nevertheless, MDA is still employed as a known biomarker of OS in various pathologies despite its basal level variations among healthy people [80][81][82].

The occurrence of 4-HNE, a sub-product originated as a consequence of oxidative damage, has been commonly associated to onset of memory loss and cognitive dysfunction, characteristic symptoms of Alzheimer's disease [83]. Furthermore, 4-HNE is a potent modulator of numerous

cell processes and can be accumulated during numerous oxidative stress-related diseases, such as neurodegenerative and cardiovascular diseases, metabolic syndrome and also cancer [84][85]. Some studies have performed 4-HNE quantification by using an enzyme immunoassay approach [39], fluorescence immunoassay [86] liquid chromatography tandem mass spectrometry (LC-MS) [87], TBARS assay [88]. Interestingly, 4-HNE should not be found in urine fluids so, urinary biomarkers for 4-HNE offer a non-invasive biomarker of lipid peroxidation and OS [89]. In sum, one still do not reach a consensus related to the cut-off of some individual biomarkers of OS, but their important relevance in the genesis of many diseases have been well established, making them ideal candidates to be investigated and applied in early screening.

2.2 BIOSENSORS

In the last decades, along with the digital and technological evolution, biosensor research has boosted in different direction areas, such as, healthcare, environment, food safety, industry, pharmacology, sportswear, regenerative medicine, among others [90][91][92][93][94]. In general, a biosensor is a chemical sensing device comprising a biologically derived recognition element coupled to a physicochemical transducer [95][96]. Mainly, biosensor devices can incorporate three distinct parts: (i) the biological component that recognizes the target molecule resulting in a signalling, (ii) the transducer platform and, finally, (iii) a reading equipment responsible for the data output (see Figure 2.6).

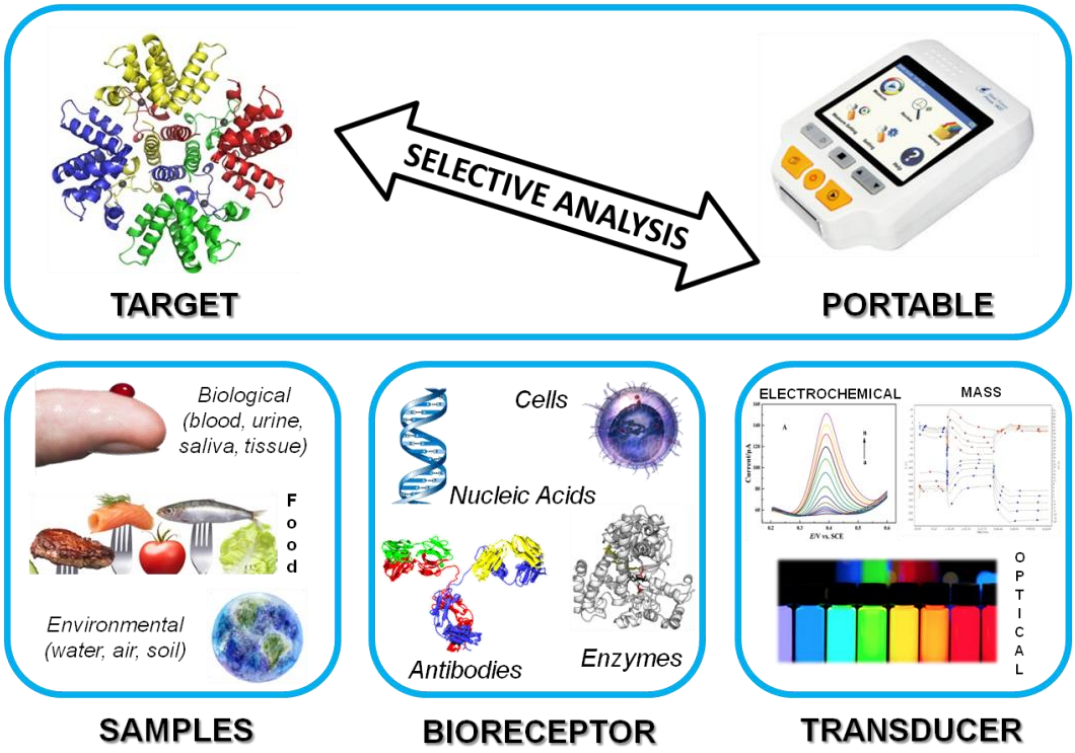

Figure 2.6: Schematic representation illustrating the main constitution, function and practical application of a biosensor device.

2.2.1 Recognition Element

Molecular recognition has been the crucial phenomenon for biosensing, as it is responsible for distinguishing the target analyte from many other analytes present in a sample. Chemical sensors and biosensors may be classified according to their type of biorecognition element, being the most common ones, enzymes, nucleic acids, antibodies and living organisms, such as, cells and cell organelles [97]. Among these, one can also include two distinct classes of sensing elements, namely, the catalytic sensors that are related to enzymes, microorganisms and other biomimetic catalysts, and the affinity-based sensors that incorporate nucleic acids, antibodies and synthetic receptors [98].

Specifically, catalytic enzyme based-biosensors have become a prominent and widely chosen approach making use of specific reaction products that can be easily measurable, like, electrons and protons. The main advantages of using enzymes as recognition elements are also due to their high selectivity and sensitivity response. In contrast, these catalytic enzymatic sensors can be quite expensive and, in some cases, during immobilization process the catalytic activity may become compromised.

Meanwhile, affinity biosensors imply the immobilization of a specific recognition layer, such as, antibodies, nucleic acids and other affinity proteins, on the surface of the electrode in order to selectively recognize the target biomolecule. Thus, the application of antibodies as the recognition element is among the most popular choices for quick detection purposes, due to the high sensitivity and specificity of antibody-antigen interaction [99]. Despite this popularity, antibodies hold some limitations associated to their solubility and stability in aqueous conditions. Concerning typical nucleic acid-based sensors, the biorecognition process involves non-covalent interactions between the complementary bases. Moreover, as recognition elements, nucleic acids are chemically more stable in comparison with their counterparts antibodies.

In parallel, the design of the sensor can also be differentiated by way the bio-receptor is immobilized that includes, physical sorption, covalent binding, immobilization in a polymer matrix, covalent binding and affinity immobilization [100]. This constitute an important and crucial step that will affect the performance and efficiency of the sensor device. Generally, the adsorption approach is the most simple and easiest to use, but the stability of the binding is limited. In contrast, covalent interactions hold a longer lifetime due to the stronger bond formation between the biomolecule and the solid support.

2.2.2 Signal Transduction

Another way to categorize biosensor devices is based on their transduction mechanism (see Figure 2.7). In this regard, one can have three main types of transducers, which are the piezoelectric (Quartz Crystal Microbalance/ QCM) [101–103], the optical (Colorimetric, Fluorescence, Surface Plasmon Resonance/ SPR) [104,105] and the electrochemical [106–108] biosensors.

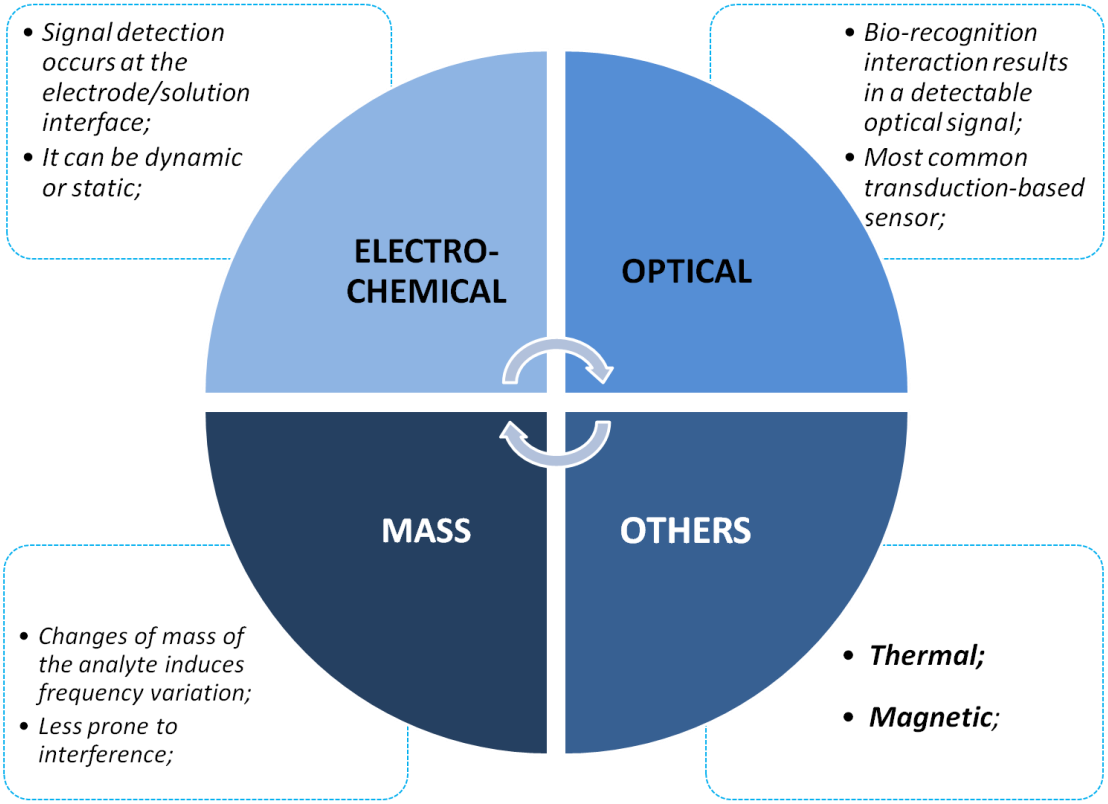

Figure 2.7: Schematic representation with the main features of the different types of sensor transduction.

Piezoelectric sensors are mass-sensitive sensors that, by tracking the resonant frequency of quartz crystal, are capable of measuring mass variations on the surface of the quartz electrode [109]. Optical sensors use light as the way of transducing and their main advantage is the quick and facile ability to give a visual response of the presence of a target molecule [110]. Among these sensors, a wide variety of optical contrasts, such as, absorption, fluorescence, Surface-Enhanced Raman Scattering (SERS) and refraction are used to detect optical changes. And finally, an electrochemical sensor holds an electrochemical transducer, measuring the variation of electrical current, potential, conductance or impedance at the interface of the electrode-sample [111]. In addition, other physical properties, such as, heat and magnetic field can be also employed for the conversion of the biological signal during the design of calorimetric and magnetic based-sensors, respectively.

In sum, the continuous development and application of these novel biosensor devices is the result of the combination of various advantages, such as [94]:

(i) high sensitivity and affinity toward their target molecules;

(ii) a suitable biological recognition that enables very selective sensing materials;

(iii) good and proper limits of detection targeted to the analyte of interest;

(iv) and their ability to be easily miniaturized in a *ready-to-use* apparatus;

So far, biosensing approach constitutes a suitable choice to be integrated in a POC device enabling special features, like, portability, automation and quick *in-loco* analysis. Among all transduction schemes, electrochemical-based biosensors are currently the most promising approach, where cost and minimized size are crucial needs.

2.3 ELECTROCHEMICAL BIOSENSORS

To overcome the growing need to develop biosensors with higher sensitivity and selectivity, electrochemical detection has been acknowledged as the more suitable strategy [112]. Electrochemical sensing technology has proven to be a valuable candidate for future clinical diagnosis, targeting relevant biomolecules, such as, proteins, nucleic acids and other small molecules [113]. Recently, an interesting review has compiled and discussed the development of versatile electrochemical genosensing of circulating biomarkers associated with cancer, neurodegenerative diseases and viral/ bacterial infections [114].

In general, an electrochemical sensor is designed to transform the effect of the physicochemical interaction between analyte and the electrode surface into an electrical signal [115]. It has been a very promising approach, due to its advantages, like high sensitivity, selectivity, a broad linear range of application and low cost instrumentation, enabling to overcome the most common challenges of analytical analysis.

Currently, a wide diversity of electrochemical studies have been conducted with biosensors, including the development of enzyme-based detection systems [116]; the establishment of microfluidic platform for therapeutic drug monitoring [117]; the construction of carbon-based paste for antioxidant estimation in wine samples [118]; the preparation of smart conductive films for cell culturing [119]; or the implementation of multiplexed immunoassay targeted for cancer biomarkers [120], among others. The use of electrochemical biosensors can also be performed under two different ways of transduction, direct or indirect, if a redox mediator is required or not to promote reversible electrochemical processes, enhancing the sensitivity and improving the detection limits. Moreover, according to the type of transducer, electrochemical techniques can be organized into conductometric, potentiometric or voltammetric biosensors or electrochemical impedance spectroscopy (EIS) biosensors [96].

In voltammetric biosensores, a potential is applied to a working electrode *versus* a reference electrode and the measured current results from an electrochemical oxidation or reduction of the electroactive species. Usually, the transducer surface is a metal or carbon electrode that can be chemically modified. Voltammetric biosensors allow to directly correlate the resulting current measured at a constant potential value with the bulk concentration of the analyte specie.

Conductometric biosensors measure changes related to the electrical conductivity of the sample solution during a chemical reaction, generally by using interdigitated microelectrodes. One of the typical advantages of working with these type of biosensors is that their capacitance measurements constitute a good indication of the insulating properties of the system.

In potentiometric biosensors the potential difference of an electrochemical cell is measure, in negligible (near-zero) current conditions. Usually, the transducer consists of an ion-selective permeable membrane, being pH electrodes the most common potentiometric devices among analytical laboratories.

EIS biosensors monitor the response of an electrochemical system (cell) to an applied potential, in which the frequency dependence may reveal underlying chemical processes. It indicates the resistive and capacitive properties of materials when a low amplitude sinusoidal perturbation is applied [121]. EIS is routinely used for the characterization of functionalized electrode surfaces, enabling sensitive measurements related to surface phenomena or variation of bulk properties.

Overall, the electrochemically-based biosensors that are most explored in recent scientific papers for POC purposes are the ones of voltammetric and EIS nature. These are addressed next in more detail.

2.3.1 Voltammetry

As mentioned before, voltammetric based-biosensors allow tracking the concentration of the target-analyte as a function of current variation. Typically, voltammetry is characterized by the occurrence of an oxidation or/ and a reduction reaction of an electroactive(s) specie(s) at the electrode surface. Briefly, the current will change accordingly to the kinetic and mass transport involved during the reaction and diffusion of the species [122]. As an alternative to the conventional approaches, some biosensing devices targeted for OS biomarkers have been reported in the literature, relying mostly on electrochemical or QCM detection modes. For instance, such devices establish a direct reading of 8-OHdG, making use of its active redox properties on glassy carbon [27][123] or pyrolytic graphitic [124] supports, modified with highly conductive nanomaterials. In general, the detection capability of these devices varies from 1.1 to 97 nM, but some methods have shown severe interference from urine elements (mostly uric acid), solved therein by the addition of specific enzyme prior to the analysis stage. Furthermore, the strategy behind electrochemical biosensors designed as relevant tools of oxidative damage allows to track directly their oxidant activity and simultaneously, their biological and physicochemical features as clinically relevant biomolecules. Nevertheless, this kind of electrochemical technique is known to enable the detection of low concentrations of analyte and different voltammetric approaches can be used according to the way the potential is applied.

2.3.2 Cyclic Voltammetry

The most common voltammetric technique used for primary research concerning the electrochemical behaviour of biomolecules is cyclic voltammetry (CV). CV measurements allow to monitor current variation while the potential applied on the working electrode is reversibly varied, under a fixed scan-rate value. As can be seen in Figure 2.8, cyclic voltammogram is the graphical representation of the current response as a function of the applied potential and the most relevant parameters to evaluate a redox system include:

(1) I_{pa} and I_{pc}, as the anodic and cathodic peak currents, respectively;

(2) υ, as the scan-rate of the applied potential;

(3) E_{pa} and E_{pc}, as the anodic and cathodic peak potentials, respectively;

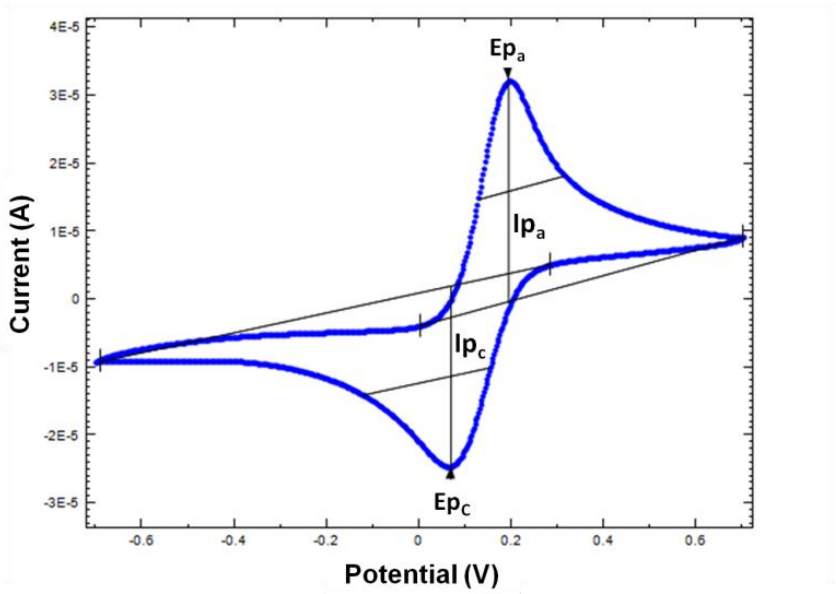

Figure 2.8: Cyclic voltammogram obtained for a reversible system.

The reversibility of a redox process is related to the rate at which the electron transfer occurs between the electroactive species and the electrode surface [125]. Firstly, in a reversible electrochemical process the Nernstian equilibrium is rapidly attained. Moreover, CV is a widely used tool to assess the reversibility of the redox reactions by simple measurement of voltammograms at distint scan-rates. Thus, one of the requirements of reversible electrochemical processes is a clear linearity between the peak current and the square root of the scan-rate. In parallel, this outcome constitutes also a intrinsic characteristic of a diffusion controlled process.

Another way to evaluate the electrochemical reversibility of a redox reaction is the difference between the anodic and cathodic peak potentials ($\Delta Ep = E_{pa} - E_{pc}$). So, for a reversible ideal electron transfer, Ep should be independent of υ and ΔEp equal to 59/n mV (at 25ºC), being n the number of electrons involved in the electrochemical reaction [122]. Finally, the ratio between the anodic and cathodic peak currents (I_{pa}/I_{pc}) is also employed to estimate the reversible behaviour of the redox system. In this case, the electron transfer is reversible when this ratio is close to 1 and for a less reversible system the ratio will move away from 1.

By contrast, in irreversible systems the linear potential sweep and CV lead to the same voltammetry profile because no reverse peaks appear upon changing the sweep direction [122]. Under these conditions, concentrations of the oxidized and reduced species do not follow the Nernst equation and the individual peaks are reduced in size and widely separated, as can be seen in Figure 2.9.

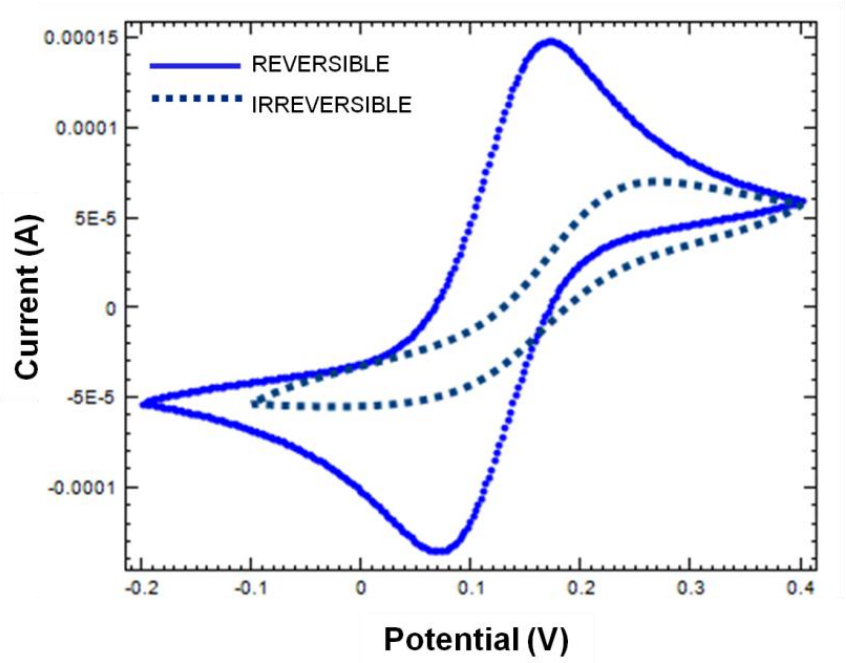

Figure 2.9: Comparison of typical voltammograms obtained for reversible and irreversible systems.

2.3.3 Square Wave Voltammetry

Square wave voltammetry (SWV) has been recognized as a crucial tool for sensible detection of relevant biomolecules, such as, proteins, nucleic acids, etc. Generally, in SWV the excitation signal is composed by a symmetrical square-wave pulse of amplitude undertaken with a staircase waveform of step height, being the forward pulse of the waveform equal to the staircase step [113]. In addition, the net current is determined by measuring the difference between the forward and reverse currents. The main advantages of this voltammetric technique are higher scan-rate during the analysis, less consumption of electroactive species and better performance related to passivation of the electrode surface [122].

2.3.4 Differential Pulse Voltammetry

The use of methodologies based on small-amplitude pulses have enhanced the sensitivity and accuracy parameters of electro-analysis. Under this scope, differential pulse voltammetry (DPV) is a technique that enables the application of the potential with a series of sequential pulses with fixed and continuous amplitudes. The current is measured immediately before the pulse application and after the end of the pulse, being determined the difference between both current values [122]. The peak representation plots the current difference for each pulse point as a function of the potential.

2.3.5 Electrochemical Impedance Spectroscopy

Electrochemical impedance spectroscopy (EIS) is another powerful electrochemical tool with great interest for the detection of relevant chemical and biological species. It has the advantage of not causing any damage or disturbance to the analysed surface of the electrochemical system. Mathematically, impedance has been expressed as a complex number comprising resistance (real part) and reactance (imaginary part) [126]. By looking to the Ohm's law (*equation 2.1*), where ***R*** is the resistance, ***V*** is the potential and ***I*** is the current:

$$R = \frac{\mathrm{V}}{\mathrm{I}} \qquad \textbf{(2.1)}$$

whereas, the impedance of the system (Z) can be calculated by means of an expression analogous to the previous Ohm's law, being $\boldsymbol{E_t}$ the applied potential and $\boldsymbol{I_t}$ the resulting current:

$$Z = \frac{\mathrm{Et}}{\mathrm{It}} \qquad \textbf{(2.2)}$$

The applied potential $\boldsymbol{E_t}$ can be expressed as a function of time:

$$\mathrm{Et} = E0\ \sin(\omega \mathrm{t}) \qquad \textbf{(2.3)}$$

where $\boldsymbol{E_0}$ is the amplitude of the voltage signal at t = 0, $\boldsymbol{\omega}$ is the angular frequency ($\omega = 2\pi f$) and ***t*** is time.

Also, the resulting current $\boldsymbol{I_t}$ has a phase shift θ with amplitude of $\boldsymbol{I_0}$, which can be expressed by:

$$\mathrm{It} = I0\ \sin(\omega t - \Theta) \qquad \textbf{(2.4)}$$

So, the expression for Ohm' Law can be applied to calculate the impedance of the system as:

$$\mathrm{Z} = \frac{Et}{It} = \frac{E0\ \sin(\omega t)}{Io\ \sin(\omega t - \Theta)} = Z0\ \frac{\sin(\omega t)}{\sin(\omega t - \Theta)} \qquad \textbf{(2.5)}$$

The impedance, ***Z***, can be expressed in term of a magnitude of $\boldsymbol{Z_0}$ and a phase shift, $\boldsymbol{\theta}$.

Then, by applying Euler's relationship (*equation 2.6*) given by:

$$e^{j\Theta} = \cos\Theta + j\ sin\Theta \qquad \textbf{(2.6)}$$

where $\boldsymbol{\theta}$ is a real number and ***j*** is the imaginary unit.

So, it is possible to express the impedance as a complex function, being the potential described as:

$$\mathrm{Et} = \mathrm{E0}\ \mathrm{e}^{j\omega t} \quad (\textbf{2.7})$$

and the current is expressed as:

$$\mathrm{It} = \mathrm{I0}\ \mathrm{e}^{j(\omega t-\Theta)} \quad (\textbf{2.8})$$

Therefore, impedance can be represented as a complex number:

$$\mathrm{Z}\ (\omega) = \frac{Et}{It} = \frac{\mathrm{E0}\ \mathrm{e}^{j\omega t}}{\mathrm{I0}\ \mathrm{e}^{\mathrm{j}(\omega \mathrm{t}-\Theta)}} = \mathrm{Z0}\ \mathrm{e}^{\mathrm{j}\Theta} \quad (\textbf{2.9})$$

$$Z\omega\ = \mathrm{Z0}\ (\cos\Theta + j\ sin\Theta) \quad (\textbf{2.10})$$

And finally, the impedance is now represented in the form of real part (Z0 cosθ) and imaginary part (Z0 sinθ):

$$ReZ\ =\ Z'\ =\ Zreal\ =\ Z0\ cos\Theta \quad (\textbf{2.11})$$

$$Z''\ =\ Zimag\ =\ Z0\ sin\Theta \quad (\textbf{2.12})$$

The most direct interpretation of EIS measurements is typically performed by fitting the impedance data to an equivalent electrical circuit that gives a representation of the physical process that occurs in the interface system. Therefore, any process occurring in an electrochemical cell can be represented in terms of equivalent circuits composed by different combinations of resistors (R), capacitors (C) and/or inductors (L). Briefly, the equivalent circuit of Randle's electrochemical cell is mainly composed by the following components [127]:

(1) $\mathbf{R_{\Omega}}$, the solution resistance, which is dependent on the ionic concentration, type of ions and electrode area;

(2) $\mathbf{R_{ct}}$, the charge-transfer resistance, which is inversely proportional to the electron transfer;

(3) $\mathbf{C_{d}}$, the double-layer capacitance;

(4) **Zw**, the Warburg impedance that can be used to assess effective diffusion coefficients;

These processes occur at the electrode-electrolyte interface comprising a fast mass-transfer reaction, a slow-paced charge transfer reaction and, finally, a diffusion phenomenon at the interface. Nyquist plots, also known as Cole-Cole plots, are one of the most popular ways to evaluate impedance information due to the facile prediction of the circuit elements as well as it allows the graphical extrapolation to obtain the R_{Ω} parameter (see Figure 2.10).

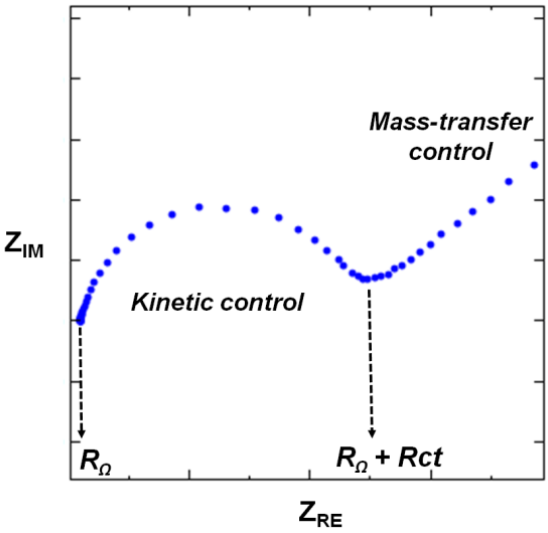

Figure 2.10: Nyquist plot for an electrochemical Faradaic system.

One of the limitations of this kind of plotting is that the information concerning the frequency is dismissed so, in order to overcome this issue, another way to express impedance data is also with a Bode diagram, by plotting absolute Z(ω) and phase angle θ(ω) in the frequency domain (see Figure 2.11).

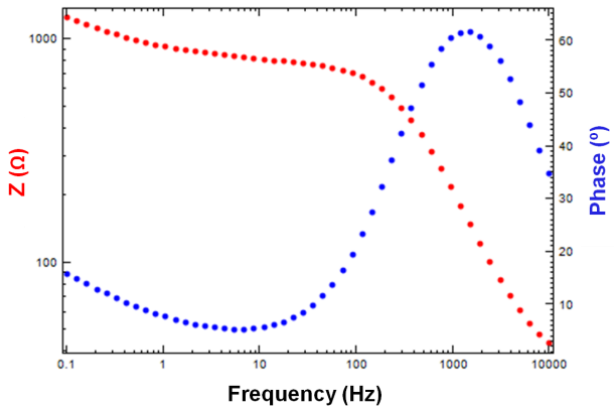

Figure 2.11: A typical example of a Bode plotting.

Typically, an electrochemical reaction can occur on the electrode surface by two distinct limiting mechanisms, such as, kinetically controlled (charge transfer based) and diffusion controlled (mass transfer based). The Nyquist plot for a Randle's cell is constituted, at higher frequency, by a single time semi-circle curve due illustrating the charge transfer process and a diagonal line of the diffusion process (Warburg impedance), at low frequency [126].

Moreover, EIS experiments can also be divided in two different types, Faradaic and non-Faradaic processes [127]. Herein, the main focus was given to the Faradaic processes where a redox marker specie is needed, and so particular attention is given to the R_{ct}. Under these

conditions, the working electrochemical cell must contain both reduced and oxidized forms of a benchmark redox probe that will undergo redox reactions at the electrode surface. In sum, the application of EIS technique has been widely open to different areas of expertise, such as, corrosion of metals, electrochemical synthesis of materials, study of ions mobility in energy storage and biosensor devices [128][129][130][131][132][133].

2.3.6 Electrode size, materials and supports

Electrochemical measurements require an electrochemical cell that combines 2- or 3-electrodes in electrical contact through the same solution. The electrodes involved are always reference electrode (RE) and working electrode (WE), and an additional counter or auxiliary electrode (CE) may be present, especially when the cell resistance is relatively high. In the 3-electrodes configuration, the potential of the WE is monitored against the RE potential, and the current passes between the WE and the CE. The RE remains a reliable reference for potential control because it has ideal nonpolarizability since no (or little) current passes through it. Experimentally, the tip of the RE is placed as close as possible to the WE in order to minimize the solution resistance. Today, there is a variety of materials and approaches that can be used to prepare the electrodes, with special relevance to the WE, which is designed to become selective to a given target analyte, and the exact cell design varies with the specific needs of a given experiment.

When the amount of analyte is not a concern, ranging from least 10 mL or more, a conventional cell may be used, employing electrodes of tubular shape that round 5×0.5 cm, or more, depending on the specific size by which these are manufactured. However, with limited quantities, it is difficult to handle the corresponding electrical measurements in a very small spot. Although the individual electrodes may be microsized and properly aligned to handle low sample volumes, limitations from current/potential measurements might arise because of the solution resistance and the heterogeneity of the electrolyte solutions.

The need to reduce the sample volume in electrochemical sensing has been targeted by suitable miniaturization of the electrode combination in use, all together in the same small spot. Screen-printed electrodes (SPEs) have become today a popular version of such miniaturization. Along with minimal volumes of sample, this specific design offers portability, low-cost of fabrication, large-scale production, and in many times short response time [112]. Following this trend, printing technology has been explored and improved, aiming to obtain the deposition of several successive layers of conducting material layers on an insulating support. At this point, the most common printing techniques used nowadays are inkjet and screen-printing [134]. The choice of the more suitable technique to perform the build-up of the sensing platform depends on the type of material used and also the type of modification required. Briefly, a typical SPE is composed by an inert substrate material holding three different electrodes together [93]. A typical configuration designed specifically for the purposes of this work is shown in Figure 2.12.

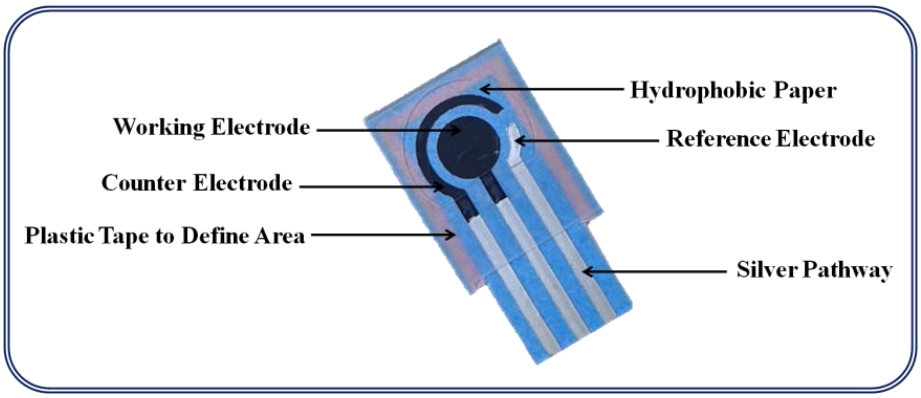

Figure 2.12: Main constituents of a paper-based assembly with three-integrated electrodes.

The analytical performance of the SPEs is directly tuned by the material used in the WE, while enabling a real-time field analysis. Thus, this electrode mostly defines the overall characteristics of the whole device and in most cases it can be printed using carbon, gold or silver inks. Various factors can tune the electrochemical performance of the SPEs, mainly the properties of the ink, the roughness of the surface, the printing process, the curing and drying temperatures, among others [135][136]. There are already several commercially available SPEs (see Figure 2.13), keeping important features such as, material diversity, facile operation, enhanced sensitivity, in some cases.

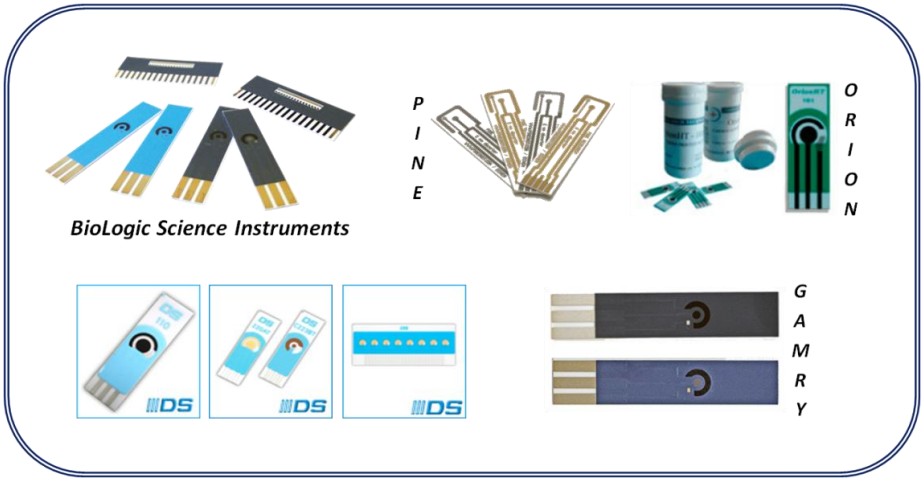

Figure 2.13: Examples of the wide diversity of SPEs commercially available.

Yet, many commercial versions still present reproducibility issues. An interesting report regarding the electrochemical performance of different commercial SPEs showed that their behaviour varied with the type of electrode, making this a critical issue for reproducibility [137]. Furthermore, this integrated electrically conducting layer can be assembled on different chemically inert insulating materials, such as, ceramic [138], plastic [139], silicon [140], glass [141] and paper [142]. In addition, the choice of the material for the working electrode results

not only from its electrochemical reactivity features but also from its effect upon the background current [143].

In terms of electrode material, metal-based electrodes, like for instance, platinum (Pt), gold (Au), tin-oxide (SnO_2) and copper (Cu), have been frequently used as working electrodes for an electrochemical detection of biological molecules [144][145]. This is also the case in the context of OS. Gutiérrez et al. reported self-assembled monolayers on gold-modified electrodes with dendrimers for 8-OHdG detection enabling limits of detection around 1 nM [26]. Moreover, an electro-chemiluminescence immunosensor based on platinum electrode modified with carbon quantum dots and gold/silica (Au/SiO_2) core-shell nanoparticles was designed for a rapid and selective detection of 8-OHdG for biological samples [146].

The most common material applied in the sensing area of WEs in SPEs today is however carbon-based. Carbon is one of the more important elements in nature and it can be found with different structures holding very distinct characteristics, such as, graphite, diamond and amorphous carbon. Carbon-based nanostructures present a wide range of interesting features, namely, good mechanical, electrical and thermal properties, holding an important and quite diversified potential use in many nanotechnology applications, as seen in Figure 2.14.

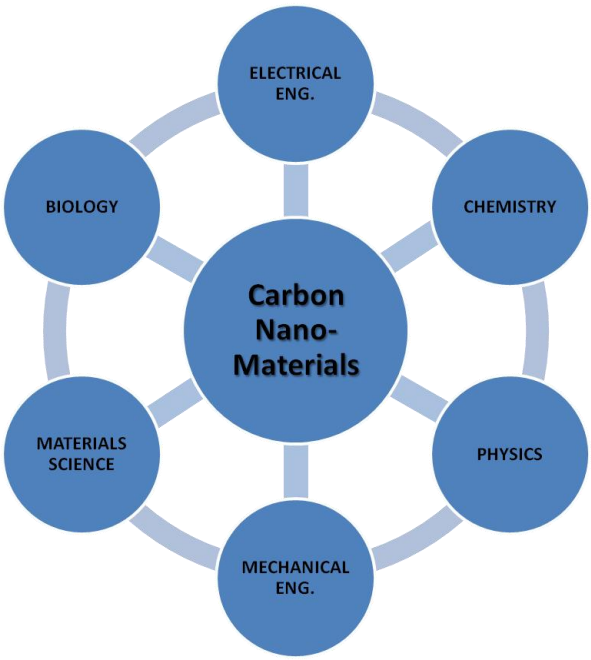

Figure 2.14: Representation of the different field of applications concerning carbon-based materials.

For instance, an electrochemical sensing approach on carbon materials based on the electro-activity of DNA bases has been employed to measure its biomolecular damage [147][148][149]. In this context, guanine and adenine were immobilized as DNA bases on carbon electrodes and their direct electrochemical response measured, as an indirect measure of DNA damage detection [150][151]. In parallel, other approaches aim the direct determination of OS biomarkers. In this case, carbon-based electrodes were widely applied, mostly due to their physical and electronic characteristics [152]. Li et al. performed some electrochemical studies

by using conducting polymer poly(3-methylthiophene) (P3MT) modified glassy carbon (GC) electrodes for an electrochemical detection of urinary 8-OHdG, enabling a limit of detection of 0.10 μM [153]. Moreover, Langmaier et al. investigated the oxidation reaction of 8-OHG on GC, and compared it to other electrodes, made with Pt, Au or SnO_2 [154]. It was observed that the rate of charge transfer reaction depends on the nature of the electrode material, following the sequence GC>Pt, Au>>SnO_2. More interestingly, these effects can be related to the density of the active surface sites (GC) or to the degree of oxidation of the electrode surface (Pt, Au, SnO_2). The determination of 8-OHG was also successfully tested on a graphitic support with suitable antibodies [155].

The nanostructural materials derived from carbon are also attracting much attention. This includes mostly carbon nanotubes (CNTs) and graphene, which constitute a good example of a simple structure constructed from sp^2 hybridized carbon bonds that, due to their high surface area, make them good model systems to be used in nanoscale analysis. CNTs can be distinguished by the number of layers that make up their cylindrical walls: single-walled nanotubes (SWNTs) and multi-walled nanotubes (MWNTs). In terms of applying graphene as the electrode material, researchers have showed that graphite control experiments have a huge impact in the electron transfer properties of the obtained electrodes, enabling different kinds of applications [156]. Overall, carbon-based nanomaterials, such as, graphene [157], carbon-black nanoparticles [158], MW-CNTs [159] are being widely used as integrated structures for sensing platforms, due to their singular electronic properties and controllable chemical functionalization. As a practical example, the incorporation of carbon materials in the composition of conductive inks to be printed as WE can highly improve the sensitivity of the biosensing device, making it ideal tool for the development of biomedical diagnostics.

Moreover, these metal- or carbon-based electrodes have to be fabricated on suitable supporting substrate. In SPEs, there are many different materials used for this purpose, such as, silicon, glass, ceramic, polyvinyl chloride (PVC), etc.. During the selection of the substrate properties, mechanical stability, facile fabrication and low-cost are important goals for the design of an efficient device. Under this scope, cellulosic paper holds a great importance as an alternative substrate material due to their unique features, like for instance, biocompatibility, high flexibility and porosity, cost effective, high surface area and it is recyclable [160][161]. Due to the incredible versatility of paper usage, the selection of the paper's type is highly dependent on the specific assay and the analytical needs. Thus, a set of properties have to be well evaluated in order to achieve the best paper-based analytical device [162], such as:

(i) Chemistry, the grade and distribution of the cellulose fibres, the presence of lignin, the degree of esterification and also the content of nitrogen can affect the deposition, adsorption and flow of species;

(ii) Surface area, it will have a great impact in the loading of the reagents, and also affects the reproducibility and sensitivity of the assay;

(iii) Flow-rate, it represents the speed of a migrating specie along the paper path, affecting the sensitivity of the paper-based device;

(iv) Size of pores, as expected is related to the size of the particles that can be retained on the paper surface;
(v) Porosity, it represents the void volume of the paper;
(vi) Thickness, it will dictate the speed of the analyte towards the testing area, meaning that thin papers will be faster in comparison with thicker ones;
(vii) Cost, sustainability is a very important issue.

As the most abundant biopolymer in nature, cellulose paper has been employed as a support material in analytical assays for centuries. The hydroxyl groups of the chains present in paper are responsible for their hydrophilic behaviour making it an ideal choice for microfluidic systems [163] in addition, studies have been performed related to how hydrophilicity of paper can be finely tuned by modification with plasma treatments [164]. Over the years, paper has been widely applied in different areas and the result was the development of new methodologies to fabricate and modify paper devices. Usually, the goal of these methods is to produce hydrophobic areas or channels on an hydrophilic porous paper substrate, being the most common fabrication techniques wax printing, photolithography, wet etching, screen and inkjet printing, among others, as seen in Figure 2.15 [165].

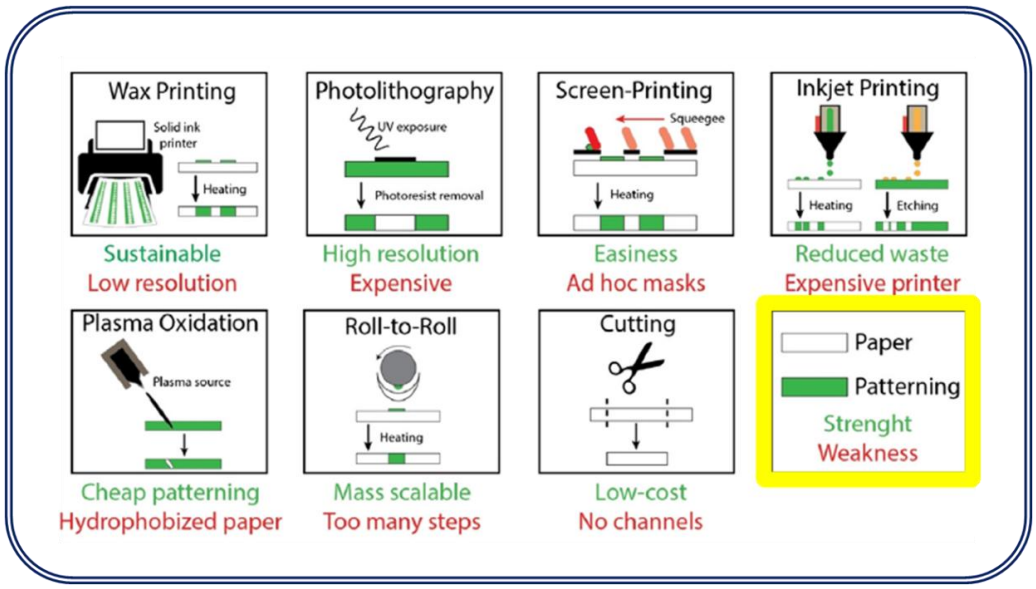

Figure 2.15: Adapted scheme with the various routes available to pattern paper-based sensors, with respective main advantages and limitations [165].

Due to their simplicity, portability and low cost, the most commonly used analysis techniques applied on paper-supported sensors are colorimetric [166][167], electrochemical [168][169], chemiluminescent [170] and electrochemiluminescent [171][172] (see Figure 2.16).

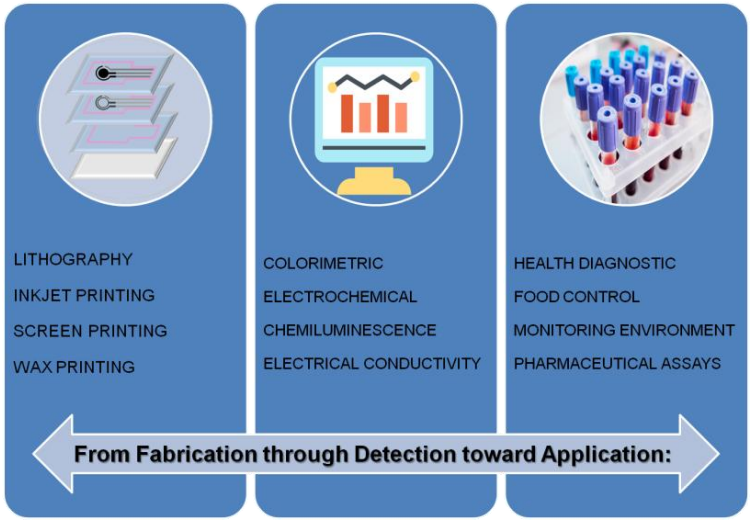

Figure 2.16: Schematic representation about techniques of nanofabrication, detection methodologies and practical applications of paper sensors.

The most widely and cost-effective used technique has been the one giving a visual colour alteration, but in most cases the results are only qualitative or semi-quantitative. Therefore, with a high sensitivity and a good selectivity, electrochemistry appears as the second most common transduction system. In addition, these paper-based biosensors are also aiming to become an environmentally safe alternative to the conventional SPEs for screening OS biomarkers. Moreover, in some cases, the reproducibility and sensitivity characteristics of the electrodes are poor and/or the fabrication process is complex, thereby hindering scaling-up processes and POC use. Table 2.2 illustrates some comparisons regarding the main features of the different materials used as substrates in the design of sensor devices.

Table 2.2: Comparison of paper as a substrate material with other traditional materials [173].

PROPERTY	MATERIAL			
	Glass	Silicon	PDMS	Paper
Surface profile	Very low	Very low	Very low	Moderate
Flexibility	No	No	Yes	Yes
Structure	Solid	Solid	Solid, gas-permeable	Fibrous
Surface-to-volume ratio	Low	Low	Low	High
Fluid flow	Forced	Forced	Forced	Capillary action
Sensitivity	No	No	No	Yes
Biocompatibility	Yes	Yes	Yes	Yes
Disposability	No	No	No	Yes
Biodegradability	No	No	To some extent	Yes
High-throughput fabrication	Yes	Yes	No	Yes
Functionalization	Difficult	Moderate	Difficult	Easy
Spatial resolution	High	Very high	High	Low to moderate
Homogeneity of material	Yes	Yes	Yes	No
Price	Moderate	High	Moderate	Low
Initial investment	Moderate	High	Moderate	Low

Another interesting benefit of paper over the traditional device materials includes portability, affordability, user-friendly and small environmental impact, when compared to other supports, making it a promising technology to be used for POC diagnostics. The high potential of using paper as a substrate in biomolecule detection has increased exponentially in the last years, for improving specificity and sensibility features. A quick overview on the last decade (see Figure 2.17) has shows the development of handmade paper-based immunosensor for electrochemical detection of influenza virus [174]; paper-based colorimetric sensor toward bacteria detection [166]; paper-based electrochemical cyto-device for sensitive cancerous cell detection [169]; and also, a microfluidic immunoarray for simultaneous detection of cancer biomarker proteins [172]. In sum, the incorporation of this light and widely available natural resource has boosted the development of compact and miniaturized electrochemical devices, holding high sensitivity and selectivity, with great expectations towards early detection biosensing devices.

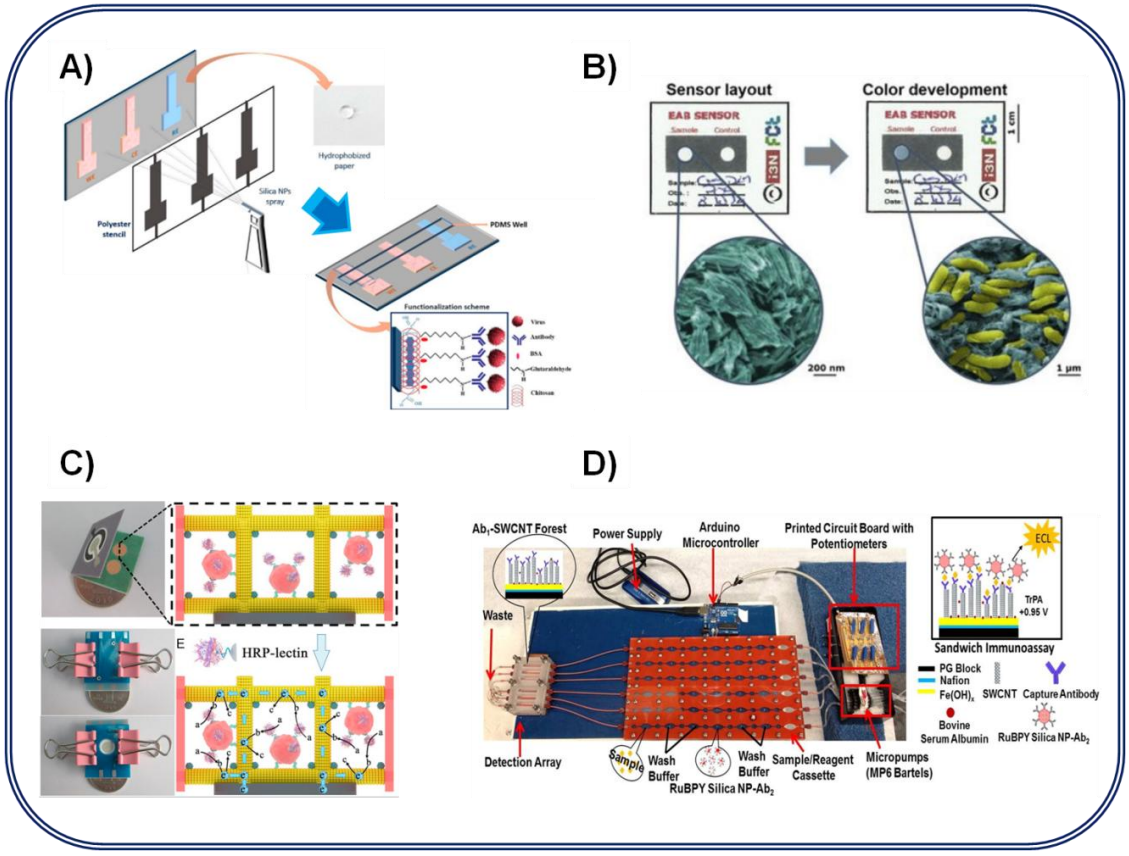

Figure 2.17: Some examples of different paper-based biosensors for A) virus [174], B) bacteria [166], C) cell [169] and D) multi-protein [172] detection.

2.4 MOLECULAR IMPRINTING POLYMER

Molecularly-imprinted polymer (MIP) has arrived to the new century has a highly improved technology to update the conventional bio-recognition methodologies. Although this concept is known since the early 1970s, this trend suffer a great income after the introduction of a general non-covalent approach by Mosbach group [175]. In a simple way, the concept of molecular imprinting is to design synthetic materials with the ability to mimic the behaviour of natural biomolecules, including antibodies and enzymes, with the great advantage of being highly stable and holding singular mechanical properties [176]. Thus, ideally, the capability of imprinted materials to recognize the target molecule should be comparable to natural bio-recognition in terms of sensitivity, affinity and selectivity. The assembly of MIPs (see Figure 2.18) can be divided into three fundamental steps: first, the template molecule to be imprinted is mixed in a solution containing the block monomers, afterwards, through a polymerization reaction the monomers (and crosslinker species) are "moulded" around the template creating a polymeric matrix and, finally, the template molecule is removed from the matrix, creating specific cavities with complementary size and shape [177].

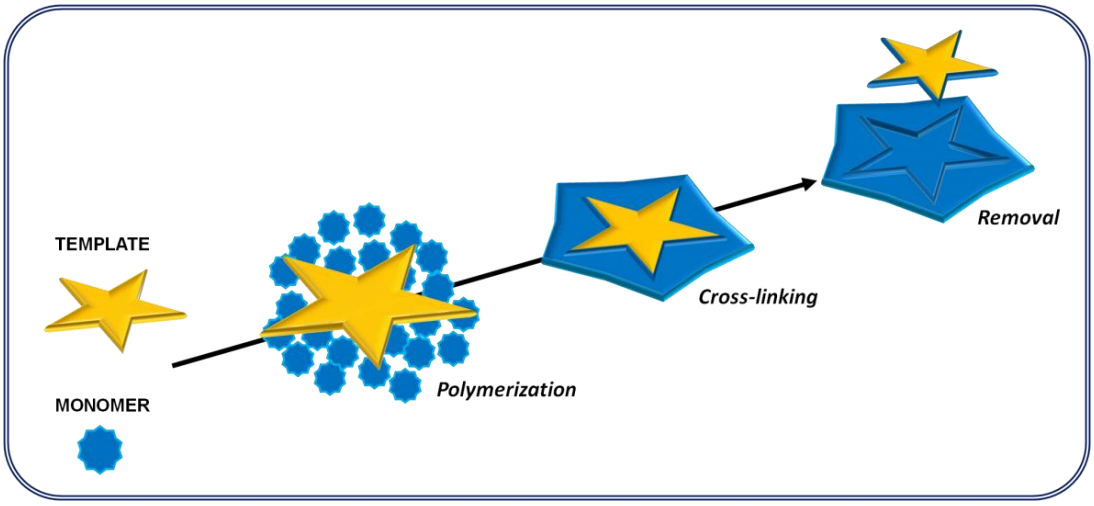

Figure 2.18: Schematic representation of the synthesis of molecularly imprinted polymers.

Many considerations have to be made in order to achieve the optimal conditions for the molecular imprinting process, such as, the choice of a suitable and compatible solvent for the polymerization reaction; the need or not to introduce a cross-linking element to ensure the best mechanical properties of the matrix; and also the optimization of the interactions between the functional monomer and the template molecule. Hence, a wide range of applications involving MIPs have been developed, including, solid phase extraction [178], chemical sensors [179], biomolecules separation [180] and controlled (targeted) drug delivery [181].

Among others, there are two main different ways to perform the imprinting of the complementary cavities that includes, bulk imprinting and surface imprinting [182]. The "bulk approach"

constitutes the most usual technique employed to imprint small molecule templates. It consists in a one-step procedure where a pre-polymer mixture is prepared with the target molecule and assembled on the surface of the transducer. Typically, all the components interact in solution, resulting in a polymeric matrix holding specific binding sites located in a homogenous distribution. In contrast, "surface imprinting" enabled the possibility to extend this biomimetic strategy to larger molecules, such as, proteins, by controlling the location of the imprinted molecules within the network. Thus, the template molecule is firstly assembled on the solid substrate surface and afterwards, the synthesis of a thin polymer film is finely tuned in order to allow the consequent diffusion and removal of this template, by creating the binding sites in proximity with the material's surface.

Another way to categorize the fabrication of MIPs is based on the covalent and non-covalent interactions between monomer and template [183]. In the beginning of molecular imprinting, the use of covalent interactions was a guarantee that the binding sites of the monomer could be employed in the exact stoichiometric ratio to the template molecule, enabling a higher control of the imprinted cavities. Later on, non-covalent imprinting become quite attractive due to the flexibility and simplicity of the method of operation, whereas the interactions occur by hydrogen bonding, ionic interactions, van der Waals. Although this last strategy requires binding site monomers to be present in large excess to ensure efficient complexation of the template molecule, creating random binding sites [184], currently the non-covalent route is the most widely used approach to fabricate MIPs. Interestingly, despite the development and application of MIP-based functionalities have been extensively spread due to the wide diversity of materials available, their "smart" incorporation in biosensing platforms is quite more restricted and a huge growing has been observed over the last two decades, as seen in Figure 2.19.

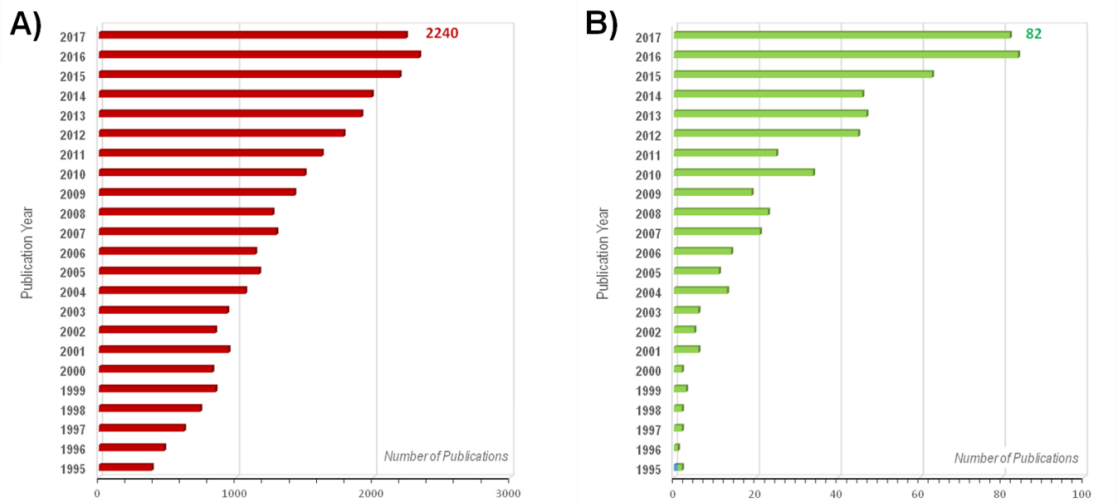

Figure 2.19: Graphical representation for the number of publications found in ISI Web of Knowledge related to A) MIP materials (molecularly-imprinted polymer* or molecular imprinting or MIP*) and B) MIP materials in biosensors (biosensor* and molecularly-imprinted polymer* or molecular imprinting or MIP*), in search made April 2018.

Therefore, molecular imprinting technology has become today an important tool to design nanostructured materials with highly tuneable recognition properties. As mentioned before, MIPs offer a wide range of applications including drug delivery systems [185], stationary phases [186], solid phase extraction [187] and also biosensing devices [188]. In parallel, several characterization techniques have been used during the assembly and application of imprinted materials [189]. Scanning electron microscopy (SEM), transmission electron microscopy (TEM) and atomic force microscopy (AFM) have been widely employed for morphological characterization; X-ray absorption and diffraction and X-ray photoelectron microscopy for structure analysis; nitrogen adsorption for measuring the specific surface area and pore size of polymers; and nuclear magnetic resonance (NMR), Fourier-transform infrared (FTIR) and ultra-violet visible (UV-Vis) spectroscopy for screening the interaction between functional monomers and template molecules.

Among the different ways of designing an efficient MIP-based biosensor, the choice of the transduction element is an important aspect to acquire the desirable sensitivity. For instance, QCM sensors have been widely used as synthetic coatings due to their special features, such as, low cost fabrication, mild conditions of operation and the ability to track extremely low mass variations [190]. Furthermore, polymeric-based MIPs with luminescent characteristics hold unique capability as signal transducers, enabling direct assessment of the binding events, which results in high selectivity and sensitivity of sensor devices [191]. Another strategy commonly used to fabricate biomimetic materials is through electrochemical transduction, whereas the main advantages are good adherence to the sensor surface, quick analysis periods and high control of the material thickness [192].

The use of MIPs as recognition elements towards the assessment of biological molecules was constantly reviewed, specifically, the effect of experimental conditions including pH, nature of the buffer and charges/functional groups have been investigated [187][193]. In recent years, the high stability and specificity of MIPs have turned these a promising alternative to immunosensors, bringing out new advantages to 8-OHdG detection. These synthetic materials are obtained by molecularly-imprinted technology and are linked to longer stability properties and lower production costs than their natural counterparts. In this context, and as far as one know, a single approach has been presented in the literature targeting 8-OHdG. It consisted in creating imprinted sensing films using metal chelating agents (used as monomers) cross-linked with bisacrylamide [194]. The affinity features of these materials towards 8-OHdG were measured by QCM gold sensing receptor surfaces, but the detection capabilities were not lower than 0.01 μM. In addition, such materials have been reported in 2008-2009, and since then no significant developments on molecular-imprinting technology have been addressed in the literature.

As said previously, the ultimate goal of molecular imprinting is to accomplish biomimetic materials with equal affinity and specificity as the biological ones. One strategy currently used is the integration of an imprinting approach with electrochemical sensing technique to enhance

both the sensitivity and selectivity of the sensors [195]. Sometimes, in order to achieve the low detection limits required, MIPs can be further improved by introducing nano-sized structures, such as, MWCNT [196], Au-NP [197], graphene [198], among others. In parallel, electrochemical technology coupled with a molecular-based approach have been successfully applied for the detection of small molecules, such as, melamine [199], glucose [200], dopamine [201], creatinine [202] and uric acid [203], which constitutes the ultimate evidence that these biological metabolites can be sensitively quantified in complex biological matrices.

From a practical perspective, the polymeric fraction of the MIP materials is prepared by radical polymerization, in the presence of suitable monomers, cross-linkers and initiators. While the conventional MIP materials use chemical reagents to generate radicals and initiate the polymerization [204], in recent years photo- [179] or electrically-driven [205] polymerization has been highlighted. For the purposed of an electrochemical sensing, electrochemical polymerization is the most straightforward approach to produce ultra-thin polymeric films deposited directly on the surface of a transducer. Electropolymerization enables to finely tune the thickness of the imprinted film by controlling the number of cycles and the scan-rate of the current that is applied in the electrode. Moreover, this *in-situ* technique allows attaching the sensor film to electrode surfaces of different shapes and sizes and, at the same time, by selecting a suitable solvent and supporting electrolyte the morphology of the polymeric matrix can be tailored. Another advantage of using the electropolymerization technique is the ability to carry out MIP synthesis and biomolecule immobilization in a one-step procedure and consequently, enabling a cost-effective approach. Recently, a MIP sensor for dopamine detection based on a chitosan-graphene mixture has demonstrated how bulk imprinting of small size molecules can be a simple and successful approach [141]. In addition, carbon nanotubes and supramolecular cyclodextrins have been chosen to modify electrodes for a simultaneous determination of DNA bases [148].

A wide range of electroactive monomers can be used for electrochemical polymerization, resulting in either conducting or non-conducting polymers. Nowadays, the most common electronically conducting polymers are polyacetylene, polyphenylene, polypyrrole, poly(aminophenylboronic acid), polythiophene, polyaniline and polyethylenedioxythiophene, among others [205]. Both conducting and non-conducting MIPs hold important advantages and limitations that should be taken into consideration during the preparation and operation of these biomimetic sensing devices. Firstly, during the electropolymerization of a conducting MIP, the growth of the polymer will proceed indefinitely, while for a non-conducting MIP film the polymer thickness is self-limited until the growth of the polymer insulates completely the underlying surface of the conductive electrode. So, for instance, if using a surface molecular imprinting approach controlling the polymer thickness around the target molecule is possible by carefully choosing the optimized conditions during the electro-deposition. In addition, the thickness of the MIP film can also have great implications in the response time and performance of the sensor [206].

Among the several electroactive functional monomers that allow the formation of non-conducting polymers, phenol-based MIPs have been widely employed as recognition units in biosensors. Briefly, phenolic compounds constitute an important class of chemical compounds consisting of a hydroxyl functional group (–OH) attached to an aromatic hydrocarbon ring structure. Phenolic compounds represent a large group of biological molecules and, specifically, biomolecules, such as tyrosine and tyramine are the building blocks of numerous natural products. The oxidation behaviour of phenol and *para*-substituted phenolic compounds was investigated by means of CV, DPV and SWV at a GC electrode in different electrolytes, with different pH values [207]. Moreover, several mechanisms regarding the oxidation of phenol and phenol derivatives have been widely described and, herein, a proposed electro-oxidation pathways for phenol is presented (see Figure 2.20) [208].

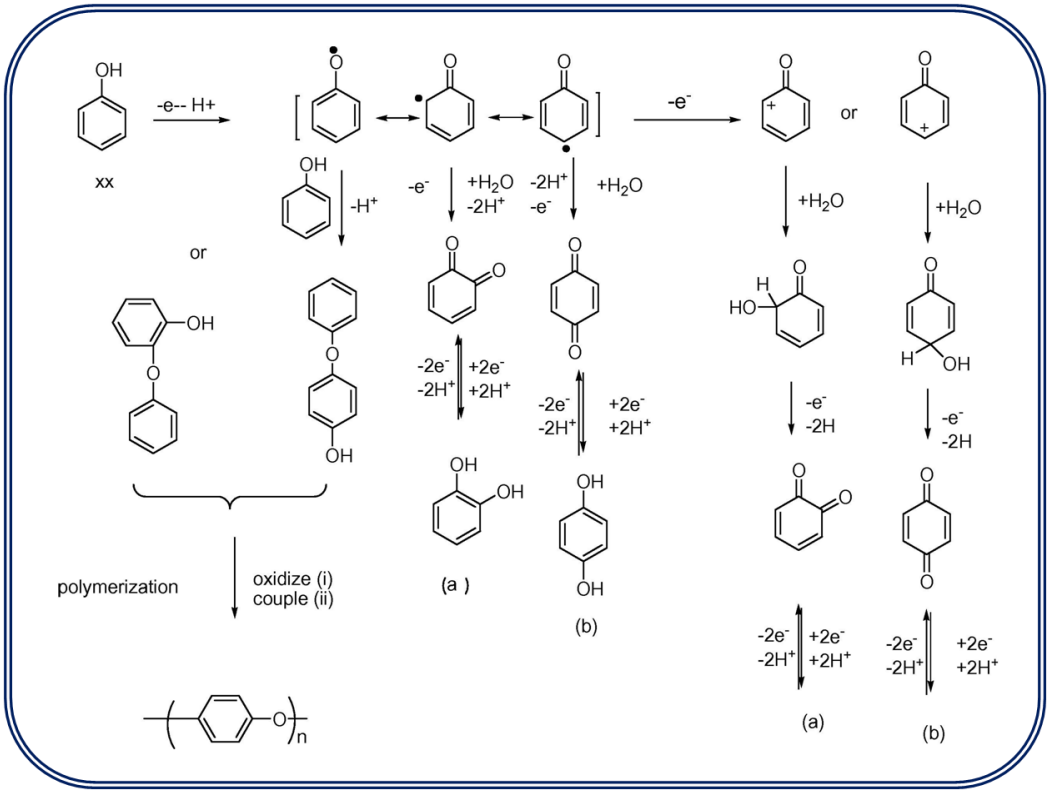

Figure 2.20: Adaptation of the proposed mechanism of phenol electro-oxidation [208].

As previously mentioned, during the electrosynthesis of MIPs, the compatibility of the functional monomer against the target-molecule is a crucial issue that also dictates the performance of the biosensing device. As far as our knowledge goes, only two studies involving a molecular imprint approach were used to detect 3-NT biomarker [209][210] and, both of these performed the synthesis of the polymeric matrix by using conventional free radical polymerization. Interestingly, in order to achieve the required low detections limits, nanostructured materials such as bimetallic nanoparticles and carbon dots were incorporated during the assembly of the biosensor. So, novelty approaches are still on-going in order to facilitate the fabrication and operation of sensing devices designed to be used in early detection context.

2.5 NANOMATERIALS

Among all requirements to develop a suitable *POC* biosensor, the ability to detect very low concentrations of the target molecule constitutes the core piece that limits the analytical performance of that device. Moreover, the sensitivity of any system can be also directly correlated between the amount of analyte and the strength of the respective output signal [184]. Over the years, nanotechnology has boosted their way towards the development of important tools for diagnostic and therapeutic applications. So, while searching for different amplification strategies, like for instance, the use of labels and electroactive molecules, the incorporation of nanomaterials during the design of electrochemical platforms have greatly enhanced the capabilities of the biosensing device [211]. A wide variety of nanoscale materials that includes, metal nanoparticles, semiconductor nanoparticles, quantum dots, carbon nanosized structures and magnetic nanoparticles (MNP) have been introduced as electrochemical signal amplifiers for the assessment of circulating biomarkers (see Figure 2.21).

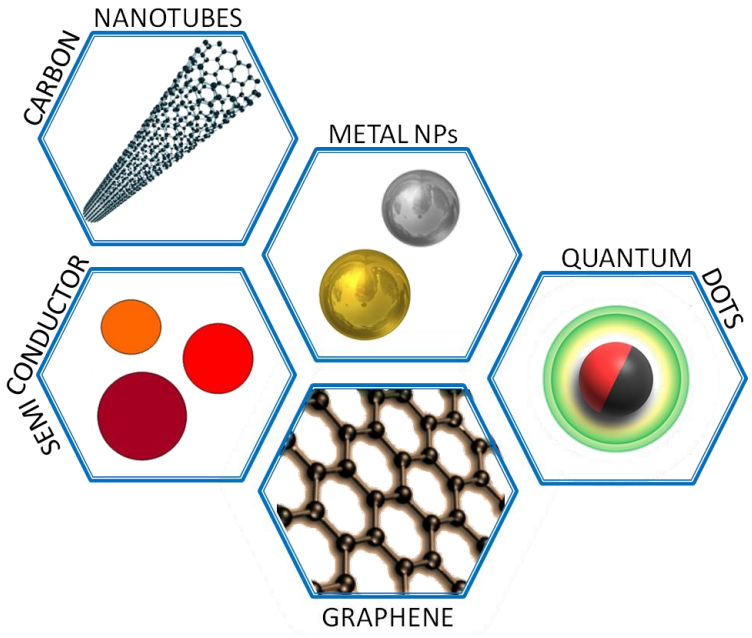

Figure 2.21: Representation of some nanostructured materials used for diagnostic applications.

The key properties of these nanostructured materials can be finely tuned by mainly controlling their size and surface features. For instance, for drug delivery applications the diameter of the particle must be well-defined in order to avoid nanotoxicity effects [212][213][214]. In addition, nanoparticles hold a unique size-dependent characteristic, particularly regarding magnetic and optical properties enabling an easy manipulation to obtain good detectable signals. Due to their high reactive surface area and small particle size, nanomaterials have been applied has an upgrade in amperometric biosensors causing an enhancement of the current analytical methodologies [215]. Au-based nanoparticles have been the most employed platform for

immobilization of biological molecules toward biomedical applications [109]. Owing to their easy preparation methods, good biocompatibility, high chemical stability and catalytic activity, Au-based nanoparticles have found attractive applications for the assessment of circulating biomarkers, making it highly compatible with novel *POC* devices [113]. Moreover, other noble metals like for instance Pt and silver (Ag) have been widely used for the preparation of nanoparticles mostly due to their good electrical conductivity, being incorporated in the development of electrochemical biosensors. Another advantage of these nano-based systems is their ability to enhance the electron transfer rate between biomolecules and the transducer platform.

Over the years, manufacturing of this type of nanomaterials has been classified as bottom-up and top-down approaches, as seen in Figure 2.22. Briefly, the bottom-up approach involves building up from the atom or molecular constituents to meso-level while the top-down approach is characterized by reducing the dimension of the original size from the bulk materials [216].

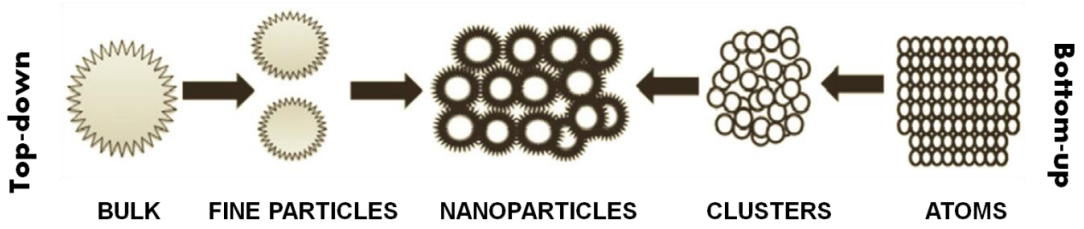

Figure 2.22: Adapted scheme of the different states during nanoparticles fabrication.

As mentioned before, carbon nanostructures have been widely employed not only as amplification signal strategies, but also as a convenient and straightforward approach to functionalize different kinds of surfaces [217][218]. However, herein the internal arrangement of these nanomaterials makes it architecture essential for the application, for which they are designed (see Figure 2.23). For instance, CNTs have been introduced in biosensor devices as biorecognition elements in different approaches, such as, a single probe [219] or a support surface onto the transducer platform [196][220] for amplification purposes.

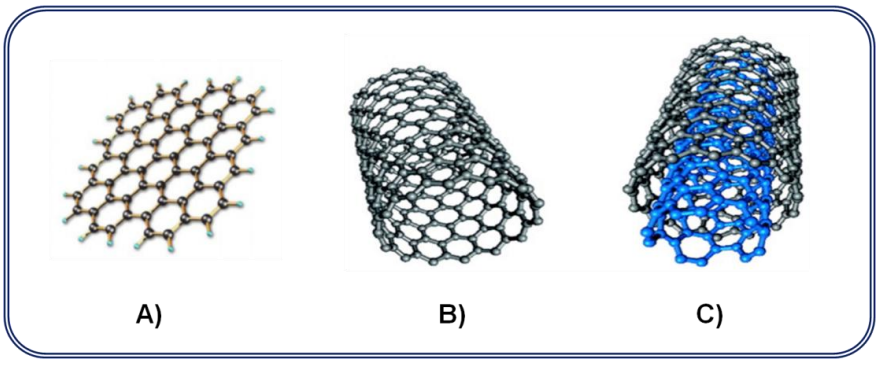

Figure 2.23: Different nanostructures of carbon A) graphene, B) SWCNTs and C) MWCNTs.

Nanoparticle-based assays can undergo at two different ways: (a) the binding of a label-nanoparticle to the target biomolecule will produce a measurable signal or (b) the nanoparticle can be directly employed as the transduction material. Besides the broad spectrum of analytical applications, another great advantage of these nanotechnology-based assays results from their ability to automation making these ideal for routinely diagnostic tools. Meanwhile, due to population variations in the expression of a single biological marker and also the lack of a known biomarker associated to a specific disease, there has been a great need to develop a biosensor array for multiplexed relevant biomarkers. Under this scope, various electrochemical biosensing devices coupled with multiplexing systems have been studied for early and minimally invasive clinical diagnosis [221]. In addition, different immobilization and biorecognition approaches can be combined and used simultaneously in order to get array-based systems, as presented in Figure 2.24.

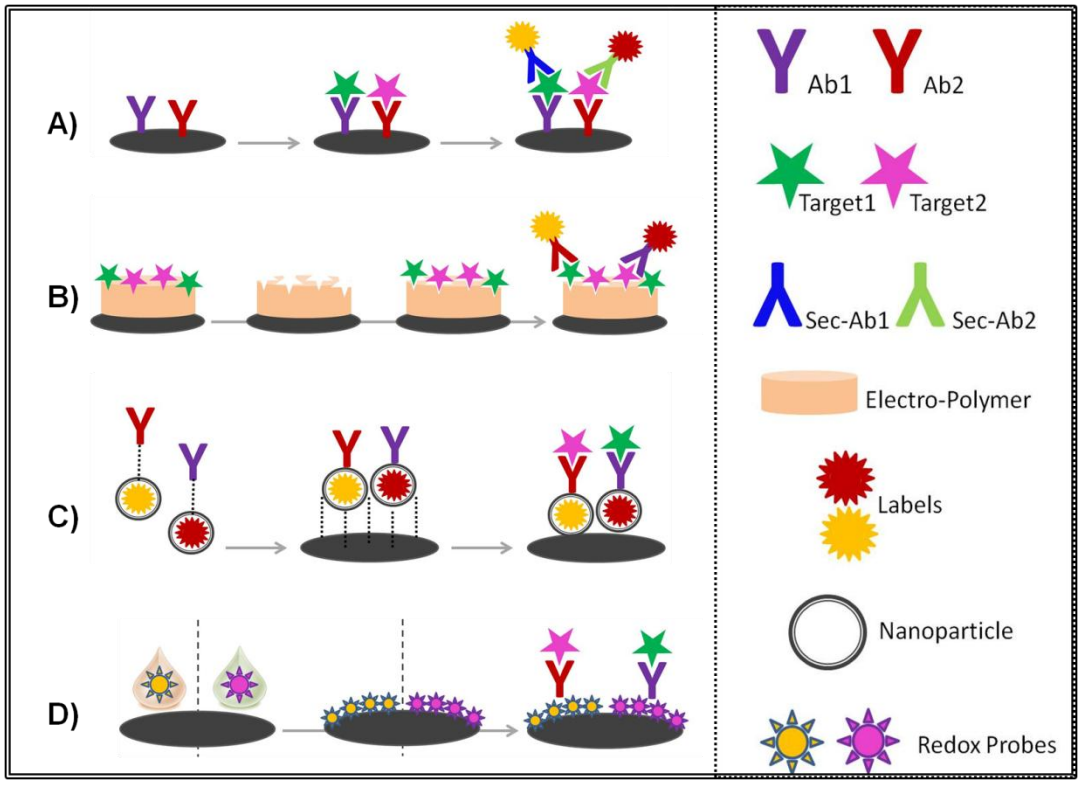

Figure 2.24: Different immobilization methodologies used during the fabrication of a sensor device: A) sandwich immunoassay approach; B) MIP-based approach; C) labeled nanoparticle approach and D) ink-based approach.

In general, nanoparticles can display electronic, magnetic and optical properties that behave in a different way against their bulk counterpart products. Among all the nanostructured materials mentioned before, magnetic nanoparticles have been extensively applied in order to immobilize different types of molecules on the transducer surface. Briefly, iron and oxygen are chemically combined to produce iron oxides, being the three most common forms of iron oxides

found in nature: magnetite (Fe_3O_4), maghemite (γ-Fe_2O_3), and hematite (α-Fe_2O_3) [222]. The preparation of magnetic-based materials, such as, Fe_3O_4, has received special attention for their incorporation in bio-related applications, like for instance, magnetic resonance imaging (MRI) [223], hyperthermia anti-cancer theraphy [224], separation [225], magnetic drug targeting [226], purification of molecules [227] and also environmental remediation applications [228]. Specifically, functionalized magnetic nanoparticles are being widely applied for sample preparation procedures due to the following advantages [229]:

(i) high extraction efficiency (due to the high surface area-to-volume ratio);

(ii) fast separation;

(iii) facile preparation and surface modification of the extraction phase;

(iv) high selectivity for the target analytes and suitability for complex matrices;

(v) good reusability;

(vi) excellent dispersibility in aqueous solution and easy to operate;

The high surface to volume ratio in parallel to their biocompatible properties, make magnetic nanoparticles quite appealing to be used as immobilization support. Moreover, the ability to induce a simply "switch on-off" magnetic moment in the presence of an external magnetic field can be a great advantage in terms of solution manipulation, separation, pre-concentration and even recovery. As shown in Figure 2.25, iron oxide magnetic nanoparticles can be prepared by three different routes: chemical, physical and biological [222].

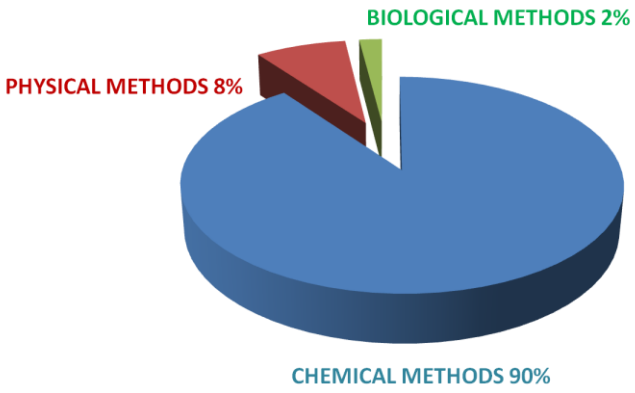

Figure 2.25: Adapted graphic concerning the different routes used for the synthesis of iron oxide magnetic nanoparticles [222].

In general, the most common method to prepare magnetic nanoparticles is by using a chemical approach, in which iron oxides are synthesized through the co-precipitation of Fe^{2+} and Fe^{3+}, with the addition of a strong base. In contrast with the physical methods that include complex procedures and show some variability related to the nano-size of the particles, the chemical method is quite simple and easy-to-use, enabling to finely tune the size, composition and shape of the magnetic nanoparticle by controlling some experimental parameters, like, type of salt, Fe^{2+} and Fe^{3+} ratio, pH, and ionic strength [230][231][232].

However, magnetic nanoparticles are not completely stable at normal physiological conditions, showing a great tendency to aggregation due to their hydrophobic nature. Among the different approaches available to enhance the dispersibility and stability of these iron oxides (see Figure 2.26), silica coating has been one of the most attractive and common technique to be implemented. With this approach, silica shells not only prevents the nanoparticles from agglomeration but, in addition, allows to modify and encapsulate other materials enhancing the versatility and utility of this kind of core-shell systems.

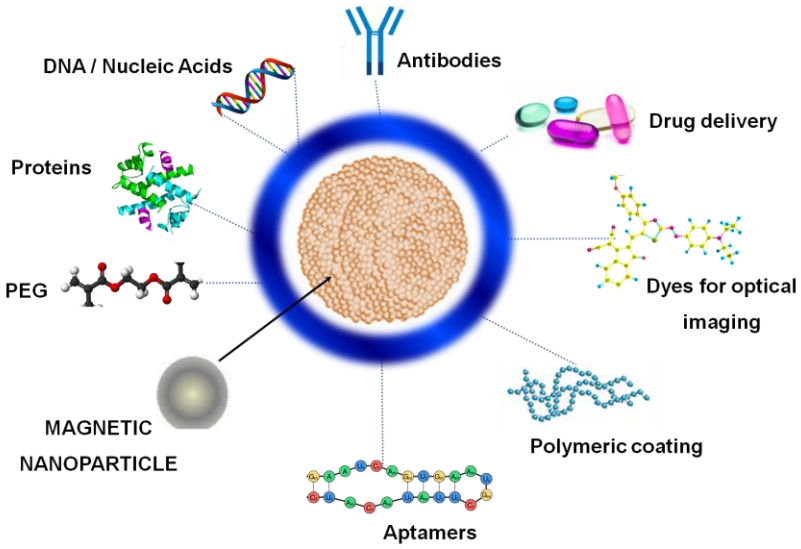

Figure 2.26: Silica applications conjugated with magnetic nanoparticles as nanoplatforms.

CHAPTER 3

3 8-Hydroxy-2'-deoxyguanosine biomarker detection down to picoMolar level on a plastic antibody film

The results presented in this chapter were published in Gabriela V. Martins, Ana C. Marques, Elvira Fortunato, M. Goreti F. Sales, *"8-hydroxy-2'-deoxyguanosine (8-OHdG) biomarker detection down to picoMolar level on a plastic antibody film*", *Biosensors and Bioelectronics* (2016), 86, p. 225-234. ***doi: 10.1016/j.bios.2016.06.052.***

3.1 INTRODUCTION

In the field of biosensors, one of the most important aspects concerning the assembling of MIPs is the proper integration between transducer and recognition elements. In this sense, electropolymerization approach enables the formation of selective binding sites, at a precise spot, closer to the electrode surface. Thus, by controlling some experimental parameters, such as, the initial concentration of the monomer and also the ratio template-monomer one can finely tune the performance of the MIP-based sensor. In addition, electrochemistry is a simple, low cost and quite sensitive tool, easily applied to electroactive species in aqueous media.

Herein, special emphasis has been given to electropolymerization of phenol for the preparation of MIP-based sensors, due to its straightforward preparation and its ability to interact with different analytes, through hydrogen bonding and ππ stacking [177][233]. An overview of the literature have showed that the electropolymerization of various phenolic compounds have been widely investigated in different electrode surfaces including vitreous carbon electrode [234], Pt [235], Au [236], carbon steel and stainless steel [237]. The preparation of MIPs of small molecules have been acknowledged as an easy approach to synthesize biomimetic materials holding specific functionalities. Combined with an electrochemical approach, MIP-based sensors have been designed with high sensitivity and selectivity for the detection of small molecules, like, melamine [238], theophylline [239], creatinine [240].

In the present work, a simple and sensitive electrochemical MIP-based sensor for detection of urinary 8-OHdG has been assembled via electropolymerization. To this end, 8-OHdG was employed as the template molecule and phenol as the functional monomer (see Figure 3.1). As mentioned before, one of the main advantages of the application of polyphenol films is their facile preparation by electropolymerization in mild aqueous media suitable for biological molecules. Several experimental parameters have been carefully optimized and the electrochemical performance of the designed MIP sensor was investigated by CV and EIS. Moreover, it was employed to detect 8-OHdG in urine samples as a non-invasive approach to assess the extent of DNA oxidative damage. Thus, the proposed biosensor provides a highly selective tool to be implemented as an easy-to-use protocol for sensitive detection of 8-OHdG in biological samples.

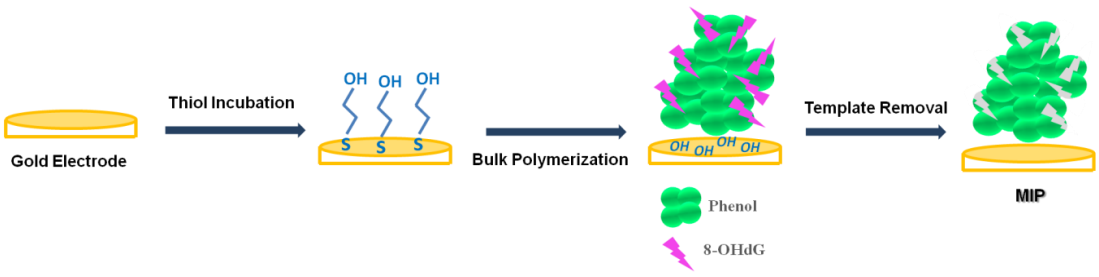

Figure 3.1: Schematic representation of the assembly of the gold-modified imprinted sensor.

3.2 EXPERIMENTAL SECTION

3.2.1 Reagents and Materials

All chemicals were of analytical grade and used as supplied without further purification. All buffer solutions were prepared in phosphate buffered saline (PBS, 0.01 M, pH 7.4) with ultrapure water Milli-Q laboratory grade. The exact pH values were measured with a pH meter (Crison Instruments, GLP 21 model). Potassium hexacyanoferrate III ($K_3[Fe(CN)_6]$) and potassium hexacyanoferrate II ($K_4[Fe(CN)_6]$) trihydrate were obtained from Riedel-de-Haen; 3-mercapto-1-hexanol, phenol (for molecular biology) and 8-OHdG (98%) from Sigma-Aldrich; ethanol absolut (99.8%) from Panreac and the Fluorescein Isothiocyanate (FITC) labeled antibody against 8-OHdG (polyclonal, 100 μg, 0.5 mg/mL in PBS) from Biorbyt. Piranha solution was prepared by carefully mixing concentrated sulfuric acid (H_2SO_4, 95%, Normapur) and hydrogen peroxide (H_2O_2, 30%, Scharlau) in 5:1 ratio. All experiments were carried out at ambient temperature.

3.2.2 Apparatus

Electrochemical measurements were performed by using a classical three-electrode system consisting of a gold-modified electrode as the working electrode, a platinum wire as the counter electrode and a Ag/AgCl wire as the reference electrode. The diameter of the working electrode was 2 mm. The electrochemical measurements were conducted with a potentiostat/ galvanostat from Metrohm Autolab and a PGSTAT302N with a FRA module, controlled by ANOVA software.

FTIR, Raman spectroscopy and SEM characterization was conducted using gold-screen printed electrodes (Au-SPE) purchased to DropSens (DRP-220AT), instead of the conventional gold electrode. FTIR measurements were performed using a Thermo Scientic Smart iTR Nicolet iS10, coupled to the Attenuated Total Reflectance (ATR) smart accessory, also from Thermo Scientific. For Raman analysis, we have used a Thermo Scientific DXR Raman microscope system with a 100 mW 532 nm excitation laser. For both FTIR and Raman measurements, data analysis was performed with OMNIC software. Surface morphology of the polymeric films was examined in a Carl Zeiss AURIGA Crossbeam SEM-FIB workstation.

The images concerning MIP and NIP labeled with FITC-anti-8-OHdG were collected by a Confocal Laser Scanning Microscope (LSM 700/ Carl Zeiss). Afterwards, the image analysis was performed using ZEN 2.1 software (Carl Zeiss).

3.2.3 Gold electrode cleaning

Before use, the bare gold electrode was cleaned by dipping in a mixture of piranha solution for 20 min, rinsing abundantly with ultra-pure water and drying. Then, the electrode was carefully polished with aqueous alumina slurries, with successive decrease in particle size (1–0.05 μm), followed by sonication in ethanol-water mixture. Finally, the electrode was

abundantly washed with ultra-pure water and allowed to dry at ambient temperature. Before each experiment, the electrode was subjected to cyclic sweeping between −0.2 and +1.5 V, in 0.5 M H_2SO_4 solution, until a stable cyclic voltammogram was obtained (more or less 5 cycles).

3.2.4 Sensor fabrication

Initially, Au surface of the electrodes was modified with a monolayer of 3-mercapto-1-hexanol. The clean Au electrode was immersed in a 20 mM thiol solution for 2 hours, at 25 ºC, in order to form the covalent attachment of thiol to the Au electrode surface. This incubation step was responsible for the formation of a stable self-assembled monolayer on the electrode surface through a strong gold-sulfur interaction.

MIPs were prepared by bulk polymerization and all experiments were carried out at ambient temperature. Previously, the phenol solution was deoxygenated by bubbling nitrogen gas for 15 min. Afterwards, the electropolymerization was performed by CV (3 cycles) in the potential range +0.1 to +0.9 V, at a scan rate of 20 mVs^{-1}, in a 0.01 M PBS solution, containing both phenol monomer and the template molecule 8-OHdG. MIP solutions were renewed every 3 experiments. Then, template removal was carried out by consecutive immersion in ethanol and PBS solutions, for 30 min each, leading to the formation of recognition cavities in the MIP structure. This solvent was chosen to ensure an efficient removal of 8-OHdG, while keeping mild conditions and avoiding pH changes upon the polymeric film.

Control electrodes (NIPs or non-imprinted polymer) were prepared by following the same procedure but without the presence of the template molecule. The NIP electrode had the same treatment as the MIP sensor, in order to ensure that variations were only attributed to the imprinting features. All the modified electrodes were stored at 4 ºC before further use.

3.2.5 Electrochemical assays

Electrochemical measurements for characterization of the modified electrodes were performed by using different electrochemical techniques, such as, CV and EIS. For CV assays, the potential was scanned from −0.1 to +0.4 V, at 50 mVs^{-1}, in 5.0×10^{-3} mol/L $K_3[Fe(CN)_6]$ and $K_4[Fe(CN)_6]$, in 0.01 M PBS solution, pH 7.4. EIS assays were conducted with the same redox couple $[Fe(CN)_6]^{3-/4-}$, at a standard potential of +0.15 V, with a number of frequencies equal to 50, logarithmically distributed over a frequency range 10^{-3}-10^{4} Hz. All experiments were conducted in triplicate at ambient temperature.

Calibration curves were made with 8-OHdG standard solutions ranging from 0.10 and 100.0 pg/mL. All standard solutions were freshly prepared in PBS pH 7.4. The time given for 8-OHdG incubation before reading of the redox probe was set to 20 min.

3.2.6 Surface analysis

Each step of chemical modification on the gold electrode was followed *ex-situ* by FTIR-ATR, Raman and SEM analysis. For this purpose, the polymeric films were grown on Au-SPE for 10 CV cycles. Before measurement, samples were left drying at room temperature, for at least one day. Regarding FTIR analysis, the infrared spectra were collected after background correction, with a number of scans set to 500. Raman spectra were recorded using a 4 mW power, exposure time 60 s, number of exposures 10 and 50 μm slit aperture. SEM images were obtained by using an accelerating voltage of 5 kV with an aperture size of 30 μm.

3.2.7 Preparation and characterization of the FITC-labeled surfaces

Fluorescence microscopy was employed to assess the presence and distribution of the rebound 8-OHdG molecule via fluorescent emission from the FITC labeled antibody. The fluorescence studies were conducted on MIP and NIP surfaces built on Au-SPE. Afterwards, the rebinding of 8-OHdG molecule was performed in the same conditions of the calibration procedure. The antibody was previously diluted 1:100 in PBS and incubated on top of the electrodes for one hour (4 ºC). All the fluorescence measurements were carried out with the excitation wavelength of 488 nm and the emission wavelength of 520 nm. Control images of non-imprinted electrodes were obtained in identical experimental parameters. Afterwards, all images were processed in equal conditions, by applying a brightness filter of 80% and a contrast filter of 90% in order to improve fluorescence visualization.

3.2.8 Selectivity studies and analysis in urine samples

The selectivity experiments were carried out through incubation of the MIP-based sensor in 8-OHdG solution (5 pg/mL) in the presence of each individual interfering species. Uric acid, citric acid and glucose were chosen as interfering molecules and used at concentrations mimicking the physiological levels. In addition, selectivity features of the MIP were assessed directly in human urine samples, due to their complex nature as a biological fluid. The urine samples were collected in sterile bottles to avoid any contamination. After collection, the fresh urine samples were directly frozen in aliquots of 1 mL. Before analysis, the samples were diluted in PBS buffer, in a 1:1000 ratio.

The detection analysis of 8-OHdG in urine samples was tested by immersing the MIP sensor in the diluted samples during a period of incubation of 20 min, followed by EIS analysis. Preliminary recovery tests were performed by adding a known concentration of 8-OHdG to urine samples.

3.3 RESULTS AND DISCUSSION

3.3.1 Optimization of experimental variables

During the fabrication of MIP materials, several parameters need to be carefully optimized. Herein, the concentration of monomer, the number of CV cycles and its ratio against the target analyte have been considered, as these are found critical steps at the MIP film assembly [201][241]. The pH was also a very important parameter, but it was kept at this stage equal to 7.4, as this is a close condition to that in biological fluids.

The electropolymerization of phenol was achieved by CV. Figure 3.2A illustrates the first voltammetric cycle concerning the electropolymerization of phenol, at pH 7.4, for different concentrations of monomer. As shown, pure phenol solutions exhibited only an oxidation peak around +0.6 V, indicating an irreversible oxidation reaction of the monomer on the electrode surface. It was clear that the peak current increased with increasing monomer concentration 0.25 < 0.50 < 1.25 mM. Due to the non-conductive behaviour of polyphenol [205], this accounted the growth of a strongly passivating polymer layer on the electrode surface. In general, a great increase in the overall resistance of the sensing layer may hinder the sensitivity of the device. On the other hand, for concentrations of monomer below 0.25 mM, the efficiency of the polymerization reaction may be small, questioning the stability of the polymeric film. Therefore, 0.25 mM was identified as the optimum phenol concentration for the preparation of the 8-OHdG sensor.

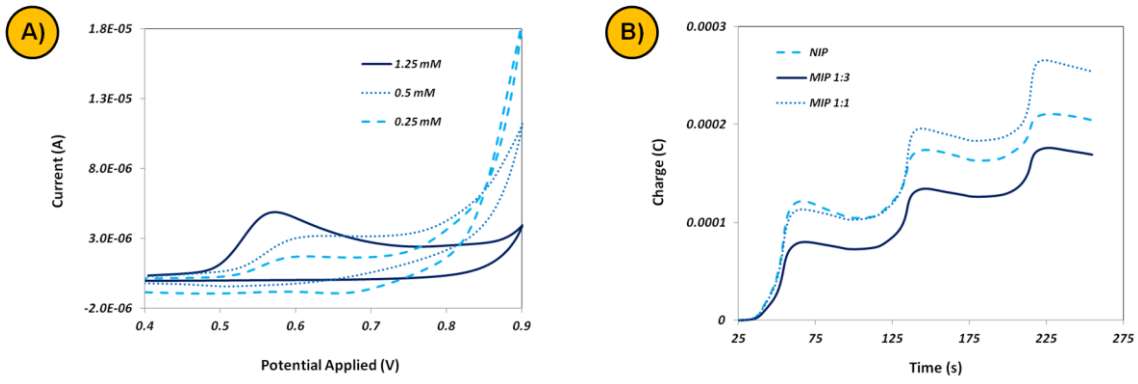

Figure 3.2: A) Cyclic voltammograms of a gold-modified electrode immersed in 0.01 M PBS aqueous solution containing different concentrations of monomer phenol (0.25, 0.5 and 1.25 mM), pH 7.4, scan rate 20 mVs-1; B) Charge variation during electropolymerization of phenol (3 cycles) obtained from MIPs with different ratios of template to monomer (1:3 and 1:1) and NIP in 0.01 M PBS.

Another challenge within the MIP technology is to find an agreement regarding the concentration and distribution of recognition sites close to the sensor surface and, simultaneously, well connected along it [242]. Likewise, the number of cycles during the

electropolymerization of the monomer can tailor both the thickness and structural characteristics of the resulting polymeric film [236]. In our investigations, no more than 3 voltammetric cycles were used during the electropolymerization of phenol to avoid that 8-OHdG molecules could be buried deep within the polymeric film, inhibiting their subsequent elution in order to create effective recognition sites. In addition, a higher number of cycles would generate a less conductive surface and, subsequently, a less sensitive device.

Next, the effect of the mole ratio of 8-OHdG molecule to phenol monomer was also investigated. Figure 3.2B presents the time-dependent charge response during electropolymerization of NIP films and MIP films with different ratios of template/monomer (1:3 and 1:1). The thickness of the polymer film can be roughly estimated from the total charge during electropolymerization [243]. According to Figure 3.2B, the total charge resulting from phenol electro-oxidation in the NIP is around 2×10^{-4} C and, therefore, the thickness of the polymeric film was about ~60 nm. This result is in agreement with previous studies performed in similar conditions [236]. Different ratios of template to monomer were investigated for the MIP material, in order to optimize the amount of binding sites available for the selective re-binding of 8-OHdG. When the ratio was 1:3, the charge response decreased comparatively with NIP, as shown in Figure 2B, while in the case of a ratio 1:1, the charge response increased again. So, although our results have showed that the presence of the target analyte affects the total charge resulting from phenol oxidation, the previous approach used to estimate the thickness of the films can only be applied to the polymer layer. Overall, the presence of the target molecule within the film hindered the growing of the polymer, as it did not participate in the polymerization stage. In addition, calibration curves of 8-OHdG in PBS solution at pH of 7.4 were performed for both MIPs and the highest electrochemical response (highest sensitivity) was obtained for the MIP with the ratio template to monomer of 1:1(see Figure 3.3). Thus, the optimal template-monomer ratio of 1:1 was chosen for the following studies expressing a final concentration of imprinted molecule of 75 μg/mL.

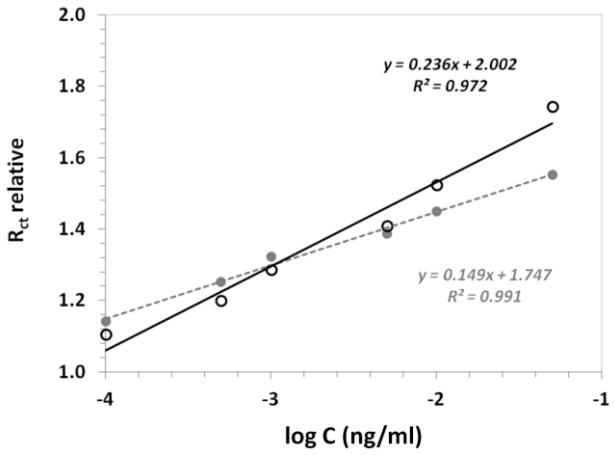

Figure 3.3: Calibration curves of 8-OHdG obtained for MIPs with different ratios of template/ monomer, 1:3 (closed gray circles) and 1:1 (open black circles).

3.3.2 Preparation and electrical follow-up of MIP sensor

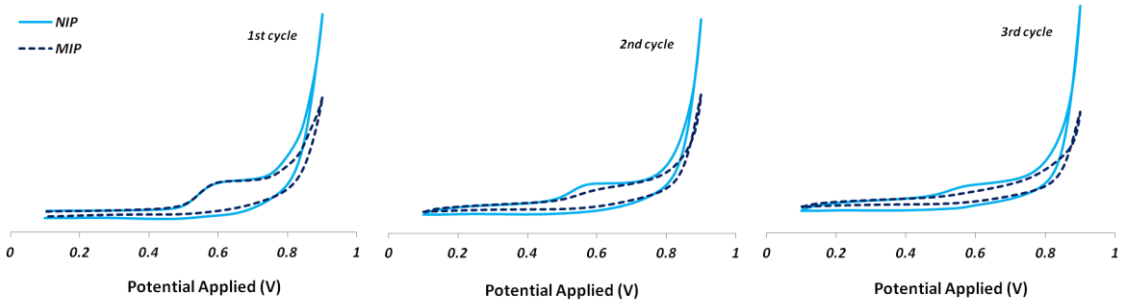

Figure 3.4: Cyclic voltammograms concerning the electropolymerization of 0.25 mM phenol in 0.01 M PBS, pH 7.4, (scan rate 20 mVs-1, 3 cycles) at gold-modified electrodes with (dashed line) and without (straight line) the template molecule 8-OHdG.

Figure 3.4 shows a typical voltammogram recorded during the electropolymerization of phenol in the presence (dashed line) and absence (solid line) of 8-OHdG. The only peak visible occurred around +0.6 V and is due to phenol oxidation. This record also indicated that 8-OHdG was not electroactive in the positive range 0.1–0.9 V, meaning that the template structure was not electrochemically altered and was preserved during the imprinting step. Furthermore, it was clear that the current decreased with increasing number of cycles and the highest current was obtained in the 1st cycle. As expected, after the 2nd and 3rd cycles, the phenol oxidation peak started to disappear, which resulted from the formation of a non-conductive layer that blocked the access of the monomers to the electrode surface. It was interesting to see that the peak current in the presence of 8-OHdG was smaller than that obtained without it, which can be a strong indication of the existing interactions between the phenol monomer and the template molecule. The hydroxyl groups in the 8-OHdG molecule could be interacting with the phenol monomer through hydrogen bonding. This is consistent with several other reports that have confirmed the importance of electrostatic interactions and hydrogen bonding between template molecules and phenol [53][197]. Recently, the construction of graphene-based MIPs have supported that hydrogen bonds between template and polymeric matrix can enhance the recognition and selectivity for the target molecule [193]. Moreover, previous studies have demonstrated that π donor-acceptor interactions between electropolymerized phenol and an imprinted template molecule can be used as a novel method to generate imprinted polymers [233].

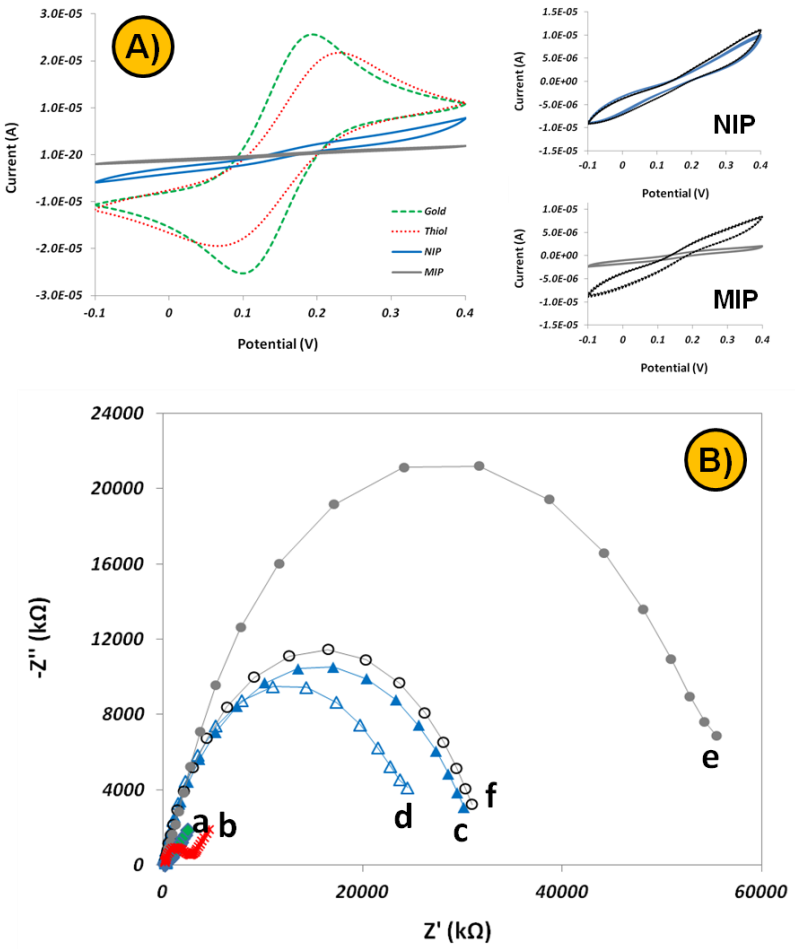

Figure 3.5: A) CV of the gold electrode (green line), thiol-modified gold electrode (red line), NIP and MIP after electropolymerization (blue and grey line, respectively) and after template removal (black lines, on the right side), measured in aqueous solution containing 5 mM $[Fe(CN)_6]^{3-/4-}$ in 0.01 M PBS pH 7.4 and B) EIS of (a) gold electrode, (b) thiol-modified gold electrode, NIP (c) before and (d) after removal, MIP (e) before and (f) after removal, in aqueous solution containing 5 mM $[Fe(CN)_6]^{3-/4-}$ in 0.01 M PBS.

The construction of NIP and MIP sensors was followed *in-situ* by CV and EIS measurements in 5 mM $[Fe(CN)_6]^{3-/4-}$ solution, prepared in 0.01 M PBS as the supporting electrolyte. Figure 3.5A shows the cyclic voltamogramms obtained with gold-modified electrodes, where a couple of well-defined redox peaks was evidenced, as a result of the reversible electron transfer of the redox pair $[Fe(CN)_6]^{3-/4-}$. After pre-incubation of thiol onto the gold surface, the current of the redox peak observed decreased, meaning that this modification slightly increased the electrical resistance of the working electrode. This outcome was expected as the result of the spontaneous formation of a closely packed monolayer via a strong gold-sulphur interaction between the –SH group and the gold. Afterwards, it was found that the formation of polyphenol polymeric layer hindered the electron transfer process resulting in a good blocking efficiency on the electrode surface. Thus, the NIP and MIP formation are characterized by the disappearance of the pair of redox peaks [244]. Interestingly, the MIP film showed lower current change throughout the voltammogram in comparison to the NIP, which was a strong evidence of the

presence of the template 8-OHdG within the polymer matrix. Once the template was extracted from the MIP, the film recovered some of the current change lost, accounting the exit of the imprinted template from the polymer matrix and thereby confirming the formation of binding sites. As expected, after the 8-OHdG removal step (with ethanol-PBS solutions), the electrochemical behaviour of the NIP was unaltered.

EIS studies were used to follow-up the variation of gold-modified electrodes after each chemical change, since this electrochemical measurement holds a high sensitivity and it is strongly suitable in the detection/follow-up of small alterations of non-conductive polymers. Randle's equivalent circuit was adopted to model the physiochemical process occurring at the gold electrode surface. In general, the impedance spectra included a semi-circular portion at higher frequencies and a linear portion at lower frequencies which corresponded to the electron-transfer resistance and the diffusion process, respectively. The diameter of this semicircle is the R_{ct} that controls the electron transfer kinetics of the redox-probe at the electrode interface. Figure 3.5B illustrates the Nyquist diagrams of the electrodes fabricated at each step in the presence of 5 mM $[Fe(CN)_6]^{3-}/[Fe(CN)_6]^{4-}$, which were carried out at the formal potential of 0.15 V with a frequency range of 10000 to 0.001 Hz. The bare gold surface presented a small semicircle domain as the result of a very fast electron-transfer process (Figure 3.5B-a). Afterwards, the modification with the thiol monolayer onto the gold surface gave rise to a subsequent increase in R_{ct} (Figure 3.5B-b). As expected, the electropolymerization of phenol resulted in a substantial increase of impedance (Figure 3.5B-c) due to the blocking of electron transfer by the polymeric matrix. Furthermore, a higher increase of the impedance was observed when the polymerization of phenol took place in the presence of 8-OHdG (Figure 3.5B-e), accounting the presence of 8-OHdG entrapped inside the polymeric matrix (consistent with the fact that the addition of 8-OHdG promotes an R_{ct} increase, evidenced in Figure 3.3. Finally, the elution of the template from the polymer matrix is acknowledged as one of the most important steps, since it holds a direct influence on the sensitivity to the template recognition. Previous studies with other small template molecules, like 8-OHdG, have performed the removal of these molecules from the MIP structure by extraction with PBS or ethanol solutions [201][241]. For instance, a capacitive sensor developed by electropolymerization of phenol has achieved theophyline template elution via aqueous-ethanol mixtures [244]. Herein, the removal of the template was achieved by incubating the MIP film in ethanol and PBS. This procedure has led to a substantial R_{ct} decrease of the MIP film (Figure 3.5B-f), accounting the formation of imprinted cavities that facilitate the diffusion of $Fe(CN)_6^{3-/4-}$ through the polymer network. The same treatment applied to the NIP film has generated only a slight R_{ct} reduction, correlated to the washout of unreacted monomer or small oligomers (Figure 3.5B-d). Thus, it seems evident that the huge R_{ct} decrease at the MIP layer is mostly linked to the successful exit of the target template from the polymeric material.

3.3.3 Characterization of the modified surfaces

FTIR and Raman measurements were conducted in order to verify each chemical modification step along the sensor assembly, specifically, the formation of polymeric films produced by electro-oxidation of 0.25 mM phenol in PBS solution. In both assays, the analysis was performed directly on Au-SPE. Figure 3.6 shows the FTIR-ATR and Raman spectra of bare Au, the thiol modification, and NIP and MIP films assembled on the working electrode area.

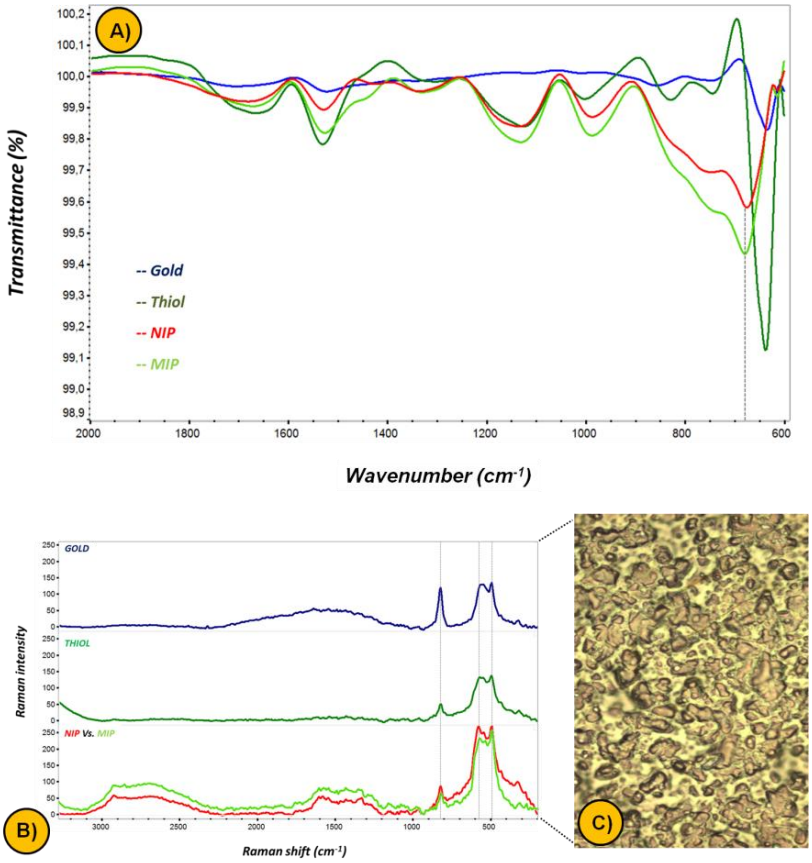

Figure 3.6: A) FTIR-ATR spectra of gold, thiol-modified gold, NIP and MIP electrodes; B) Raman spectra of gold, thiol-modified gold, NIP and MIP electrodes and C) typical image from Raman, measured at 50x magnification, of the gold-screen printed electrodes (Au-SPE).

Regarding the FTIR data, the assembling of a thiol layer on the gold surface was confirmed by the appearance of a well define band around 1100 cm^{-1} that could be attributed to the stretching vibration of the C–O bound [235]. The formation of the polymeric layer of polyphenol was confirmed by the broad band associated with the aromatic out-of-plane C–H deformation vibrations in the range 750-650 cm^{-1} (only visible in NIP and MIP spectra) [245]. No differences could be verified on the FTIR spectra of NIP and MIP materials, but this was consistent with the fact that their main chemical composition was the same.

The Raman spectra of the Au-SPE showed 3 bands at 500, 550 and 830 cm^{-1} that could be assigned to carbon compounds that are present in the manufacturing of the gold ink paste.

Comparison between Au-SPE and thiol-modified spectra showed a substantial reduction in the intensity of the 830 cm^{-1} peak as the result of the assembling of a monolayer of thiol, thus covering the gold surface. Spectra of NIP and MIP films produced over the Au-modified-SPEs presented a significant increase of the Raman shift at 500 and 550 cm^{-1}, that could be attributed to the aromatic ring deformation, confirming the growth of the polymeric chain. Interestingly, the two broad undefined bands around 1500 and 2900 cm^{-1} are probably a strong indication of surface modification due to polymerization, as these are expected to be related with the emission of fluorescence coming from the aromatic rings.

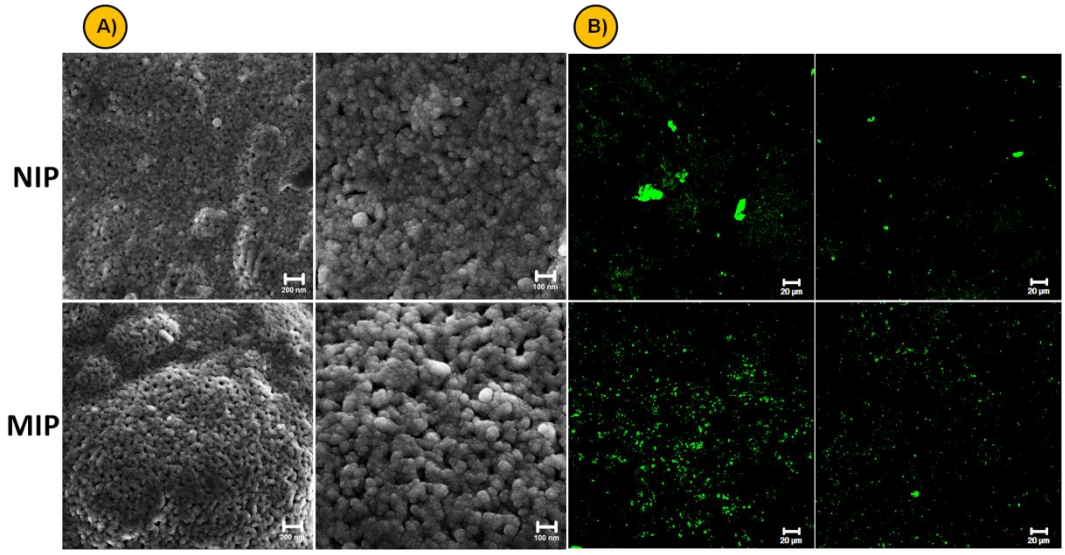

Figure 3.7: A) SEM micrographs of NIP and MIP electrodes and B) confocal imaging of FITC antibody against 8-OHdG attached to NIP and MIP surfaces.

Surface morphology of the prepared NIP and MIP electrodes was further studied by means of SEM. From figure 3.7A, we verified that the formation of the phenol polymer seems to be well distributed/spread on the surface. As expected, due to the small dimension of 8-OHdG molecule, it was impossible to visualize the imprinted cavities but, interestingly, MIP surface seems to hold a more globular morphology, with more islets, compared with the NIP one. Moreover, the comparison between NIP and MIP images have showed that the MIP surface presents a higher porosity than NIP. This different behaviour in the polymer morphology can be another strong indication that the presence of 8-OHdG molecule during electropolymerization resulted in a different structural polymeric growth.

Previous studies have reported the design and development of aqueous phase molecular imprinting coupled to confocal microscopy imaging, aiming to visualize the imprinting effect [246]. Herein, we have followed the binding of a FITC labelled antibody targeted against 8-OHdG to the surface of the sensor in order to track the 8-OHdG oxidative stress biomarker rebound into the imprinted cavities. Figure 3.7B presents confocal micrograph images of FITC-labelled antibody 8-OHdG on the electrode surfaces. The well-localized fluorescence signals

present on MIP sample indicated that the FITC labelled antibody have selectively bound to the target molecule. Moreover, fluorescence signal points were localized in a homogeneous manner only on the MIP electrode, which is strong evidence that the target molecule was rebound and, consequently, imprinted cavities have been successfully created. In parallel, the image of a non-imprinted polymer control taken at identical experimental parameters presents a distinct lack of a homogeneous distribution of fluorescence. Furthermore, our findings also confirmed that non-specific labelling almost did not occur. This approach has already been acknowledged as a useful tool to assess the specific and selective attachment of target molecules for sensoring purposes [247].

Overall, the combined information of FTIR and Raman spectra, the electron microscopy images and confocal microscopy photographs confirmed the successful formation of NIP and MIP films and the ability of MIP film to rebind selectively and sensitively to its target compound.

3.3.4 Performance of MIP sensor

3.3.4.1 Calibration curve

The analytical performance of 8-OHdG sensory materials was evaluated by recording calibration curves. Figures 3.8A-B presents EIS calibration curves plotted with the R_{ct} of MIP and NIP sensors against the logarithm concentration of 8-OHdG. For each calibration study, sensors were previously incubated in PBS solution until a stable response was obtained. Afterwards, the time given for 8-OHdG incubation was set to 20 min.

In order to evaluate the specificity and selectivity of the assembled biosensors, the value of the imprinting factor (IF = [*template rebound by MIP*] / [*template rebound by NIP*]) can be used as a comparative tool. From the ratio of sensitivity of the MIP sensor to 8-OHdG and to the NIP one, the IF was determined to be ~6.3.

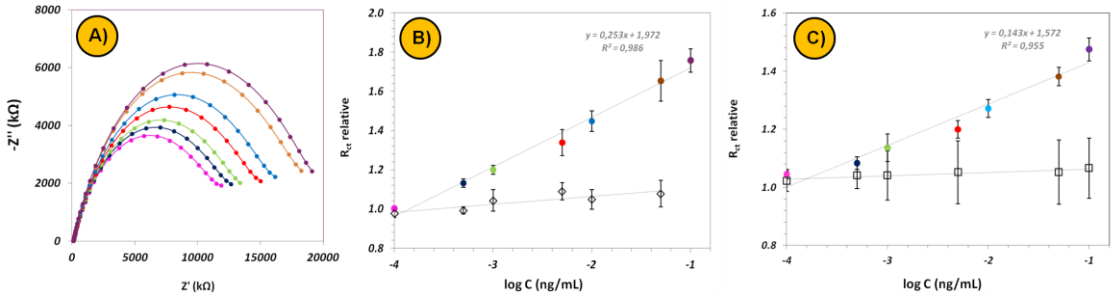

Figure 3.8: A) Nyquist plot of MIP sensor in 5 mM [Fe(CN)6]3-/4- in 0.01 M PBS pH 7.4, previously incubated in increasing concentrations of 8-OHdG and B) the corresponding calibration curves for both MIP and NIP sensors; C) Calibration curves of NIP and MIP sensors for different 8-OHdG concentrations in urine samples, measured in 5 mM [Fe(CN)6]3-/4- in 0.01 M PBS pH 7.4. All error bars represent the standard deviation for three independent measurements.

The results obtained demonstrated that the resistance of the sensing layer increased after incubating an 8-OHdG solution in the MIP film, which could be due to the re-binding of 8-OHdG onto the imprinted cavities that hindered the electrical features of the sensing surface $[Fe(CN)_6]^{3-/4-}$. In general, increasing concentrations of 8-OHdG increased the diameter of the semicircles in the Nyquist plot (R_{ct}), indicating that 8-OHdG bound to the sensory layer increased the charge-transfer resistance of the probe. The calibration curve obtained for the MIP sensor showed a linear relationship over 8-OHdG concentration in the range [0.1−100] pg/mL. The limit of detection (*LOD*), was 0.74 pg/mL, calculated by extracting the first standard from the calibration curve and extending the linear ranges observed, as in potentiometric devices that respond to concentration in a logarithm basis. The response of the control electrode (NIP) was independent of the 8-OHdG concentration and it was kept at very low values for all concentrations within that range (random and small R_{ct} values). All the results were normalized against the blank value (PBS). Furthermore, the reproducibility of the sensors for quantification of 8-OHdG was investigated over the entire linear range and the results showed that the relative standard deviation (RSD) was 0.5-8.8 %.

3.3.4.2 Selectivity studies

Uric acid is typically identified as the major electrochemical interfering species in biological samples, mainly due to its relatively high concentrations, and, here specifically, the similar structural characteristics to the 8-OHdG molecule. Therefore, in order to verify the selectivity of the sensory device, uric acid, citric acid and glucose were selected as interfering species. Data presented on Figure 3.9 showed that these molecules almost have no interference in the determination of 8-OHdG, showing variations of 3.0, 12.0 and 0.5% for uric acid, citric acid and glucose, respectively. Moreover, to assess its effect upon the biosensor response, the calibration curves were performed directly in human urine samples (uric acid levels of ~500 μg/ml). EIS calibration curves against 8-OHdG concentration for MIP and NIP sensors are presented in Figure 3.7C. It was interesting to observe that the MIP maintained the linear EIS response over the considered concentration range, with just a small decrease of the sensitivity. In contrast, the NIP sensor presented a quite random behaviour which can be a strong indication that its response is caused by non-specific adsorption at the electrode modified-surface. Thus, the proposed sensor showed good analytical performance in terms of sensitivity, selectivity and rapid response towards 8-OHdG determination.

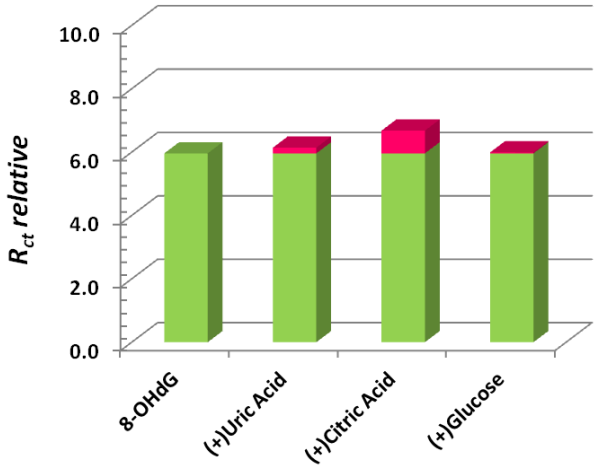

Figure 3.9: EIS measurement of MIP-based sensor recorded after incubation in 5 pg/mL 8-OHdG solution, alone and in the presence of uric acid (0.4 μg/mL), citric acid (0.5 μg/mL) and glucose (0.1 mg/mL). All solutions were prepared freshly on PBS pH 7.4.

3.3.4.3 Analysis of spiked human urine samples

Urine samples were assayed and recovery experiments were carried out via the standard addition method by adding 0.25, 2.5 and 50 pg/mL. Assuming a null concentration of the urine sample (because it was used as background media for the overall calibration), the obtained recovery values were of 92.6, 111.6 and 110.3%, respectively. But, in biological samples 8-OHdG molecule is present in vestigial levels and so, herein, we also estimated this "background concentration". Thus, we have employed the Gran's method of multiple standard addition to estimate the original concentration of the 8-OHdG in urine samples [248].

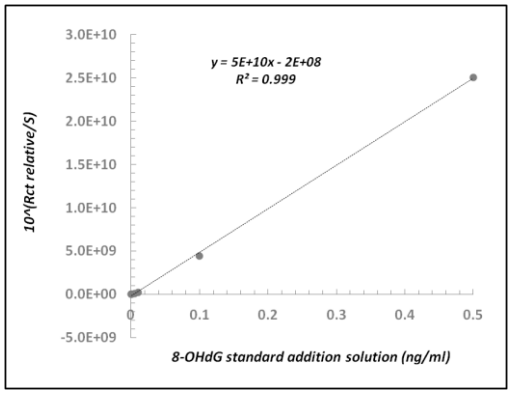

Figure 3.10: Calibration curve of 8-OHdG in a urine sample. Rct relative corresponds to the normalized value of charge transfer resistance against the PBS measurement for each spiked level and S is the slope of the experimental calibration, obtained from three independent measurements.

As can be seen in Figure 3.10, the plot of $10^{(\text{Rct relative/Slope})}$ *versus* the concentration of 8-OHdG (added) results in a linear behaviour where the *x* axis interception is a direct indication of the unknown 8-OHdG concentration initially present in the urine real sample (before spiking). The calculated 8-OHdG concentration in the real urine sample (before 1:1000 dilution) was 4.1 ng/mL, a value that still is below the maximum limit in healthy humans.

Overall, these results demonstrated that the method was suitable for the determination of the total content of 8-OHdG in urine samples. Although there are already few researches on the application of sensitive sensors for detection of 8-OHdG, these often require the sample pre-treating stages to eliminate the presence of interfering species [249].

3.4 CONCLUSIONS

In the present study, an electropolymerization method was selected for the synthesis of a MIP-based electrochemical sensor targeted for 8-OHdG recognition and detection. Under this approach, phenol was electrochemically deposited on gold-modified electrodes in the presence of the template molecule 8-OHdG. The control of some experimental parameters of the electropolymerization reaction enabled the preparation of thin homogenous films, which constitute an important issue in order to achieve trustable, accurate and repeatable sensor responses. Our results demonstrated that 8-OHdG molecule was successfully entrapped into the polymeric matrix, enabling a three-dimensional structure with numerous imprinted cavities sites. The developed electrochemical biosensor showed high sensitivity and selectivity towards 8-OHdG over the wide concentration range. The successful application of the proposed sensor in the analysis of human urine samples has evidenced its promising features in the early diagnosis of cancer in point-of-care.

Overall, a simple and easy-to-go detection method of 8-OHdG in biological samples was possible without any previous sample preparation, providing a great advantage for this new analytical methodology. Compared to previous methods (see Table 3.1), the work described herein showed the best lower limit of linear range and limit of detection, coupled with a wide range of concentrations of linear response.

Table 3.1: Comparison of the main characteristics of some reported assays used in the detection of 8-OHdG.

Electrodes	Detection method	Linear range (nM)	LOD (nM)	References
Dendrimer/Au[a]	HPLC-ECD[b]	__	1.2	[26]
Nafion/SWCNTs[c]/GCE[d]	DPV[e]	30-1250	8	[27]
P3MT[f]/GCE	CV[g]	700-70000	100	[250]
ECL[h] immunosensor/ CQD[i]/Au/SiO_2	ECL	0.7-700	*0.3*	[146]
GO[j]/Nafion/GCE	LSV[k]	70-33040	1120	[251]
PICA[l]/CHI[m]/GCE immunosensor	DPV	0.35-35000	0.11	[252]
Metal-Chelate/ Au/QCM[n]	QCM	10.0-3500	7.5	[194]
ssDNA[o]/GNs[p]/GCE	CV	5.6-36155	0.875	[249]
Immunosensor/Au	EIS[q]/ SWV[r]	0.071-25	__	[253]
EPPGE[s]	SWV	500-100000	28	[124]
Ph[t]-MIP/Au	**EIS**	**0.0035-3.5**	**0.0074**	***This work***

[a]AU: Gold; [b]HPLC-ECD: High Performance Liquid Performance with Electrochemical Detection; [c]SWCNTs: Single-Walled Carbon Nanotubes; [d]GCE: Glassy Carbon Electrode; [e]DPV: Differential Pulse Voltammetry; [f]P3MT: Poly(3-methylthiophene); [g]CV: Cyclic Voltammetry; [h]ECL: Electrochemiluminescence; [i]CQDs: Carbon Quantum Dot ;[j]GO: Graphite Oxide; [k]LSV: Linear Sweep Voltammetry; [l]PICA: Poly(indole-5-carboxylic acid); [m]CHI: Chitosan; [n]QCM: Quartz Crystal Microbalance; [o]ss-DNA: Single-Stranded DNA; [p]GNs: Graphene Nanosheets; [q]EIS: Electrochemical Impedance Spectroscopy; [r]SWV: Square Wave Voltammetry; [s]EPPGE: Pyrolytic Graphite Electrode; [t]Ph: Phenol.

CHAPTER 4

4 Paper-based sensing device for electrochemical detection of oxidative stress biomarker 8-hydroxy-2'-deoxyguanosine in point-of-care

The results presented in this chapter were published in Gabriela V. Martins, Ana P. M. Tavares, Elvira Fortunato, M. Goreti F. Sales, "*Paper-Based Sensing Device for Electrochemical Detection of Oxidative Stress Biomarker 8-Hydroxy-2'-deoxyguanosine (8-OHdG) in Point-of-Care*", Scientific Reports (2017), 7, p. 14878-14887. ***doi: 10.1038/s41598-017-14878-9.***

4.1 INTRODUCTION

As the most abundant oxidative product of DNA, 8-OHdG detection allows a premature assessment of cancer disease, thereby improving diagnosis, prognostics and survival rates. Therefore, the relevance of 8-OHdG as OS biomarker is also confirmed by the numerous methods published in the literature aiming its determination. A sensitive automated flow immunosensor has been developed for detection of urinary 8-OHdG at concentrations of 0.05 ng/mL [249]. Also, the combination of sensitive semi-conducting silicon nanowire with the specificity of immunoassays have resulted in a biosensor device to detect few nanomolar concentrations of 8-OHdG [254].

Overall, electrochemical sensors are increasingly gaining attention due to their high sensitivity (low detection limits), small dimensions, low cost, easy automation and operation. Special importance has been given to carbon electrodes and the use of nanostructured materials, such as graphene, nanoparticles and carbon nanotubes. These nanomaterials are currently used as a surface modification approach to accelerate electron transfer and enhance the electrochemical activity of biomolecules due to their intrinsic characteristics such as, higher surface area, good conductivity and signal stability [250][251]. Even after such amazing developments, an urging need for OS assessment in POC remains. Specifically, there is a gap regarding rapid, portable, inexpensive and simple screening platforms for biomarker analysis.

In turn, paper-based sensors have become a promising platform for *lab-on-a-chip* devices, offering high selectivity and sensitivity for application areas such as, health diagnostic, food quality control and environmental monitoring [131]. In particular, a recent overview about diagnostic paper-based biosensors has discussed the integration of nanomaterials for the detection of nucleic acids, proteins and cells [254]. Although there are already very few studies performed on paper electrode devices for quantitative analysis of 8-OHdG biomarker, these still require the immobilization of antibodies [255].

Thus, this work aims the development of low cost easy-to-use label-free paper-based, electrochemical sensor for the determination of OS biomarkers, which targets 8-OHdG as proof-of-concept. For this, we have investigated the redox behaviour of 8-OHdG on different carbon-modified surfaces and the optimization conditions for its selective detection in biological samples. The redox reaction of 8-OHdG is presented elsewhere [147] and the detection process of the modified electrodes can be found in Figure 4.1. Here, the electrochemical performance of the biomarker 8-OHdG at the modified-paper electrode was followed by means of DPV and the several electrochemical and chemical variables optimized and evaluated.

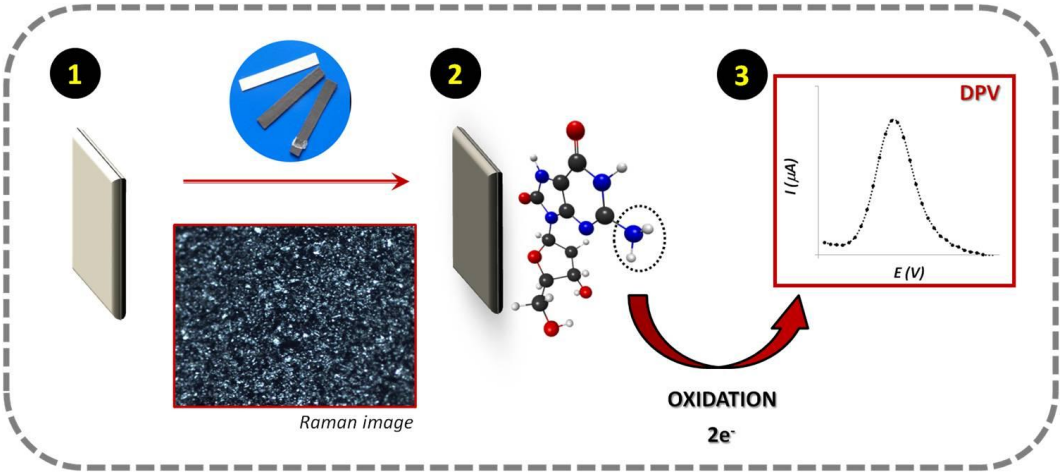

Figure 4.1: Schematic representation of the oxidation process of 8-OHdG molecule followed on a conductive carbon paper substrate: 1) hydrophobic white paper as substrate; 2) conductive carbon-coated paper; 3) in-situ electrochemical measurement.

4.2 EXPERIMENTAL SECTION

4.2.1 Reagents and Materials

All reagents were of analytical grade and used without further purification. PBS (0.01 M, pH 7.4), TRIS (hydroxymethyl)aminomethane (0.01 M, pH 9.1 and 9.5) and acetate buffer (1 mM, pH 5.1) were used as buffer solutions and prepared with ultrapure water Milli-Q laboratory grade. The pH values were measured with a pH meter (Crison Instruments, GLP 21 model). Graphite powder (fine extra pure, particle size < 50 μm) was purchased from Merck and used as received. Poly(3,4-ethylenedioxythiophene) (PEDOT) nanoparticles dispersion in H_2O, 8-OHdG (98%), uric acid (>99% crystalline), sulphuric acid (H_2SO_4, 95-97 %), MWCNT and multi-walled carbon nanotube, carboxylic acid functionalized (MWCNT-COOH) were obtained from Sigma Aldrich; poly(vinyl chloride) carboxylated (PVC-COOH) from Fluka; *N,N*-dimethylformamide (DMF) from Analar Normapur and ascorbic acid from Riedel-de-Haen. All measurements were carried out at ambient temperature.

4.2.2 Apparatus

Electrochemical measurements were performed by using a three-electrode system composed by a carbon-ink coated paper with an electrode area of 20 mm^2 as the working electrode, a Pt wire as the counter electrode and an Ag/AgCl (KCl 3.0 M) wire as the reference electrode. All the electrochemical measurements including CV and DPV experiments were conducted with a potentiostat/galvanostat from Metrohm Autolab and a PGSTAT302N with a FRA module, controlled by ANOVA software.

4.2.3 Fabrication and characterization of the paper-based sensor

The working electrode was constituted by small parts of cellulose paper (5 x 2 mm) hand-coated with a conductive carbon-based ink. The protocol for the preparation of this conductive carbon-based surface is described elsewhere [255]. Briefly, graphite powder was doped with PVC-COOH and dispersed in DMF with magnetic stirring at room temperature. In addition, a small amount of different nanostructured materials were added (separately) to the previous mixture and left stirring for several hours before using. Specifically, we have tested PEDOT nanoparticles dispersed in water, MWCNT and MWCNT-COOH powders. The sensor was prepared by drop-coating the surface of the hydrophobic paper with the conductive carbon-based ink. Afterwards, the electrode area was precisely delimited by using paraffin wax.
Carbon-coated paper was characterized by means of Raman spectroscopy. The Raman spectral analysis was carried out using a Thermo Scientific DXR Raman microscope system with a 100 mW 532 nm excitation laser (operational conditions: 20 min of photobleach and 5 min of collect time). Data analysis was performed with OMNIC software.

4.2.4 Electrochemical assays

Initially, the working electrode was electrochemically cleaned by performing voltammetric sweeps between -0.2 V and +1.5 V in PBS pH 7.4, until a stable voltammogram was obtained (more or less 50 cycles). Before use, sensors were dried and stored at room temperature.
The electrochemical response of 8-OHdG in PBS solution at pH 7.4 was investigated by performing CV measurements over the potential range of +0.1 - +0.8 V, in order to find the oxidation potential. During the electrochemical measurements the three-electrode system was always submersed into 1 mL of sample volume. Afterwards, differential pulse voltammograms were recorded after pre-conditioning the working electrode in 8-OHdG solution at a specific potential. The DPV experimental conditions used were a potential range between +0.2 V and +0.7 V, pulse amplitude of 25 mV, pulse width of 50 ms, scan-rate of 100 mVs^{-1} and an equilibration time of 5 s. In order to regenerate the sensors, a cleaning protocol was performed to remove the analyte adsorbents by immersion of the used sensors in 0.01 M PBS pH 7.4, followed by (5) successive CV scannings over the potential range 0 - +0.7 V at a scan-rate of 50 mVs^{-1}.

Calibration curves were performed by DPV analysis for 8-OHdG in the range 50-1000 ng/mL in PBS solution at pH 7.4 and all the logarithmic scales were calculated from ng/mL values. Selectivity studies were carried out by competitive assays between 8-OHdG (0.1 mM) and each interfering specie, with similar concentration. Here, uric acid and ascorbic acid were selected as interfering molecules due to the fact that they may co-exist with 8-OHdG in biological fluids, holding also electro-active properties. Additionally, different buffer solutions were prepared at different pH environments, such as, PBS at neutral pH (pH 7.4, 10 mM), Tris buffer at basic pH (pH 9.1, 2 mM) and Acetate buffer at acidic pH (pH 5.1, 1 mM). The performance of the sensor

was tested directly in Foetal Bovine Serum doped with 8-OHdG in the concentration range 20-1000 ng/mL. The serum was previously 1:10 diluted in PBS buffer.

4.3 RESULTS AND DISCUSSION

4.3.1 Electrochemical behaviour of 8-OHdG

Figure 4.2 shows the cyclic voltammograms of 8-OHdG (50 μg/mL) on PBS pH 7.4 performed for different scan rates onto the surface of the paper-modified electrodes. Here, a well-defined oxidation peak appeared around +0.42 V and a small reduction peak was visible at +0.40 V. Thus, the peak shape of the CV demonstrated a typical quasi-reversible electrochemical reaction. In agreement with previous electrochemical studies, it was also observed that the oxidation peak potential shifted gradually towards more positive values with the increase of scan-rate [153].

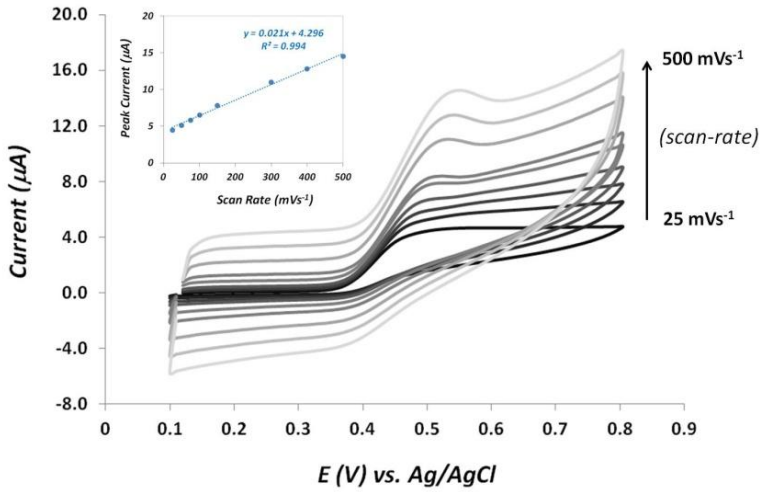

Figure 4.2: Successive cyclic voltammograms performed in PBS at pH 7.4 with 8-OHdG molecule at different scan rates. Inset: calibration plot of the 8-OHdG oxidation peak current versus scan rate.

Additionally, the influence of scan-rates on the electrochemical oxidation of 8-OHdG on these graphite-coated electrodes was also investigated. As can be seen on the inset figure, a linear relationship (R^2 = 0.994) between the anodic peak current and the scan rate is evident, suggesting that the electrochemical oxidation process of 8-OHdG is mainly adsorption-controlled. Our results are in good agreement with other studies performed on various carbon-modified surfaces [249][251]. Herein, CV was employed to determine the oxidation potential of 8-OHdG to be used in further electrochemical experiments (+0.41 V), a value that is in agreement with other similar electrochemical sensors [256][257][258].

4.3.2 DPV analysis of 8-OHdG on paper-modified electrodes

Graphitic materials are known for their good structural, electronic, mechanical, optical, thermal and chemical properties [217]. In the last years, carbon-based nanomaterials, such as, graphene [259], nanotubes [260], nanoparticles [261] and conductive polymers [262] are being widely employed for biosensing devices. Due to their high surface area and high electrical conductivity, these electrochemical sensors have become a potential alternative to the conventional labour intensive and time consuming assays that are currently used for biomarker analysis. Since the electrochemical performance of the sensor is mainly affected by coating characteristics, developing a suitable ink for a specific target should be an important issue to design novel sensing devices.

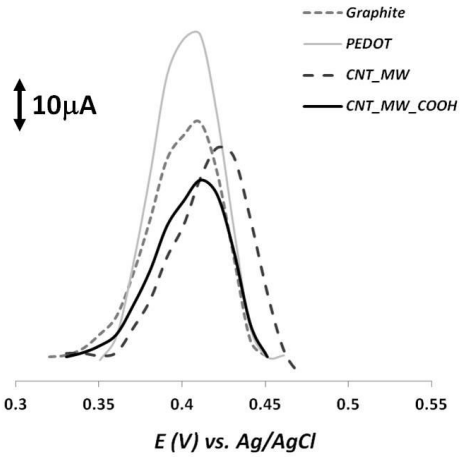

Figure 4.3: DPV detection of 200 ng/mL 8-OHdG solution in PBS pH 7.4 on different graphite-based electrodes prepared after the incorporation of various nanomaterials dispersed in the graphite ink, such as, PEDOT nanoparticles, CNTMW and CNTMW-COOH.

Under the scope of this work, DPV was chosen as a highly sensitive and selective electrochemical tool for quantitative analysis, with great application for nucleic acid sensing [109][151]. Meanwhile, the ability of 8-OHdG to undertake an electrochemical oxidation through 2-electron transfer reaction on carbon surfaces has already been reported [32]. So, in order to enhance the DPV signal of the oxidation of 8-OHdG on the paper-modified electrodes, we have incorporated and tested the effect of some highly conductive materials into the graphite-ink. Figure 4.3 displays the corresponding peaks of oxidation of 8-OHdG on different graphite-based electrodes, prepared through the incorporation of some conductive materials such as, PEDOT nanoparticles, CNTMW and CNTMW-COOH. Our data showed that the presence of the conducting polymer PEDOT seems to greatly improve the electro-catalytic properties of the substrate leading to an enhancement of the electrochemical response of 8-OHdG in comparison with the electrode coated with the graphite alone. This outcome can be attributed to the symbiotic combination of the good electronic mobility of the PEDOT polymer with the high

surface area of the nanoparticles resulting in a facilitated charge transfer for 8-OHdG redox biomarker. Although nano-based materials are often employed in order to accelerate electron transference, here the introduction of nanotubes during the ink production did not reflect on a improvement of the peak current intensity. Hence, the obtained oxidation potentials were quite similar between the different carbon-based surfaces and so, the graphite ink doped with PEDOT was chosen for the further experiments.

4.3.3 Characterization of the paper-modified electrodes

Raman spectroscopy has become a popular, powerful and non-invasive tool to characterize the structural organization of carbon and related materials. Figure 4.4 shows the Raman spectra for the different graphite-based electrodes prepared with the inks doped with various nanomaterials.

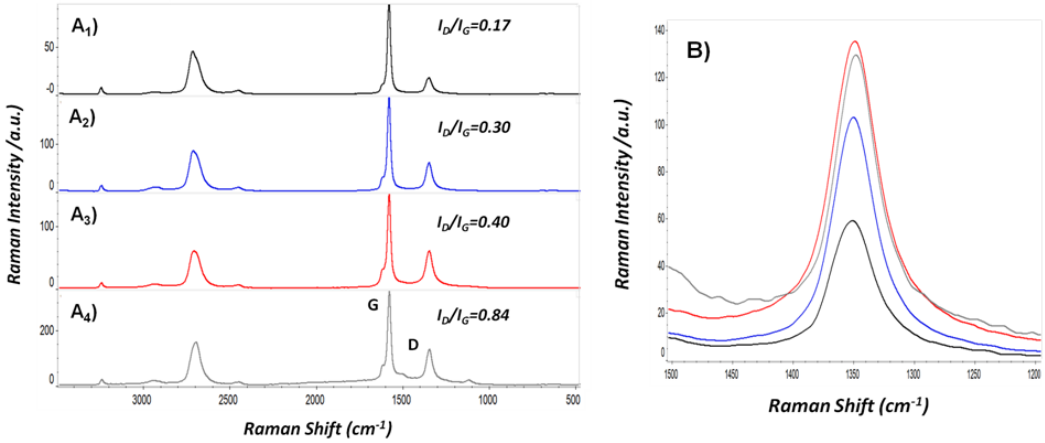

Figure 4.4: Raman spectra of the different graphite-based electrodes prepared after the incorporation of nanomaterials dispersed in the graphite ink, such as, A1) PEDOT nanoparticles, A2) Graphite, A3) CNTMW and A4) COOH-CNTMW, with the calculated ID/IG ratios and B) RAMAN spectra with the magnification of the D (Disorder) band, in full-scale mode.

Firstly, in all samples, the typical G and D bands appeared at 1581 cm^{-1} and 1350 cm^{-1}, respectively, which is in accordance with previous Raman spectrum for graphite samples [255][263][264]. The G band is often associated to the stretching of the C-C in graphitic materials, common to all sp^2 carbon systems, and the D band is assigned to the presence of disorder in the sp^2-hybridized carbon system [265]. In addition, another peak was also clearly visible around 2700 cm^{-1} that is assigned to the 2D band. As expected, the spectra of all observed materials are quite similar because the main constituent of the doped inks was graphite. Nevertheless, by analysing the intensity peak ratio between the D and G bands (I_D/I_G), we are able to evaluate the level of disorder or defects within the carbon material. The most common information extracted from the direct comparison between Raman spectrum is that an

increasing tendency of the I_D/I_G intensity ratios reflects the presence of additional structural disorder. Here, the I_D/I_G ratios of the graphite ink alone, with PEDOT, MWCNT and COOH-MWCNT were 0.30, 0.17, 0.40 and 0.84, respectively. An interesting work have demonstrated a correlation between the number of edge plane type defects on graphite-based substrates and the voltammetry of guanine oxidation. The authors have concluded that as the number of defects sites on the electrode surface increases, there is a small shift in peak potential and, more importantly, the peak height is enhanced [266]. In our case, it was interesting to observe that the carbon-based material with less level of disorder (less ratio I_D/I_G, 0.17) was achieved for the ink doped with PEDOT nanoparticles, which enabled the higher intensity current for DPV signaling of 8-OHdG oxidation. This is consistent with the fact that PEDOT displays a structure where carbon atoms hold an sp^2 hybridization. In addition, the material assigned with the higher number of structural defects (high ratio I_D/I_G, 0.84) was found to give the weaker DPV response.

4.3.4 Optimization of DPV experimental conditions

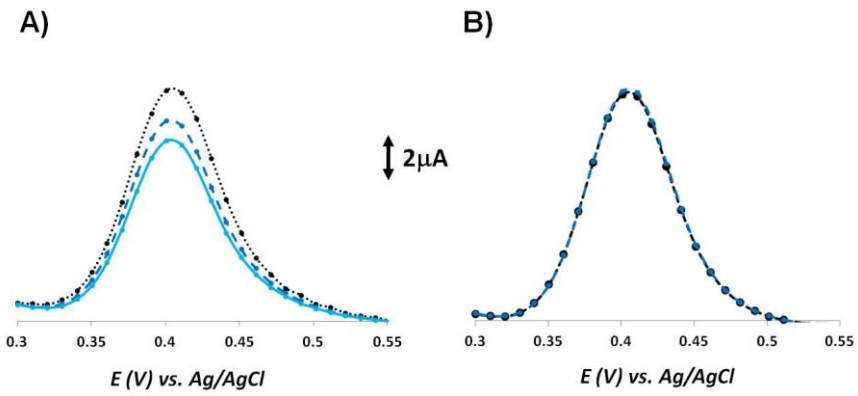

Figure 4.5: Successive differential pulse voltammograms of 0.1 mg/mL 8-OHdG in PBS pH 7.4 recorded (A) without any application of conditioning potential and (B) with a conditioning potential of +0.20V applied before each measurement.

Here, the oxidation of 8-OHdG in pH 7.4 PBS was found to be around +0.41 V. Initially, the effect of performing a pre-conditioning step at a specific potential on the DPV electrochemical performance was investigated (see Figure 4.5). Our data showed that applying a conditioning potential of +0.20 V for pre-concentrating of 8-OHdG greatly improved the stability and reproducibility of the DPV measurement. Therefore, the subsequent DPV measurements were conducted over a positive potential range, after applying a fixed step potential for the pre-concentration of 8-OHdG on the surface of the modified electrodes.

Afterwards, the influence of the potential and accumulation time during the pre-concentration step on the electrochemical response of 8-OHdG was also investigated, as shown in Figure 4.6. Two different potentials were tested and the highest current signal was achieved at +0.20 V so, this potential value was chosen for further studies. Concerning the accumulation time, it was

observed that the oxidation current increased from 180 s to 300 s and then it decreased for 500 s. Hence, the optimal time pre-concentration for the determination of 8-OHdG by DPV analysis was chosen to be 300 s.

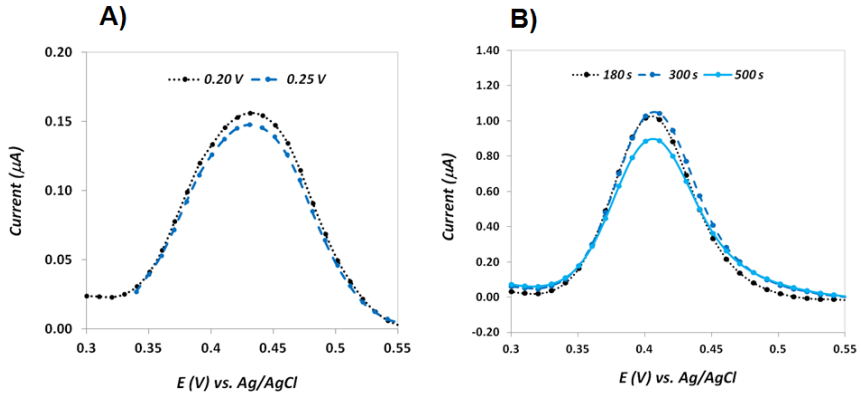

Figure 4.6: Dependence of the sensor response on the (A) pre-accumulation potential and (B) time of accumulation during 8-OHdG oxidation in PBS pH 7.4.

Nowadays, one of the most popular electrochemical transducer in biosensor field is carbon-based surface (graphite, glassy carbon (GC), carbon paste). Due to their great stability and suitable electronic properties, these nanostructured materials have been widely applied, nevertheless, appropriate cleaning methodologies are still needed in order to enhance the material response. Herein, we have studied the effect of different kinds of washing solutions, such as, ethanol, buffers and acids, on the electrochemical response of our target molecule (data not shown). We have concluded that the best performance was achieved after applying voltammetric sweeps on PBS at a pH 7.4 (see Figure 4.7A). More interestingly, by applying the same cleaning protocol after each DPV measurement (see Figure 4.7B), we were able to completely regenerate the sensor by returning the current to its original level, enabling multiple use of the same electrode.

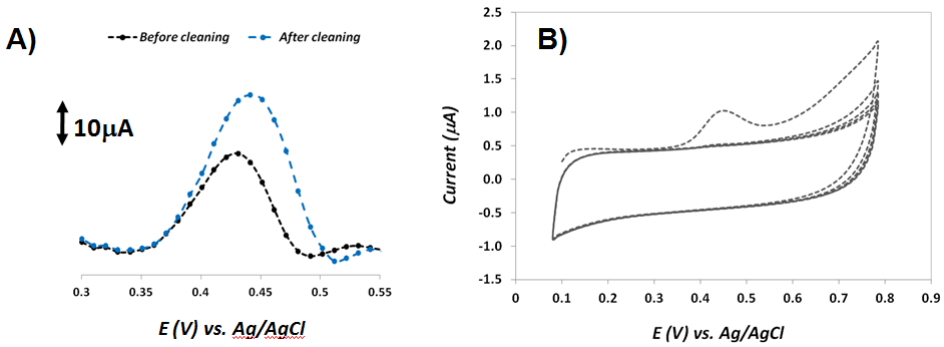

Figure 4.7: (A) Cleaning effect (after CV in PBS pH 7.4) on the 8-OHdG detection by DPV signal and (B) sensor regeneration after voltammetric cycles performed in PBS pH 7.4.

We have tested the performance of the DPV signal for different pH environments (see Figure 4.8) and, as expected, we have found that the electrochemical oxidation of 8-OHdG is pH dependent. Our data seems to be in agreement with previous studies in which the anodic peak potential shifted towards negative values with the increase of the supporting electrolyte pH from 3.0 to 9.0, indicating that the electrochemical process of 8-OHdG is associated with a proton-transfer process [153]. As shown here, the tendency seems to be that the oxidation peak current decreases with the increasing of pH (Tris pH 9.5), has it was observed previously for guanine and adenine oxidation [150]. Although the maximum value of the current intensity was obtained for PBS when the pH was 6.0, it was quite similar when compared with the pH of 7.4. Thus, the physiological pH was selected and used in further studies.

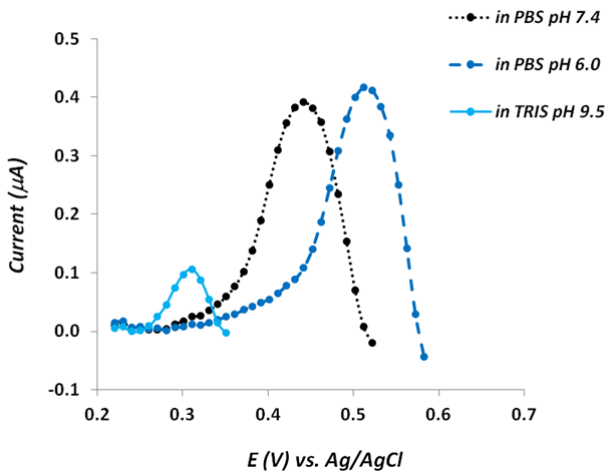

Figure 4.8: Differential pulse voltammograms recorded for 8-OHdG solutions prepared in different buffer solutions, with different pH values.

4.3.5 Analytical applications

4.3.5.1 Calibration curve

Figure 4.9A shows the corresponding dependence of the oxidation peak current on the concentration of 8-OHdG. As it can be seen, with the increase of concentration, the DPV signaling was also increased. Figure 4.9B displays the calibration graph for 8-OHdG showing a linear relationship between the log peak intensity and the log concentration of 8-OHdG over the range 50-1000 ng/mL. The calibration plot showed excellent linearity (r^2 = 0.9919) and the LOD was found to be 14.4 ng/mL, calculated by the intersection of two straight lines, between the linear response range and the lower concentration range.

The reproducibility of the modified-electrodes for quantifying 8-OHdG was investigated over the entire linear range and data showed that the RSD was less than 3.5 %, for five independent experiments.

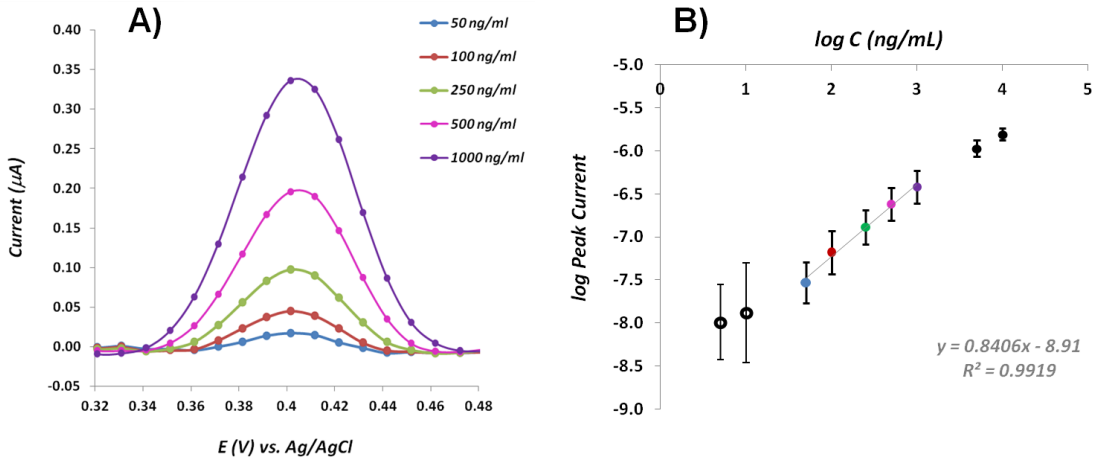

Figure 4.9: A) Differential pulse voltammograms for different concentrations of 8-OHdG prepared in PBS pH 7.4 and (B) calibration plot of the concentration of 8-OHdG.

Although the LOD of our paper-based sensor might not fully satisfy the cut-off of all the biological samples, it has a relatively wide linear range and a good sensitivity compared to other works. Moreover, despite the fact that there are some known methodologies for 8-OHdG assessment down to picoMolar [267], various clinical studies have reported that the levels of serum 8-OHdG in healthy subjects can suffer variations between 3 and 160 ng/mL [29],[62],[268],[269],[270]. Thus, our electrochemical label-free sensor is a valuable tool in providing quick and low-cost information concerning the level of OS at DNA context.

4.3.5.2 Selectivity

The selectivity of the proposed sensor is crucial to grant its successful application. Meanwhile, one of the main limitations of most conventional methodologies involving biological samples is the need to include pre-treatment steps in order to minimize possible matrix interference effects. Herein, the target is to allow a direct sample analysis, with only dilution, if necessary.

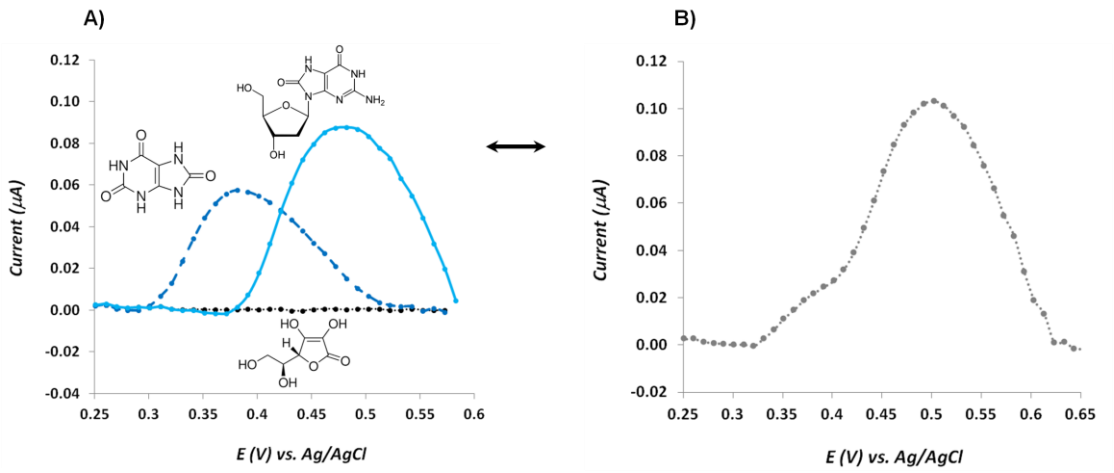

Figure 4.10: (A) DPV recordings for individual solutions with concentrations of 0.1 mM of 8-OHdG, ascorbic acid and uric acid in PBS at pH of 7.4; (B) DPV recording of a mixture with all of the 3 compounds, in the same concentrations.

Uric acid and ascorbic acid were chosen as main interfering species in the determination of 8-OHdG, due to their similar structure and high abundance in biological samples, respectively. Both molecules are also electro-active and, very often, they are oxidized almost at the same potential value, resulting in the overlap of voltammetric signaling. In order to test the selectivity behaviour of our sensor, we have investigated the oxidation peak potential of both target-molecule and interfering species, individually (see Figure 4.10A) and in an equimolar mixture (see Figure 4.10B). Our data showed that over the tested potential range, ascorbic acid did not exhibit any redox peak that could affect the analysis (see Figure 4.10A, black line). On the other hand, an oxidation peak was observed for the uric acid molecule (see Figure 4.10A, dashed dark blue line), but it occurs at a lower potential value compared with the oxidation potential of 8-OHdG (see Figure 4.10A, light blue line). Meanwhile, both molecules were analysed at the same concentration level (0.1 mM), however 8-OHdG presented an oxidation peak with higher current than uric acid. The differential pulse voltammogram obtained from the equimolar mixture of the three molecules showed that the oxidation potential peak of 8-OHdG in the mixture was shifted to values above +0.5V may be due to the presence of high concentration of uric acid. Concerning the peak intensity current, the same value was obtained in comparison with the individual solution. In addition, the oxidation peak of uric acid was not visible but instead a small shoulder appeared at lower potentials, enabling a clear separation between the oxidation process of 8-OHdG and uric acid.

4.3.5.3 Serum samples

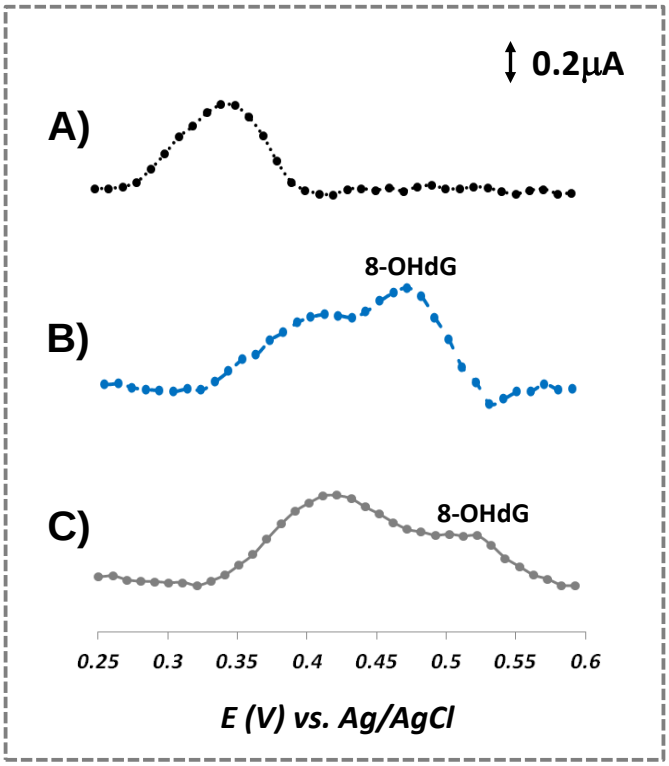

Figure 4.11: Differential pulse voltammograms for serum samples diluted 1:10 in different buffers, such as, (A) Tris pH 9.1, (B) PBS pH 7.4 and (C) Acetate pH 5.1, doped with 1 ug/mL of 8-OHdG.

In order to investigate the applicability of our paper-modified electrode for assessment of 8-OHdG levels in POC, we performed some electrochemical studies using real serum samples. Biological fluids, such as, urine, blood and serum are complex matrices, composed by high levels of small biomolecules, some of which are electrochemically active and thereby act as possible interfering species. Thus, to optimize some experimental conditions, we have tested the dependence of the oxidation peak potential of both the target-molecule and possible interferent species for different electrolytes and pH values, aiming for a good voltammetric separation of the compounds. Figure 4.11 shows the differential pulse voltammograms obtained for 8-OHdG spiked serum samples 1:10 diluted in different buffers at different pH environments (basic, neutral and acid). Although it is not displayed here, all the tested diluted serum samples presented a broad DPV signal between +0.35 V and +0.45 V due to the presence of other interferent species holding electroactivity characteristics, such as, ascorbic acid and uric acid, among others. Our data showed that by doping these serum samples with a known concentration of 8-OHdG we were able to obtain a second DPV peak assigned to the oxidation of our target-molecule, with the exception of the buffer Tris pH 9.1 that presented no extra peak (see Figure 4.11A). This outcome is in agreement with our previous pH study showing that the oxidation peak current is negatively affected by the increasing of pH. For the other tested pH

values (see Figures 4.11B and 4.11C), the best enhancement in the oxidation current of 8-OHdG was achieved for the sample diluted in PBS pH 7.4. The obtained results are in good agreement with other similar studies that showed that the peak current of 8-oxoguanine, in the presence of interferents, was maximum in the pH range 6-8 [271]. In sum, PBS at 7.4 pH was the optimal choice for 8-OHdG electrochemical detection since the peak current is higher and sufficiently good separation between peaks was reached.

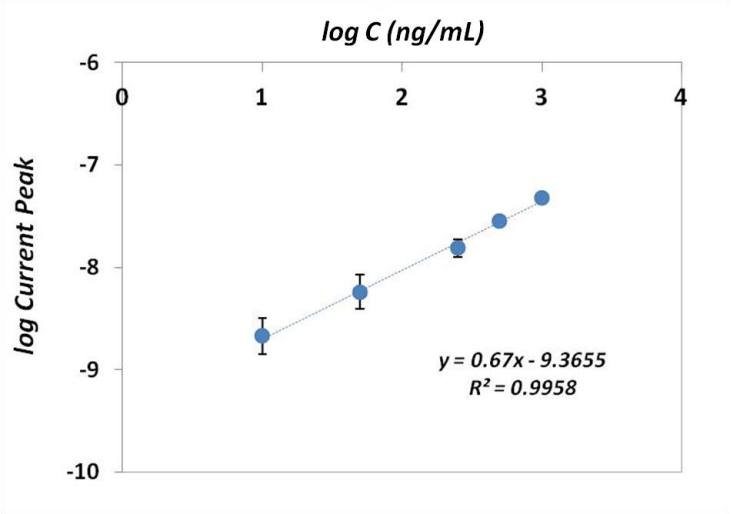

Figure 4.12: Calibration curve of the concentration of 8-OHdG in diluted serum samples.

Meanwhile, the application of the proposed sensor in the quantification of 8-OHdG was tested in serum samples by using a spiking approach. All samples were previously diluted 1:10 in PBS pH 7.4. Three independent measurements were performed for each concentration. Figure 4.12 presents the calibration graph for 8-OHdG concentration obtained from the DPV response. A linear regression equation (*log current (A) = 0.67 log concentration (ng/mL) - 9.3655*) was achieved over the concentration range 10-1000 ng/mL with a correlation coefficient of 0.9958. Moreover, the reproducibility of the modified-electrodes was confirmed and RSD was less than 2.5 %.

Although other works have been reported with better sensitivity (see Table 4.1), they have used more complex and expensive protocols in comparison with our paper-based sensor. For instance, some interesting studies related to the modification of GCE surface with materials that effectively increased their surface area enabled the detection of 8-OHdG molecule at very low levels (0.1-0.2 ng/mL) but in both cases the immobilization of antibodies was performed [146],[252]. One of the main advantages of our 3-electrode system assembled on paper substrate is their ability to work with small sample volumes. Moreover, there are very few papers concerning the application of rapid and cost-effective biosensing devices for real serum samples. Thus, the analysis of 8-OHdG in serum samples was successfully achieved in less time and with low cost input, allowing the detection of OS biomarkers in biological samples.

4.4 CONCLUSIONS

We have investigated the electrochemical performance of 8-OHdG biomarker at the surface of paper-modified electrodes for *in-situ* detection purposes. Different carbon-based nanomaterials were tested for coating the paper support and it was found that the presence of the conducting polymer PEDOT could effectively enhance the oxidation peak current of 8-OHdG. In parallel, several experimental conditions, such as, scan-rate, potential of pre-accumulation, accumulation time, supporting electrolyte and pH have been carefully optimized and the electrochemical response of the designed sensor was investigated by means of DPV. Overall, the combination of electrical properties of PEDOT with the electrochemical sensing of 8-OHdG enhanced the electro-catalytic activity of the working electrode, which resulted in favourable analytical features, such as, high reproducibility and selectivity, with low cost resources.

One main advantage of this sensor is easy and quick way to regenerate it, simply by performing voltammetric cycles in buffer solution, enabling continuous real-time detection of several samples. The developed electrochemical paper-based sensor showed high sensitivity towards 8-OHdG over the concentration range 50-1000 ng/mL, enabling low detection limit. Thus, the proposed electrochemical sensor holds high selectivity, reproducibility and stability, which constitutes a promising low-cost approach to be implemented as an easy-to-use protocol for sensitive detection of 8-OHdG in biological samples.

Table 4.1: Comparison of different electrochemical sensors for determination of 8-OHdG.

Working electrode/ Substrate	Working electrode/ Modification	Detection technique	Range of linear concentration dependence	Type of Sensor	Real application	Reference
2 electrode system/ CNT conductive paper	___	Chrono-amperometric (and colorimetric)	0-530 nM	Immuno-sensor	Urine samples	[256]
3 electrode system/ GCE electrode	SWCNTs- Nafion dispersion	DPV	0.03-1.25 μM 1.25-8.75 μM		Urine samples	[257]
3 electrode system/ GCE electrode	Graphene- Nafion film	LSV	0.07-3.64 μM 3.64-16.24 μM 16.24-33.04 μM		Urine samples	[251]
3 electrode system/ GCE electrode	MWCNT film	LSV	80-5000 nM		Urine samples	[272]
3 electrode system/ GCE electrode	Poly(3-methyl thiophene)	CV	0.700-35.0 μM 35.0-70.0 μM		Urine samples	[153]
3 electrode system/ GCE electrode	Poly(indole-5-carboxylic acid) and chitosan	DPV	0.35-35305 nM	Immuno-sensor	Urine samples	[252]
3 electrode system/ Pt electrode	Carbon quantum dot coated with Au/SiO_2 core-shell nanoparticles	ECL	0.71-706 nM	Immuno-sensor	Milk samples	[146]
3 electrode system/ Au electrode	Phenol polymer	EIS	0.35-353 pM	MIP	Urine samples	[267]
3 electrode system/ GCE electrode	Sulfur-doped graphene	DPV	0.002-20 μM		Urine samples	[258]
3 electrode system/ GCE electrode	DNA functionalized graphene nanosheets	CV	0.005-1.155 μM 1.155-11.65 μM 11.65-36.15 μM		Urine samples	[249]

Au: gold; CNT: carbon nanotube; CV: cyclic voltammetry; DPV: differential pulse voltammetry; ECL: electrochemiluminescence; EIS: electrochemical impedance spectroscopy; GCE: glass carbon electrode; HPLC-ECD: High Performance Liquid Chromatography with Electrochemical Detection; LSV: linear sweep voltammetry; MIP: molecularly imprinting polymer; MWCNT: multi walled carbon nanotubes; PAMAM: poly(amidoamine); Pt: platinum; SAM: self-assembled monolayers; SWCNTs: single walled carbon nanotubes.

CHAPTER 5

5 Novel wax-printed paper-based device for a direct electrochemical detection of 3-nitrotyrosine

The results presented in the chapter were published in Gabriela V. Martins, Ana C. Marques, Elvira Fortunato, M. Goreti F. Sales, "*Wax-printed paper-based device for direct electrochemical detection of 3-nitrotyrosine*", Electrochimica Acta (2018), 284, p. 60-68.
doi: 10.1016/j.electacta.2018.07.150.

5.1 INTRODUCTION

In the near future, clinical analysis are no longer confined to clinical laboratories but instead, the new trend is to be routinely carried out in other environments, like for instance, hospital for POC assessment and monitoring. In this context, paper seems the perfect choice as support material in diagnostic devices, due to its special features, like porosity, affordability, flexibility, high surface area, sustainability and biocompatibility [171][166][273]. Arduinin and colleagues have developed a paper-based electrochemical biosensor to detect ethanol in commercial beers and alcohol oxidase was immobilized onto the modified SPEs [274]. Interestingly, the same group have reported the first example of an integrated paper-based SPE for the assessment of nerve agents [275]. Looking forward to the last trends in the field of printed sensors, the investigation of innovative materials is driven by the ability to accomplish cost-effective devices for continuous monitoring. Printed platforms are becoming a more affordable and reliable choice in comparison with the conventional three electrode system because they are disposable, easy-to-use and environmentally-friendly. This issue has been addressed in a recent paper that developed screen-printed conductive patterns from a water-based conductive ink assembled on paper substrate [136].

Herein, we have presented the first paper-based electrochemical sensor towards the detection of 3-NT, a relevant OS biomarker. Mostly due to their high sensitivity and portability, electrochemical technology has showed to be an attractive approach to detect and quantify various biological compounds [276][277], in the POC context. Few studies on the electrochemical behaviour of 3-NT (and their derivatives) at solid substrates, mostly in 3-electrode system, have been performed [278][279]. The investigation of the redox behaviour of these electro-active compounds not only contributes to obtain valuable information related to the molecules, but also enables additional selectivity as different electro-active molecules can be oxidized and/or reduced at different potential values. In this way, the nature of the conductive surface of the sensor can be finely tuned and designed towards the detection and quantification of the target-molecule, hindering the interference of other electro-active compounds [251].

The design and assembly of this voltammetric sensor allowed performing the analysis without the need for an extra electrocatalyst mediator specie. This innovative sensor was designed by, first, modifying paper to become a hydrophobic support and, second applying carbon and silver conductive inks to generate a three electrode-system on a small spot. In addition, we have used the advantage of paper to design a low-cost, disposable and user-friendly flexible platform for POC assessment. The optimization performed on the fabrication of the device in parallel with the experimental conditions of the electrical measurements allowed to obtain an integrated 3-electrode device that sensitively and selectively quantified 3-NT biomarker (see Figure 5.1).

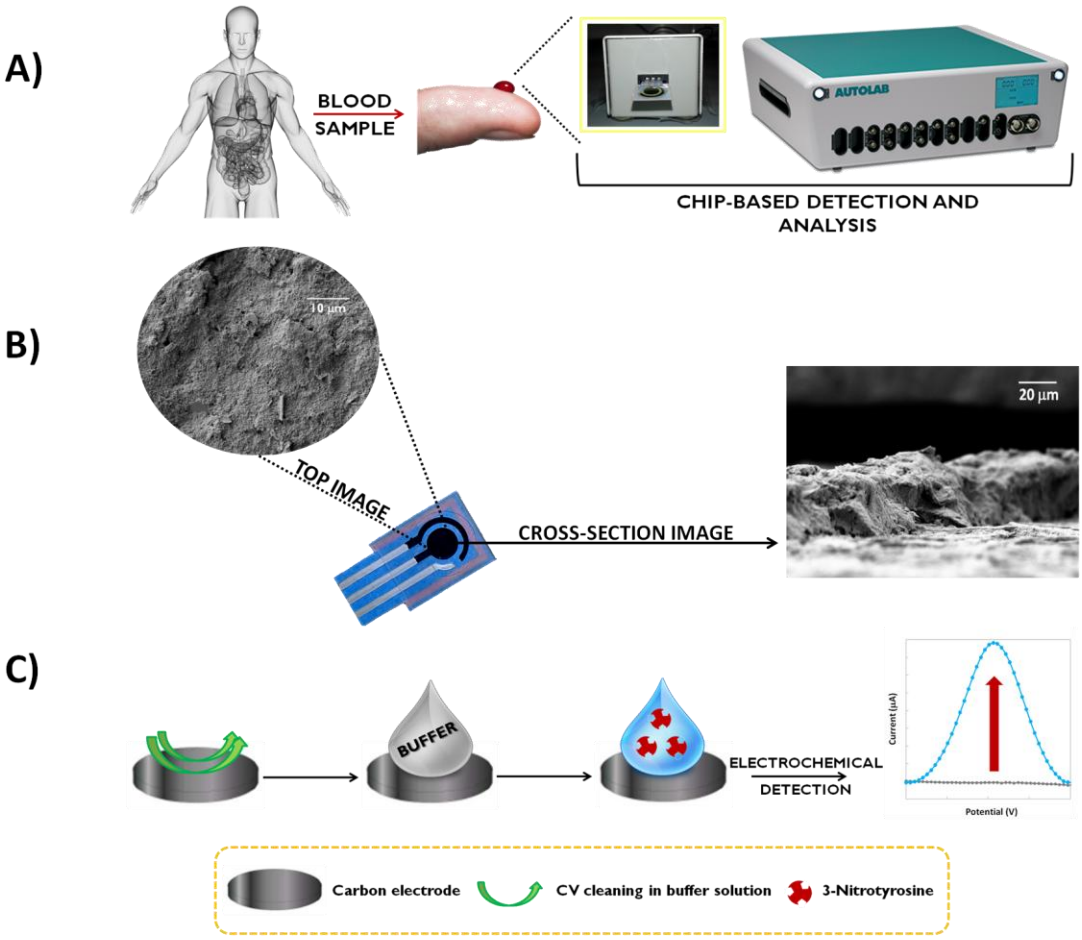

Figure 5.1: Schematic illustration of the different steps related to the sensor device, namely, A) the electrochemical apparatus for biological samples assessment; B) photo and morphological characterization of the paper-based electrodes; and C) the assembly of the electrochemical sensing platform.

5.2 EXPERIMENTAL SECTION

5.2.1 Reagents and Materials

All reagents were of analytical grade and used as supplied without purification. Potassium hexacyanoferrate III ($K_3[Fe(CN)_6]$), potassium hexacyanoferrate II ($K_4[Fe(CN)_6]$) trihydrate, dipotassium hydrogen phosphate (K_2HPO_4) and L-ascorbic acid p.a. were obtained from Riedel-de-Häen; hexaammineruthenium (III) chloride ($Ru(NH_3)_6Cl_3$) from Acros Organics; potassium chloride (KCl) from Merck; PBS tablets from Amresco; potassium di-hydrogenophosphate (KH_2PO_4) from Panreac; TRIS (hydroxymethyl)aminomethane (TRIS) from Fisher BioReagents; 3-NT (*98% purity*) from Alfa-Aesar; L-tyrosine pure from AppliChem; uric acid from Sigma-Aldrich and creatinine from Fluka.

The supporting electrolytes and the buffer solutions were prepared with ultrapure water Milli-Q laboratory grade. The pH measurements were performed with a pH meter, from Crison Instruments, GLP 21 model. All experiments were carried out at room temperature.

5.2.2 Fabrication of paper-based SPE

Herein, white office paper (*Bright White Paper* for colour laser printing 160 g/m^2) was employed as the substrate for the fabrication of the paper-based SPE (see Figure 5.2). A vector drawing software (Adobe Illustrator from Adobe Systems Software) was used to design the electrodes configuration and, afterwards, the hydrophobic pattern was printed directly onto the paper by means of a wax printer (Xerox ColorQube model 8580). Then, the wax printed paper was cured at 120 °C for 3 min, allowing the wax to diffuse vertically throughout the paper. After producing the hydrophobic confinement, the 3-electrode system was manually painted using a silver ink (*AG-530 Flexible Silver* from Applied Ink Solutions) as the pseudo-reference electrode and a carbon-based ink (*PE-C-774 Carbon Resistive Ink* from Applied Ink Solutions) to print both working and counter electrodes. In order to apply the three-electrode system we have used tape-masks designed (*kapton tape*, 0.25 mm thickness), which were patterned by means of a laser-cutting machine (model VLS 3.50, CO_2 infrared laser with 10.6 μm wavelength from Universal Laser Systems).

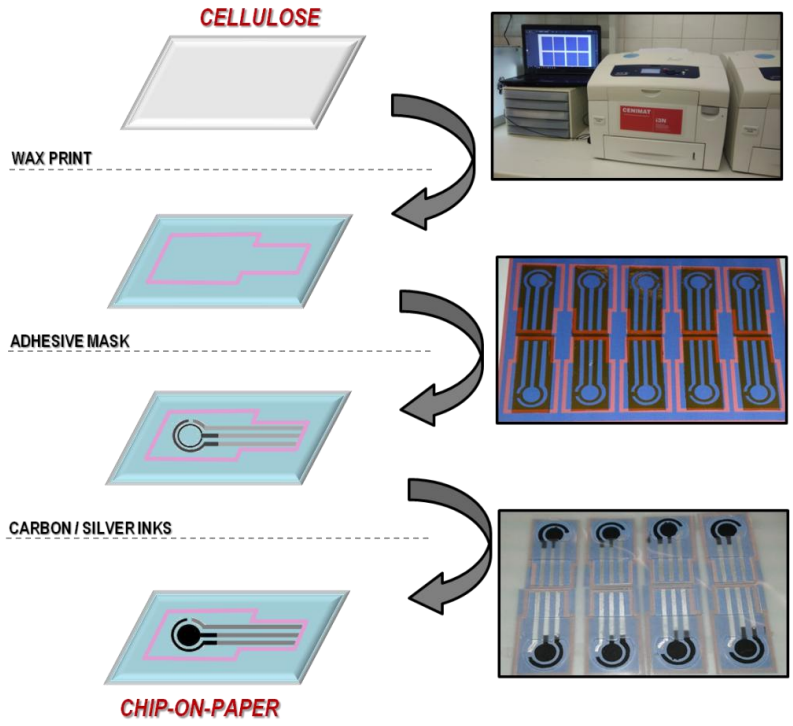

Figure 5.2: Detailed scheme of the fabrication of the paper-based electrodes.

5.2.3 Electrochemical assay

Electrochemical measurements were conducted by using the fabricated paper-based electrodes composed by a carbon-ink electrode as the counter and working (*5 mm diameter*) electrodes. Silver-ink was used as pseudo-reference. For comparison studies, commercial carbon-screen printed electrodes (SPEs-DRP-C110) from DropSens were also used. The electrodes were electrochemically characterised with a potentiostat/galvanostat from Metrohm Autolab and a PGSTAT302N with a FRA module, through an interface switch box from BioTid Eletrónica and controlled by ANOVA software. All the presented potential values are related to the silver pseudo-reference of the SPEs.

Initially, the working electrode was electrochemically cleaned by performing voltammetric sweeps between -0.20 V and +1.50 V in PBS pH 7.4, until a stable voltammogram was obtained. Before use, sensors were air dried and stored at room temperature. $[Fe(CN)_6]^{4-/3-}$ couple and $[Ru(NH_3)_6]^{3+}$ were selected as electrochemical indicators to evaluate the performance of the paper-based SPEs by CV. The measurements were performed by covering the three electrodes with 200 μl of an appropriate solution. Two different supporting electrolytes were tested during this study, namely, 0.1 M KCl and PBS pH 7.4. For the $[Fe(CN)_6]^{4-/3-}$ probe, CV was performed from -0.50 V to +0.70 V and in the case of the $[Ru(NH_3)_6]^{3+}$ probe, a potential range between -0.70 V and +0.20 V was chosen.

5.2.4 Surface characterization of the paper-based SPEs

SEM analysis was performed in order to evaluate the morphology of the surface of the fabricated paper-based SPEs. The samples were examined in a Carl Zeiss AURIGA Crossbeam SEM-FIB workstation, by using an accelerating voltage of 5 kV with an aperture size of 30 mm. Cross section imaging was also performed to estimate the thickness of the carbon layer on the working electrode.

5.2.5 Detection of 3-Nitrotyrosine onto the paper-based SPE

The electrochemical response of 3-NT was firstly investigated by performing CV recordings between -1.0 V and +1.0 V and, afterwards, by means of SWV, without the use of any redox probe. The voltammetric parameters used during SWV were pulse: amplitude 20 mV, frequency 5 Hz and scan-rate 25 mV/s. Electroactivity studies were made in different buffer and supporting electrolytes, such as, 10 mM PBS pH 7.4, 0.1 M Phosphate Buffer pH 6-8, 1 M TRIS buffer pH 8.3 and 0.1 M KCl pH 5.8. Calibration curves were performed with 3-NT standard solutions ranging from 250 nM and 1 mM, prepared in the appropriate solution.

5.2.6 Selectivity assay

Under this study, tyrosine, ascorbic acid, uric acid and creatinine were chosen as interfering molecules. The selectivity studies were carried out, firstly, by performing SWV

measurements for each individual compound at high concentration, in the conditions described above. Afterwards, 3-NT calibration curves were carried out with and without the presence of the interfering tyrosine molecule.

5.3 RESULTS AND DISCUSSION

5.3.1 Electrochemical performance of the paper-based SPEs

Herein, the electrochemical characterization of the paper-based electrodes was carried out with CV method by choosing $[Fe(CN)_6]^{4-/3-}$ couple as the redox-probe. Figure 5.3 displays the CV recordings at several scan-rates, in 2 different electrolyte solutions, namely, 0.1 M KCl (Figure 5.3A) and PBS pH 7.4 (Figure 5.3B). All experiments were performed in triplicate.

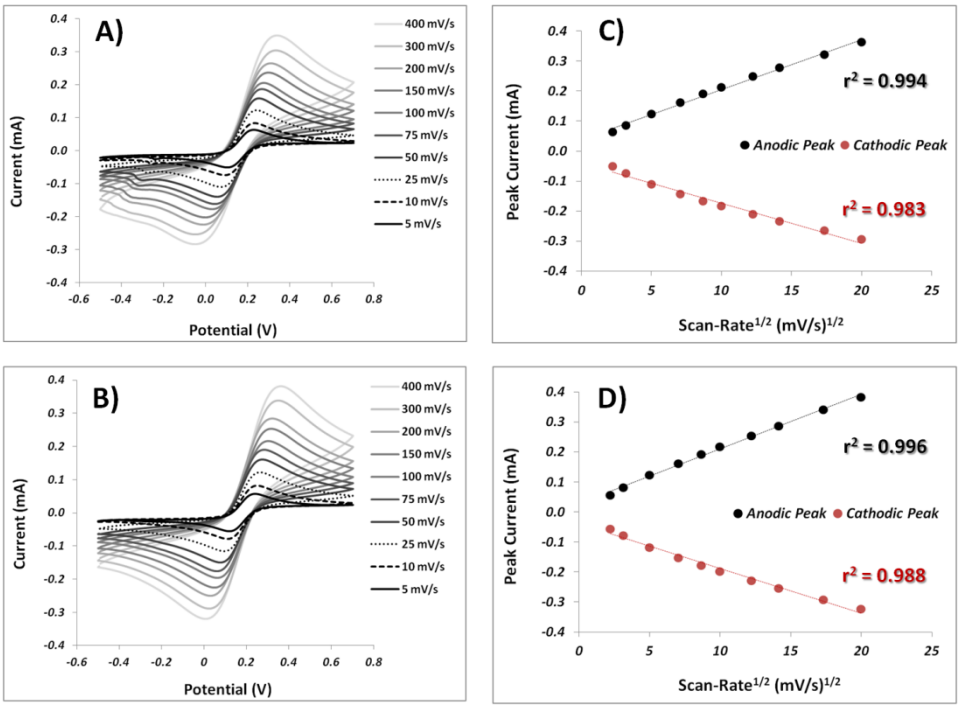

Figure 5.3: Cyclic voltammograms for 5 mM $[Fe(CN)_6]^{4-/3-}$ redox couple in A) 0.1 M KCl solution and B) PBS pH 7.4, at different scan-rates; Plot representation of both the anodic and cathodic peak currents versus the square-root of the scan-rate for 5 mM $[Fe(CN)_6]^{4-/3-}$ redox couple in C) 0.1 M KCl solution and D) PBS pH 7.4.

The analysis of the results showed that both electrolytes enabled good anodic and cathodic peaks with high peak amplitudes. Moreover, the increasing separation between the reduction and oxidation peaks potentials with increasing scan-rate reflects the quasi-reversible redox process of $[Fe(CN)_6]^{4-/3-}$ redox couple at the surface of our electrodes. Therefore, the currents of both anodic and cathodic peaks were plotted against the square-root of the scan-rate for the 2

studied systems, 0.1 M KCl and PBS, as can be seen in Figure 5.3C and Figure 5.3D, respectively. Our data showed a linear dependent behaviour along the scan-rate range 5 - 400 mV/s which is an indication of a diffusion-controlled mechanism responsible for the electrochemical process occurring at the electrode surface [280].

As previously explained, the nature of the conductive ink and its interaction with the substrate are key elements for the electrochemical performance of the electrode. Therefore, in most cases, the real area where electron exchange takes place, also known by active electrochemical surface area, is different from the geometrical surface of the electrode. To overcome this issue, the effective active surface area of the electrode can be estimated using the Randles-Sevcik equation [281]:

$$\mathbf{I_p = 268600 \times n^{3/2} \times A \times D^{1/2} \times C \times \upsilon^{1/2}}$$

where I_p is the peak current intensity (A), n is the number of electrons transferred in the electrochemical reaction, A is the electrode area (cm^2), D is the diffusion coefficient of the analyte, C is the bulk concentration of the analyte (mol/cm^3) and υ is the scan-rate (V/s).

Herein, we have employed the data from 5 mM $[Fe(CN)_6]^{4-/3-}$ redox couple in 0.1 M KCl since it was the system with better electrochemical reversibility behaviour. Accordingly, from the graphic representation of the peak current versus the square-root of the scan-rate we have applied the slope of this plot to the previous equation in order to estimate the electroactive surface area of our fabricated electrodes. Under these conditions, the value obtained for the effective active surface area of the electrodes was 0.138 ± 0.007 cm^2. Although this result is lower than the respective geometric area of the electrode, the activity ratio S_a/S_g, where Sa is the electroactive surface area and Sg is the geometric surface area, is quite similar to the respective value obtained for the commercial carbon-SPEs from Dropsens, which was around 30% (see Figure 5.4).

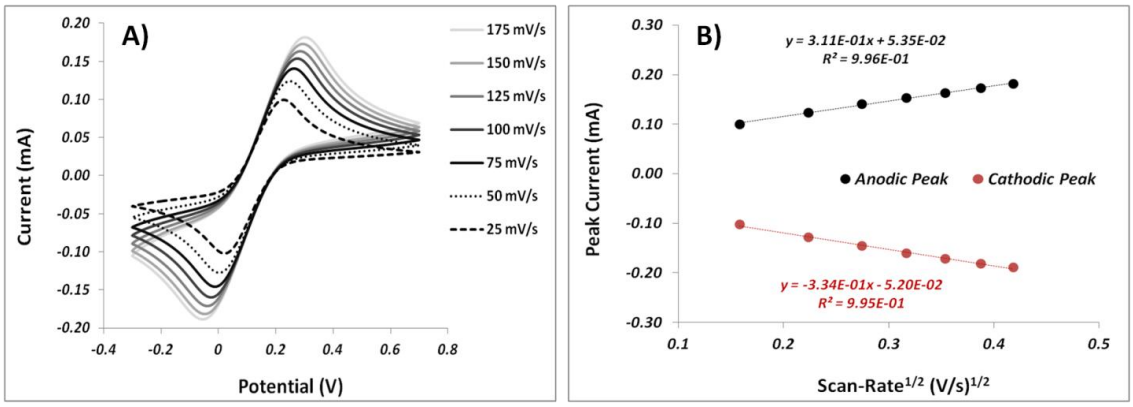

Figure 5.4: A) Cyclic voltammograms for 5 mM $[Fe(CN)_6]^{4-/3-}$ redox couple in 0.1 M KCl, at different scan-rates and B) plot representation of both the anodic and cathodic peak currents versus the square-root of the scan-rate for 5 mM $[Fe(CN)_6]^{4-/3-}$ redox couple.

In this study, CV was employed to investigate the electrochemical performance of the carbon-based electrode towards the negatively charged $[Fe(CN)_6]^{4-/3-}$ redox couple and the positively charged $[Ru(NH_3)_6]^{3+}$. Herein, $[Ru(NH_3)_6]^{3+}$ was selected as a redox probe because it undergoes a rapid and chemically quasi-reversible one-electron redox reaction, with both the oxidized and reduced forms of the ruthenium complex. Figure 5.5A shows the variation ΔE for both type of probes versus the scan-rate, in 0.1 M KCl. It was interesting to observe a quite similar behaviour for $[Fe(CN)_6]^{4-/3-}$ and $[Ru(NH_3)_6]^{3+}$ probes, that was a high increase of ΔE for lower scan-rates and at higher scan-rates it tends to stabilize. Moreover, the ratio Ip_A/Ip_C was calculated and plotted over the scan-rate range 5 - 400 mV/s, for both probes (Figure 5.5B). The estimation of this parameter allowed evaluating the reversibility character of the electrochemical system. As this ratio moves way from the value of 1, the system becomes less reversible [125]. The analysis of both graphs (ΔE and Ip_A/Ip_C versus scan-rate) seems to indicate a higher reversibility for $[Fe(CN)_6]^{4-/3-}$ system because peak-to-peak separation is lower and the ratio Ip_A/Ip_C is closer to 1 in comparison with $[Ru(NH_3)_6]^{3+}$ system. However, this may be related to the fact that only one ionic form of ruthenium was present, against the redox couple of iron.

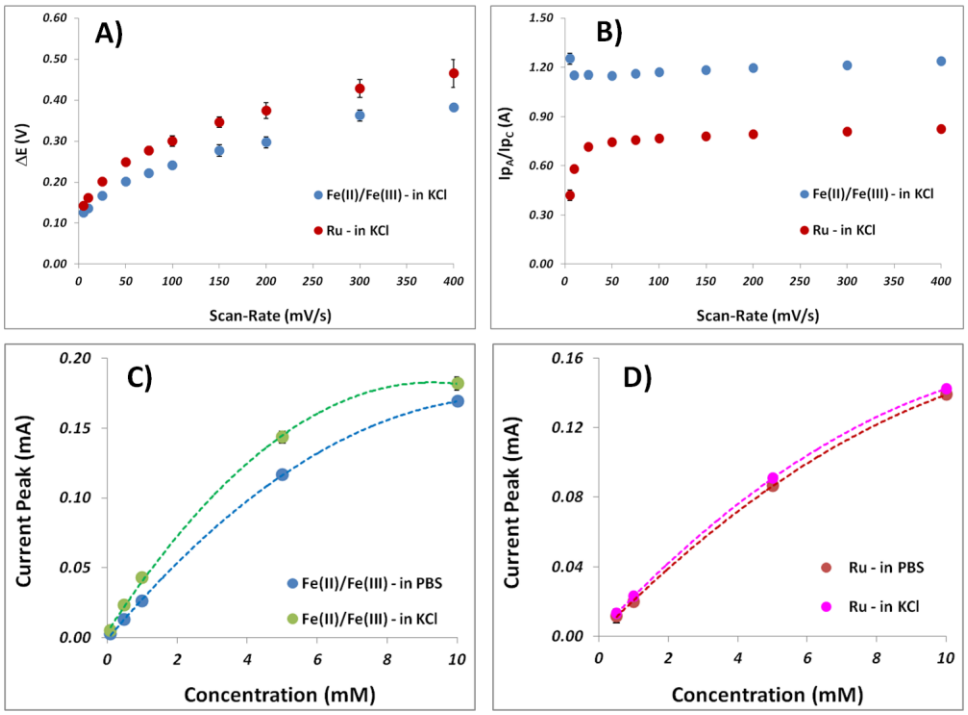

Figure 5.5: Effect of the different redox probes upon the electrochemical response. A) plots the peak potential separation (ΔE) versus the scan-rate and B) the anodic and cathodic peak current ratio (Ip_A/Ip_C) versus the scan-rate for $[Fe(CN)_6]^{4-/3-}$ and $[Ru(NH_3)_6]^{3+}$ probes at 5 mM concentration in 0.1 M KCl; Plots of current peak versus the probe concentration for C) $[Fe(CN)_6]^{4-/3-}$ and D) $[Ru(NH_3)_6]^{3+}$, at a scan-rate of 50 mV/s, in 0.1 M KCl and PBS pH 7.4.

Different concentrations of the redox probe, for an applied potential scan-rate of 50 mV/s, were tested and the current-voltage characteristics were recorded for $[Fe(CN)_6]^{4-/3-}$ (Figure 5.5C) and $[Ru(NH_3)_6]^{3+}$ (Figure 5.5D), in 0.1 M KCl and PBS pH 7.4 conditions. Although in both cases, the current peak amplitude increases with increasing probe concentration, the tendency of the response is different for the 2 types of probe. Not only the current peak amplitude is higher for the $[Fe(CN)_6]^{4-/3-}$ couple, the $[Ru(NH_3)_6]^{3+}$ probe did not seem to be sensitive to a supporting electrolyte variation, as depicted in Figure 5.5D, from the identical tendency in PBS and KCl solutions. In sum, for future applications, $[Fe(CN)_6]^{4-/3-}$ redox-probe seems to be a more suitable choice.

5.3.2 Morphological characterization of the paper-based SPEs

SEM analysis was also conducted to further investigate the surface morphology of the carbon electrode assembled onto the paper substrate. As can be seen in Figures 5.6A-B, the WE surface of carbon ink is a more or less uniform carbon layer composed by small islets, with very few cracks on the surface. In addition, the paper-based electrodes were vertically cut, and cross-section imaging were performed. Figure 5.6C shows the thickness of the applied carbon layer: by performing suitable measurements, the obtained values ranged from 33.1 to 39.9 μm. Furthermore, as depicted in Figure 5.6D, it was quite obvious to distinguish the borderline between the applied carbon layer and the paper substrate with its characteristic cellulose fibers.

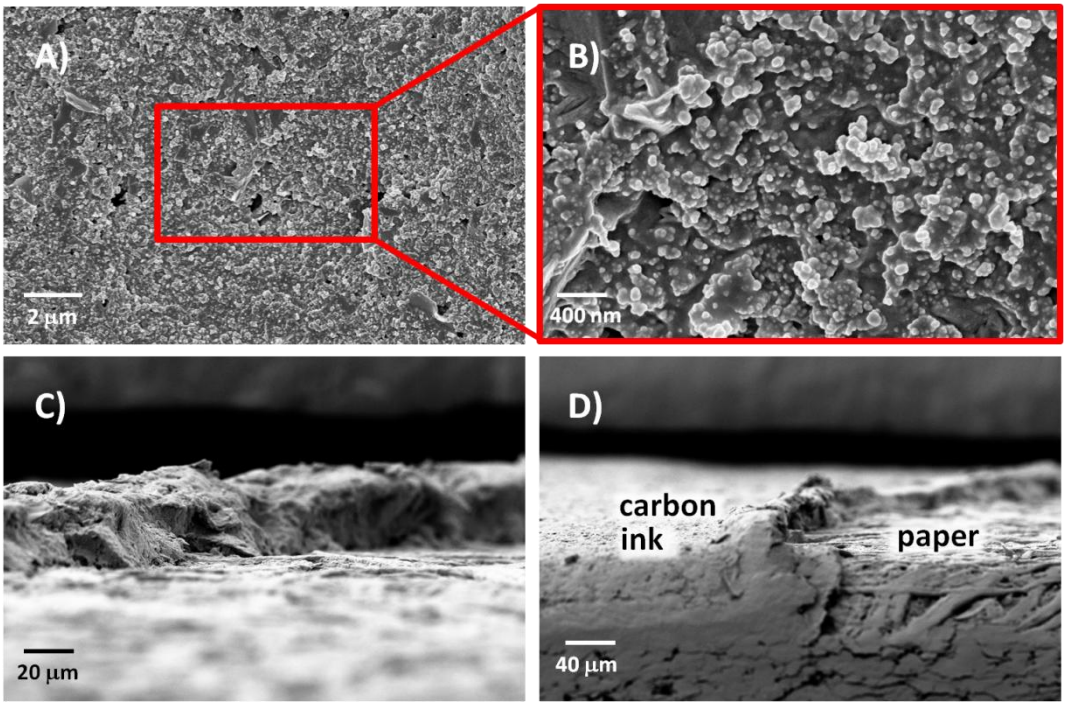

Figure 5.6: SEM images of the A) and B) WE carbon-surface at different magnifications and C) and D) Cross-section imaging of the carbon-layer at different magnifications.

5.3.3 Direct detection of 3-Nitrotyrosine

The electrochemical behaviour of 3-NT was studied by performing CV swept over the potential range -1.0 V and +1.0 V, in phosphate buffer solution. Figure 5.7 displays two well-defined oxidation peaks at +0.10 V and +0.80 V and, in the negative-moving direction, we were able to observe a cathodic peak at -0.84 V. Although not displayed here, during our study we found that the first anodic peak at +0.10 V was dependent of the occurrence of the cathodic peak, meaning that this oxidation reaction corresponds to the species formed at the carbon-based surface after 3-NT reduction at -0.84 V. According to previous studies [282][131][209], this reduction peak was assigned to the four-electron reduction of the nitro group to the corresponding hydroxylamine. Although mechanistic studies related to the electrochemical behaviour of 3-NT are not very common, herein, the characteristic oxidation peak of L-tyrosine structure was +0.80 V, attributed to a two-electron and two-proton process [283][279]. So, for further electrochemical experiments, this potential peak was chosen to study the electro-oxidation of 3-NT.

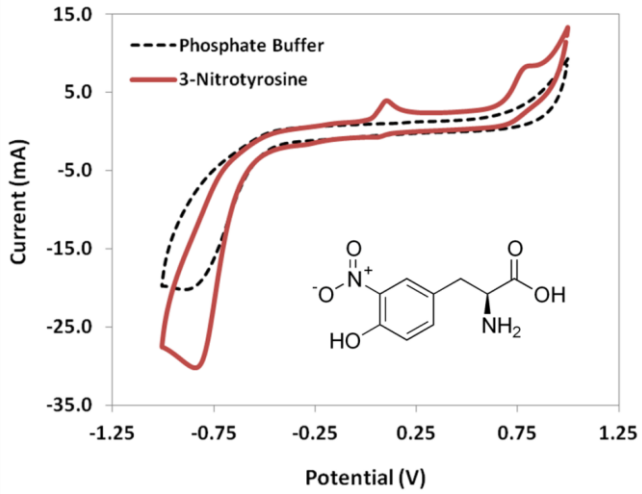

Figure 5.7: CV recordings over the potential range -1 V to +1 V in 0.1 M phosphate buffer with (colour line) and without (dashed line) 1 mM of 3-NT, at a scan-rate of 50 mV/s, and in the inset figure the chemical structure of 3-NT.

Under the scope of this work, SWV was the preferred voltammetric technique to follow the oxidation behaviour of 3-NT due to its high sensitivity combined with a fast response [113]. Firstly, as illustrated in Figure 5.8A, different electrolytes at different concentrations, such as, 0.1 M phosphate buffer, 10 mM PBS, 1 M TRis buffer and 0.1 M KCl were investigated to determine the most appropriate supporting electrolyte matrix. Although there were substantial differences related to the oxidation peak current, mostly due to the salts concentration, the more interesting issue here was the shift in the peak potential. Moreover, we observed that 3-NT in KCl solution (*at a 5.7 pH*) did not exhibit any peak over the potential range +0.60 V to +1.0 V.

So, along this study, phosphate buffer was chosen as the supporting electrolyte, showing the best peak amplitude/resolution and an oxidation peak displaced at less positive value, thereby revealing a more favourable process.

Afterwards, the effect of pH on the electrochemical oxidation of 3-NT was also studied by SWV in a 0.1 M phosphate buffer solution containing 1 mM of 3-NT (Figure 5.8B_1). Our data showed that with increasing pH from 6 to 7.5, the oxidation potential was moved towards less positive values and, in addition, a linear-dependent behaviour on the pH value of the buffer solution was found (Figure 5.8B_2), implying that both electrons and protons are involved in the electro-oxidation of 3-NT [207]. Furthermore, results showed that the oxidation peak current changed slightly with pH variation. Thus, subsequent experiments were carried out at pH 7.4, not only because it was near the best amplitude obtained, but also because we target to work under physiological conditions. In sum, besides electrolyte composition, the pH value also influences the detection performance of 3-NT.

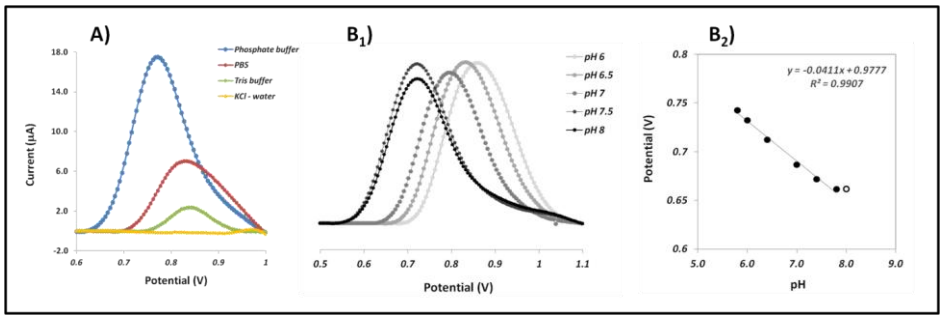

Figure 5.8: SWV response of 1 mg/mL 3-NT A) in different supporting electrolyte solutions and B_1) in 0.1 M phosphate buffer solution at different pH values ranging from 6 to 8. B_2) Plot of the potential value of the SWV versus the pH obtained in 1 mg/mL 3-NT in phosphate buffer solution.

5.3.4 Calibration and interference assay

Under the optimized parameters, the carbon-based electrode was tested with different concentrations of 3-NT. As displayed in Figure 5.9A, the peak current in SWV increased for increasing concentrations. Figure 5.9B shows the calibration curve for 3-NT with and without the application of pre-accumulation potential [*+0.40 V*] previous to the reading. The use of a pre-accumulation step has already been investigated as an approach to enhance the electrochemical signal for direct detection of electro-active species [257]. Herein, both results presented a quite similar behaviour and the sensor device showed a good linearity (r^2 = 0.9937 and 0.9927) over the concentration range 500 nM to 1 mM. The LOD, calculated by applying 3σ of the blank as three times the standard deviation of the first 3-NT concentration that enabled a current measurement, was found equal to 49.2 nM. Also, for 3 different independent experiments, the paper-modified electrodes showed excellent reproducibility with RSD lower than 1.5 %.

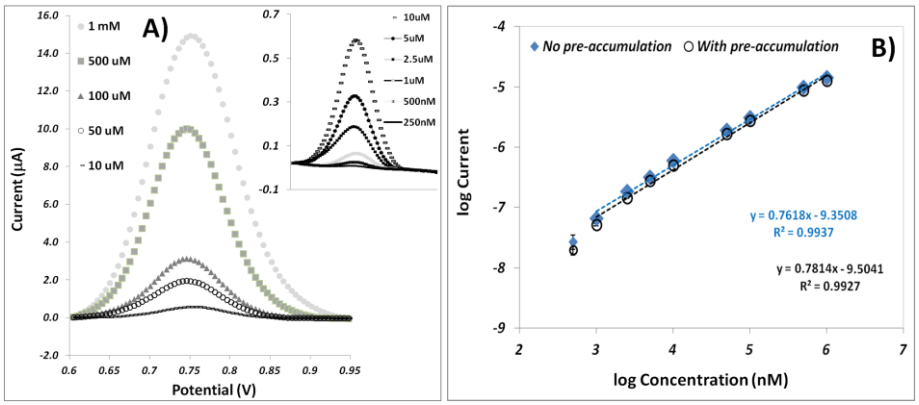

Figure 5.9: A) SWV recordings of 3-NT at different concentrations, in 0.1 M phosphate buffer at 7.4 pH (inset figure is for lower concentrations) and B) calibration curve of 3-NT, with and without the application of an accumulation potential.

Although this LOD was found slightly higher in comparison with other electrochemical studies reported in literature [209][278][47], our work appears as the voltammetric sensor device with more potential to become portable and suitable for *POC* application. In addition, some of these approaches have incorporated nanostructured materials during the sensor assembly as a requirement to obtain the required low detection limits. Firstly, the introduction of a flexible and low-cost substrate as paper to be use as the sensing platform enables a new generation of sensors towards the future sustainability. Moreover, the integration of the 3-electrodes system in the same structure holds many advantages, such as, simplicity, quick response, small feature size and low-cost instrumentation. Another issue that still needs to be well understood is the clinical value of the basal levels of 3-NT reported. In spite of the fact that has been an increasing evidence that the plasma concentrations of free 3-NT in healthy humans are in the order of 1 nM [29], another work have reported basal concentrations for 3-NT in a certain biological matrix that varied up to a factor of 1000 between different methods [44]. Thus, differences in the quality of the samples or in the composition of the study groups may contribute to a variability in 3-NT concentration.

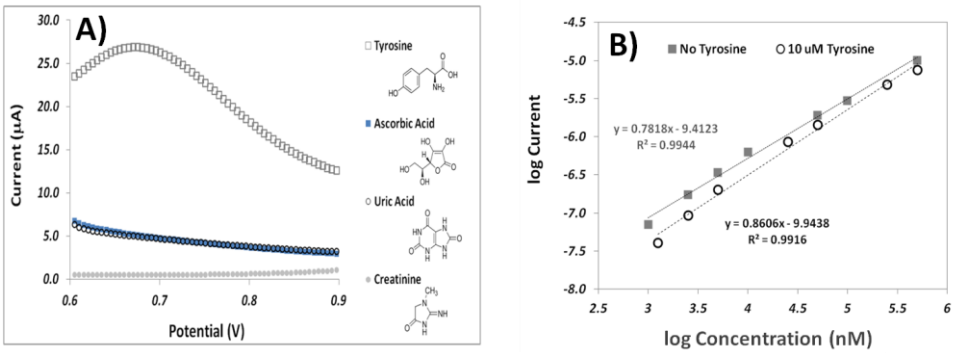

Figure 5.10: A) Electrochemical response of tyrosine, ascorbic acid, uric acid and creatinine over the studied potential range and B) the curves of calibration for 3-NT only and in the presence of 10 µM of tyrosine.

Herein, tyrosine, ascorbic acid, uric acid and creatinine were chosen as interfering molecules due to their similar structure, their presence in biological fluids and also their ability to behave like electro-active species. In this work, we have performed SWV recordings with each individual molecule in phosphate buffer solution under the potential range applied to the detection of 3-NT. As can be displayed in Figure 5.10A, only tyrosine gave a signal around +0.67 V, while the other molecules did not show any type of electro-activity. Since this oxidation potential is earlier to the oxidation of 3-NT, we applied the pre-accumulation potential described before (+0.40 V) to eliminate the interference of tyrosine. The results are illustrated in Figure 5.10B and there seems to be a strong evidence that, in the presence of a high concentration of tyrosine, the calibration curve of 3-NT holds the same tendency with a slight variation in the slope. Thus, in sum, we have demonstrated the fabrication and application of a label-free sensor device towards the detection and quantification of 3-NT. Although the desirable LOD was not yet achieved, in the future, to enhance the performance of this sensor some amplification steps can be included, such as, the introduction of nanomaterials [107] or even the integration of molecular imprinting materials [284]. In addition, the previous approaches can also improve the selectivity behaviour of this electrochemical sensor when applied to complex biological matrices.

5.4 CONCLUSIONS

In the present work we have designed and fabricated a paper-based device for electrochemical detection of 3-NT. Herein, these carbon-modified electrodes were electrochemically characterized, and the outcome data was quite similar to the available commercial-ones, which are constructed in a ceramic based support. Afterwards, the electro-oxidation of 3-NT was assessed over the concentration range 500 nM to 1 mM. The optimization of some experimental parameters, such as, pH and supporting electrolyte solution was performed and enabled a low detection limit for the direct determination of 3-nitrotyrosine. As a *proof-of-concept*, the proposed electrochemical label-free sensor holds high sensitivity, selectivity and reproducibility, representing a valuable alternative to the complex, time-consuming and high costly methodologies currently used. In addition, the fabrication of sensing devices on flexible substrates is likely to find further application *in-loco* and routine analysis outside the laboratory environment.

CHAPTER 6

6 Electrochemical paper-based biosensor for label-free detection of 3-nitrotyrosine in human urine samples using molecular imprinted polymer

The results presented in this chapter are currently submitted as Gabriela V. Martins, Ana C. Marques, Elvira Fortunato, M. Goreti F. Sales, "*Electrochemical paper-based biosensor for label-free detection of 3-nitrotyrosine in human urine samples using molecular imprinted polymer*" (2018).

6.1 INTRODUCTION

As mentioned previously, 3-NT is a sub-product generated during protein attack by free radicals [285][286] and has been proposed as a biomarker of OS [16]. An interesting overview concerning the routes for nitric oxide metabolism and its role in 3-NT biosynthesis was recently presented [287]. Aiming for an accurate quantification, different methodologies have been proposed including electrochemical detection [45][75]. For now, we still do not reach a consensus related to the basal levels of free 3-NT in human urine samples but most reported methods have presented concentrations of few nM in healthy subjects. In sum, portable, low-cost and quick analysis of clinical samples is an urging need in POC screening of 3-NT. To overcome this issue, biosensor technology has been introduced as the design of analytical devices that respond to a specific chemical specie in a biological matrix [288]. Among others, biosensors gained great interest due to their special features, such as, automation, quick response time, high sensitivity, miniaturisation and portable-size [92].

In parallel, SPE have been preferred against the conventional three-electrode system because these are disposable, easy-to-use and may operate with minimal volumes of analyte solutions. Following the last trends, paper has been chosen as the ideal support material to develop a screen-printed biosensor device for 3-NT, due to their special characteristics, such as, flexibility, porosity, biocompatibility, facile modification and functionalization, low-cost and sustainability [164][160]. Recently, a facile paper-based visual sensor for detecting anthrax biomarker has been developed by using filter paper immobilized with Tb/DPA@SiO_2-Eu/GMP, enabling direct observation of the colour switch from green to red by naked eyes under a UV lamp [289]. Moreover, a disposable paper-based platform with a bipolar electrochemical device was reported for the sensitive detection of the cancer marker prostate specific antigen (PSA), highlighting important sensing characteristics, such as simplicity, portability and disposability [290].

The other important component of an SPE is the biorecognition element. In order to achieve high sensitivity and selectivity standards, molecular imprinting technique coupled with electrochemical transduction has proven its potential in the fabrication of innovative biomimetic sensors. Among the different ways of MIP synthesis, electropolymerization enables the direct deposition of the sensing material on the transducer surface, allowing a facile and easy control of the film growth [205]. In terms of transducing element, electrochemical approaches have been widely applied for the detection and quantification of relevant electro-active markers and, due to their high sensitivity and selectivity [291][261][292].

Currently, the most commonly studied oxidation biomarkers of damaged DNA are purine bases (adenine and guanine) and 8-OHdG [30]. In this work, we have taken advantage of paper to design a low-cost and user-friendly electrochemical sensing platform against 3-NT, a sub-product originated during protein damage. Although there are few reported sensors for detection of 3-NT in biological matrices (Table 6.1), generally the use of signal amplification steps, such

as, the incorporation of nano-structured materials, was required in order to obtain low detection limits.

Table 6.1: Comparison of the different sensors for 3-nitrotyrosine detection in biological matrices.

Method	Substrate	Linear Range	LOD	Sample	Ref.
Electrochemical detection + MIP	Bimetallic Fe/Pd nanoparticles	21.6-3833 nM	5.3 nM	Human blood Urine	[209]
Electrochemical detection + MIP	GCE electrode with AuNPs	0.2-50.0 μM	50.0 nM	Human serum Urine	[47]
Fluorescent detection + MIP	Carbon dots	0.050-1.85 μM	17 nM	Human serum	[210]
HPLC detection with SPE + MIP	___	11.1-243 nM	3.1 nM	Human urine	[293]
Electrochemical detection	Mercury drop electrode	6.6-597 nM	0.25 nM	Cerebrospinal fluid, Plasma	[278]
SPR detection	Graphene	2.21-4421 pM	0.57 pM	Human serum	[294]

AuNPs: gold nanoparticles; Fe: iron; GCE: glassy carbon electrode; HPLC: High-performance liquid chromatography; MIP: molecular imprint; Pd: palladium; SPE: solid phase extraction; SPR: surface plasmon resonance.

Herein, we have employed a molecular imprinting approach based on the assembly of a non-conducting phenol matrix in order to develop a sensitive and selective label-free electrochemical biosensor assembled on a paper substrate and aimed at the sensitive detection of 3-NT biomarker (see Figure 6.1).

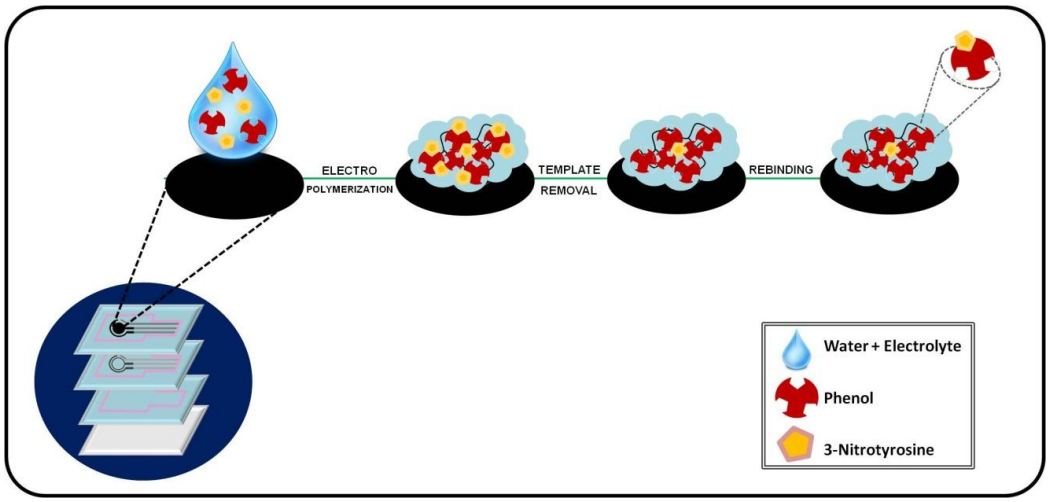

Figure 6.1: Illustration of the sensor film fabrication by molecular imprinting for recognition of 3-nitrotyrosine.

6.2 EXPERIMENTAL SECTION

6.2.1 Reagents and Materials

All reagents were of analytical grade and used without further purification. Buffer and electrolyte solutions were prepared with ultrapure water Milli-Q laboratory grade. The pH measurements were made in a pH meter from *Crison Instruments*, GLP21 model. Potassium hexacyanoferrate III ($K_3[Fe(CN)_6]$), potassium hexacyanoferrate II ($K_4[Fe(CN)_6]$) trihydrate and dipotassium hydrogen phosphate (K_2HPO_4) were obtained from Riedel-de-Haen; potassium dihydrogenophosphate (KH_2PO_4) was obtained from Panreac; potassium chloride (KCl) was from Merck; phenol (C_6H_5OH, for molecular biology) and sulphuric acid 95-97% (H_2SO_4) were from Sigma-Aldrich; PBS tablets from Amresco and 3-NT (98%) from Alfa Aesar. Potassium phosphate buffer solutions (0.1 M, pH 6.0) and (0.2 M, pH 7.0) were prepared by mixing the proper amount of K_2HPO_4 and KH_2PO_4. All experiments were performed at ambient temperature.

6.2.2 Apparatus

The biosensor device was assembled on fabricated paper-based electrodes composed by a carbon-ink as the counter and working (5 mm diameter) electrodes and, silver-ink as pseudo-reference electrode. Detailed description of the procedure of fabrication of these electrodes was described elsewhere [295]. The electrochemical measurements were carried out with a potentiostat/galvanostat from *Metrohm Autolab* and a PGSTAT302N with an FRA module, through an interface switch box from *BioTid Eletrónica*, and controlled by ANOVA software. All the presented potential values are against the silver pseudo-reference.

Raman spectroscopy was performed by using a Thermo Scientific DXR Raman microscope system with a 785 nm excitation laser, combined with a 50× objective magnification. Raman spectra were collected with an incident maximum laser power of 3 mW and through a slit aperture of 50 μm. Photobleaching was set to 20 min. For Raman measurements, data analysis was performed with OMNIC software.

SEM analysis was performed in order to evaluate the morphology of the polymeric films modified on the electrode surface, by using a Carl Zeiss AURIGA Crossbeam SEM-FIB workstation, operating with a voltage of 5 kV.

6.2.3 Electrochemical assay

Initially, the carbon surface of the electrodes was electrochemically cleaned by performing voltammetric sweeps between −0.2 V and +1.5 V in PBS at pH 7.4, until a stable voltammogram was obtained (more or less 100 cycles). Before use, sensors were well dried with nitrogen and stored at room temperature.

CV assays were performed at different potential windows in order to evaluate the electroactive behaviour of the compounds. Each modification performed on the paper-based electrodes was

electrochemically characterized by EIS of a 5 mM solution of $K_3[Fe(CN)_6]$ and $K_4[Fe(CN)_6]$, prepared in phosphate buffer solution (0.1 M, pH 6.0). EIS experiments were carried out over the frequency range 0.01 Hz to 100 kHz. All measurements were performed by covering the three electrodes of the paper-based sensor with a volume solution of 200 μl.

The detection of 3-NT molecule was followed by means of DPV in the potential range 0 V to +0.4 V, at a scan-rate 25 mV/s, pulse amplitude 25 mV and pulse width 50 ms. Before DPV measurement, the analyte was pre-concentrated at the electrode surface by applying a potential value of −1 V, for an optimized time. All experiments were conducted in triplicate at room temperature. Calibration curves were made with fresh 3-NT standard solutions ranging from 100 nM to 1 mM.

6.2.4 Assembly of the imprinted-based biosensor

The MIP film was deposited on the surface of the carbon-coated electrode through bulk polymerization. Initially, the electrodes were subjected to 5 voltammetric scans over the potential range −0.2 V to +1.5 V in H_2SO_4 0.5 M solution, as an electrochemical cleaning procedure. Afterwards, the electropolymerization was performed by applying cyclic voltammetry sweeps ranging between +0.2 V and +0.8 V, at a scan-rate of 50 mV/s, in KCl solution (0.1 M, pH 5.9) containing both phenol monomer and the template molecule 3-NT. Then, the template removal was made by incubation of the working electrode in a methanol:water solution (1:10, *v/v*) for 2 hours, at room temperature, followed by 1 hour stabilization in phosphate buffer solution. These solutions were prepared daily and all experiments were carried out at room temperature. Moreover, excluding the presence of 3-NT molecule, a similar procedure was taken in the fabrication of blank control material, named NIP-modified electrodes.

6.2.5 Analysis of urine samples

The selectivity features of the MIP-based sensor were directly assessed in human urine samples, due to their complex matrix. The urine samples were collected in sterile falcon tubes to avoid contamination and, afterwards, the fresh urine samples were frozen and stored in aliquots of 1 mL. Before the analysis, the samples were diluted in phosphate buffer solution (0.1 M, pH 6.0) in a 1:10 ratio. The detection of 3-NT in urine samples was performed by immersing the MIP-based device in the diluted samples, followed by a negative potential accumulation and finally DPV analysis. The same procedure was taken to the NIP control electrode.

6.3 DISCUSSION AND RESULTS

6.3.1 Electrochemical study

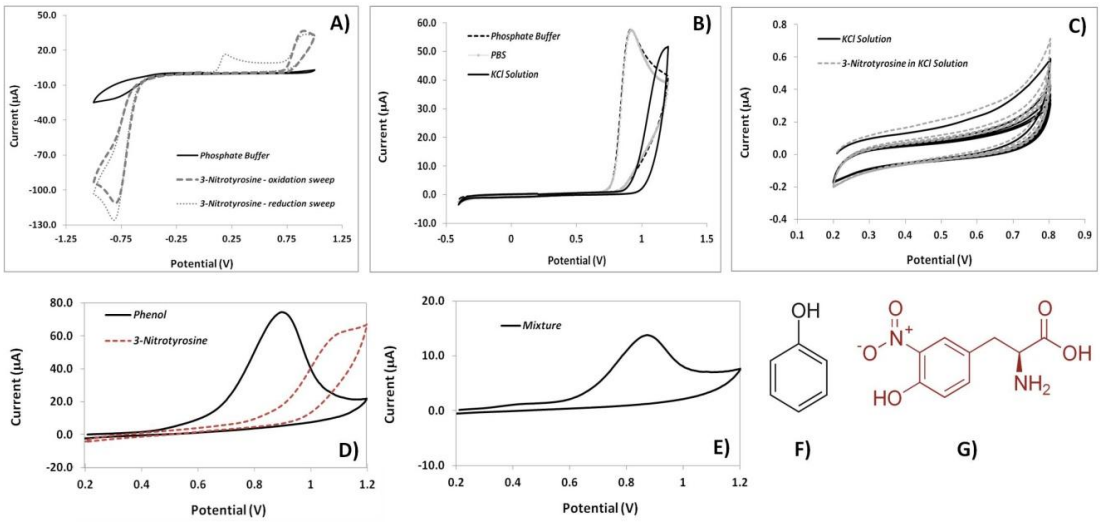

Figure 6.2: Cyclic voltammograms of 3-nitrotyrosine in A) PBS solution, at different scan directions, over the potential range -1 V to +1 V; B) three different electrolyte solutions, over the potential range -0.4 V to +1.2 V; and C) KCl solution, over the potential range +0.2 V to +0.8 V. Cyclic voltammograms of D) phenol and 3-nitrotyrosine, individually and E) mixture phenol + 3-nitrotyrosine. Chemical representation of F) phenol and G) 3-nitrotyrosine.

In the last years, the study of electrochemical oxidation of organic substances has been employed as a promising technique for analytical purposes. Herein, in order to evaluate the electrochemical behaviour of 3-NT in PBS solution (10 mM, pH 7.4), cyclic voltammetric sweeps were scanned in different directions over the potential range −1.0 V and +1.0 V, at a scan-rate of 50 mV/s. As depicted in Figure 6.2A, two well-defined oxidation peaks were observed at +0.20 V and +0.93 V, and a reduction peak around -0.85 V. This outcome is in accordance with our previous electrochemical study performed with the same modified-electrodes [295] and interestingly, we have found that the first anodic peak at +0.20 V depended of the occurrence of the cathodic peak. Hence, the results obtained by CV seemed to indicate that the earlier oxidation reaction corresponded to sub-species generated at the carbon surface after the reduction of 3-NT occurred at −0.85 V.

Although there are already some electrochemical sensor devices based on the electro-oxidation of 3-NT for detection applications [209][47], to the best of our knowledge, this is the first time that this low oxidation peak potential (+0.20 V) has been chosen to follow this target molecule. The main advantages of working with this narrow potential window are that the oxidation

reaction occurring on the surface of the modified electrode is more favourable; there is no need to apply high voltage to the electrode system that can cause an overcharge and, consequently, could compromise the performance of the silver pseudo-reference; and also, it allows to eliminate the interference of other electroactive species found in biological matrices (uric acid, ascorbic acid, etc), which occurs at higher potential values [296][251][259].

The effect of different buffer and electrolyte species on the oxidation peak potential was also assessed by CV in a solution containing 4 mM of 3-NT (Figure 6.2B). For this study, we have tested phosphate buffer solution (0.2 M, pH 7.0), PBS solution (10 mM, pH 7.4) and KCl solution (0.1 M, pH 5.9). Despite the difference on the salt species and concentration, it could be noticed that PBS and phosphate buffer solutions exhibited similar current and potential behaviour, while in KCl solution we could observe that the oxidation peak potential of 3-NT shifted to a more positive position. This last result can be advantageous in order to guarantee a wider potential window in which 3-NT molecule does not display electroactive properties. Furthermore, Figure 6.2C shows cyclic voltammograms in KCl solution alone and 3-NT in KCl solution, confirming that in the potential range +0.2 V to +0.8 V there is no evidence of oxidation reaction of 3-NT.

Under the scope of this work, phenol has been chosen as the structural monomer to grow the imprinted polymeric matrix. It is a non-conducting material, holding good stability properties and typically known electro-oxidation properties. Several mechanisms regarding the oxidation of phenol and phenol derivatives have been described on gold [49] and platinum [50][51] surfaces, but less on glassy carbon electrodes [52]. Among others, experimental parameters, such as, temperature, concentration of the monomer, electrolyte type and pH of the applied electrolyte have proven to influence the electrochemical oxidation of phenol [48][51][54].

Figure 6.2D displays cyclic voltammograms scanned over the potential range +0.2 V to +1.2 V, at a scan-rate of 50 mV/s, for a 10 mM solution of phenol and a 4 mM solution of 3-NT, individually, both prepared in KCl 0.1 M solution (pH 5.9). As expected, these results indicated an irreversible oxidation reaction of the phenol monomer occurring on the electrode surface, around +0.9 V. Furthermore, in accordance with our previous data, 3-NT alone exhibited an anodic peak at higher potential values. Meanwhile, Figure 6.2E showed the voltammetric sweep performed on the mixture phenol and 3-NT in KCl 0.1 M solution and only one well-defined oxidation peak was observed, meaning that under this experimental conditions it was not possible to separate accurately phenol (Figure 6.2F) and 3-NT (Figure 6.2G) electro-oxidations. In sum, the electropolymerization of phenol was carried out herein over the potential range +0.2 V to +0.8 V, in order to avoid any kind of oxidation reaction that could modify or entrap irreversible 3-NT molecule in the polymeric matrix.

6.3.2 Electropolymerization of phenol - MIP versus NIP

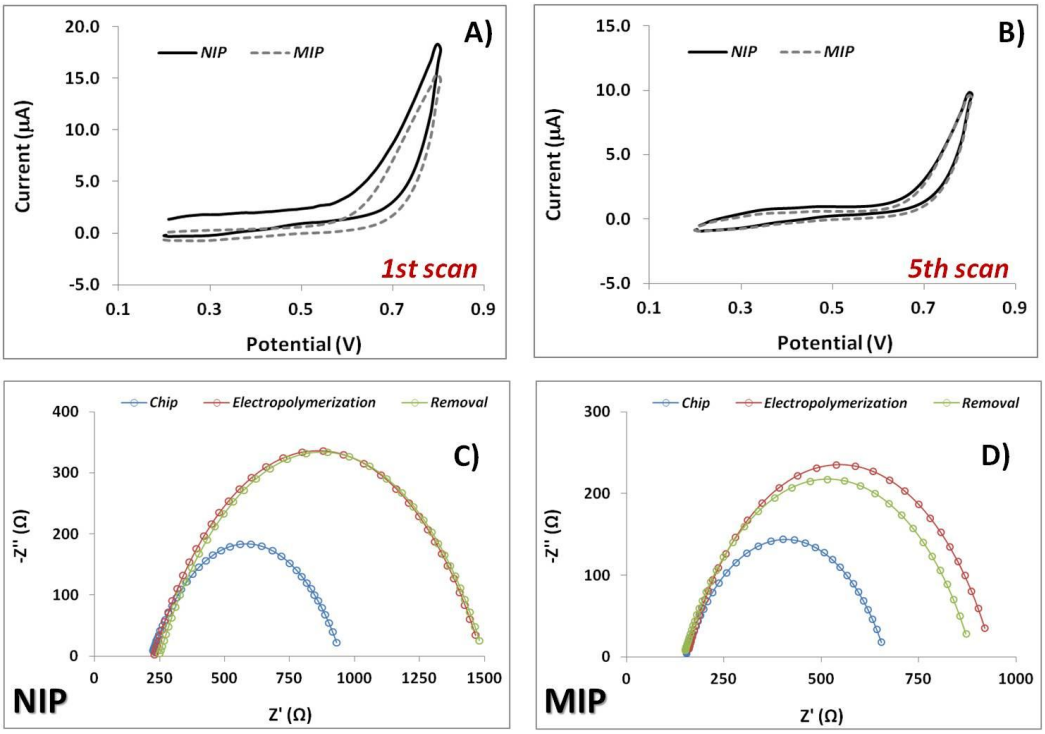

Figure 6.3: Cyclic voltammograms of NIP and MIP electrodes during electrochemical polymerization of phenol for the A) 1st and B) 5th scan cycle, in KCl solution (0.1 M, pH 5.9). EIS obtained for each step of the construction for C) NIP and D) MIP electrodes, in 5 mM solution of $K_3[Fe(CN)_6]$ and $K_4[Fe(CN)_6]$ prepared in phosphate buffer solution (0.1 M, pH 6.0).

Herein, electropolymerization was the approach chosen to assemble the biomimetic material because we can precisely tune the thickness and growth of the film *in-situ*, without using additional initiator species. Briefly, electro-oxidation of phenol occurs through the formation of the phenoxy radical, that can react with other species present in the solution generating products or else reacts with other phenol molecules producing a dimeric radical. Usually, the rate-determining step for phenolic compounds is one electron reaction, such as phenoxy radical forming [47]. The polymerization curves corresponding to the MIP and NIP imprint polymers for the 1st and 5th scan cycles are shown in Figure 6.3A and Figure 6.3B, respectively. As expected, voltammograms displayed an irreversible oxidation reaction of the monomer for both NIP and MIP materials, with NIP holding a higher current peak. It was also observed that the potential of the oxidation peak did not suffer any change with the increasing of the number of cycles. This behaviour was attributed to the electrode fouling produced by the formation of a non-conductive polymeric layer resulting from phenol oxidation that blocks the electrode surface. Moreover, the current peaks gradually decreased with the number of cycles, which is another characteristic assigned to the growth of non-conducting polymers [49]. In addition, no significant difference was observed in the cyclic voltammograms with and without

the template molecule, shown in Figure 6.3B, by the similar amplitude current obtained in the end of the polymerization reaction.

One of the great advantages of using an electropolymerization approach is their ability to finely tune the amount of deposited polymer, by adjusting the duration of the applied voltage (number of cycles), the scan-rate and the potential window. The thickness (*d*) of the polymer film can be roughly estimated from the charge (*Q*) passed during electropolymerization, according to Faradays law [243]. By applying the following relation:

$$d = QM/FA\rho$$

where *M* is the molar mass of the monomer, *F* is the Faraday constant (96485 C/m^2), ρ is the density of the polymer, taken to be 1 g/cm^3 for polyphenols and *A* is the electrode surface area. Herein, the thickness of the polymeric film was about ~2.5 nm. One of the limitations of using non-conducting polymers, such as phenol and phenol derivatives, is because of their self-limited growth on the electrode surface and, therefore, resulting in very thin films (< 100 nm) [297]. Here, the target molecule to be imprinted is quite small and, consequently, there is no need to assemble thicker films. Moreover, previous electrochemical studies have used imprinted electrodes, modified with non-conducting films, holding ultrathin polymeric layers in order to improve the sensitivity of the device [298].

Nowadays, impedance techniques are being widely applied to monitor variations in electrical properties as a direct response of the bio-recognition events that take place at the surface of the electrodes. Moreover, EIS holds the advantage of not causing any damage to the analyzed surface and do not introduce any disturbance in the studied system. Herein, along the fabrication of MIP and NIP, the electrodes were stepwise characterized by means of EIS, using as redox probe a 5 mM solution of $K_3[Fe(CN)_6]$ and $K_4[Fe(CN)_6]$ prepared in 0.1 M phosphate buffer. Usually, the impedance spectrum includes a semi-circular portion at higher frequencies and a linear portion at lower frequencies which corresponds to *Rct* and the diffusion process, respectively. Figure 6.3 also displays the Nyquist plots showing each step of the modification of the fabricated NIP (Figure 6.3C) and MIP (Figure 6.3D) electrodes. As expected, the electropolymerization of phenol resulted in a substantial increase of the Rct value due to the blocking of electron transfer by the polymeric matrix. Moreover, the results obtained for NIP and MIP after electropolymerization suggested that the non-imprinted coated electrode exhibited stronger insulating properties, which constitutes an evidence of the presence of the template molecule on the imprinted material, which partially hinders the growth of polyphenol film. Afterwards, the removal step caused a small decrease of the Rct value only on the MIP modified electrode, suggesting that the formation of the imprinted cavities occurred and, consequently, electronic diffusion was facilitated. In the literature, there are different approaches to extract a template molecule from the polymeric matrix of MIP-based sensing devices, including washing with sulphuric acid, acetic acid, methanol, ethanol, etc. Furthermore, previous works have already been well succeeded in the removal of template protein by using mixed organic solvents, such as, PBS:methanol (10:1, *v/v*), without causing degradation of the

polyphenol film [49] or even incubation in ethanol:water (5:1, *v/v*) mixture [52]. In the current study, a mixture methanol:water (1:10, *v/v*) was chosen as the mix solvent with more satisfactory results, because it was able to efficiently extract the 3-NT template without causing any degradation or modification to the polymeric material.

6.3.3 Optimization of experimental conditions during MIP assembly

6.3.3.1 Effect of scan-rate and number of electropolymerization cycles

Beside thickness, the density of polyphenol films can also be adjusted by controlling some variables during electropolymerization, such as, the rate of film growth and the number of voltammetric sweeps. Hence, comparative studies were performed by using EIS to characterize the charge transfer properties of different modified electrodes, at various experimental conditions.

Herein, the MIP-based electrodes were assembled with three different scan-rate values, as shown in the Nyquist plots of Figures 6.4A-C. Firstly, the only MIP-coated material that presented a decrease of the Rct value as the result of the creation of imprinted cavities was the one assembled at a scan-rate of 50 mV/s, while the others suffered an increasing variation. Moreover, the electropolymerization performed at 50 mV/s scan-rate was responsible for the formation of a less insulating surface (366 Ω), which could be an advantage for the successful extraction of the template molecule from the MIP matrix [49]. In addition, Figures 6.4D-F, illustrate the Nyquist diagrams obtained during the fabrication of the MIP electrodes using 2, 5 and 10 CV cycles, respectively. Generally, the detection capability of a sensor is highly affected by the number of scanning cycles used in the formation of the polymeric material. For instance, a lower number of cycles is often associated to a favourable analytical performance whereas a higher number of voltammetric cycles can led to the formation of a thicker film with less accessible imprinted sites and, consequently, less sensitivity [102][299]. Furthermore, a high number of scanning cycles increased the possibility of 3-NT template molecules becoming trapped in the polymer matrix. Herein, our data showed that the higher % of template removal was obtained for the MIP prepared with 5 scanning cycles (~10 %), when compared with 2 cycles (~4 %) and 10 cycles (~3 %). Therefore, 5 cycles with a scan-rate of 50 mV/s were selected for the growth of the non-conductive polymer layer.

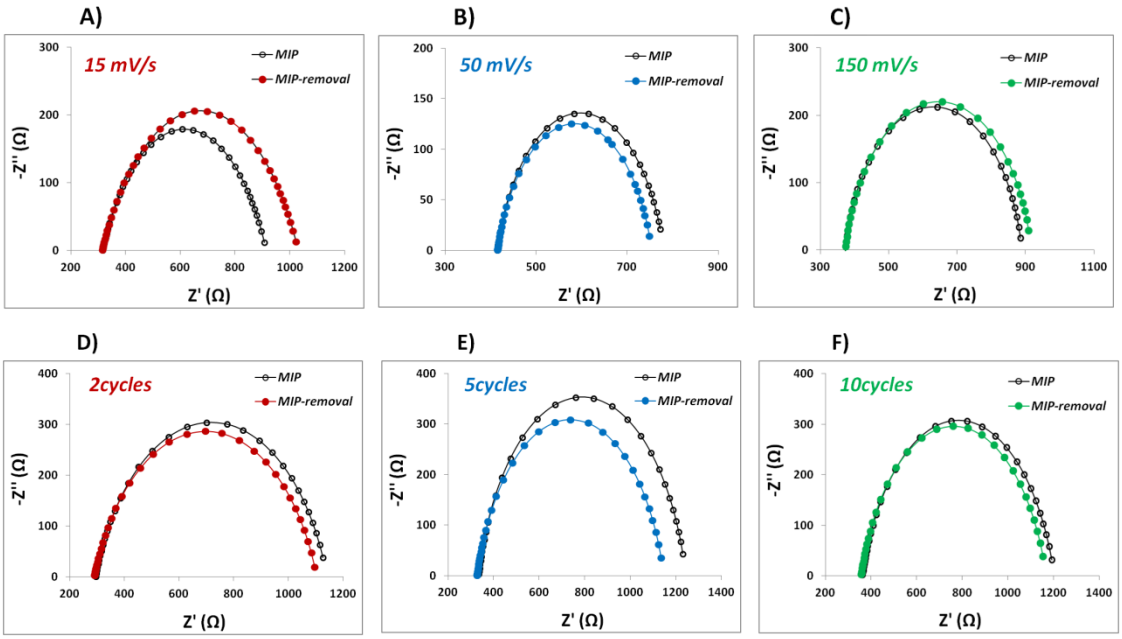

Figure 6.4: A) EIS measurements obtained before and after template removal, at different scan-rates: A) 15 mV/s; B) 50 mV/s and C) 150 mV/s and, with different number of cycles: D) 2; E) 5 and F) 10, recorded during phenol electropolymerization.

6.3.3.2 Effect of monomer concentration

Among others already mentioned, polyphenol films hold a great advantage as a biomimetic matrix because it can be easily synthetized by electropolymerization from aqueous solutions of the monomer. In addition, the thickness of the imprinted layer can also be adjusted by optimization of the monomer concentration. Herein, EIS was used to follow the construction of NIP and MIP sensors, with two distinct concentrations of phenol: 1.0 mM (Figure 6.5A) and 0.25 mM (Figure 6.5B). As expected, the Rct values of both NIP and MIP are shifted towards higher values for increasing phenol bulk concentration. It was interesting to observe that the stronger insulating character of the non-imprinted coated electrode compared to the imprinted-device was maintained in both concentrations. The obtained data also have showed that in the case of 1 mM of phenol (Figure 6.5A) the films formed were quite resistive (4 kΩ < Rct < 7 kΩ), which may be a limitation in terms of sensor sensitivity.

In addition, the rebinding of 3-NT molecule was quantified by means of differential pulse voltammetry (DPV). In practice, the current data accounted the occupation of the imprinted cavities in the MIP electrode by the template molecules, followed by their electro-oxidation. Figure 6.5C presents DPV calibration curves plotted with the logarithm of current of MIP sensors against the logarithm concentration of 3-NT. The comparison of the two curves have showed that a lower concentration of phenol (0.25 mM) enabled lower detection limits when compared to 1 mM concentration of phenol, which is in agreement with our previous

conclusions that thicker films hold less number of imprinted cavities and, consequently, less sensitive responses. So, a concentration of phenol monomer of 0.25 mM was chosen for further studies.

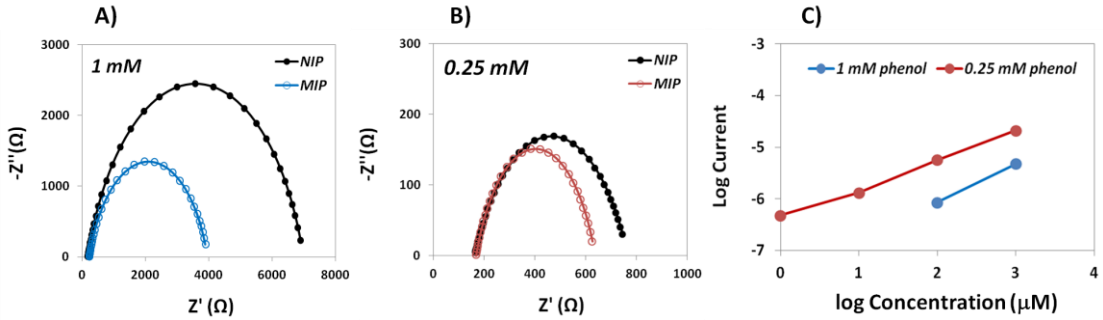

Figure 6.5: EIS obtained for NIP and MIP sensors at two different phenol concentrations, A) 1 mM and B) 0.25 mM. C) 3-Nitrotyrosine response for both MIP electrodes, obtained from DPV measurements.

6.3.3.3 Effect of imprinted 3-NT concentration

The concentration of the template was another crucial parameter that could influence the MIP performance. Specifically, the ratio template-monomer of MIP determines the number of binding sites available for the selective rebinding of the molecules and, consequently, the detection limit of the biosensor. In parallel, the interaction of these molecules with the phenol units during the assembly of the polymeric matrix also dictates the formation of stable and specific binding cavities. Phenol-based MIP films have been widely applied as recognition matrices in biosensors due to their ability to interact with other molecules through the existence of the π donor-acceptor interactions [51].

Herein, the effect of 3 different concentrations of 3-NT was investigated during phenol electropolymerization. Figure 6.6A illustrates the charge variation that MIP electrodes suffer during the 5 scanning cycles and Figure 6.6B displays the corresponding Nyquist diagrams obtained after the electropolymerization step. Data showed that for increasing concentrations of 3-NT the tendency was to obtain a less insulating polymeric layer, which is in agreement with our previous results, where the presence of the template molecule can partially hinder the growth of polyphenol film. Afterwards, the rebinding of 3-NT molecule was also investigated by means of DPV for the 3 different concentrations, 0.05 mM (Figure 6.6C), 0.25 mM (Figure 6.6D) and 0.50 mM (Figure 6.6E). Overall, the higher concentration of imprinted molecule (0.50 mM) enabled the detection of lower concentrations in comparison with the other imprinted concentrations of 3-NT, which constitutes a strong indication that using higher concentration of template molecule results in the creation of more imprinting sites available for the rebinding (see Figure 6.6F).

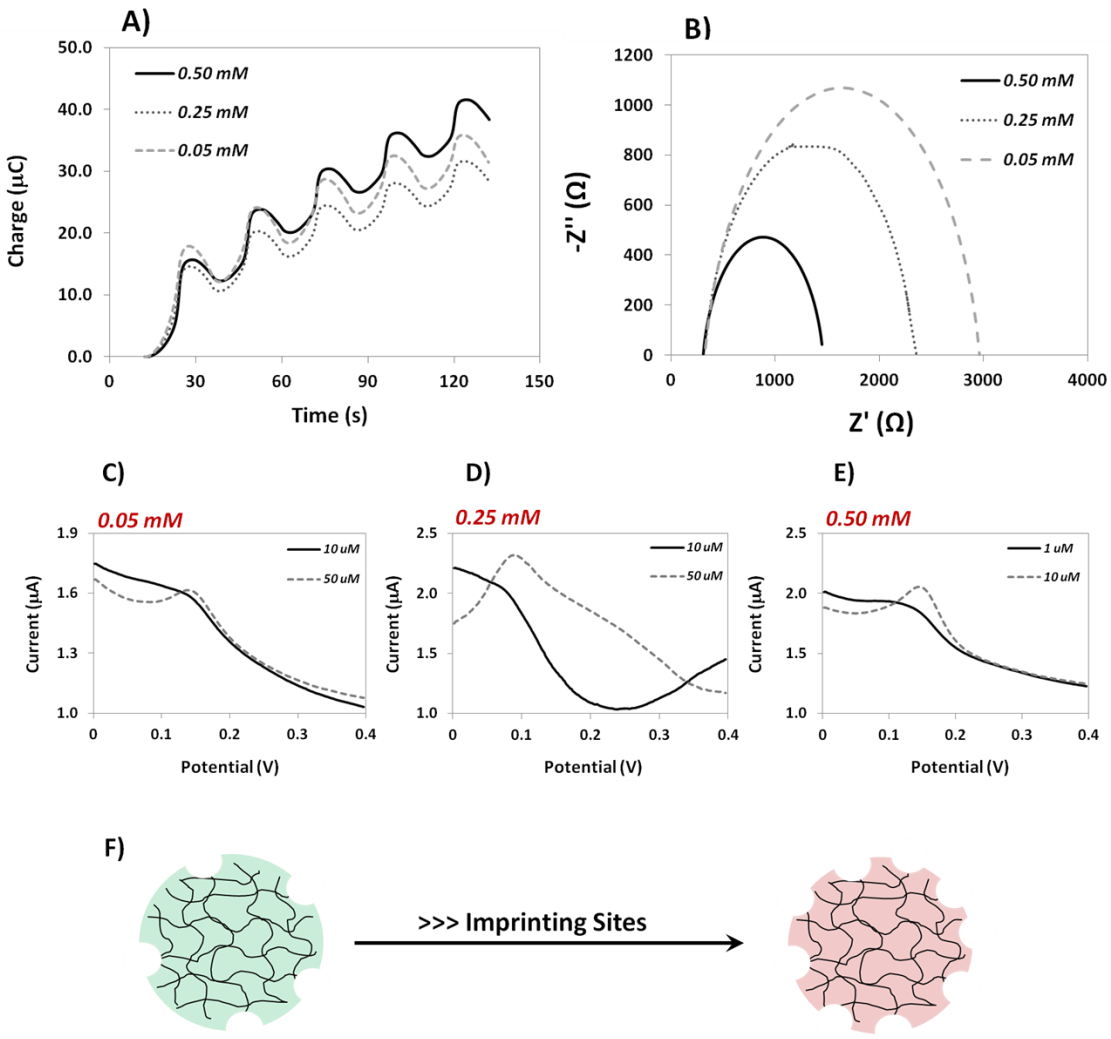

Figure 6.6: A) Charge variation during phenol electropolymerization (5 cycles) obtained from MIPs with different concentrations of template molecule; B) EIS obtained for the MIPS with different concentrations of template molecule; DPV measurements after contact with different concentrations of 3-NT for MIPs with C) 0.05 mM, D) 0.25 mM and E) 0.50 mM concentration of template molecule; F) Scheme related to the distribution of imprinting sites.

Although not presented here, along this optimization study the experimental conditions of the DPV measurements where finely tuned in order to get the higher response current. Specifically, one of the great advantages of our approach was the elimination of long incubation periods, by applying a pre-accumulation potential before each electrical measurement. In all experiments, the accumulation potential value used before the DPV measurement was −1 V and different accumulation times were tested, namely 30, 60 and 180 s. Our best electrochemical response was obtained for 60 s of accumulation at −1 V and so, these conditions were applied along this work.

6.3.4 Characterization of the modified paper-electrodes

Raman spectroscopy has been widely used as a popular tool for the characterization and structural organization of carbon materials. Herein, Figure 6.7A presented the Raman spectra for the different modifications performed on the paper-based electrodes. Firstly, all samples presented two well distinct peaks occurring typically in graphite-based substrates, the so-called G and D peaks, lying at around 1570 and 1310 cm^{1}, respectively. In the clean carbon-coated electrode, the G band appeared at 1584 cm^{-1} and was assigned to the C/C stretching in graphitic materials, composed of sp^2 bonded carbon in planar sheets [300]; the D band appeared around 1307 cm^{-1} and is often referred to as the disorder band or the defect band. In order to characterize the level of disorder within the carbon material, the intensity peak ratio between the D and G bands (I_D/I_G) was analysed.

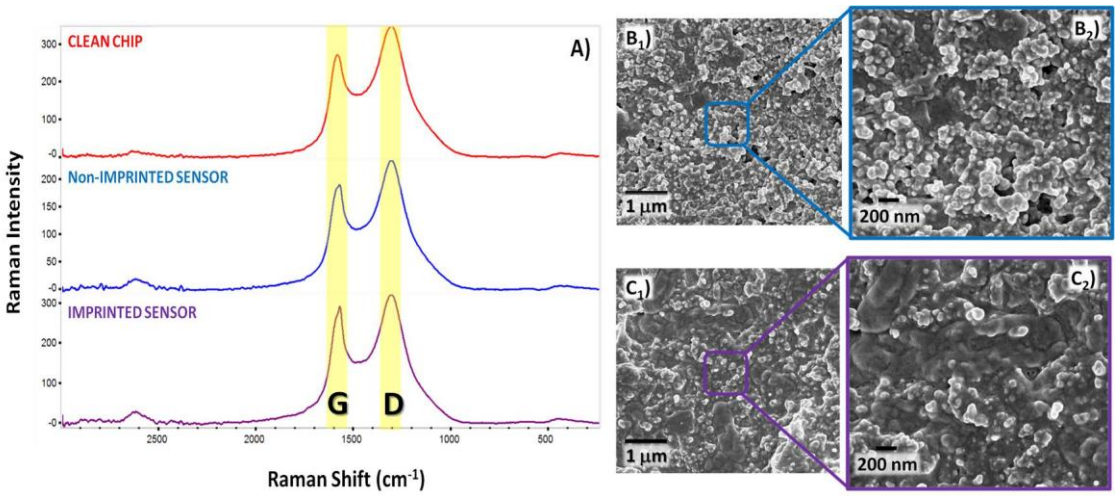

Figure 6.7: A) Raman spectra of clean carbon-based electrode, NIP and MIP-modified surfaces. SEM images of B) NIP and C) MIP materials.

Table 6.2: Analytical data obtained from the Raman spectra related to the different modifications.

Sample	*D* Position (cm^{-1})	Intensity	*G* Position (cm^{-1})	Intensity	I_D/I_G
Clean chip	1307.21	347.10	1584.77	269.56	***1.29***
NIP	1308.13	233.63	1574.36	188.59	***1.24***
MIP	1310.11	320.74	1572.68	290.53	***1.10***

Table 6.2 displays the peak positions of the G and D bands in the materials that were investigated, as well as the corresponding intensities. Although the I_D/I_G ratios showed a similar tendency among the different electrodes, it was interesting to observe that the introduction of

the polymeric material, on both NIP and MIP cases, resulted in a carbon system with less level of disorder. Moreover, another typical Raman band of carbon related materials is the 2D band, usually located around 2700 cm^{-1}. As can be seen on Figure 7.7A, this band is almost absent in the spectrum of the clean carbon-coated chip, but on both NIP and MIP materials this signal appears enhanced, which constitutes another strong evidence of the deposition of the polymeric material.

Surface morphology of the prepared NIP and MIP electrodes was further studied by means of SEM, as can be seen in Figure 6.7B and Figure 6.7C, respectively. The main difference observed between both materials was that the NIP surface presented a higher distribution of small islets while in the MIP surface the growth of the polymeric film seemed more even and well spread on the electrode. Moreover, the globular structure obtained for the phenol polymeric film was in agreement with a previous study, performed in a different substrate material [267]. Although it was not possible to visualize the imprinted cavities, due to the small dimensions of 3-NT molecule, the differences observed in the SEM images can be an indication of the presence of 3-NT molecule during electropolymerization that resulted in a different structural polymeric growth.

6.3.5 Performance of the imprinted-sensor

6.3.5.1 Calibration curve

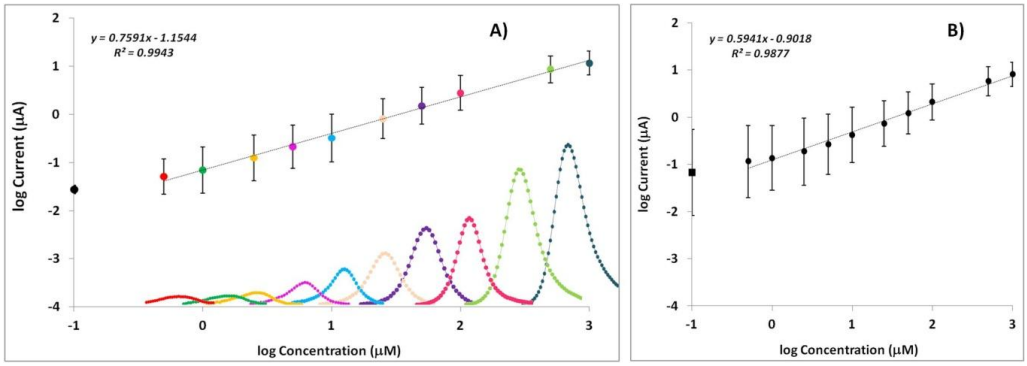

Figure 6.8: Calibration curves corresponding to the response of A) MIP and B) NIP sensors against the concentration of 3-nitrotyrosine. The inset figure is related to the DPV recordings for each standard concentration.

The main analytical features of the 3-NT biosensor were evaluated by DPV calibration curves, carried out under the optimal experimental conditions. Figures 6.8A and 6.8B show the calibration curves plotted with the logarithm concentration of 3-NT versus the logarithm of

current for MIP and NIP sensors, respectively. As can be seen, a linear tendency was obtained for both imprinted and non-imprinted materials from 500 nM to 1000 μM, but the MIP sensor showed higher sensitivity (*slope = 0.7591*), better linearity (r^2 = *0.9943*) and better reproducibility (smaller error-bars) in comparison with the NIP. The *LOD* was 22.3 nM, calculated as three times the standard deviation from the blank measurement (in the absence of template molecule). The inset graphic representation illustrated in Figure 6.8A concerns the DPV data obtained for the MIP-based sensor for the respective concentrations of 3-NT molecule. The precision of both modified-electrodes, for 3 different independent experiments, is also presented on Figure 6.8, over the entire concentration range.

Compared with other methods (see Table 6.1), the *LOD* found here is in agreement with other works reported in literature involving a molecular imprinting technology coupled with electrochemical sensing. Interestingly, when reviewing the construction of these imprinted-based sensors, it was generally found that the use of amplification steps, such as, the incorporation of nanomaterials, was required to achieve such low detection limits. Besides, another relevant advantage of our electrochemical device is the use of a label-free approach that enables decreasing substantially the analysis time and, consequently, becoming more affordable. The use of a paper support is also a great advantage in terms of cost.

6.3.5.2 Urine samples

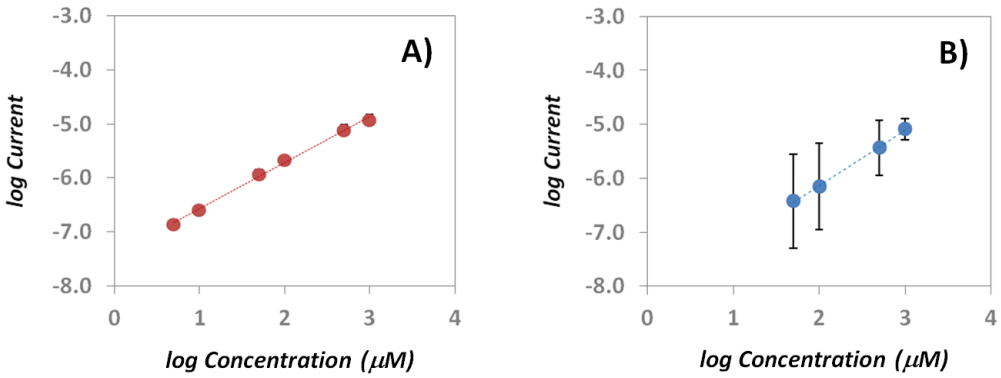

Figure 6.9: Calibration curves corresponding to the response of A) MIP and B) NIP sensors against the concentration of 3-nitrotyrosine, performed in 1:10 diluted human urine samples.

In order to evaluate the applicability of the proposed MIP-modified electrode in real samples, the electrochemical readings of 3-NT standards were performed in a background of human urine samples. Thus, diluted blank urine samples (1:10 in phosphate buffer) were spiked with different concentrations of 3-NT and analysed by means of DPV measurements. As can be seen in Figure 6.9A, the MIP material enabled the quantification of 3-NT from 5 μm to 1 mM, with RSD ranging 1 to 2 %. In contrast, the NIP material (Figure 6.9B) showed a non-reproducible response along a narrow range of concentrations, which could be a strong

indication of the non-specific adsorption phenomena occurring at the surface of the polymeric material.

Overall, these results demonstrated the capability of this imprinted-modified sensor assembled on paper support to sensitively quantify 3-NT in urine samples. Despite the existence of few sensor devices with similar *LODs* for the detection of 3-NT, our purpose herein was the development of a quick, facile, reproducible and low-cost paper-based biosensor suitable to be applied as a portable tool in *POC* screening.

6.4 CONCLUSIONS

This study reports a label-free electrochemical biosensor platform for *in-situ* detection of 3-NT. Herein, the application of an imprinted material could enable specific rebinding of molecules into the imprinted cavities of MIP-modified films, improving selectivity features of the biosensor device. The optimization of some experimental parameters during electropolymerization, such as, scan-rate, number of cycles, monomer and template concentration, among others, allowed to finely tune the thickness and growth of the polymeric matrix. In sum, the imprinted-based sensor showed high sensitivity and selectivity towards 3-NT over a wide range of concentrations and was successfully applied to the analysis of biological samples. Although the obtained LOD was not the lower value found in the literature, the electrochemical performance of this paper-based biosensor greatly satisfies the requirements of a selective, reproducible, disposable and sustainable sensing platform that can be easily and costly miniaturized in the future.

CHAPTER 7

7 Synthesis and characterization of core-shell magnetic nanoparticles

7.1 INTRODUCTION

As previously mentioned, MNP are being widely used as an efficient solid platform for the isolation, purification and pre-concentration of target molecules due to their straightforward application, hindering occasional losses of analyte [110]. Moreover, through the facile application of an external magnetic field, these nano-sized particles can be easily retained during the application of a magnetic force and then, quickly release after the exposure, without suffering significant changes. In addition, magnetic-based delivery approaches have the intention to associate drugs with magnetic vehicles in order to concentrate and, afterwards, release the same drug at the local of interest [301]. Thus, the incorporation of magnetic nanoparticles as novel sensing substrates holds great advantages, such as, the use of small sample volumes and easy-to-use procedures, which also diminish the analysis time. In addition, the properties of nanomaterials are usually size dependent and, often, they exhibit unique physical and chemical properties when compared to the bulk counterparts [302]. Herein, the integration of magnetic nano-sized structures into the assembly of biosensor devices, specifically electrochemical-based sensors, can be used as a way to amplify the signal. So, under this scope, the development of core-shell nanoparticles enables the combination of the magnetic properties of the core combined with the functionalized properties of the shell's material.

In parallel, silica coated core–shell structured particles constitute a popular choice, mostly because silica is nontoxic, biocompatible and can be easily functionalized with different functional groups [303]. Among the wide range of applications of silica-based nanoparticles, the most common are construction materials, drug delivery systems, preparation of polymer composites and also treatment of diseases [304][305][306]. For instance, fluorescent iron oxide-silica nanoparticles have been synthesized by introducing organic fluorescent dyes into the silica shell, resulting in a unique combination of magnetic and optical characteristics [224]. In addition to biocompatibility and hydrophilicity, the formation of a silica shell can also prevents

the oxidation of magnetic particles and, simultaneously, enables different approaches for surface modification through the covalent attachment of specific ligands on the surface of these nanostructured materials. Another approach that can be employed to preserve the integrity of the magnetic core, is the layer-by-layer growth of noble metals such as Ag, Au and Cu [307]. The reason why such metals were used is the fact that they are biocompatible, resistant to physiological conditions and their shells do not allow agglomeration of the cores. Nevertheless, the incorporation of noble metals into nano-sized structures is typically limited to expensive and more complex fabrication technologies. Thus, herein, the silica shell not only prevents the magnetic cores from oxidation, but also provides a surface with the ability to incorporate additional materials holding other functionalities, such as, optical or electrochemical behaviour.

There are two different routes that have been commonly explored in order to generate silica coatings on the surfaces of iron oxide particles. The first method relies on a sol-gel process, also called the coprecipitation method or the well-known "Stöber process", in which silica is formed in-situ through the hydrolysis and condensation of a sol-gel precursor [302]. Generally, the Stöber method was employed to cover nanoparticles that hold the ability to become disperse in polar solvents, like water or ethanol. In the late 1960s, Stöber *et al.* developed a process capable of forming controlled silica particles (500 nm - 2 μm) using tetraethoxysilane (TEOS) as silica precursor, water, ethanol and ammonia [308]. Briefly, silica particles had a narrow size distribution and could be adjusted by controlling the pH of solution, composition of reactants and temperature. One of the main advantages of the sol-gel technique is that it offers a low temperature method for synthesizing and mixing inorganic with organic materials. The other method is based on microemulsion synthesis, in which micelles or inverse micelles, stabilized by surfactant film, are used as nano-reactors to confine and control the formation of nanomaterials [216].

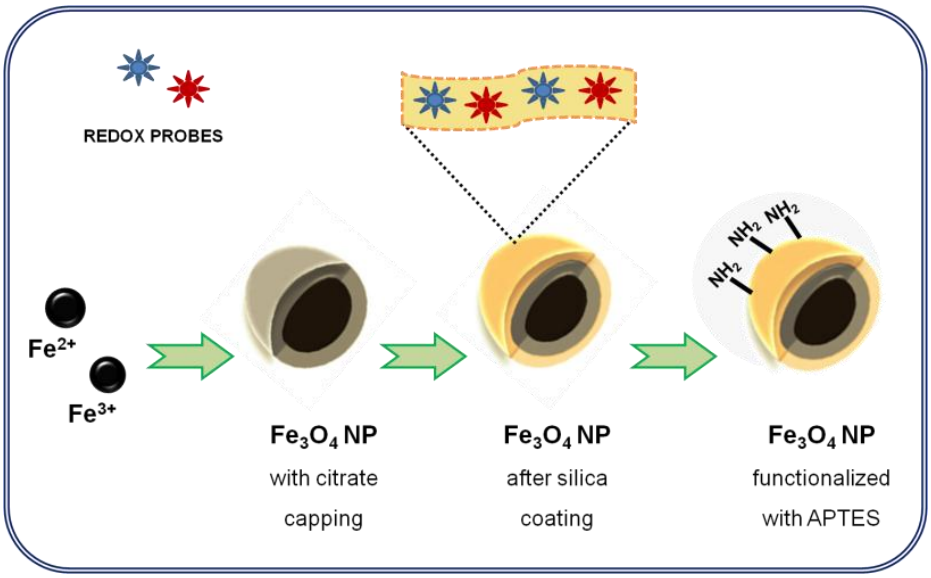

Figure 7.1: Schematic representation of the different steps related to the synthesis of the core-shell magnetic nanoparticles.

In this work, silica (SiO_2) was chosen as the surface coating of magnetic nanoparticles because probe molecules can be easily encapsulated into the silica shell, allowing in parallel the functionalization of the surface for bioconjugation and targeting for biological applications. Various labelling agents can be incorporated into nanoparticle structures yielding materials with a broad spectrum of applications, such as, fluorescent beads, redox probes, dye-labeled nanoparticles or semiconductor quantum dots. For instance, a study have performed the synthesis of bifunctional nanoparticles, SPIO@SiO_2(FITC) with both fluorescent and magnetic properties, in order to develop contrast agent-loaded nanoparticles with which stem cells could be efficiently and harmlessly labeled and then imaged with a clinical MRI analyzer at low cell number [309]. Thus, herein, we describe a sol-gel method based on the hydrolysis of TEOS for coating iron oxide nanoparticles with an uniform silica shell, enabling the encapsulation of redox probe species (see Figure 7.1).

Novel strategies for signal amplification have been extensively investigated, specifically, for the development of ultrasensitive immunoassay. Thus, combining Fe_3O_4 magnetic nanoparticles with silicon dioxide shell and gold nanoparticles (Fe_3O_4@SiO_2@Au) enabled the fabrication of an electrochemical immunoassay for the detection of C-reactive protein in serum samples [310]. Due to their large surface area, the functionalization of magnetic nanoparticles holds a great potential application in the biotechnology field, allowing the pre-concentration of analyte molecules. In a similar way, electrochemical redox-active species, such as, methylene blue (MB) have been incorporated with gold-modified magnetic nanoparticles for signal generation and amplification [311]. Interestingly, functionalized nano Fe_3O_4 particles (magnetic cores) have also been combined with molecularly imprinted polymer to accomplish adsorbent materials for imidacloprid target with amplified signal [312]. In sum, herein we present the fabrication and characterization of Fe_3O_4@SiO_2 nanoparticles modified with an redox-active probe with potential to be used as labels in an amplified multiplexed array.

7.2 EXPERIMENTAL SECTION

7.2.1 Reagents and Materials

All chemicals were of analytical grade and used as supplied without further purification. PBS (0.01 M, pH 7.4) solutions were prepared with ultrapure water Milli-Q laboratory grade. NADH (grade II, disodium salt 98%), tetraethyl orthosilicate (TEOS), 3-triethoxysilylpropylamine (98% purity, APTES), citric acid and ethanol absolute (≥99.9% p.a.) were obtained from Sigma-Aldrich; hexaammineruthenium (III) chloride ($Ru(NH_3)_6Cl_3$) was from Acros Organic; iron (II) sulfate 7-hydrate ($FeSO_4 \cdot 7H_2O$) was from Panreac; iron (III) chloride hexahydrate ($FeCl_3 \cdot 6H_2O$) was from Scharlau; PBS tablets from Amresco; sodium hydroxide (NaOH) from EKA; ammonium hydroxide (25% p.a.) from Fluka and sodium docedyl sulfate (SDS) from TCI.

The exact pH values were measured with a pH meter (Crison Instruments, GLP 21 model). All experiments were carried out at ambient temperature.

7.2.2 Apparatus

The electrochemical measurements were conducted with a potentiostat/galvanostat from Metrohm Autolab and a PGSTAT302N with a FRA module, through an interface switch box from BioTid Eletrónica and controlled by ANOVA software. Commercial carbon-screen printed electrodes (SPEs-DRP-C110) were purchased from DROPSENS. All the presented potential values are related to the silver pseudo-reference of the SPEs.

In order to follow the introduction of functional groups during each step of modification of the nanoparticles, FTIR measurements were performed in the ATR mode, using a Thermo Scientific Smart iTR Nicolet iS10, coupled with sampling accessory of diamond contact crystal, also from Nicolet.

To assess the morphology of the surface as well as the distribution of sizes of the nanoparticles, both SEM and TEM techniques were employed. For TEM analysis, visualization was carried out on a JEOL JEM 1400 TEM at 120kV (Tokyo, Japan). Images were digitally recorded using a CCD digital camera Orious 1100W Tokyo, Japan at the HEMS / i3S of the University of Porto. SEM studies were performed on a FE-CryoSEM/EDS, from JEOL JSM 6301F, Oxford INCA Energy 350, Gatan Alto 2500 microscope, operating at 15 and 25 kV.

The thermal behaviour of the magnetic nanoparticles was assessed by performing thermogravimetric (TG) experiments with an Hitachi TG/DTA/7200 analyzer.

7.2.3 Synthesis of core-shell nanoparticles

7.2.3.1 Fabrication of iron oxide nanoparticles

The preparation of MNPs was performed by a chemical co-precipitation process involving Fe^{2+} and Fe^{3+} ions (1:2 molar ratio) in an alkali medium (see Figure 7.2). Briefly, 20 ml of 0.55 M Fe^{3+} and 0.275 M Fe^{2+} solution was prepared with ultrapure water in an Erlenmeyer flask. Afterwards, this mixture was kept with magnetic stirring at 40ºC under nitrogen atmosphere until complete dissolution of the reagents. An inert atmosphere (without oxygen) is essential to obtain pure magnetite particles. Then, sodium hydroxide (25 wt%) was added to the reaction mixture, leading to the formation of a green rust at the early stage of precipitation, followed by a black colour after precipitation process was completed (~30 min). The surface of the MNP was stabilized with citric acid (2 M) and the reaction was maintained at 40 ºC for 90 min with continuous stirring. Finally, the reaction mixture was left cooling and afterwards, the nanoparticles were washed several times with ultrapure water until a pH of 7 was obtained. The wet suspension was stored in the fridge.

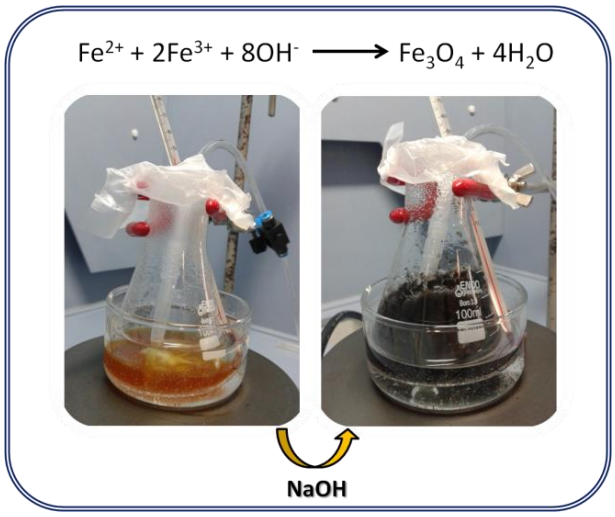

Figure 7.2: Synthesis reaction of the iron-oxide nanoparticles via co-precipitation method.

7.2.3.2 Preparation of iron oxide-silica core-shell

SiO_2-MNPs were prepared following the conventional Stöber method, as described in the literature with some modifications. Firstly, 125 mg of the as-prepared iron oxide solution was re-suspended in 20 mL of water with continuous magnetic stirring and then, 0.1 % (wt) solution of SDS was added. Afterwards, the stirring process was continued followed by the addition of 10 mL of ammonia solution. In parallel, the redox probe (NADH or $Ru(NH_3)_6Cl_3$) was dispersed in a mixture water:ethanol and then, a small volume of TEOS was added. Finally, the previous mixture was added to the previous nanoparticles solution and magnetic stirring was continued for more 3 hours, at room temperature. Different concentrations of TEOS precursor were investigated. The modified nanoparticles were re-suspended and washed several times with ultrapure water and ethanol.

In order to prepare amino-functionalized MNPs, 100 mg of SiO_2-MNPs were firstly dispersed in a mixture 1:1 (*v/v*) ethanol: water with continuous magnetic stirring at room temperature. Afterwards, APTES (2 %, *v/v* in ethanol) was introduced into the solution and left stirring for 5 h at room temperature. In the end, the modified nanoparticles were removed from the mixture and thoroughly washed with ultrapure water and ethanol.

7.2.4 Characterization of the modified nanoparticles

Each step along the synthesis and modification of nanoparticles was followed by FTIR, TEM, SEM and TG analysis. Regarding FTIR experiments, spectra were collected under room temperature, after background correction. The number of scans for sample was set to 32 and the resolution was fixed at 8. FTIR data analysis was performed with OMNIC software. For TEM analysis, the nanoparticles were dispersed in ultrapure water, sonicated for 10 min and

afterwards, 10 μL of samples were mounted on Formvar/carbon film-coated mesh nickel grids (Electron Microscopy Sciences, Hatfield, PA, USA) and left standing for 2 min. The liquid in excess was removed with filter paper. Before SEM analysis, nanoparticle samples were dried at 80 ºC, for 24 hours. Finally, TG experiments were performed in aluminium crucibles with a heating rate of 5ºC/min, from +30 ºC until 550 ºC, under a nitrogen atmosphere of 200 mL/min.

7.2.5 Electrochemical assays

Electrochemical measurements for characterization of the modified magnetic nanoparticles were performed by using different electrochemical techniques, such as, CV and SWV. For CV assays, the potential was scanned from –0.7 to +0.7 V, at 50 mVs^{-1}, in a magnetic nanoparticle solution prepared in 0.01 M PBS solution, pH 7.4. The measurements were performed by covering the three electrodes with 80 μl of the appropriate solution.
Initially, NADH and $Ru(NH_3)_6Cl_3$ were selected as electrochemical probes and their redox behaviour was investigated by SWV, over a wide potential range. Afterwards, for the modified M-NP containing labeled $Ru(NH_3)_6Cl_3$, SWV was performed from -0.40 V to +0.20 V, at a very low scan-rate. For this procedure, the nanoparticles were prepared in PBS solution, transferred to the SPEs and then concentrated, with the aid of a magnet under the sensing platform. The magnet is maintained during the entire electrochemical reading.

7.3 DISCUSSION AND RESULTS

7.3.1 Synthesis of iron oxide nanoparticles

Herein, we have performed a chemical co-precipitation of Fe^{2+} and Fe^{3+} under alkaline media for the preparation of nanosized Fe_3O_4 particles. In order to assess the size distribution and the morphology of the nanoparticle, TEM analysis was performed. As shown in Figures 7.3A and 7.3B, MNPs were about 20 nm in average size presenting a nearly-spherical morphology with a quite narrow size distribution. Although not presented here, the incorporation of citric acid during the synthesis of the magnetic particles was crucial to stabilize the surface of MNPs in an aqueous dispersion, hindering the formation of agglomerates. This outcome is in accordance with literature whereas agglomeration is a common result of the synthesis by the co-precipitation technique if a capping agent, like citric acid, is not used [313][314]. Furthermore, the resulting black precipitate (Fe_3O_4) obtained presented good magnetic properties in the presence of a magneto, as displayed in Figure 7.3C.

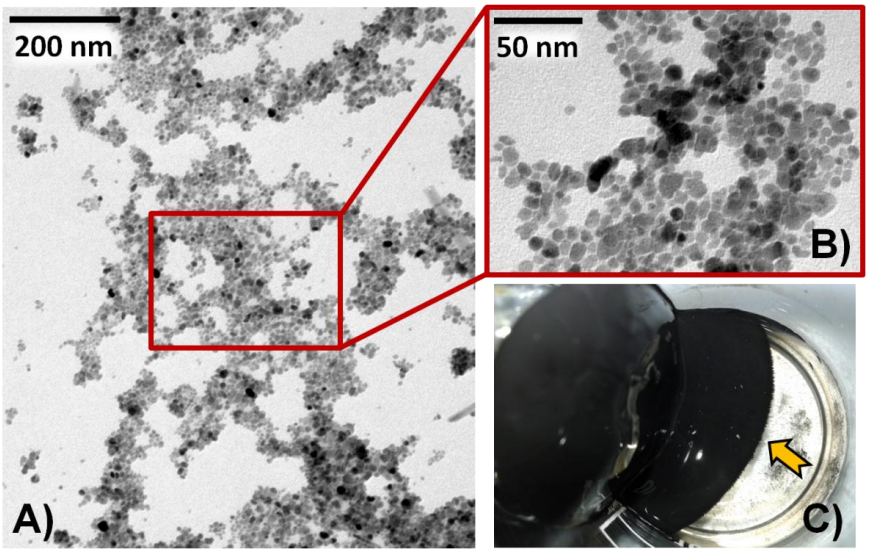

Figure 7.3: (A-B) TEM images of iron-oxide nanoparticles at different magnifications and C) image of the MNPs under the application of a magnetic field.

7.3.2 Fabrication of iron oxide-silica core-shell

Along this study, two different redox-active species were tested that includes, ruthenium (Ru^{3+}/Ru^{2+}) and NADH (NAD^{+}/NADH). In order to assess the electrochemical behaviour of these two probes, SWV was the chosen technique mostly due to their high sensitivity and quick analysis time. Figure 7.4 shows the voltammograms for both individual solutions prepared in PBS at a pH of 7.4. The oxidation peak of ruthenium was around -0.25 V while NADH oxidation occurred at +0.50 V. These two probes were selected because their oxidation peaks were well separated and thus, no overlapping would take place.

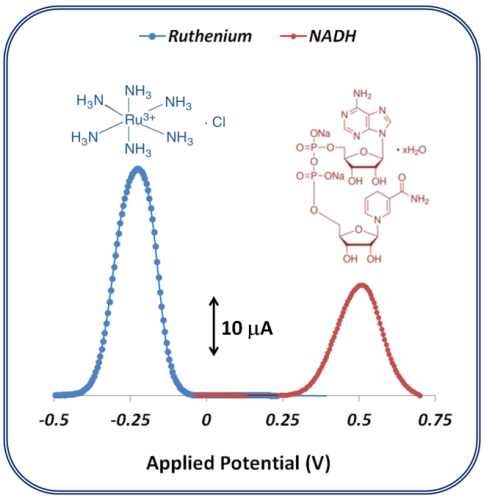

Figure 7.4: Square-wave voltammograms concerning the two (individual) redox probes ruthenium and NADH, in PBS at a pH 7.4, applied in a clean, bare carbon-SPE.

Among others, magnetic Fe_3O_4 nanoparticles hold important characteristics, such as, superparamagnetic property, good biocompatibility, low toxicity and facile preparation, making it a popular choice as anchoring platforms. Under this scope, coating this nanostructured materials with redox-active species encapsulated in inert shells is an interesting approach to preserve the functional characteristics of the species. Moreover, coating can also prevent nanoparticles from contacting other nanoparticles, so that aggregation of nanoparticles, which spoils blood flow, can be hindered [315]. Herein, SiO_2-MNP were synthesized based on a sol-gel chemistry in order to incorporate ruthenium or NADH probe in the silica shell. Similarly, a variety of fluorophore compounds can be encapsulated within the silica coating, resulting in a fluorescence emission in the near-infrared region that is beneficial for the analysis of biological tissues [316]. Another strategy used to synthesize labeled-nanoparticles for biosensing purposes is the incorporation of electroactive metals into phosphate-based nanoparticles to be used in an electrochemical multiplex biosensor [317]. Moreover, the fabrication of different electrochemical redox-active species based on $HAuCl_4$ and Na_2PdCl_4 as co-oxidating agents and aniline derivatives as monomers have also been reported [318].

The sol-gel-based Stöber synthesis is usually described with three reaction as shown below for silicon: hydrolysis, alcohol condensation and water condensation. The reaction mechanism is well described in the literature [308]:

1. Hydrolysis

$$Si(OCH_2CH_3)_4 + H_2O \longrightarrow (CH_3CH_2O)_3Si\text{-}OH + CH_3CH_2OH$$

2. Alcohol condensation

$$Si(OCH_2CH_3)_4 + (CH_3CH_2O)_3Si\text{-}OH \longrightarrow (CH_3CH_2O)_3Si\text{-}O\text{-}Si(OCH_2CH_3)_3 + CH_3CH_2OH$$

3. Water condensation

$$(CH_3CH_2O)_3Si\text{-}OH + (CH_3CH_2O)_3Si\text{-}OH \longrightarrow H_2O + (CH_3CH_2O)Si\text{-}O\text{-}Si(OCH_2CH_3)_3$$

Finally, a SiO_2 network is produced:

$$Si(OCH_2CH_3)_4 + H_2O \longrightarrow SiO_2 + 4CH_3CH_2OH$$

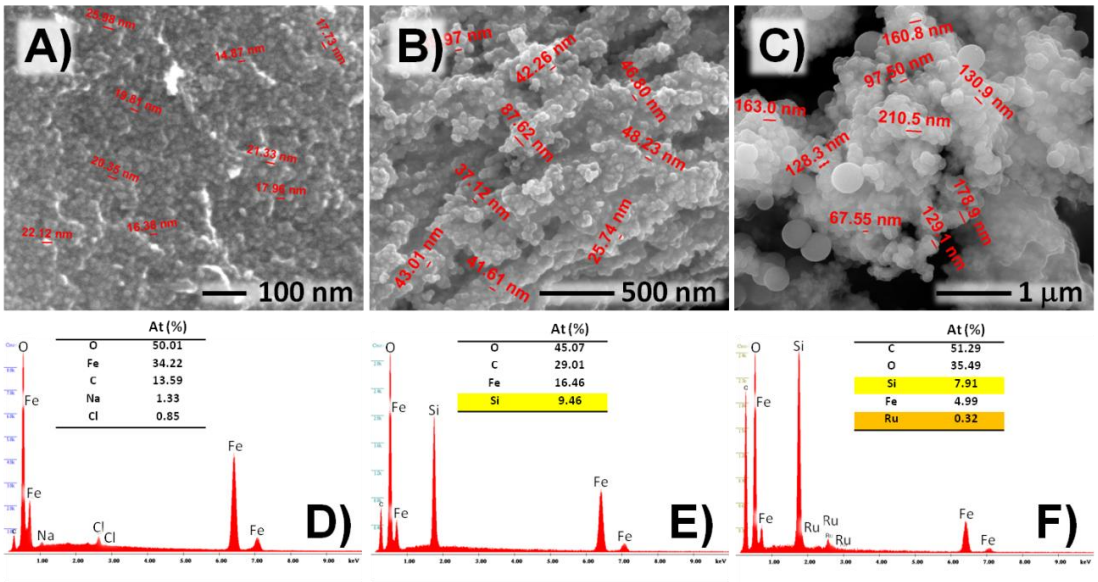

Figure 7.5: SEM images of the MNPs A) non-modified, modified with B) SiO_2 with NADH and C) SiO_2 with ruthenium; EDS spectra of the MNPs D) non-modified, modified with E) SiO_2 with NADH and F) SiO_2 with ruthenium.

To evaluate the morphology and the size distribution of the as-prepared nanoparticles, SEM was performed. Figure 7.5A, 7.5B and 7.5C displayed the surface of the nanoparticles and the size measurements concerning magnetic nanoparticles non-modified, SiO_2-M-NP with NADH and SiO_2-M-NP with ruthenium, respectively. As expected, a substantial increase of the diameter was observed which constitutes a good indication that the silica coating was successfully incorporated into the particle. Moreover, it seems that the spherical shape of the modified particles was also maintained. Although the size distribution in the modified magnetic nanoparticles was not very narrow, it was interesting to observe that the type of redox probe used during the formation of the silica shell had a great impact on the size of the obtained nanoparticle. In addition, the presence of silicon element in the silica-modified magnetic nanoparticles was also confirmed by Energy Dispersive X-Ray Spectroscopy (EDS) analysis, as can be seen in Figures 7.5E and 7.5F, in contrast with the absence of this element in Figure 7.5D (non modified MNPs). Moreover, EDS results also indicated a decreasing in the silicon content when the ruthenium probe was incorporated, thereby confirming the presence of the ruthenium element.

Covalent immobilization of simultaneous electroactive molecules into modified Stöber silica nanoparticles have been combined in a unique environment for biotechnology purposes. Concerning their catalytic properties, previous electrochemical studies have reported that the redox potentials of the ferrocene and ruthenium(II) complex species immobilized on the silica particles are not very different from those of the corresponding solution species [319]. Figure 7.6A shows the application of CV to study the electrochemical behaviour of the magnetic nanoparticles. For this study, each type of nanoparticles was dispersed in PBS pH 7.4 and a drop of this solution was used to cover the 3-electrodes of carbon-SPEs. By looking to the

voltammograms, we can verified that non-modified magnetic particles do not display any electrochemical behaviour, while the nanoparticles modified with the redox ruthenium showed several oxidation and reduction peaks. Specifically, comparing this data with the solution specie presented previously, the characteristic oxidation peak around -0.25 V was maintained. Moreover, these results also showed that the silica-modified nanoparticles prepared in the presence of NADH did not exhibit any redox peak.

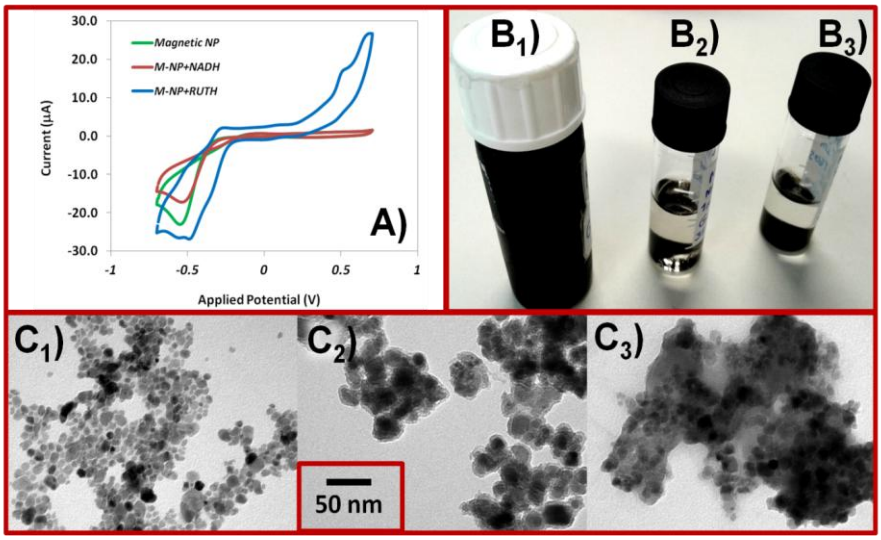

Figure 7.6: A) Cyclic voltammogram applied in PBS at pH 7.4 of the different types of MNPs; B) images of the wet suspension of the MNPs B_1) non-modified, modified with B_2) SiO_2 with NADH and B_3) SiO_2 with ruthenium and TEM images of the MNPs C_1) non-modified, modified with C_2) SiO_2 with NADH and C_3) SiO_2 with ruthenium.

Figure 7.6B displays the magnetic nanoparticles in aqueous solution and we observed that, in contrast with the bare magnetic particles, the modified nanoparticles had the tendency to deposit in the bottom of the flask, which can be the result of more heavy particles. Although there are some evidences that magnetic properties of coated materials can decrease substantially upon the increase of outer shell thickness [224], herein, the magnetic properties of the obtained nanoparticles were preserved.

TEM analysis (see Figure 7.6C) pointed out a great level of agglomeration of the magnetic nanoparticles after the silica sol-gel step, which constitutes a common issue during this type of synthesis [302]. Despite the aggregation, Figures $7.6C_2$ and $7.6C_3$ clearly showed a darker core correspondent to magnetic nanoparticles surrounded by a large silica shell. So, although the silica modification was successfully achieve, more optimization studies are needed in order to tune the coating growth, in order to prevent agglomeration problems. Moreover, among other factors, the thickness of silica coating can be easily controlled in the range of 2-100 nm by changing the concentration of the TEOS precursor [224]. In sum, for the following optimization studies, silica-modified magnetic nanoparticles with ruthenium probe was the chosen system due to the fact that enabled an electrochemical signal.

7.3.2.1 Optimization of the sol-gel process

Solvent and surfactant effect:

More systematic studies have been performed in order to understand how polydispersity of nanoparticles in a synthesis process can be highly influenced by the synthesis kinetics [320]. So, they have concluded that a faster reaction will result in a higher polydispersity if allowed to react for longer periods. An overview of the literature have showed that the key factors responsible for controlling the particle size and distribution during silica sol-gel synthesis include ammonia, solvent (water versus alcohol), concentration of TEOS and temperature. Herein, ammonia was used as the catalyst of the hydrolysis and condensation of the silicate species and apparently, has great influence in the morphology of the particles [224][321].

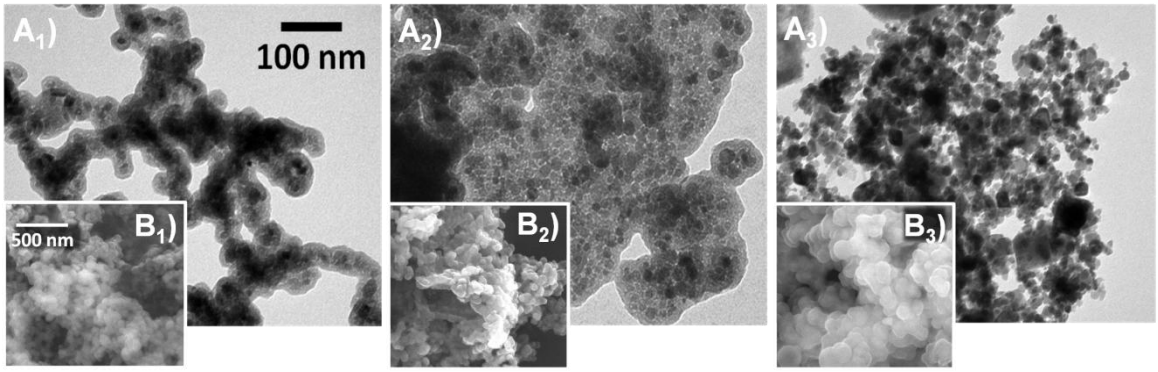

Figure 7.7: TEM (A) and SEM (B) imaging of the silica-based nanoparticles prepared (1) without ethanol and SDS, (2) without ethanol and with SDS and (3) with ethanol and SDS.

In this work, the effect of using a surfactant (SDS) and also the influence of water and/ or ethanol presence was investigated through the analysis of TEM (see Figure 7.7A) and SEM (see Figure 7.7B). It is well known that the use of surfactants with relatively high concentrations is usually necessary to prevent aggregation of nanoparticles. So, it was observed that the use of a small concentration of SDS during the sol-gel synthesis (see Figure 7.7A_2) resulted in less particle aggregation with a more homogenous distribution of the magnetic cores in comparison with the non-surfactant system (see Figure 7.7A_1). Moreover, another important parameter with great impact in the size distribution of silica-based nanoparticles that was also investigated along this study is the effect of ethanol. An important role of ethanol presence in the medium is the enhancement of TEOS solubility during the polymerization reaction. Thus, both Figures 7.7A3 and 7.7B3 displayed nanoparticles dispersions with less agglomeration phenomenon and enabling well-defined particles. In sum, the optimal nanoparticle system was obtained when using ethanol as solvent and small amounts of SDS surfactant.

TEOS concentration:

In this work, we investigated the effect of the concentration of TEOS precursor not only on the size distribution of the nanoparticles but only on their electrochemical performance. The TEM analysis presented in Figures 7.8D, 7.8E and 7.8F showed that the particle size increased with increasing concentration of TEOS, which is in agreement with similar works [322]. Moreover, in our case, more important than the size of the nanoparticle is the growth of the silica-based coating and, consequently, the level of aggregation between those particles. So, the analysis of SEM data indicated that a better dispersion was obtained for the sol-gel synthesis conducted at lower TEOS concentration, enabling the formation SiO2-MNP with a regular spherical shape and diameters around 20 nm. Nanoparticle solutions prepared with the same concentration were prepared in PBS and analysed by SWV. As can be seen in Figures 7.8A-C, the higher amplitude of the oxidation peak was accomplished for the lower concentration of TEOS, which can be a strong indication that the use of more TEOS resulted in a thicker silica coating and thus, hindering the electrochemical signalling.

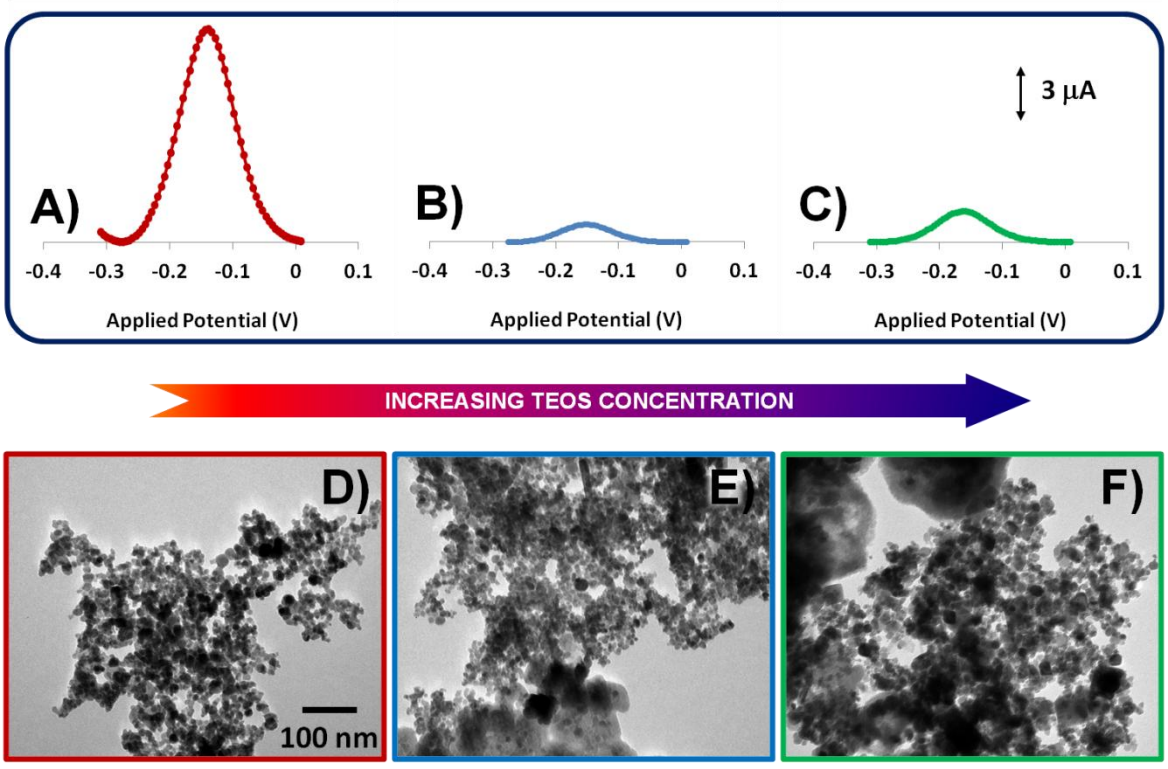

Figure 7.8: Square wave voltammograms of the silica-based MNPs synthesized with increasing concentration of TEOS A) 0.1 mL, B) 0.5 mL and C) 1.0 mL; TEM images of the silica-based MNPs obtained with different TEOS concentration D) 0.1 mL, E) 0.5 mL and F) 1.0 mL.

7.3.2.2 Functionalization with APTES

As mentioned before, besides behaving as a biocompatible and protective shell, the formation of SiO_2 coatings offers many possibilities for surface modification through the covalent attachment of specific functional groups. Moreover, the application of magnetic nanoparticles has shown to be an effective approach for immobilization of different redox probes on the nanoparticle surface in order to generate an electrochemical signal. Along this study, optimization of the experimental conditions during the nanoparticles synthesis and the choice of solvent were crucial to achieve modified nanostructured that were chemically stable, well-disperse in liquid media and uniform in both size and shape. Figure 7.9 shows the multi-step procedure for the fabrication of magnetic nanoparticles and their application as label-less nanoprobes in electrochemical platforms for biosensing purposes. For instance, a sandwich-type electrochemical immunosensor combined with gold magnetic nanoparticles have been designed for simultaneous detection of four different antigen species [323].

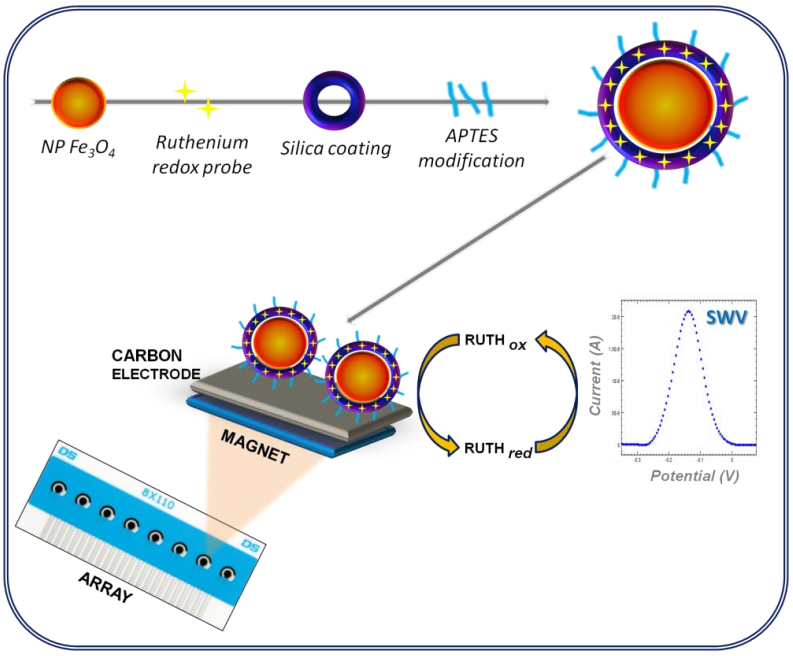

Figure 7.9: Schematic illustration of the fabrication procedure of the core-shell magnetic nanoparticles and their application as electrochemical probes.

After selecting the optimum condition of the precursor composition, and its effect on the SiO_2NP size distribution, APTES was used as a chemical modifier to form amino-end groups onto the surfaces of the silica coated nanoparticles. This approach is commonly used to facilitate the combination of these nanostructured materials with biomolecules, such as, drugs, proteins or antibodies [324]. Specifically, IgG antigens can be covalently attached via their carboxyl group activated by EDAC/NHS chemistry to the amino groups of silica coated MNPs. Figures 7.10A

and 7.10B shows the SWV measurements related to the silica coated magnetic nanoparticles, in order to evaluated their electrochemical stability. Firstly, it can be seen that the three consecutive measurements for each step displayed a quite reproducible behaviour. In addition, the application of a magnetic field enabled an enhancement of the electrochemical signal as a result of the attraction an concentration of the nanoparticles in the transducer surface. As can be seen in Figure 7.10C, after the chemical modification of silica surface with APTES, the peak amplitude obtained during the SWV measurement decreased substantially which constitutes a strong indication that the amino groups were successfully introduced in the nanoparticles surface.

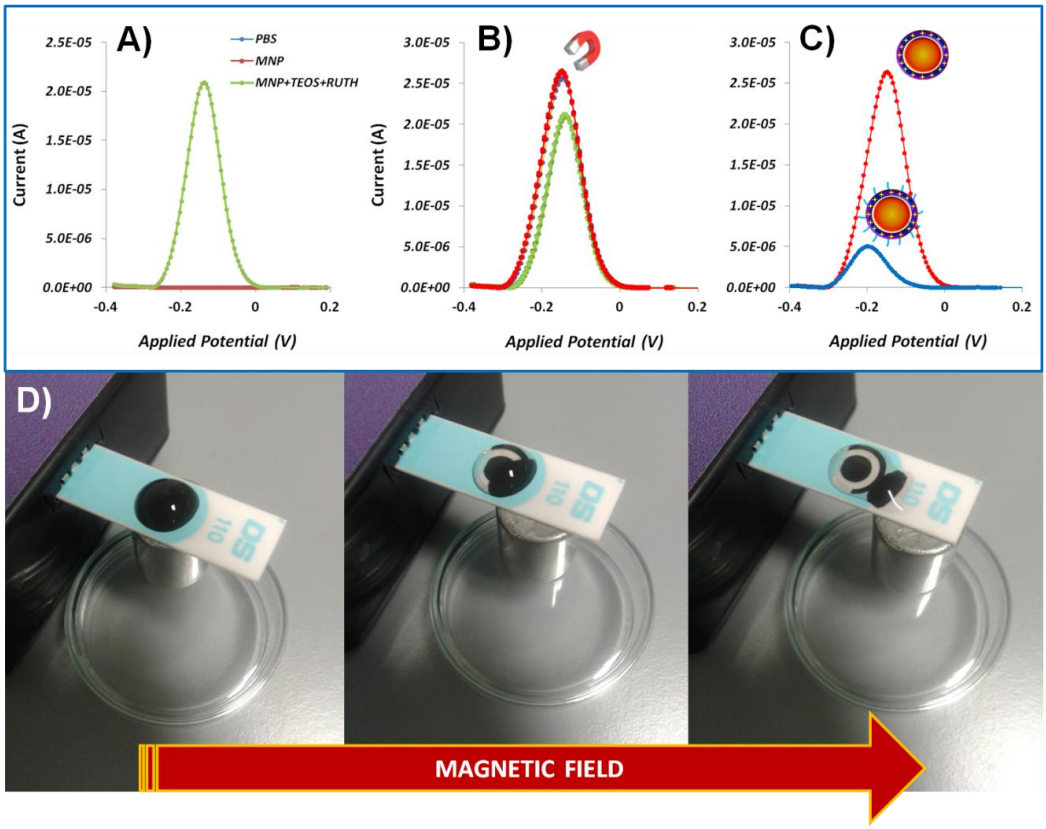

Figure 7.10: Square wave voltammograms of the developed silica-based MNPs at different stages of fabrication: A) TEOS with ruthenium, B) effect of a magnetic field on the previous MNPs and C) the effect of functionalization with APTES; D) Image of the electrochemical measurement of MNPs using a magneto.

Generally, the chemical modification of silica surface using APTES agents can be performed via aqueous or non-aqueous system. The non-aqueous system is the most common used because silanes, like APTES, carries amine groups that can undergo uncontrollable hydrolysis and polycondensation reactions in the aqueous conditions [302]. Herein, the use of ethanol solvent during the coupling reaction with APTES was meant to achieve a better control of the reaction conditions. Although there are some studies where the formation of the APTES coating could hindered the magnetic properties of the nanoparticles [325], in our work the APTES-modified nanoparticles exhibited a strong magnetization in the presence of a magnetic field. As shown in Figure 7.10D, they displayed a good magnetic response being easily attracted by a magnet.

7.3.3 Characterization of the modified-nanoparticles

During each step of the synthesis and modification of the iron oxide core-shell nanoparticles, FTIR and TG analysis were performed in order to confirm each modification. The FTIR spectra of bare MNPs, Fe_3O_4@SiO_2 MNPs and Fe_3O_4@SiO_2@APTES MNPs are presented in Figure 7.11. The characteristic band attributed to the Fe-O stretching vibration mode of the magnetic nanoparticles appeared around 550 cm^{-1}, which is in agreement with previous works [224]. An intense band was also observed at 3300 cm^{-1} that may be assigned to the existence of non-dissociated OH groups from citric acid capping. In addition, the peak at 1650 cm^{-1} may be assigned to the symmetric stretching of OH from COOH group, as a result of the binding of citric acid radical to the iron-oxide nanoparticles. Afterwards, the silica network was adsorbed on the magnetite surface through the formation of Fe–O–Si bonds. Thus, the adsorption of silane polymer onto the surface of the magnetic nanoparticles was confirmed by the strong peaks near 1100 and 900 cm^{-1} assigned to Si–O–Si and Si–O stretching vibrations, respectively. This outcome is in accordance with other studies that confirms the condensation reaction between hydroxyl groups on the magnetite nanoparticle surface and the alkoxysilane molecule [326]. The introduction of APTES can be confirmed by the broad FTIR absorption band around 3300 cm^{-1} from N–H stretching vibration and also a sharp peak was observed at 1600 cm^{-1} assigned to the NH_2 bending mode of free NH_2 group [325][327].

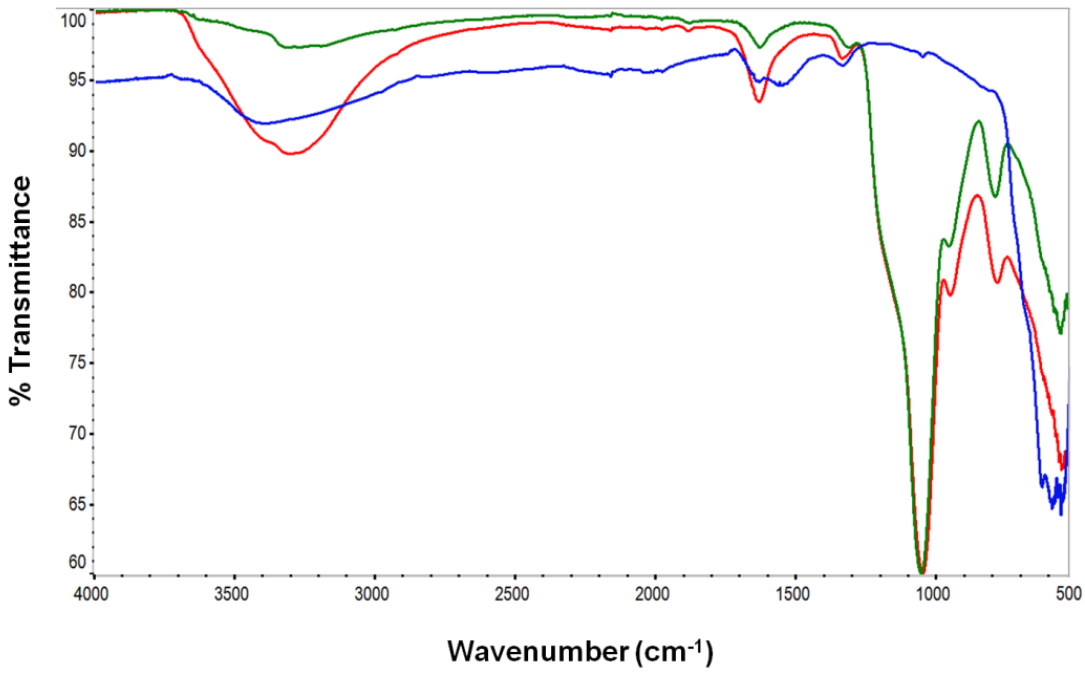

Figure 7.11: FTIR spectra of the magnetic nanoparticles at each step of the fabrication and modification reaction: blue line (MNPs); green line (Fe_3O_4@SiO_2 MNPs) and red line (Fe_3O_4@SiO_2@APTES MNPs).

Figure 7.12 shows the TG analysis weight loss curves correspondent to the iron oxide magnetic nanoparticles during each modification step. Firstly, as can be seen, Fe_3O_4@SiO_2 and APTES-coated Fe_3O_4@SiO_2 MNPs presented a distinct mass-loss profile compared to that obtained in the naked Fe_3O_4 core. The initial weight loss from 80-180 ºC is generally caused by the removal of the adsorbed (free) water and ethanol molecules, which is in agreement with similar works [230]. Afterwards, an accentuated decrease of mass was observed for the bare magnetic nanoparticles in the range 180-300 ºC that can be attributed to the decomposition of the citric acid capping [328]. In addition, the sharp increase in weight loss that occurred in the region 180-400 ºC is the result of the thermal decomposition of organic materials that composed the shell of the magnetic nanoparticles. It was observed that no significant differences were detected for both Fe_3O_4@SiO_2 and APTES-coated Fe_3O_4@SiO_2 MNPs, being the total weight loss amounted to 11.7% and 11.2%, respectively. This outcome can be explained due to the very small amount of APTES on the surface of the nanoparticles, as observed in other similar studies [326]. After the organic shell had been completely decomposed, the residual mass was mainly Fe_3O_4.

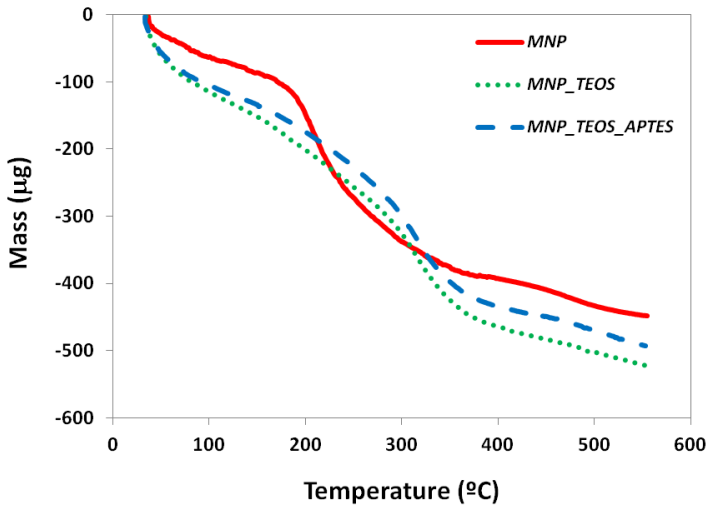

Figure 7.12: TG analysis of the different stages of the magnetic nanoparticles.

7.4 CONCLUSIONS

Firstly, this work have presented a promising approach to synthesize and modify magnetic nanoparticles to be incorporated in multiplexed arrays as electrochemical nanoprobes. The effect of the redox-active specie, the concentration of the organosilane precursor and the use of a surfactant were important parameters that affected the size and electrochemical performance of the nanosized particles. Moreover, the growth of an inorganic structure, such

as, silica, was successfully accomplished enabling the encapsulation of ruthenium in the shell, while preserving its electroactive behaviour. Preliminary results have also showed that the use of magnetic nanoparticles as a sensing platform allowed the amplification of signal. In the future, this dual-stimulus nanoparticles are proposed to be included in the design of a novel multiplexed array sensor towards various OS biomarkers. To accomplish this goal, another redox probe, different from ruthenium, will be encapsulated into the SiO_2-MNP core-shell structures in order to get two different electrochemical nano-labels for the simultaneous detection of MDA and 4-HNE biomarkers.

CHAPTER 8

8 Conclusions and future perspectives

Overall, the design of the electrochemical sensors developed along this thesis have showed to accomplish the same requirements of the current methodologies used, mainly, sensitivity, reproducibility and selectivity, combined with the advantages of using environmental friendly materials, with a cost-effective analysis suitable for *POC* screening. Although some limitations were found during the work associated to the function of some devices, the introduction of nanomaterials and also the incorporation of biomimetic films enabled obtaining the needed standards of performance required for these novel electrode systems.

In the future, it is important to keep in mind that sensitivity is also controlled by the type and nature of the transducer. Thus, herein the electrocatalytic behaviour of the selected material can also influence the LOD of the sensor. Specifically, the comparison of all sensing devices developed along this thesis showed that, as expected, the lowest LOD value was accomplished by the gold electrode (*chapter 3*) against the other carbon materials (*chapters 4-6*). Despite this great advantage, the use of this kind of gold electrodes imposes multi-step and time-consuming cleaning protocols that are essential to assure the reproducibility of the experiments. Therefore, from the point-of-view of biosensor application in routinely conditions, rapid and practical devices are highly preferred. Moreover, it is important to understand that this response is not directly transposed into commercial screen-printed electrodes of gold, as these are made by an composite of gold and not the pure metal.

One of the most important issues that influenced the electrochemical performance of the MIP-based sensing materials was the assembly of very thin films due to the need that ideally the recognition event should take place as closer as possible to the electronic transduction surface. So, regarding the synthesis strategy of the biomimetic polymer, electropolymerization was acknowledged as the most suitable technique since it enabled a high adherence to the transducer substrate, an easy control of the film thickness and growth, with the possibility to work at mild conditions, such as, aqueous solutions and ambient temperature. In addition, phenol was identified as a suitable material to produce the polymeric matrix that creates the recognition sites, due to its high stability and specific affinity to the target molecules.

Along the construction, characterization and application of each of the electrochemical sensors developed herein for the detection of different OS biomarkers, important complementary

techniques, such as, Raman spectroscopy, SEM and FTIR were employed in order to confirm the formation and growth of the different materials. In addition, an innovative strategy based on FITC-labelled 8-OHdG antibodies was used to verify the existence and distribution of the MIP cavities along the surface by specific electron microscopy technique.

In parallel, an intensive voltammetric investigation of the paper-based printed-electrodes has confirmed their suitable and reliable electrochemical performance. The simple procedure of microfabrication of this transducer platform started with the hydrophobization of paper, followed by the application of a suitable conductive ink into the planar substrate materials and then, a proper thermal cure. Once again, this quick and facile procedure opens new opportunities to create and implement routine and low-cost assays that can be used in detection, monitoring and prevention context. Herein, the first attempt of homemade carbon-based electrodes constructed onto paper substrates (*chapter 4*) was accomplished with a system of three electrodes, separately. Although the developed sensor hold important features, such as, good stability and reproducibility, the capability of regeneration and quick analysis time, the evolution for an integrated 3-electrode system applied in the same platform was necessary (*chapter 5 and 6*).

Overall, the combination of a molecular imprinting strategy responsible for tuning the specific binding of the target molecule with the fabrication of a flexible paper-based sensor seems to be the best outcome of this work. Thus, the biosensor described in *chapter 6* enabled the required selectivity and sensitivity and, at the same time, the reproducibility issues of the commercially available SPEs was overcome, with the introduction of a substrate that was environmental-friendly. Furthermore, another great advantage of these electrodes is also their ability to be drawn in different shapes and sizes, using different kinds of materials. In this way, for enhanced results, the optimization of the dimensions used along this work for the paper integrated with 3-electrode system could be tried out in order to obtain a better analytical response.

The fabrication and functionalization of iron-oxide core-shell nanoparticles has proven to be a potential approach to be incorporated in novel signal amplified multiplexed array. Ideally, two magnetic nanoparticles may be functionalized with different labels and targeted to different biomarkers and, afterwards, applied together in the sensing surface for simultaneous electrochemical detection. Herein, silica coating was successfully used not only to encapsulate an electrochemical redox-active element but also allowed to stabilize the magnetic nanoparticles in solution. It constitutes a promising way to fabricate novel sensing platforms holding dual-stimulus that are able to eliminate, or hinder, some usual artefacts present during the samples analysis.

Looking towards the future, additionally to ruthenium-Fe_3O_4@SiO_2@APTES MNPs, a different redox specie can be also used in order to get different electrochemical labels that can be applied in a multiplexed array sensor for the simultaneous detection of MDA and 4-HNE biomarkers.

In order to better understand and follow, at a nanostructured level, each step-to-step modification along the assembly of the molecular imprinted film, other characterization

methodologies can be employed in the future, such as, ellipsometry, AFM and additional microscope strategies.

Additionally, the introduction of paper as the scaffold material of a biosensor device enabled also the possibility to combine electrical and optical measurements simultaneously. Although the electrochemical performance of the developed sensors was thoroughly explored, a different option can be the incorporation of gold nanoparticles into the paper matrix, in order to develop a facile colorimetric strategy. The main advantage of this kind of nanomaterials is that they can be easily functionalized towards our target molecules and their aggregation behaviour can be employed as colorimetric response.

In sum, the attributes of our biosensing approach can be compared to a very limited number of other electrochemical devices, that are still using a conventional three electrode system, making the paper-sustained device created herein the first electrochemical biosensor with potential to become a portable and low-cost diagnostic tool towards OS biomarker detection.

REFERENCES

1. Thakkar, J. P.; McCarthy, B. J.; Villano, J. L. Age-specific cancer incidence rates increase through the oldest age groups. *Am. J. Med. Sci.* **2014**, *348*, p. 65–70.

2. White, M. C.; Holman, D. M.; Boehm, J. E.; Peipins, L. A.; Grossman, M.; Jane Henley, S. Age and cancer risk: A potentially modifiable relationship. *Am. J. Prev. Med.* **2014**, *46*, p. 1–16.

3. Ziech, D.; Franco, R.; Georgakilas, A. G.; Georgakila, S.; Malamou-Mitsi, V.; Schoneveld, O.; Pappa, A.; Panayiotidis, M. I. The role of reactive oxygen species and oxidative stress in environmental carcinogenesis and biomarker development. *Chem. Biol. Interact.* **2010**, *188*, p. 334–9.

4. Bergmann, N. M.; Peppas, N. a. Molecularly imprinted polymers with specific recognition for macromolecules and proteins. *Prog. Polym. Sci.* **2008**, *33*, p. 271–288.

5. Harman, D. Aging: A Theory Based on Free Radical and Radiation Chemistry. *J. Gerontol.* **1956**, *11*, p. 298–300.

6. Lobo, V.; Patil, A.; Phatak, A.; Chandra, N. Free radicals, antioxidants and functional foods: Impact on human health. *Pharmacogn. Rev.* **2010**, *4*, p. 118-126.

7. Reuter, S.; Gupta, S. C.; Chaturvedi, M. M.; Aggarwal, B. B. Oxidative stress, inflammation, and cancer: how are they linked? *Free Radic. Biol. Med.* **2010**, *49*, p. 1603–16.

8. Schieber, M.; Chandel, N. S. ROS function in redox signaling and oxidative stress. *Curr. Biol.* **2014**, *24*, p. 453–462.

9. Repine JE, Bast A, L. I. State of the Art Oxidative Stress in Chronic Obstructive. *Am. J. Respir. Crit. Care Med.* **1997**, *156*, p. 341–57.

10. de Zwart, L. L.; Meerman, J. H. .; Commandeur, J. N. .; Vermeulen, N. P. . Biomarkers of free radical damage. *Free Radic. Biol. Med.* **1999**, *26*, p. 202–226.

11. Pylväs, M.; Puistola, U.; Laatio, L.; Kauppila, S.; Karihtala, P. Elevated serum 8-OHdG is associated with poor prognosis in epithelial ovarian cancer. *Anticancer Res.* **2011**, *31*, p. 1411–1415.

12. Monaghan, P.; Metcalfe, N. B.; Torres, R. Oxidative stress as a mediator of life history trade-offs: Mechanisms, measurements and interpretation. *Ecol. Lett.* **2009**, *12*, p. 75–92.

13. Valko, M.; Rhodes, C. J.; Moncol, J.; Izakovic, M.; Mazur, M. Free radicals, metals and antioxidants in oxidative stress-induced cancer. *Chem. Biol. Interact.* **2006**, *160*, p. 1–40.

14. Kregel, K. C.; Zhang, H. J. An integrated view of oxidative stress in aging : basic mechanisms , functional effects , and pathological considerations. *Am. Physiol. Soc.* **2007**, *292*,

p. 18–36.
15. Stoddart, R. W.; Ph, D. The Generation of Cancer : Initiation , promotion , progression and the multiple influences of the environment. *Nutrition and* Health **1983**, 2, p. 153–162.
16. Syslová, K.; Böhmová, A.; Mikoška, M.; Kuzma, M.; Pelclová, D.; I, P. K. Multimarker Screening of Oxidative Stress in Aging. *Oxid. Med. Cell. Longev.* **2014**, *2014*, p. 1–14.
17. Loft, S.; Vistisen, K.; Ewertz, M.; Tjønneland, a; Overvad, K.; Poulsen, H. E. Oxidative DNA damage estimated by 8-hydroxydeoxyguanosine excretion in humans: influence of smoking, gender and body mass index. *Carcinogenesis* **1992**, *13*, p. 2241–7.
18. Suzen, S.; Gurer-Orhan, H.; Saso, L. Detection of reactive oxygen and nitrogen species by electron paramagnetic resonance (EPR) technique. *Molecules* **2017**, *22*, p. 1–9.
19. Brandes, R. P.; Janiszewski, M. Direct detection of reactive oxygen species ex vivo. *Kidney Int.* **2005**, *67*, p. 1662–1664.
20. Zitka, O.; Krizkova, S.; Skalickova, S.; Kopel, P.; Babula, P.; Adam, V.; Kizek, R. *Electrochemical Study of DNA Damaged by Oxidation Stress*; Bentham Science Publishers, 2013.
21. Xiao, F.; Wang, L.; Duan, H. Nanomaterial based electrochemical sensors for in vitro detection of small molecular metabolites. *Biotechnol. Adv.* **2016**, *34*, p. 234–249.
22. Herber, R. F. M.; Duffus, J. H.; Christensen, J. M.; Olsen, E.; Park, M. V Risk Assessment for Occupational Exposure to Chemicals. A Review of Current Methodology. *Pure Appl. Chem.* **2001**, *73*, p. 993–1031.
23. Trevisan, M.; Browne, R.; Ram, M.; Muti, P.; Freudenheim, J.; Carosella, A. M.; Armstrong, D. Correlates of markers of oxidative status in the general population. *Am. J. Epidemiol.* **2001**, *154*, p. 348–56.
24. Abreu, C. M.; Soares-dos-reis, R.; Melo, P. N.; Relvas, J. B. Emerging Biosensing Technologies for Neuroinflammatory and Neurodegenerative Disease Diagnostics. *Front. Mol. Neurosci.* **2018**, *11*, p. 1–13.
25. Inaba, Y.; Koide, S.; Yokoyama, K.; Karube, I. Development of urinary 8-hydroxy-2'-deoxyguanosine (8-OHdG) measurement method combined with SPE. *J. Chromatogr. Sci.* **2011**, *49*, p. 303–309.
26. Gutiérrez, A.; Osegueda, S.; Gutiérrez-Granados, S.; Alatorre, A.; García, M. G.; Godínez, L. A. Amperometric Detection and Quantification of 8-Hydroxy-2′-deoxyguanosine (8-OHdG) Using Dendrimer Modified Electrodes. *Electroanalysis* **2008**, *20*, p. 2294–2300.
27. Yang, L.; Wang, B.; Qi, H.; Gao, Q.; Li, C.; Zhang, C. Highly Sensitive Electrochemical Sensor for the Determination of 8-Hydroxy-2'-deoxyguanosine Incorporating SWCNTs-Nafion Composite Film. *Journal of Sensors* **2015**, *2015*, p. 1–11.
28. Koide, S.; Kinoshita, Y.; Ito, N.; Kimura, J.; Yokoyama, K.; Karube, I. Determination of human serum 8-hydroxy-2'-deoxyguanosine (8-OHdG) by HPLC-ECD combined with solid phase extraction (SPE). *J. Chromatogr. B. Analyt. Technol. Biomed. Life Sci.* **2010**, *878*, p. 2163–7.
29. Bolner, A.; Pilleri, M.; Riva, V. D. E.; Nordera, G. P. Plasma and Urinary HPLC-ED

Determination of the Ratio of 8-OHdG / 2-dG in Parkinson's Disease. *Clin. Lab.* **2011**, *57*, *p.* 859–866.

30. Wang, J. C.; Wang, Y. S.; Rang, W. Q.; Xue, J. H.; Zhou, B.; Liu, L.; Qian, Q. M.; Wang, Y. S.; Yin, J. C. Colorimetric determination of 8-hydroxy-2′-deoxyguanosine using label-free aptamer and unmodified gold nanoparticles. *Microchim. Acta* **2014**, *181*, p. 903–910.

31. Abe, T.; Tohgi, H.; Isobe, C.; Murata, T.; Sato, C. Remarkable increase in the concentration of 8-hydroxyguanosine in cerebrospinal fluid from patients with Alzheimer's disease. *J. Neurosci. Res.* **2002**, *70*, p. 447–450.

32. Goyal, R. N.; Jain, N.; Garg, K. Electrochemical and enzymic oxidation of guanosine and 8-hydroxyguanosine and the effects of oxidation productts in mice. *Bioelectrochemistry Bioenerg.* **1997**, *43*, p. 105–114.

33. Hasanzadeh, M.; Mokhtari, F.; Shadjou, N.; Eftekhari, A.; Mokhtarzadeh, A.; Jouyban-Gharamaleki, V.; Mahboob, S. Poly arginine-graphene quantum dots as a biocompatible and non-toxic nanocomposite: Layer-by-layer electrochemical preparation, characterization and non-invasive malondialdehyde sensory application in exhaled breath condensate. *Mater. Sci. Eng. C* **2017**, *75*, p. 247–258.

34. Yuan, L.; Lan, Y.; Han, M.; Bao, J.; Tu, W.; Dai, Z. Label-free and facile electrochemical biosensing using carbon nanotubes for malondialdehyde detection. *Analyst* **2013**, *138*, p. 3131–4.

35. Yalcin, S.; Kilinç, A.; Cobek, B. Evaluation of a simple colorimetric analysis for urinary malondialdehyde determination. *Pathol. Lab. Med. Int.* **2010**, *2009*, *p.* 23–26.

36. Zamani-Kalajahi, M.; Hasanzadeh, M.; Shadjou, N.; Khoubnasabjafari, M.; Ansarin, K.; Jouyban-Gharamaleki, V.; Jouyban, A. Electrodeposition of taurine on gold surface and electro-oxidation of malondialdehyde. *Surf. Eng.* **2015**, *31*, p. 194–201.

37. Kaur, J.; Politis, C.; Jacobs, R. Salivary 8-hydroxy-2-deoxyguanosine, malondialdehyde, vitamin C, and vitamin E in oral pre-cancer and cancer: diagnostic value and free radical mechanism of action. *Clin. Oral Investig.* **2016**, *20*, p. 315–319.

38. Xu, D.; Thiele, G. M.; Kearley, M. L.; Haugen, M. D.; Klassen, L. W.; Sorrell, M. F.; Turna, D. J. Epitope characterization of malondialdehyde-acetaldehyde adducts using an enzyme-Linked immunosorbent assay. *Chem. Res. Toxicol.* **1997**, *10*, p. 978–986.

39. Guéraud, F.; Peiro, G.; Bernard, H.; Alary, J.; Créminon, C.; Debrauwer, L.; Rathahao, E.; Drumare, M. F.; Canlet, C.; Wal, J. M.; Bories, G. Enzyme immunoassay for a urinary metabolite of 4-hydroxynonenal as a marker of lipid peroxidation. *Free Radic. Biol. Med.* **2006**, *40*, p. 54–62.

40. Houglum, K.; Filip, M.; Witztum, J. L.; Chojkier, M. Malondialdehyde and 4-hydroxynonenal protein adducts in plasma and liver of rats with iron overload. *J. Clin. Invest.* **1990**, *86*, p. 1991–1998.

41. Sánchez-Tirado, E.; González-Cortés, A.; Yudasaka, M.; Iijima, S.; Langa, F.; Yáñez-Sedeño, P.; Pingarrón, J. M. Electrochemical immunosensor for the determination of 8-isoprostane aging biomarker using carbon nanohorns-modified disposable electrodes. *J.*

Electroanal. Chem. **2016**, *793*, p. 197–202.

42. Uchiyama, S.; Inaba, Y.; Kunugita, N. Determination of acrolein and other carbonyls in cigarette smoke using coupled silica cartridges impregnated with hydroquinone and 2,4-dinitrophenylhydrazine. *J. Chromatogr. A* **2010**, *1217*, p. 4383–4388.

43. Li, H.; Wang, J.; Kaphalia, B. S.; Ansari, G. A. S.; Khan, M. F. Quantitation of acrolein–protein adducts: Potential biomarker of acrolein exposure. *J. Toxicol. Environ. Heal. - Part A* **2004**, *67*, p. 513–524.

44. Ryberg, H.; Caidahl, K. Chromatographic and mass spectrometric methods for quantitative determination of 3-nitrotyrosine in biological samples and their application to human samples. *J. Chromatogr. B Anal. Technol. Biomed. Life Sci.* **2007**, *851*, p. 160–171.

45. Ishida, N.; Hasegawa, T.; Mukai, K.; Watanabe, M.; Nishino, H. Determination of nitrotyrosine by HPLC-ECD and its application. *J. Vet. Med. Sci.* **2002**, *64, p.* 401–4.

46. Hensley, K.; Maidt, M. L.; Yu, Z.; Sang, H.; Markesbery, W. R.; Floyd, R. a Electrochemical analysis of protein nitrotyrosine and dityrosine in the Alzheimer brain indicates region-specific accumulation. *J. Neurosci.* **1998**, *18*, p. 8126–8132.

47. Wang, S.; Sun, G.; Chen, Z.; Liang, Y.; Zhou, Q.; Pan, Y.; Zhai, H. Constructing a novel composite of molecularly imprinted polymer-coated AuNPs electrochemical sensor for the determination of 3-nitrotyrosine. *Electrochim. Acta* **2018**, *259*, p. 893–902.

48. Jin, J.; Wang, C.; Tao, Y.; Tan, Y.; Yang, D.; Gu, Y.; Deng, H.; Bai, Y.; Lu, H.; Wan, Y. Determination of 3-nitrotyrosine in human urine samples by surface plasmon resonance immunoassay. *Sensors Actuators B Chem.* **2011**, *153*, p. 164–169.

49. Ren, H.; Wang, L.; Wang, X.; Liu, X.; Jiang, S. Measurement of acid dissociation constants and ionic mobilities of 3-nitro-tyrosine and 3-chloro-tyrosine by capillary zone electrophoresis. *J. Pharm. Biomed. Anal.* **2013**, *77*, p. 83–87.

50. Akesson, B.; Jonsson, B. A. Biological monitoring of N-methyl-2-pyrrolidone using 5-hydroxy-N-methyl-2-pyrrolidone in plasma and urine as the biomarker. *Scand J Work Env. Heal.* **2000**, *26*, p. 213–218.

51. Valavanidis, A.; Vlachogianni, T.; Fiotakis, C. 8-hydroxy-2'-deoxyguanosine (8-OHdG): A critical biomarker of oxidative stress and carcinogenesis. *J. Environ. Sci. Health. C. Environ. Carcinog. Ecotoxicol. Rev.* **2009**, *27*, p. 120–39.

52. Abu-Shakra, A.; Zeiger, E. Formation of 8-hydroxy-2'-deoxyguanosine following treatment of 2'-deoxyguanosine or DNA by hydrogen peroxide or glutathione. *Mutat. Res. - Genet. Toxicol. Environ. Mutagen.* **1997**, *390*, p. 45–50.

53. Guo, H.; Xue, K.; Yan, L. Resonance Rayleigh scattering spectral method for determination of urinary 8-hydroxy-2′-deoxyguanosine using gold nanoparticles as probe. *Sensors Actuators B Chem.* **2012**, *171–172*, p. 1038–1045.

54. Mei, S.; Yao, Q.; Wu, C.; Xu, G. Determination of urinary 8-hydroxy-2'-deoxyguanosine by two approaches - Capillary electrophoresis and GC/MS: An assay for in vivo oxidative DNA damage in cancer patients. *J. Chromatogr. B Anal. Technol. Biomed. Life Sci.* **2005**, *827*, p. 83–87.

55. Yano, T.; Shoji, F.; Baba, H.; Koga, T.; Shiraishi, T.; Orita, H.; Kohno, H. Significance of the urinary 8-OHdG level as an oxidative stress marker in lung cancer patients. *Lung Cancer* **2009**, *63*, p. 111–114.

56. Kasai, H. Analysis of a form of oxidative DNA damage , 8-hydroxy-2'-deoxyguanosine , as a marker of cellular oxidative stress during carcinogenesis. *Mutat. Res.* **1997**, *387*, p. 147–163.

57. Subash, P.; Gurumurthy, P.; Sarasabharathi, a; Cherian, K. M. Urinary 8-OHdG: A marker of oxidative stress to DNA and total antioxidant status in essential hypertension with South Indian population. *Indian J. Clin. Biochem.* **2010**, *25*, p. 127–32.

58. Guan, Y.; Zhou, G.; Ye, J. Fast Quantification of Salivary 8-Hydroxy-2′-deoxyguanosine as DNA Damage Biomarker Using CE with Electrochemical Detection. *Chromatographia* **2014**, *77*, p. 603–607.

59. Arnett, S. D.; Osbourn, D. M.; Moore, K. D.; Vandaveer, S. S.; Lunte, C. E. Determination of 8-oxoguanine and 8-hydroxy-2'-deoxyguanosine in the rat cerebral cortex using microdialysis sampling and capillary electrophoresis with electrochemical detection. *J. Chromatogr. B. Analyt. Technol. Biomed. Life Sci.* **2005**, *827*, p. 16–25.

60. Richard G. Cutler, H. R. Critical Reviews of Oxidative Stress and Aging: Advances in Basic Science, Diagnostics and Intervention. *Critical Reviews of Oxidative Stress and Aging Advances in Basic Science, Diagnostics and Intervention.* **2002**, *2*, p. 1–1624.

61. Black, C. N.; Bot, M.; Scheffer, P. G.; Penninx, B. W. J. H. Sociodemographic and lifestyle determinants of plasma oxidative stress markers 8-OHdG and F2-isoprotanes, and associations with metabolic syndrome. *Oxid. Med. Cell. Longev.* **2016**, *7530820*, p. 1-10.

62. Szymańska-Chabowska, A.; Beck, A.; Poręba, R.; Andrzejak, R.; Antonowicz-Juchniewicz, J. Evaluation of DNA damage in people occupationally exposed to arsenic and some heavy metals. *Polish J. Environ. Stud.* **2009**, *18*, p. 1131–1139.

63. Halliwell, B. Antioxidants and human disease: a general introduction. *Nutr. Rev.* **1997**, *55*, p. 44–49.

64. Chen, X.; Chen, H.; Deng, R.; Shen, J. Pros and cons of current approaches for detecting peroxynitrite and their applications. *Biomed. J.* **2014**, *37*, p. 120–126.

65. Conventz, A.; Musiol, A.; Brodowsky, C.; Müller-Lux, A.; Dewes, P.; Kraus, T.; Schettgen, T. Simultaneous determination of 3-nitrotyrosine, tyrosine, hydroxyproline and proline in exhaled breath condensate by hydrophilic interaction liquid chromatography/electrospray ionization tandem mass spectrometry. *J. Chromatogr. B Anal. Technol. Biomed. Life Sci.* **2007**, *860*, p. 78–85.

66. Khan, F.; Siddiqui, A. A. Prevalence of anti-3-nitrotyrosine antibodies in the joint synovial fluid of patients with rheumatoid arthritis, osteoarthritis and systemic lupus erythematosus. *Clin. Chim. Acta* **2006**, *370*, p. 100–107.

67. Daiber, A.; Münzel, T. Increased circulating levels of 3-nitrotyrosine autoantibodies: Marker for or maker of cardiovascular disease? *Circulation* **2012**, *126*, p. 2371–2373.

68. Thomson, L. 3-Nitrotyrosine Modified Proteins in Atherosclerosis. *Dis. Markers* **2015**, *708282*, *p. 1-8*.

69. Petruzzelli, S.; Puntoni, R.; Mimotti, P.; Pulerá, N.; Baliva, F.; Fornai, E.; Carlo, G. Plasma 3-Nitrotyrosine in Cigarette Smokers. *Am. J. Respir. Crit. Care Med.* **1997**, *156*, p. 1902–1907.

70. Frost, M. T.; Halliwell, B.; Moore, K. P. Analysis of free and protein-bound nitrotyrosine in human plasma by a gas chromatography/mass spectrometry method that avoids nitration artifacts. *Biochem. J.* **2000**, *345*, p. 453-8.

71. Schwedhelm, E.; Tsikas, D.; Gutzki, F.-M.; Frölich, J. C. Gas Chromatographic–Tandem Mass Spectrometric Quantification of Free 3-Nitrotyrosine in Human Plasma at the Basal State. *Anal. Biochem.* **1999**, *276*, p. 195–203.

72. Yang, H.; Zhang, Y.; Pöschl, U. Quantification of nitrotyrosine in nitrated proteins. *Anal. Bioanal. Chem.* **2010**, *397*, p. 879–886.

73. Kaur, H.; Halliwell, B. Evidence of nitric oxide mediated oxidative damage in chronic inflammation. *FEBS Lett.* **1994**, *350*, p. 9–12.

74. Sharov, V. S.; Dremina, E. S.; Galeva, N. A.; Gerstenecker, G. S.; Li, X.; Dobrowsky, R. T.; Stobaugh, J. F.; Schöneich, C. Fluorogenic Tagging of Peptide and Protein 3-Nitrotyrosine with 4-(Aminomethyl)-benzenesulfonic Acid for Quantitative Analysis of Protein Tyrosine Nitration. *Chromatographia* **2010**, *71*, p. 37–53.

75. Richards, D. a; Silva, M. a; Devall, A. J. Electrochemical detection of free 3-nitrotyrosine: application to microdialysis studies. *Anal. Biochem.* **2006**, *351*, p. 77–83.

76. Ho, E.; Karimi Galougahi, K.; Liu, C.-C.; Bhindi, R.; Figtree, G. A. Biological markers of oxidative stress: Applications to cardiovascular research and practice. *Redox Biol.* **2013**, *1*, p. 483–91.

77. Ahmad, R.; Tripathi, A. K.; Tripathi, P.; Singh, S.; Singh, R.; Singh, R. K. Malondialdehyde and protein carbonyl as biomarkers for oxidative stress and disease progression in patients with chronic myeloid leukemia. *In Vivo* **2008**, *22*, p. 525–8.

78. Yonny, M. E.; García, E. M.; López, A.; Arroquy, J. I.; Nazareno, M. A. Measurement of malondialdehyde as oxidative stress biomarker in goat plasma by HPLC-DAD. *Microchem. J.* **2016**, *129*, p. 281–285.

79. Ates, I.; Ulker, O. C.; Akdemir, C.; Karakaya, A. Correlation of Ochratoxin A exposure to urinary levels of 8-hydroxydeoxyguanosine and malondialdehyde in a Turkish population. *Bull. Environ. Contam. Toxicol.* **2011**, *86*, p. 258–262.

80. Khoubnasabjafari, M.; Ansarin, K.; Jouyban, A. Reliability of malondialdehyde as a biomarker of oxidative stress in psychological disorders. *BioImpacts* **2015**, *5*, p. 123–127.

81. Del Rio, D.; Stewart, A. J.; Pellegrini, N. A review of recent studies on malondialdehyde as toxic molecule and biological marker of oxidative stress. *Nutr. Metab. Cardiovasc. Dis.* **2005**, *15*, p. 316–328.

82. Nielsen, F.; Mikkelsen, B. B.; Nielsen, J. B.; Andersen, H. R.; Grandjean, P. Plasma malondialdehyde as biomarker for oxidative stress: Reference interval and effects of life-style factors. *Clin. Chem.* **1997**, *43*, p. 1209–1214.

83. Siegel, S. J.; Bieschke, J.; Powers, E. T.; Kelly, J. W. The oxidative stress metabolite 4-hydroxynonenal promotes Alzheimer protofibril formation. *Biochemistry* **2007**, *46*, p. 1503–1510.

84. Dalleau, S.; Baradat, M.; Guéraud, F.; Huc, L. Cell death and diseases related to oxidative stress:4-hydroxynonenal (HNE) in the balance. *Cell Death Differ.* **2013**, *20*, p. 1615–1630.

85. Zhong, H.; Yin, H. Role of lipid peroxidation derived 4-hydroxynonenal (4-HNE) in cancer: Focusing on mitochondria. *Redox Biol.* **2015**, *4*, p. 193–199.

86. Chen, Q.; Esterbauer, H.; Jurgens, G. Studies on epitopes on low-density lipoprotein modified by 4-hydroxynonenal. Biochemical characterization and determination. *Biochem. J.* **1992**, *288*, p. 249–254.

87. Connor, R. E.; Marnett, L. J.; Liebler, D. C. Protein-selective capture to analyze electrophile adduction of Hsp90 by 4-hydroxynonenal. *Chem. Res. Toxicol.* **2011**, *24*, p. 1275–1282.

88. Peroxidation, L.; Slater, T. F.; Cheeseman, K. H.; Slater, T. F.; Zollner, H.; Schaur, R. J.; Zollner, H.; Schaur, R. J.; Raton, B.; Zollner, H.; Esterbauer, H.; Zollner, H.; Occurrence, N. Determination of Aldehydic Li pid Peroxidation Products: Malonaldehyde and 4-Hydroxynonenal. *Methods Enzymol.* **1990**, *186*, p. 407–421.

89. Lowe, F. J.; Luettich, K.; Gregg, E. O. Lung cancer biomarkers for the assessment of modified risk tobacco products: an oxidative stress perspective. *Biomarkers* **2013**, *18*, p. 183–195.

90. Turner, A. P. F. Biosensors: sense and sensibility. *Chem. Soc. Rev.* **2013**, *42*, p. 3175–3648.

91. Owens, P. K.; Karlsson, L.; Lutz, E. S. M.; Andersson, L. I. Molecular imprinting for bio- and pharmaceutical analysis. *TrAC - Trends Anal. Chem.* **1999**, *18*, p. 146–154.

92. Arduini, F.; Cinti, S.; Scognamiglio, V.; Moscone, D.; Palleschi, G. How cutting-edge technologies impact the design of electrochemical (bio)sensors for environmental analysis. A review. *Anal. Chim. Acta* **2017**. *959*, p. 15-42.

93. Hayat, A.; Marty, J. L. Disposable screen printed electrochemical sensors: Tools for environmental monitoring. *Sensors (Switzerland)* **2014**, *14*, p. 10432–10453.

94. Shafiee, A.; Ghadiri, E.; Kassis, J.; Pourhabibi Zarandi, N.; Atala, A. Biosensing Technologies for Medical Applications, Manufacturing, and Regenerative Medicine. *Curr. Stem Cell Reports* **2018**, 4, p. 1–11.

95. Corcuera, I. R. De; Cavalieri, R. P. Biosensors. *Encycl. Agric. Food Biol. Eng.* **2003**, p. 119–123.

96. Thevenot, D. R. Electrochemical Biosensors: Recommended Definitions and Classification. *Pure Appl. Chem.* **1999**, *71*, p. 2333–2348.

97. Justino, A. C. I. L.; Freitas, A. C.; Pereira, R.; Duarte, A. C.; Santos, T. A. P. R.; Justino, C. I. L.; Freitas, A. C.; Pereira, R.; Duarte, A. C. Recent developments in recognition elements for chemical sensors and biosensors. *Trends Anal. Chem.* **2015**, *68*, p. 2–17.

98. Chambers, J. P.; Arulanandam, B. P.; Matta, L. L.; Weis, A.; Valdes, J. J. Biosensor Recognition Elements. **2002**, 1–12.

99. Tang, Z.; Ma, Z. Multiple functional strategies for amplifying sensitivity of amperometric immunoassay for tumor markers: A review. *Biosens. Bioelectron.* **2017**, *98*, p. 100–112.

100. Kozitsina, A.; Svalova, T.; Malysheva, N.; Okhokhonin, A.; Vidrevich, M.; Brainina, K.

Sensors Based on Bio and Biomimetic Receptors in Medical Diagnostic, Environment, and Food Analysis. *Biosensors* **2018**, *8*, p. 35–95.

101. Diltemiz, S. E.; Hür, D.; Ersöz, a; Denizli, a; Say, R. Designing of MIP based QCM sensor having thymine recognition sites based on biomimicking DNA approach. *Biosens. Bioelectron.* **2009**, *25*, p. 599–603.

102. Fang, G.; Liu, G.; Yang, Y.; Wang, S. Quartz crystal microbalance sensor based on molecularly imprinted polymer membrane and three-dimensional Au nanoparticles@mesoporous carbon CMK-3 functional composite for ultrasensitive and specific determination of citrinin. *Sensors Actuators B Chem.* **2016**, *230*, p. 272–280.

103. Uygun, Z. O.; Deniz, H.; Uygun, E. Molecularly Imprinted Sensors — New Sensing Technologies. *Biosens. - Micro Nanoscale Appl.* **2015**, *1*, p. 85–108.

104. Hakimian, F.; Ghourchian, H.; Hashemi, A. sadat; Arastoo, M. R.; Behnam Rad, M. Ultrasensitive optical biosensor for detection of miRNA-155 using positively charged Au nanoparticles. *Sci. Rep.* **2018**, *8*, p. 2943–2952.

105. Xu, Z.; Deng, P.; Li, J.; Xu, L.; Tang, S. Molecularly imprinted fluorescent probe based on FRET for selective and sensitive detection of doxorubicin. *Mater. Sci. Eng. B* **2017**, *218*, p. 31–39.

106. Xiao, F.; Wang, L.; Duan, H. Nanomaterial based electrochemical sensors for in vitro detection of small molecule metabolites. *Biotechnol. Adv.* **2016**, *34*, p. 234–249.

107. Farzin, L.; Shamsipur, M. Recent advances in design of electrochemical affinity biosensors for low level detection of cancer protein biomarkers using nanomaterial-assisted signal enhancement strategies. *J. Pharm. Biomed. Anal.* **2018**, *147*, p. 185–210.

108. Rusling, J. F.; Bishop, G. W.; Doan, N. M.; Papadimitrakopoulos, F. Nanomaterials and biomaterials in electrochemical arrays for protein detection. *J. Mater. Chem. B.* **2014**, *2*, p. 12–30.

109. Sassolas, A.; Leca-Bouvier, B. D.; Blum, L. J. DNA biosensors and microarrays. *Chem. Rev.* **2008**, *108*, p. 109–39.

110. Wang, Y.; Duncan, T. V Nanoscale sensors for assuring the safety of food products. *Curr. Opin. Biotechnol.* **2017**, *44*, p. 74–86.

111. Grieshaber, D.; MacKenzie, R.; Vörös, J.; Reimhult, E. Electrochemical Biosensors - Sensor Principles and Architectures. *Sensors* **2008**, *8*, p. 1400–1458.

112. Arduini, F.; Micheli, L.; Moscone, D.; Palleschi, G.; Piermarini, S.; Ricci, F.; Volpe, G. Electrochemical biosensors based on nanomodified screen-printed electrodes: Recent applications in clinical analysis. *TrAC - Trends Anal. Chem.* **2016**, *79*, p. 114–126.

113. Labib, M.; Sargent, E. H.; Kelley, S. O. Electrochemical Methods for the Analysis of Clinically Relevant Biomolecules. *Chem. Rev.* **2016**, *116*, p. 9001–9090.

114. Campuzano, S.; Yáñez-Sedeño, P.; Pingarrón, J. Electrochemical Genosensing of Circulating Biomarkers. *Sensors* **2017**, *17*, p. 1–20.

115. Hulanicki, A.; Glab, S.; Ingman, F. Chemical sensors: definitions and classification. *Pure Appl. Chem.* **1991**, *63*, p. 1247–1250.

116. Wisitsoraat, a.; Pakapongpan, S.; Sriprachuabwong, C.; Phokharatkul, D.; Sritongkham, P.; Lomas, T.; Tuantranont, a. Graphene–PEDOT:PSS on screen printed carbon electrode for enzymatic biosensing. *J. Electroanal. Chem.* **2013**, *704*, p. 208–213.

117. Liu, J.; Zhang, Y.; Jiang, M.; Tian, L.; Sun, S.; Zhao, N.; Zhao, F.; Li, Y. Electrochemical microfluidic chip based on molecular imprinting technique applied for therapeutic drug monitoring. *Biosens. Bioelectron.* **2017**, *91*, p. 714–720.

118. Souza, L. P.; Calegari, F.; Zarbin, A. J. G.; Marcolino-Junior, L. H.; Bergamini, M. F. Voltammetric determination of the antioxidant capacity in wine samples using a carbon nanotube modified electrode. *J. Agric. Food Chem.* **2011**, *59*, p. 7620–5.

119. Greco, F.; Zucca, A.; Taccola, S.; Menciassi, A.; Fujie, T.; Haniuda, H.; Takeoka, S.; Dario, P.; Mattoli, V. Ultra-thin conductive free-standing PEDOT/PSS nanofilms. *Soft Matter* **2011**, *7*, p. 10642–10650.

120. Chen, X.; Jia, X.; Han, J.; Ma, J.; Ma, Z. Electrochemical immunosensor for simultaneous detection of multiplex cancer biomarkers based on graphene nanocomposites. *Biosens. Bioelectron.* **2013**, *50*, p. 356–361.

121. Felix, F. S.; Angnes, L. Electrochemical Immunosensors – a Powerful Tool for Analytical Applications. *Biosens. Bioelectron.* **2017**, *102*, p. 470–478.

122. Brett, A. M. O.; Brett, C. M. a. *Electroquímica: Princípios, Métodos e Aplicações*; Oxford University Press: Coimbra, 1993.

123. Gutiérrez, A.; Gutierrez, F.; Eguílaz, M.; González-Domínguez, J. M.; Hernández-ferrer, J.; Ansón-casaos, A.; Martínez, M. T.; Rivas, G. Electrochemical sensing of guanine, adenine and 8-hydroxy-2′-deoxyguanosine at glassy carbon modified with single-walled carbon nanotubes covalently functionalized with lysine. *RSC Adv.* **2016**, *6*, p. 13469–13477.

124. Gupta, P.; Oyama, M.; Goyal, R. N. Electrochemical investigations of 8-hydroxydeoxyguanosine and its determination at an edge plane pyrolytic graphite electrode. *RSC Adv.* **2016**, *6*, p. 1722–1728.

125. Martín-Yerga, D.; Costa Rama, E.; Costa García, A. Electrochemical study and determination of electroactive species with screen-printed electrodes. *J. Chem. Educ.* **2016**, *93*, p. 1270–1276.

126. Zia, A. I.; Mukhopadhyay, S. C. Electrochemical Sensing: Carcinogens in Beverages-Chapter 2 Impedance Spectroscopy and Experimental Setup. *Smart Sensors* **2016**, *20*, p. 21–37.

127. Muñoz, J.; Montes, R.; Baeza, M. Trends in Electrochemical Impedance Spectroscopy involving nanocomposite transducers: characterization, architecture surface and bio-sensing Trends in Electrochemical Impedance Spectroscopy involving nanocomposite transducers: characte. *Trends Anal. Chem.* **2017**, *97*, p. 201-215.

128. Rajasekar, A.; Ting, Y. P. Inhibition of biocorrosion of aluminum 2024 aeronautical alloy by conductive ladder polymer poly(o -phenylenediamine). *Ind. Eng. Chem. Res.* **2011**, *50*, p. 2040–2046.

129. Sharifirad, M.; Kiani, F.; Koohyar, F. Glassy carbon electrode modified by Poly (m-

aminobenzoic acid)/ nano SiO 2 film and electrical and electrochemical properties. **2013**, *2*, p. 366–378.

130. Balint, R.; Cassidy, N. J.; Cartmell, S. H. Conductive polymers: Towards a smart biomaterial for tissue engineering. *Acta Biomater.* **2014**, *10*, p. 2341–2353.

131. Zhou, C.; Liu, Z.; Dong, Y.; Li, D. Electrochemical behavior of o-nitrophenol at hexagonal mesoporous silica modified carbon paste electrodes. *Electroanalysis* **2009**, *21*, p. 853–858.

132. Zheng, J. S.; Zhang, L.; Shellikeri, A.; Cao, W.; Wu, Q.; Zheng, J. P. A hybrid electrochemical device based on a synergetic inner combination of Li ion battery and Li ion capacitor for energy storage. *Sci. Rep.* **2017**, *7*, p. 1–8.

133. Hájková, A.; Barek, J.; Vyskočil, V. Electrochemical DNA biosensor for detection of DNA damage induced by hydroxyl radicals. *Bioelectrochemistry* **2017**, *116*, p. 1-9.

134. Liana, D. D.; Raguse, B.; Justin Gooding, J.; Chow, E. Recent advances in paper-based sensors. *Sensors (Switzerland)* **2012**, *12*, p. 11505–11526.

135. Obaje, E. A.; Cummins, G.; Schulze, H.; Mahmood, S.; Desmulliez, M. P. Y.; Bachmann, T. T. Carbon screen-printed electrodes on ceramic substrates for label-free molecular detection of antibiotic resistance. *J. Interdiscip. Nanomedicine* **2016**, *1*, p. 93–109.

136. Barras, R.; Cunha, I.; Gaspar, D.; Fortunato, E.; Martins, R.; Pereira, L. Printable cellulose-based electroconductive composites for sensing elements in paper electronics. *Flex. Print. Electron.* **2017**, *2*, p. 1-12.

137. Mistry, K. K.; Sagarika Deepthy, T.; Chaudhuri, C. R.; Saha, H. Electrochemical characterization of some commercial screen-printed electrodes in different redox substrates. *Curr. Sci.* **2015**, *109*, p. 1427–1436.

138. Khan, M. A. R.; T.C. Moreira, F.; Riu, J.; F. Sales, M. G. Plastic antibody for the electrochemical detection of bacterial surface proteins. *Sensors Actuators, B Chem.* **2016**, *233*, p. 697–704.

139. Aoun, S. Ben Nanostructured carbon electrode modified with N-doped graphene quantum dots – chitosan nanocomposite : a sensitive electrochemical dopamine sensor. *R. Soc.* **2017**, *4*, p. 0–11.

140. Balakrishnan, S. R.; Hashim, U.; Letchumanan, G. R.; Kashif, M.; Ruslinda, A. R.; Liu, W. W.; Veeradasan, P.; Haarindra Prasad, R.; Foo, K. L.; Poopalan, P. Development of highly sensitive polysilicon nanogap with APTES/GOx based lab-on-chip biosensor to determine low levels of salivary glucose. *Sensors Actuators, A Phys.* **2014**, *220*, p. 101–111.

141. Patel, M. K.; Solanki, P. R.; Khandelwal, S.; Agrawal, V. V; Ansari, S. G.; Malhotra, B. D. Self-assembled monolayer based electrochemical nucleic acid sensor for Vibrio cholerae detection. *J. Phys. Conf. Ser.* **2012**, *358*, p. 12009-12018.

142. Määttänen, A.; Vanamo, U.; Ihalainen, P.; Pulkkinen, P.; Tenhu, H.; Bobacka, J.; Peltonen, J. A low-cost paper-based inkjet-printed platform for electrochemical analyses. *Sensors Actuators, B Chem.* **2013**, *177*, p. 153–162.

143. Wang, J.; Tian, B.; Nascimento, V. B.; Angnes, L. Performance of screen-printed carbon electrodes fabricated from different carbon inks. *Electrochim. Acta* **1998**, *43*, p. 3459–3465.

144. Rezaei, B.; Damiri, S. Fabrication of a nanostructure thin film on the gold electrode using continuous pulsed-potential technique and its application for the electrocatalytic determination of metronidazole. *Electrochim. Acta* **2010**, *55*, p. 1801–1808.

145. Ragones, H.; Schreiber, D.; Inberg, A.; Berkh, O.; Kósa, G.; Freeman, A.; Shacham-Diamand, Y. Disposable electrochemical sensor prepared using 3D printing for cell and tissue diagnostics. *Sensors Actuators, B Chem.* **2015**, *216*, p. 434–442.

146. Zhang, T.-T.; Zhao, H.-M.; Fan, X.-F.; Chen, S.; Quan, X. Electrochemiluminescence immunosensor for highly sensitive detection of 8-hydroxy-2′-deoxyguanosine based on carbon quantum dot coated Au/SiO2 core–shell nanoparticles. *Talanta* **2015**, *131*, p. 379–385.

147. Stempkowska, I.; Ligaj, M.; Jasnowska, J.; Langer, J.; Filipiak, M. Electrochemical response of oligonucleotides on carbon paste electrode. *Bioelectrochemistry* **2007**, *70*, p. 488–494.

148. Paleček, E.; Jelen, F. Electrochemistry of Nucleic Acids and Development of DNA Sensors. *Crit. Rev. Anal. Chem.* **2002**, *32*, p. 261–270.

149. Wang, Z.; Xiao, S.; Chen, Y. B-Cyclodextrin incorporated carbon nanotubes-modified electrodes for simultaneous determination of adenine and guanine. *J. Electroanal. Chem.* **2006**, *589*, p. 237–242.

150. Kamel, A. H.; Moreira, F. T. C.; Delerue-Matos, C.; Sales, M. G. F. Electrochemical determination of antioxidant capacities in flavored waters by guanine and adenine biosensors. *Biosens. Bioelectron.* **2008**, *24*, p. 591–9.

151. Kowalski, J.; Oszyn, J. P. Electrochemical oxidation of 8-Oxoganine. *Tetrahedron Lett.* **1998**, *28*, p. 1261–1264.

152. Sharma, V.; Jelen, F.; Trnkova, L. Functionalized Solid Electrodes for Electrochemical Biosensing of Purine Nucleobases and Their Analogues: A Review. *Sensors* **2015**, *15*, p. 1564–1600.

153. Li, T. H.; Jia, W. L.; Wang, H. S.; Liu, R. M. Electrochemical performance of 8-hydroxy-2'-deoxyguanosine and its detection at poly(3-methylthiophene) modified glassy carbon electrode. *Biosens. Bioelectron.* **2007**, *22*, p. 1245–1250.

154. Langmaier, J.; Samec, Z.; Samcová, E. Electrochemical Oxidation of 8-Oxo-2′-Deoxyguanosine on Glassy Carbon, Gold, Platinum and Tin(IV) Oxide Electrodes. *Electroanalysis* **2003**, *15*, p. 1555–1560.

155. Tehrani, Z.; Burwell, G.; Azmi, M. a M.; Castaing, a; Rickman, R.; Almarashi, J.; Dunstan, P.; Beigi, a M.; Doak, S. H.; Guy, O. J. Generic epitaxial graphene biosensors for ultrasensitive detection of cancer risk biomarker. *2D Mater.* **2014**, *1*, *025004*.

156. Randviir, E. P.; Brownson, D. A. C.; Metters, J. P.; Kadara, R. O.; Banks, C. E. The fabrication, characterisation and electrochemical investigation of screen-printed graphene electrodes. *Phys. Chem. Chem. Phys.* **2014**, *16*, p. 4598-4611.

157. Haslam, C.; Damiati, S.; Whitley, T.; Davey, P.; Ifeachor, E.; Awan, S. Label-Free Sensors Based on Graphene Field-Effect Transistors for the Detection of Human Chorionic Gonadotropin Cancer Risk Biomarker. *Diagnostics* **2018**, *8*, p.1-13.

158. Della Pelle, F.; Di Battista, R.; Vázquez, L.; Palomares, F. J.; Del Carlo, M.; Sergi, M.; Compagnone, D.; Escarpa, A. Press-transferred carbon black nanoparticles for class-selective antioxidant electrochemical detection. *Appl. Mater. Today* **2017**, *9*, p. 29–36.

159. Carneiro, M. C. C. G.; Moreira, F. T. C.; Dutra, R. A. F.; Fernandes, R.; Sales, M. G. F. Homemade 3-carbon electrode system for electrochemical sensing: Application to microRNA detection. *Microchem. J.* **2018**, *138*, p. 35–44.

160. Sharma, N.; Barstis, T.; Giri, B. Advances in paper-analytical methods for pharmaceutical analysis. *Eur. J. Pharm. Sci.* **2018**, *111*, p. 46-56.

161. Parolo, C.; Merkoçi, A. Paper-based nanobiosensors for diagnostics. *Chem. Soc. Rev.* **2013**, *42*, p. 450–457.

162. Arduini, F.; Cinti, S.; Scognamiglio, V.; Moscone, D. Paper-Based Electrochemical Devices in Biomedical Field: Recent Advances and Perspectives. *Comprehen. Anal. Chem.* **2017**, 17, p. 351-366.

163. Martinez, A. W.; Phillips, S. T.; Whitesides, G. M.; Carrilho, E. Diagnostics for the developing world: microfluidic paper-based analytical devices. *Anal. Chem.* **2010**, *82*, p. 3–10.

164. Parolo, C.; Medina-Sánchez, M.; Montõn, H.; De La Escosura-Muñiz, A.; Merkoçi, A. Paper-based electrodes for nanoparticles detection. *Part. Part. Syst. Charact.* **2013**, *30*, p. 662–666.

165. Toley, B. J.; Das, D.; Ganar, K. A.; Kaur, N.; Meena, M.; Rath, D.; Sathishkumar, N.; Soni, S. Multidimensional Paper Networks: A New Generation of Low-Cost Pump-Free Microfluidic Devices. *J. Indian Inst. Sci.* **2018**, *98*, p. 1–34.

166. Marques, A. C.; Santos, L.; Costa, M. N.; Dantas, J. M.; Duarte, P.; Gonçalves, A.; Martins, R.; Salgueiro, C. A.; Fortunato, E. Office Paper Platform for Bioelectrochromic Detection of Electrochemically Active Bacteria using Tungsten Trioxide Nanoprobes. *Scientific Reports* **2015**, *3*, p. 1–7.

167. Morales-narváez, E.; Golmohammadi, H.; Naghdi, T.; Kostiv, U.; Horak, D.; Pourreza, N.; Merkoçi, A. Nanopaper as an Optical Sensing Platform. *ACS Nano* **2015**, *9*, p. 7296-7305.

168. Glavan, A. C.; Christodouleas, D. C.; Mosadegh, B.; Yu, H. D.; Smith, B. S.; Lessing, J.; Ferna, M. T.; Whitesides, G. M. Folding Analytical Devices for Electrochemical ELISA in Hydrophobic R. *Anal. Chem.* **2014**, *86*, p. 11999-12007.

169. Su, M.; Ge, L.; Kong, Q.; Zheng, X.; Ge, S.; Li, N.; Yu, J.; Yan, M. Cyto-sensing in electrochemical lab-on-paper cyto-device for in-situ evaluation of multi-glycan expressions on cancer cells. *Biosens. Bioelectron.* **2014**, *63C*, p. 232–239.

170. Liu, W.; Guo, Y.; Luo, J.; Kou, J.; Zheng, H.; Li, B.; Zhang, Z. A molecularly imprinted polymer based a lab-on-paper chemiluminescence device for the detection of dichlorvos. *Spectrochim. Acta Part A Mol. Biomol. Spectrosc.* **2015**, *141*, p. 51–57.

171. Liana, D. D.; Raguse, B.; Justin Gooding, J.; Chow, E. Recent advances in paper-based sensors. *Sensors (Switzerland)* **2012**, *12*, p. 11505–11526.

172. Kadimisetty, K.; Malla, S.; Sardesai, N. P.; Joshi, A. a.; Faria, R. C.; Lee, N. H.; Rusling, J. F. Automated Multiplexed ECL Immunoarrays for Cancer Biomarker Proteins. *Anal. Chem.*

2015, *87*, p. 4472–4478.

173. Nery, E. W.; Kubota, L. T. Sensing approaches on paper-based devices: A review. *Anal. Bioanal. Chem.* **2013**, *405*, p. 7573–7595.

174. Devarakonda, S.; Singh, R.; Bhardwaj, J.; Jang, J. Cost-Effective and Handmade Paper-Based Immunosensing Device for Electrochemical Detection of Influenza Virus. *Sensors* **2017**, *17*, p. 2597-2610.

175. Ramström, O.; Nicholls, I. A.; Mosbach, K. Synthetic peptide receptor mimics: highly stereoselective recognition in non-covalent molecularly imprinted polymers. *Tetrahedron: Asymmetry* **1994**, *5*, p. 649–656.

176. Chen, L.; Wang, X.; Lu, W.; Wu, X.; Li, J. Molecular imprinting: perspectives and applications. *Chem. Soc. Rev.* **2016**, *45*, p. 2137-2211.

177. Malitesta, C.; Mazzotta, E.; Picca, R. a; Poma, A.; Chianella, I.; Piletsky, S. a MIP sensors--the electrochemical approach. *Anal. Bioanal. Chem.* **2012**, *402*, p. 1827–46.

178. Basozabal, I.; Gomez-Caballero, A.; Diaz-Diaz, G.; Guerreiro, A.; Gilby, S.; Goicolea, M. A.; Barrio, R. J. Rational design and chromatographic evaluation of histamine imprinted polymers optimised for solid-phase extraction of wine samples. *J. Chromatogr. A* **2013**, *1308*, p. 45–51.

179. Panasyuk-Delaney, T.; Mirsky, V. M.; Ulbricht, M.; Wolfbeis, O. S. Impedometric herbicide chemosensors based on molecularly imprinted polymers. *Anal. Chim. Acta* **2001**, *435*, p. 157–162.

180. Tan, S.; Saito, K.; Hearn, M. T. Stimuli-responsive polymeric materials for separation of biomolecules. *Curr. Opin. Biotechnol.* **2018**, *53*, p. 209–223.

181. Barde, L. N.; Ghule, M. M.; Roy, A. a.; Mathur, V. B.; Shivhare, U. D. Development of molecularly imprinted polymer as sustain release drug carrier for propranolol HCL. *Drug Dev. Ind. Pharm.* **2012**, *39*, p. 1–7.

182. Frasco, M. F.; Truta, L. A. A. N. A.; Sales, M. G. F.; Moreira, F. T. C. Imprinting Technology in Electrochemical Biomimetic Sensors. **2017**, 17, p. 523-552.

183. Sergey, P.; Anthony, T. *Molecular Imprinting of Polymers*; **2006**.

184. Sellergren, B.; Dickert, F. L.; Hayden, O.; Mcniven, S.; Karube, I.; Murray, G. M.; Manuel Uy, M.; Kriz, D.; Ansell, R. J.; Kempe, M.; Schweitz, L.; Nilsson, S.; Lanza, F.; Andersson, L. I.; Matsui, J.; Takeuchi, T.; Mayes, A. G.; Perez, N.; Alexander, C.; Vulfson, E. N.; Dhal, P. K.; Kulkarni, M. G.; Mashelkar, R. A.; Tsukagoshi, K.; Murata, M.; Maeda, M.; Sasaki, D. Y.; Whitcombe, M. J.; Vulfson, E. N.; Wulff, G.; Biffis, A.; Nicholls, I. A.; Andersson, H. S.; Hall, A. J. *Techniques and Instrumentation in Analytical Chemistry* **2001**, Vol. 23.

185. Alvarez-Lorenzo, C.; Concheiro, A. Molecularly imprinted polymers for drug delivery. *J. Chromatogr. B Anal. Technol. Biomed. Life Sci.* **2004**, *804*, p. 231–245.

186. Vallano, P. T.; Remcho, V. T. Highly selective separations by capillary electrochromatography: Molecular imprint polymer sorbents. *J. Chromatogr. A* **2000**, *887*, p. 125–135.

187. Sahebnasagh, A.; Karimi, G.; Mohajeri, S. A. Preparation and Evaluation of Histamine

Imprinted Polymer as a Selective Sorbent in Molecularly Imprinted Solid-Phase Extraction Coupled with High Performance Liquid Chromatography Analysis in Canned Fish. *Food Anal. Methods* **2014**, *7*, p. 1–8.

188. Whitcombe, M. J.; Chianella, I.; Larcombe, L.; Piletsky, S. a; Noble, J.; Porter, R.; Horgan, A. The rational development of molecularly imprinted polymer-based sensors for protein detection. *Chem. Soc. Rev.* **2011**, *40*, p. 1547–1571.

189. Chen, L.; Wang, X.; Lu, W.; Wu, X.; Li, J. Molecular imprinting: perspectives and applications. *Chem. Soc. Rev.* **2016**, *45*, p. 2137–2211.

190. Mujahid, A.; Mustafa, G.; Dickert, F. L. Label-Free Bioanalyte Detection from Nanometer to Micrometer Dimensions — Molecular Imprinting. *Biosensors* **2018**, *8*, p. 1–21.

191. Ma, Y.; Xu, S.; Wang, S.; Wang, L. Luminescent molecularly-imprinted polymer nanocomposites for sensitive detection. *TrAC Trends Anal. Chem.* **2015**, *67*, p. 209-216.

192. Shekarchizadeh, H.; Ensafi, A. a; Kadivar, M. Selective determination of sucrose based on electropolymerized molecularly imprinted polymer modified multiwall carbon nanotubes/glassy carbon electrode. *Mater. Sci. Eng. C. Mater. Biol. Appl.* **2013**, *33*, p. 3553–61.

193. Luo, J.; Jiang, S.; Liu, X. Electrochemical sensor for bovine hemoglobin based on a novel graphene-molecular imprinted polymers composite as recognition element. *Sensors Actuators B Chem.* **2014**, *203*, p. 782–789.

194. Say, R.; Gültekin, A.; Ozcan, A. A.; Denizli, A.; Ersöz, A. Preparation of new molecularly imprinted quartz crystal microbalance hybride sensor system for 8-hydroxy-2'-deoxyguanosine determination. *Anal. Chim. Acta* **2009**, *640*, p. 82–86.

195. Li, L.; Yang, L.; Xing, Z.; Lu, X.; Kan, X. Surface molecularly imprinted polymers-based electrochemical sensor for bovine hemoglobin recognition. *Analyst* **2013**, *138*, p. 6962–8.

196. Rezaei, B.; Rahmanian, O.; Ensafi, A. A. An electrochemical sensor based on multiwall carbon nanotubes and molecular imprinting strategy for warfarin recognition and determination. *Sensors Actuators B Chem.* **2014**, *196*, p. 539–545.

197. Yola, M. L.; Eren, T.; Atar, N. A sensitive molecular imprinted electrochemical sensor based on gold nanoparticles decorated graphene oxide: Application to selective determination of tyrosine in milk. *Sensors Actuators B Chem.* **2015**, *210*, p. 149–157.

198. da Silva, H.; Pacheco, J. G.; Magalhães, J. M. C. S.; Viswanathan, S.; Delerue-Matos, C. MIP-graphene-modified glassy carbon electrode for the determination of trimethoprim. *Biosens. Bioelectron.* **2014**, *52*, p. 56–61.

199. Liu, B.; Xiao, B.; Cui, L.; Wang, M. Molecularly imprinted electrochemical sensor for the highly selective and sensitive determination of melamine. *Mater. Sci. Eng. C* **2015**, *55*, p. 457-461.

200. Yang, Y.; Yi, C.; Luo, J.; Liu, R.; Liu, J.; Jiang, J.; Liu, X. Glucose sensors based on electrodeposition of molecularly imprinted polymeric micelles: a novel strategy for MIP sensors. *Biosens. Bioelectron.* **2011**, *26*, p. 2607–12.

201. Liu, B.; Lian, H. T.; Yin, J. F.; Sun, X. Y. Dopamine molecularly imprinted electrochemical sensor based on graphene–chitosan composite. *Electrochim. Acta* **2012**, *75*, p. 108–114.

202. Patel, A. K.; Sharma, P. S.; Prasad, B. B. Development of a Creatinine Sensor Based on a Molecularly Imprinted Polymer-Modified Sol-Gel Film on Graphite Electrode. *Electroanalysis* **2008**, *20*, p. 2102–2112.

203. Lian, H.; Sun, Z.; Sun, X.; Liu, B. Graphene Doped Molecularly Imprinted Electrochemical Sensor for Uric Acid. *Anal. Lett.* **2012**, *45*, p. 2717–2727.

204. Ribeiro, C. M.; Miguel, E. M.; Silva, J. dos S.; Silva, C. B. d.; Goulart, M. O. F.; Kubota, L. T.; Gonzaga, F. B.; Santos, W. J. R.; Lima, P. R. Application of a nanostructured platform and imprinted sol-gel film for determination of chlorogenic acid in food samples. *Talanta* **2016**, *156–157*, p. 119–125.

205. Sharma, P. S.; Pietrzyk-Le, A.; D'Souza, F.; Kutner, W. Electrochemically synthesized polymers in molecular imprinting for chemical sensing. *Anal. Bioanal. Chem.* **2012**, *402*, p. 3177–204.

206. Rosy; Chasta, H.; Goyal, R. N. Molecularly imprinted sensor based on o-aminophenol for the selective determination of norepinephrine in pharmaceutical and biological samples. *Talanta* **2014**, *125*, p. 167–173.

207. Enache, T. A.; Oliveira-Brett, A. M. Phenol and para-substituted phenols electrochemical oxidation pathways. *J. Electroanal. Chem.* **2011**, *655*, p. 9–16.

208. Nady, H.; El-Rabiei, M. M.; El-Hafez, G. M. A. Electrochemical oxidation behavior of some hazardous phenolic compounds in acidic solution. *Egypt. J. Pet.* **2017**, 26, p. 669–678.

209. Roy, E.; Patra, S.; Madhuri, R.; Sharma, P. K. Developing electrochemical sensor for point-of-care diagnostics of oxidative stress marker using imprinted bimetallic Fe/Pd nanoparticle. *Talanta* **2015**, *132*, p. 406–415.

210. Jalili, R.; Amjadi, M. Bio-inspired molecularly imprinted polymer–green emitting carbon dot composite for selective and sensitive detection of 3-nitrotyrosine as a biomarker. *Sensors Actuators, B Chem.* **2018**, *255*, p. 1072–1078.

211. Liu, G.; Lin, Y. Nanomaterial labels in electrochemical immunosensors and immunoassays. *Talanta* **2007**, *74*, p. 308–317.

212. Zarschler, K.; Rocks, L.; Licciardello, N.; Boselli, L.; Polo, E.; Garcia, K. P.; De Cola, L.; Stephan, H.; Dawson, K. A. Ultrasmall inorganic nanoparticles: state-of-the-art and perspectives for biomedical applications. *Nanomedicine Nanotechnology, Biol. Med.* **2016**, *12*, p. 1663-1701.

213. Moritz, M.; Geszke-Moritz, M. The newest achievements in synthesis, immobilization and practical applications of antibacterial nanoparticles. *Chem. Eng. J.* **2013**, *228*, p. 596–613.

214. Ishkuh, F. A.; Javanbakht, M.; Esfandyari-Manesh, M.; Dinarvand, R.; Atyabi, F. Synthesis and characterization of paclitaxel-imprinted nanoparticles for recognition and controlled release of an anticancer drug. *J. Mater. Sci.* **2014**, *49*, p. 6343–6352.

215. Hayat, A.; Catanante, G.; Marty, J. L. Current trends in nanomaterial-based amperometric biosensors. *Sensors (Switzerland)* **2014**, *14*, p. 23439–23461.

216. Singh, L. P.; Bhattacharyya, S. K.; Kumar, R.; Mishra, G.; Sharma, U.; Singh, G.; Ahalawat, S. Sol-Gel processing of silica nanoparticles and their applications. *Adv. Colloid Interface Sci.* **2014**, *214*, p. 17–37.

217. Vera, S. Chemical sensors based on polymer composites with carbon nanotubes and graphene : the role of the polymer. *J. Mater. Chem. A* **2014**, *2*, p. 14289–14328.
218. Maduraiveeran, G.; Sasidharan, M.; Ganesan, V. Electrochemical sensor and biosensor platforms based on advanced nanomaterials for biological and biomedical applications. *Biosens. Bioelectron.* **2018**, *103*, p. 113-129.
219. Wang, N.; Pandit, S.; Ye, L.; Edwards, M.; Mokkapati, V. R. S. S.; Murugesan, M.; Kuzmenko, V.; Zhao, C.; Westerlund, F.; Mijakovic, I.; Liu, J. Efficient surface modification of carbon nanotubes for fabricating high performance CNT based hybrid nanostructures. *Carbon N. Y.* **2017**, *111*, p. 402–410.
220. Wang, H.; Qian, D.; Xiao, X.; Deng, C.; Liao, L.; Deng, J.; Lin, Y.-W. Preparation and application of a carbon paste electrode modified with multi-walled carbon nanotubes and boron-embedded molecularly imprinted composite membranes. *Bioelectrochemistry* **2018**, *121*, p. 115–124.
221. Campuzano, S.; Paloma, Y. Current trends and challenges in bioelectrochemistry for non-invasive and early diagnosis. *Curr. Opin. Electrochem.* **2018**, *in press*.
222. Zia, M.; Phull, A. R.; Ali, J. S. Synthesis, characterization, applications, and challenges of iron oxide nanoparticles. *Nanotechnol. Sci. Appl.* **2016**, *9*, p. 49–67.
223. Feng, B.; Hong, R. Y.; Wang, L. S.; Guo, L.; Li, H. Z.; Ding, J.; Zheng, Y.; Wei, D. G. Synthesis of Fe3O4/APTES/PEG diacid functionalized magnetic nanoparticles for MR imaging. *Colloids Surfaces A Physicochem. Eng. Asp.* **2008**, *328*, p. 52–59.
224. Cheraghipour, E.; Javadpour, S.; Mehdizadeh, A. R. Citrate capped superparamagnetic iron oxide nanoparticles used for hyperthermia therapy. *J. Biomed. Sci. Eng.* **2012**, *05*, p. 715–719.
225. Yang, H. M.; Jang, S. C.; Hong, S. B.; Lee, K. W.; Roh, C.; Huh, Y. S.; Seo, B. K. Prussian blue-functionalized magnetic nanoclusters for the removal of radioactive cesium from water. *J. Alloys Compd.* **2016**, *657*, p. 387–393.
226. Mody, V. V.; Cox, A.; Shah, S.; Singh, A.; Bevins, W.; Parihar, H. Magnetic nanoparticle drug delivery systems for targeting tumor. *Appl. Nanosci.* **2014**, *4*, p. 385–392.
227. Safarik, I.; Safarikova, M. Magnetic techniques for the isolation and purification of proteins and peptides. *Biomagn. Res. Technol.* **2004**, *2*, p. 1–17.
228. Ghafoor, S.; Ata, S. Synthesis of carboxyl-modified Fe3O4@SiO2 nanoparticles and their utilization for the remediation of cadmium and nickel from aqueous solution. *J. Chil. Chem. Soc.* **2017**, *62*, p. 3588-3592.
229. Xie, L.; Jiang, R.; Zhu, F.; Liu, H.; Ouyang, G. Application of functionalized magnetic nanoparticles in sample preparation. *Anal. Bioanal. Chem.* **2014**, *406*, p. 377–399.
230. Darmawan, A.; Smart, S.; Julbe, A.; da Costa, J. C. D. Iron oxide silica derived from sol-gel synthesis. *Materials (Basel).* **2010**, *4*, p. 448–456.
231. Ullah, R.; Deb, B. K.; Yousuf, M.; Mollah, A. Synthesis and Characterization of Silica Coated Iron-Oxide Composites of Different Ratios. *Int. J. Compos. Mater.* **2014**, *4*, p. 135–145.
232. Gao, J.; Ran, X.; Shi, C.; Cheng, H.; Cheng, T.; Su, Y. One-step solvothermal synthesis of

highly water-soluble, negatively charged superparamagnetic Fe3O4 colloidal nanocrystal clusters. *Nanoscale* **2013**, *5*, 7026-7033.

233. Riskin, M.; Tel-Vered, R.; Willner, I. The Imprint of Electropolymerized Polyphenol Films on Electrodes by Donor-Acceptor Interactions: Selective Electrochemical Sensing of N,N′-dimethyl-4,4′-bipyridinium (Methyl Viologen). *Adv. Funct. Mater.* **2007**, *17*, p. 3858–3863.

234. Tahar, B. Electropolymerization of phenol on a vitreous carbon electrode in acidic aqueous solution at different temperatures. **2011**, *41*, p. 983–989.

235. Lapuente, R.; Cases, F.; Garce, P. A voltammetric and FTIR – ATR study of the electropolymerization of phenol on platinum electrodes in carbonate medium Influence of sulfide. *J. Electroanal. Chem.* **1998**, *451*, p. 163–171.

236. Ferreira, M.; Varela, H.; Torresi, R. M.; Tremiliosi-Filho, G. Electrode passivation caused by polymerization of different phenolic compounds. *Electrochim. Acta* **2006**, *52*, p. 434–442.

237. Garcés, P.; Lapuente, R.; Andíon, L. G.; Cases, F.; Morallón, E.; Vásquez, J. L. Electropolymerization of phenol on carbon steel and stainless steel electrodes in carbonate aqueous medium. *Polym. J.* **2000**, *32*, p. 623-628.

238. Deng, J.; Ju, S.; Liu, Y.; Xiao, N.; Xie, J.; Zhao, H. Highly sensitive and selective determination of melamine in milk using glassy carbon electrode modified with molecularly imprinted copolymer. *Food Anal. Methods* **2015**, *8*, p. 2437-2446.

239. Zayas, H.; Holdsworth, C. I.; Bowyer, M. C.; McCluskey, A. Evaluation of 4-substituted styrenes as functional monomers for the synthesis of theophylline-specific molecularly imprinted polymers. *Org. Biomol. Chem.* **2014**, *12*, p. 6994–7003.

240. Subrahmanyam, S.; Piletsky, S. a.; Piletska, E. V.; Chen, B.; Karim, K.; Turner, a. P. F. “Bite-and-Switch” approach using computationally designed molecularly imprinted polymers for sensing of creatinine. *Biosens. Bioelectron.* **2001**, *16*, p. 631–637.

241. Huang, J.; Xing, X.; Zhang, X.; He, X.; Lin, Q.; Lian, W.; Zhu, H. A molecularly imprinted electrochemical sensor based on multiwalled carbon nanotube-gold nanoparticle composites and chitosan for the detection of tyramine. *Food Res. Int.* **2011**, *44*, p. 276–281.

242. Blanco-López, M. C.; Lobo-Castañón, M. J.; Miranda-Ordieres, a J.; Tuñón-Blanco, P. Voltammetric sensor for vanillylmandelic acid based on molecularly imprinted polymer-modified electrodes. *Biosens. Bioelectron.* **2003**, *18*, p. 353–62.

243. Panasyuk, T. L.; Mirsky, V. M.; Piletsky, S. A.; Wolfbeis, O. S. Electropolymerized Molecularly Imprinted Polymers as Receptor Layers in Capacitive Chemical Sensors. *Anal. Chem.* **1999**, *71*, p. 4609–4613.

244. Wang, Z.; Kang, J.; Liu, X.; Ma, Y. Capacitive Detection of Theophylline Based on Electropolymerized Molecularly Imprinted Polymer. *Int. J. Polym. Anal. Charact.* **2007**, *12*, p. 131–142.

245. Socrates, G. *Infrared and Raman Characteristic Group Frequencies*; 2004.

246. Hawkins, D. M.; Trache, A.; Ellis, E. A.; Stevenson, D.; Holzenburg, A.; Meininger, G. a.; Reddy, S. M. Quantification and confocal imaging of protein specific molecularly imprinted polymers. *Biomacromolecules* **2006**, *7*, p. 2560–2564.

247. Daniel J. Thomas; Zari Tehrani; Mohd Azraie B. Mohd Azmi Silicon nanowire immunosensor for detection of 8-hydroxy-2′-deoxyguanosine oxidative stress cancer biomarker. *J. Surf. Sci. Nanotechnol.* **2014**, *12*, p. 349–357.

248. Galvis-Sanchez, A. C.; Santos, J. R.; Rangel, A. O. S. S. Standard addition flow method for potentiometric measurements at low concentration levels: Application to the determination of fluoride in food samples. *Talanta* **2015**, *133*, p. 1–6.

249. Jia, L.-P.; Liu, J.-F.; Wang, H.-S. Electrochemical performance and detection of 8-Hydroxy-2′-deoxyguanosine at single-stranded DNA functionalized graphene modified glassy carbon electrode. *Biosens. Bioelectron.* **2015**, *67*, p. 139–145.

250. Khan, M. Z. H.; Liu, X.; Tang, Y.; Liu, X. Ultra-sensitive Electrochemical Detection of Oxidative Stress Biomarker 8-Hydroxy-2′-deoxyguanosine with Poly (L-arginine)/Graphene Wrapped Au Nanoparticles Modified Electrode. *Biosens. Bioelectron.* **2018**, *117*, p. 508-514.

251. Jia, L.; Wang, H. Electrochemical reduction synthesis of graphene/Nafion nanocomposite film and its performance on the detection of 8-hydroxy-2'-deoxyguanosine in the presence of uric acid. *J. Electroanal. Chem.* **2013**, *705*, p. 37–43.

252. Pan, D.; Zhou, Q.; Rong, S.; Zhang, G.; Zhang, Y.; Liu, F.; Li, M.; Chang, D.; Pan, H. Electrochemical immunoassay for the biomarker 8-hydroxy-2′-deoxyguanosine using a glassy carbon electrode modified with chitosan and poly(indole-5-carboxylic acid). *Microchim. Acta* **2016**, *183*, p. 361–368.

253. Ferreira, N. S.; Sales, M. G. F. Disposable immunosensor using a simple method for oriented antibody immobilization for label-free real-time detection of an oxidative stress biomarker implicated in cancer diseases. *Biosens. Bioelectron.* **2014**, *53*, p. 193–9.

254. Mohd Azmi, M. a; Tehrani, Z.; Lewis, R. P.; Walker, K. D.; Jones, D. R.; Daniels, D. R.; Doak, S. H.; Guy, O. J. Highly sensitive covalently functionalised integrated silicon nanowire biosensor devices for detection of cancer risk biomarker. *Biosens. Bioelectron.* **2014**, *52*, p. 216–24.

255. Tavares, A. P. M.; Ferreira, N. S.; Truta, L. A. A. N. A.; Sales, M. G. F. Conductive Paper with Antibody-Like Film for Electrical Readings of Biomolecules. *Sci. Rep.* **2016**, *6*, p. 26132.

256. Zhu, X.; Shah, P.; Stoff, S.; Liu, H.; Li, C. A paper electrode integrated lateral flow immunosensor for quantitative analysis of oxidative stress induced DNA damage. *Analyst* **2014**, *139*, p. 2850–7.

257. Yang, L.; Wang, B.; Qi, H.; Gao, Q.; Li, C.; Zhang, C. Highly Sensitive Electrochemical Sensor for the Determination of 8-Hydroxy-2'-deoxyguanosine Incorporating SWCNTs-Nafion Composite Film. *J. Sensors* **2015**, *2015*, 1–11.

258. Shahzad, F.; Zaidi, S. A.; Koo, C. M. Highly sensitive electrochemical sensor based on environmentally friendly biomass-derived sulfur-doped graphene for cancer biomarker detection. *Sensors Actuators B Chem.* **2017**, *241*, p. 716–724.

259. Martín, A.; Batalla, P.; Hernández-Ferrer, J.; Martínez, M. T.; Escarpa, A. Graphene oxide nanoribbon-based sensors for the simultaneous bio-electrochemical enantiomeric resolution and analysis of amino acid biomarkers. *Biosens. Bioelectron.* **2015**, *68*, p. 163–167.

260. Xing, X.; Liu, S.; Yu, J.; Lian, W.; Huang, J. Electrochemical sensor based on molecularly imprinted film at polypyrrole-sulfonated graphene/hyaluronic acid-multiwalled carbon nanotubes modified electrode for determination of tryptamine. *Biosens. Bioelectron.* **2012**, *31*, p. 277–83.

261. Santharaman, P.; Das, M.; Singh, S. K.; Sethy, N. K.; Bhargava, K.; Claussen, J. C.; Karunakaran, C. Label-free electrochemical immunosensor for the rapid and sensitive detection of the oxidative stress marker superoxide dismutase 1 at the point-of-care. *Sensors Actuators, B Chem.* **2016**, *236*, p. 546–553.

262. Ahuja, T.; Mir, I. A.; Kumar, D.; Rajesh Biomolecular immobilization on conducting polymers for biosensing applications. *Biomaterials* **2007**, *28*, p. 791–805.

263. Moreira, F. T. C.; Sharma, S.; Dutra, R. A. F.; Noronha, J. P. C.; Cass, A. E. G.; Sales, M. G. F. Detection of cardiac biomarker proteins using a disposable based on a molecularly imprinted polymer grafted onto graphite. *Microchim. Acta* **2015**, *182*, p. 975–983.

264. Kudin, K. N.; Ozbas, B.; Schniepp, H. C.; Prud'homme, R. K.; Aksay, I. A.; Car, R. Raman spectra of graphite oxide and functionalized graphene sheets. *Nano Lett.* **2008**, *8*, p. 36–41.

265. Ferrari, A. C. Raman spectroscopy of graphene and graphite: Disorder, electron-phonon coupling, doping and nonadiabatic effects. *Solid State Commun.* **2007**, *143*, p. 47–57.

266. Li, Q.; Batchelor-Mcauley, C.; Compton, R. G. Electrochemical oxidation of guanine: Electrode reaction mechanism and tailoring carbon electrode surfaces to switch between adsorptive and diffusional responses. *J. Phys. Chem. B* **2010**, *114*, p. 7423–7428.

267. Martins, G. V.; Marques, A. C.; Fortunato, E.; Sales, M. G. F. 8-hydroxy-2'-deoxyguanosine (8-OHdG) biomarker detection down to picoMolar level on a plastic antibody film. *Biosens. Bioelectron.* **2016**, *86*, p. 225–234.

268. Kikuchi, A.; Takeda, A.; Onodera, H.; Kimpara, T.; Hisanaga, K.; Sato, N.; Nunomura, A.; Castellani, R. J.; Perry, G.; Smith, M. A.; Itoyama, Y. Systemic Increase of Oxidative Nucleic Acid Damage in Parkinson's Disease and Multiple System Atrophy. *Neurobiol. Dis.* **2002**, *9*, p. 244–248.

269. Jin, Y.; Qiu, C.; Zheng, Q.; Liu, L.; Liu, Z.; Wang, Y. Efficacy of different doses of atorvastatin treatment on serum levels of 8-hydroxy-guanin (8-OHdG) and cardiac function in patients with ischemic cardiomyopathy. *Pakistan J. Med. Sci.* **2014**, *31*, p. 1–6.

270. Kato, A.; Odamaki, M.; Hishida, A. Blood 8-hydroxy-2'-deoxyguanosine is associated with erythropoietin resistance in haemodialysis patients. *Nephrol. Dial. Transplant.* **2003**, *18*, p. 931–936.

271. Rebelo, I.; Piedade, J. A. P.; Brett, A. M. O. Electrochemical determination of 8-oxoguanine in the presence of uric acid. *Bioelectrochemistry* **2004**, *63*, p. 267–270.

272. Wan, C.; Liu, T.; Wei, S.; Zhang, S. Electrochemical determination of 8-hydroxydeoxyguanosine using a carbon nanotube modified electrode. *Russ. J. Electrochem.* **2008**, *44*, p. 327–331.

273. Costa, M. N.; Veigas, B.; Jacob, J. M.; Santos, D. S.; Gomes, J.; Baptista, P. V; Martins, R.; In, J. A low cost , safe , disposable , rapid and self-sustainable paper-based platform for diagnostic testing , lab-on-paper. *Nanotechnology* **2014**, *25*, p. 1-12.

274. Cinti, S.; Basso, M.; Moscone, D.; Arduini, F. A paper-based nanomodified electrochemical biosensor for ethanol detection in beers. *Anal. Chim. Acta* **2017**, *960*, p. 123–130.
275. Cinti, S.; Minotti, C.; Moscone, D.; Palleschi, G.; Arduini, F. Fully integrated ready-to-use paper-based electrochemical biosensor to detect nerve agents. *Biosens. Bioelectron.* **2017**, *93*, p. 46–51.
276. Oliveira-Brett, a. M.; Piedade, J. a P.; Silva, L. a.; Diculescu, V. C. Voltammetric determination of all DNA nucleotides. *Anal. Biochem.* **2004**, *332*, p. 321–329.
277. Ping, J.; Wu, J.; Wang, Y.; Ying, Y. Simultaneous determination of ascorbic acid, dopamine and uric acid using high-performance screen-printed graphene electrode. *Biosens. Bioelectron.* **2012**, *34*, p. 70–76.
278. Acar, E. T.; Onar, A. N.; Onar, M. K. Investigation of electrochemical behavior and development of a validated adsorptive stripping square wave voltammetry method for 3-nitrotyrosine in human plasma and cerebrospinal fluid. *J. Anal. Chem.* **2016**, *71*, p. 581–589.
279. Yu, X.; Mai, Z.; Xiao, Y.; Zou, X. Electrochemical behavior and determination of L-tyrosine at single-walled carbon nanotubes modified glassy carbon electrode. *Electroanalysis* **2008**, *20*, p. 1246–1251.
280. Anderson, L. B.; Reillev, C. N. Teaching Electroanalytical Chemistry: Diffusion-controlled processes. *J. Chem. Educ.* **1967**, *44*, p. 9–16.
281. Kissinger, P. T.; Heineman, W. R. Cyclic voltammetry. *J. Chem. Educ.* **1983**, *60*, p. 702-706.
282. Lu, S.; Wu, K.; Dang, X.; Hu, S. Electrochemical reduction and voltammetric determination of metronidazole at a nanomaterial thin film coated glassy carbon electrode. *Talanta* **2004**, *63*, p. 653–657.
283. Zinola, C. F.; Rodríguez, J. L.; Arévalo, M. C.; Pastor, E. Electrochemical and FTIR spectroscopic studies of tyrosine oxidation at polycrystalline platinum surfaces in alkaline solutions. *J. Solid State Electrochem.* **2008**, *12*, p. 523–528.
284. Gui, R.; Jin, H.; Guo, H.; Wang, Z. Recent advances and future prospects in molecularly imprinted polymers-based electrochemical biosensors. *Biosens. Bioelectron.* **2018**, *100*, p. 56–70.
285. Dalle-Donne, I.; Rossi, R.; Colombo, R.; Giustarini, D.; Milzani, A. Biomarkers of oxidative damage in human disease. *Clin. Chem.* **2006**, *52*, p. 601–23.
286. Ahsan, H. 3-Nitrotyrosine: A biomarker of nitrogen free radical species modified proteins in systemic autoimmunogenic conditions. *Hum. Immunol.* **2013**, *74*, p. 1392–1399.
287. Teixeira, D.; Fernandes, R.; Prudêncio, C.; Vieira, M. 3-Nitrotyrosine quantification methods: Current concepts and future challenges. *Biochimie* **2016**, *125*, p. 1–11.
288. Yamanaka, K.; Vestergaard, M. C.; Tamiya, E. Printable electrochemical biosensors: A focus on screen-printed electrodes and their application. *Sensors (Switzerland)* **2016**, *16*, p. 1–16.
289. Wang, Q. X.; Xue, S. F.; Chen, Z. H.; Ma, S. H.; Zhang, S.; Shi, G.; Zhang, M. Dual lanthanide-doped complexes: the development of a time-resolved ratiometric fluorescent probe

for anthrax biomarker and a paper-based visual sensor. *Biosens. Bioelectron.* **2017**, *94*, p. 388–393.

290. Feng, Q.-M.; Pan, J.-B.; Zhang, H.-R.; Xu, J.-J.; Chen, H.-Y. Disposable paper-based bipolar electrode for sensitive electrochemiluminescence detection of a cancer biomarker. *Chem. Commun. (Camb).* **2014**, *50*, p. 2–4.

291. Rusling, J. F. Sensors for toxicity of chemicals and oxidative stress based on electrochemical catalytic DNA oxidation. *Biosens. Bioelectron.* **2004**, *20*, p. 1022–8.

292. Wang, L.; Liao, X.; Ding, Y.; Gao, F.; Wang, Q. DNA biosensor based on a glassy carbon electrode modified with electropolymerized Eriochrome Black T. *Microchim. Acta* **2014**, *181*, p. 155–162.

293. Mergola, L.; Scorrano, S.; Del Sole, R.; Lazzoi, M. R.; Vasapollo, G. Developments in the synthesis of a water compatible molecularly imprinted polymer as artificial receptor for detection of 3-nitro-l-tyrosine in neurological diseases. *Biosens. Bioelectron.* **2013**, *40*, p. 336–341.

294. Ng, S. P.; Qiu, G.; Ding, N.; Lu, X.; Wu, C.-M. L. Label-free detection of 3-nitro-l-tyrosine with nickel-doped graphene localized surface plasmon resonance biosensor. *Biosens. Bioelectron.* **2017**, *89*, p. 468-476.

295. Martins, G. V.; Marques, A. C.; Fortunato, E.; Sales, M. G. F. Wax-printed paper-based device for a direct electrochemical detection of 3-nitrotyrosine biomarker. *Electrochim. Acta.* **2018**, *284*, p. 60-68.

296. Chandra, U. Determination of Dopamine in Presence of Uric Acid at Poly (Eriochrome Black t) Film Modified Graphite Pencil Electrode. *Am. J. Anal. Chem.* **2011**, *02*, p. 262–269.

297. Spehar-Délèze, A. M.; Anastasova, S.; Vadgama, P. Electropolymerised Phenolic Films as Internal Barriers for Oxidase Enzyme Biosensors. *Electroanalysis* **2014**, *26*, p. 1335–1344.

298. Ribeiro, J. A.; Pereira, C. M.; Silva, A. F.; Sales, M. G. F. Electrochemical detection of cardiac biomarker myoglobin using polyphenol as imprinted polymer receptor. *Anal. Chim. Acta* **2017**, *981*, p. 41-52.

299. Duan, D.; Yang, H.; Ding, Y.; Ye, D.; Li, L.; Ma, G. Three-dimensional molecularly imprinted electrochemical sensor based on Au NPs@Ti-based metal-organic frameworks for ultra-trace detection of bovine serum albumin. *Electrochim. Acta* **2018**, *261*, p. 160–166.

300. Cançado, L. G.; Jorio, A.; Ferreira, E. H. M.; Stavale, F.; Achete, C. A.; Capaz, R. B.; Moutinho, M. V. O.; Lombardo, A.; Kulmala, T. S.; Ferrari, A. C. Quantifying defects in graphene via Raman spectroscopy at different excitation energies. *Nano Lett.* **2011**, *11*, p. 3190–3196.

301. Yoon, T. J.; Kim, J. S.; Kim, B. G.; Yu, K. N.; Cho, M. H.; Lee, J. K. Multifunctional nanoparticles possessing a “magnetic motor effect” for drug or gene delivery. *Angew. Chemie - Int. Ed.* **2005**, *44*, p. 1068–1071.

302. Rahman, I. A.; Padavettan, V. Synthesis of Silica nanoparticles by Sol-Gel: Size-dependent properties, surface modification, and applications in silica-polymer nanocomposites: a review. *J. Nanomater.* **2012**, *2012*, p. 1-15.

303. Chen, F.; Hableel, G.; Zhao, E. R.; Jokerst, J. V. Multifunctional nanomedicine with silica: Role of silica in nanoparticles for theranostic, imaging, and drug monitoring. *J. Colloid Interface*

Sci. **2018**, *521*, p. 261–279.
304. Williams, H. M. The application of magnetic nanoparticles in the treatment and monitoring of cancer and infectious diseases. *Biosci. Horizons Int. J. Student Res.* **2017**, *10*, p. 1–10.
305. Yildiz, I.; Sizirici Yildiz, B. Applications of thermoresponsive magnetic nanoparticles. *J. Nanomater.* **2015**, *2015*, p. 1-12.
306. Bonci, A.; Lupica, C. R.; Morales, M. Magnetic Nanoparticles: Material Engineering and Emerging Applications in Lithography and Biomedicine. **2015**, *18*, p. 386–392.
307. Kalska-Szostko, B.; Wykowska, U.; Satuła, D. Magnetic nanoparticles of core-shell structure. *Colloids Surfaces A Physicochem. Eng. Asp.* **2015**, *481*, p. 527–536.
308. Brinker, C. J. Hydrolysis and condensation of silicates: effects on structure. *J. Non. Cryst. Solids* **1963**, *100*, p. 31–50.
309. Lu, C.-W.; Hung, Y.; Hsiao, J.-K.; Yao, M.; Chung, T.-H.; Lin, Y.-S.; Wu, S.-H.; Hsu, S.-C.; Liu, H.-M.; Mou, C.-Y.; Yang, C.-S.; Huang, D.-M.; Chen, Y.-C. Bifunctional Magnetic Silica Nanoparticles for Highly Efficient Human Stem Cell Labeling. *Nano Lett.* **2007**, *7*, p. 149–154.
310. Gan, N.; Xiong, P.; Wang, J.; Li, T.; Hu, F.; Cao, Y.; Zheng, L. A novel signal-amplified immunoassay for the detection of C-reactive protein using HRP-doped magnetic nanoparticles as labels with the electrochemical quartz crystal microbalance as a detector. *J. Anal. Methods Chem.* **2013**, *2013*, p. 1-12.
311. Tang, Z.; He, J.; Chen, J.; Niu, Y.; Zhao, Y.; Zhang, Y.; Yu, C. A sensitive sandwich-type immunosensor for the detection of galectin-3 based on N-GNRs-Fe-MOFs@AuNPs nanocomposites and a novel AuPt-methylene blue nanorod. *Biosens. Bioelectron.* **2018**, *101*, p. 253–259.
312. Kumar, N.; Narayanan, N.; Gupta, S. Application of magnetic molecularly imprinted polymers for extraction of imidacloprid from eggplant and honey. *Food Chem.* **2018**, *255*, p. 81-88.
313. Racuciu, M.; Creanga, D. E.; Airinei, A. Citric-acid-coated magnetite nanoparticles for biological applications. *Eur. Phys. J. E* **2006**, *21*, p. 117–121.
314. De Sousa, M. E.; Fernández Van Raap, M. B.; Rivas, P. C.; Mendoza Zélis, P.; Girardin, P.; Pasquevich, G. A.; Alessandrini, J. L.; Muraca, D.; Sánchez, F. H. Stability and relaxation mechanisms of citric acid coated magnetite nanoparticles for magnetic hyperthermia. *J. Phys. Chem. C* **2013**, *117*, p. 5436–5445.
315. Kobayashi, Y.; Inose, H.; Nakagawa, T.; Gonda, K.; Takeda, M.; Ohuchi, N.; Kasuya, A. Synthesis of Au–silica core–shell particles by sol–gel process. *Surf. Eng.* **2012**, *28*, p. 129–133.
316. Zane, A.; McCracken, C.; Knight, D. A.; Young, T.; Lutton, A. D.; Olesik, J. W.; Waldman, W. J.; Dutta, P. K. Uptake of bright fluorophore core-silica shell nanoparticles by biological systems. *Int. J. Nanomedicine* **2015**, *10*, p. 1547–1567.
317. Carrasco-Rodríguez, J.; García Alonso, F. J.; Costa-García, A.; Martín-Yerga, D. Tuning the incorporation of electroactive metals into titanium phosphate nanoparticles and the reverse metal extraction process: Application as electrochemical labels in multiplex biosensing. *Electrochem. commun.* **2017**, *83*, p. 1–5.

318. Wang, L.; Feng, F.; Ma, Z. Novel electrochemical redox-active species: One-step synthesis of polyaniline derivative-Au/Pd and its application for multiplexed immunoassay. *Sci. Rep.* **2015**, *5*, p. 1–9.

319. Budny, A.; Novak, F.; Plumer, N.; Schetter, B.; Speiser, B.; Straub, D.; Mayer, H. A.; Reginek, M. Redox-active silica nanoparticles. Part 1. Electrochemistry and catalytic activity of spherical, nonporous silica particles with nanometric diameters and covalently bound redox-active modifications. *Langmuir* **2006**, *22*, p. 10605–10611.

320. Dixit, C. K.; Bhakta, S.; Kumar, A.; Suib, S. L.; Rusling, J. F. Fast nucleation for silica nanoparticle synthesis using a sol–gel method. *Nanoscale* **2016**, *8*, p. 19662–19667.

321. Fernandes, M. T. C.; Garcia, R. B. R.; Leite, C. A. P.; Kawachi, E. Y. The competing effect of ammonia in the synthesis of iron oxide/silica nanoparticles in microemulsion/sol-gel system. *Colloids Surfaces A Physicochem. Eng. Asp.* **2013**, *422*, p. 136–142.

322. Rahman, I. A.; Vejayakumaran, P.; Sipaut, C. S.; Ismail, J.; Bakar, M. A.; Adnan, R.; Chee, C. K. An optimized sol-gel synthesis of stable primary equivalent silica particles. *Colloids Surfaces A Physicochem. Eng. Asp.* **2007**, *294*, p. 102–110.

323. Zhu, Q.; Chai, Y.; Zhuo, Y.; Yuan, R. Ultrasensitive simultaneous detection of four biomarkers based on hybridization chain reaction and biotin-streptavidin signal amplification strategy. *Biosens. Bioelectron.* **2015**, *68*, p. 42–48.

324. Ho, K. C.; Tsai, P. J.; Lin, Y. S.; Chen, Y. C. Using biofunctionalized nanoparticles to probe pathogenic bacteria. *Anal. Chem.* **2004**, *76*, p. 7162–7168.

325. Yamaura, M.; Camilo, R. L.; Sampaio, L. C.; Macêdo, M. A.; Nakamura, M.; Toma, H. E. Preparation and characterization of (3-aminopropyl)triethoxysilane-coated magnetite nanoparticles. *J. Magn. Magn. Mater.* **2004**, *279*, p. 210–217.

326. Villa, S.; Riani, P.; Locardi, F.; Canepa, F. Functionalization of Fe3O4NPs by silanization: Use of amine (APTES) and thiol (MPTMS) silanes and their physical characterization. *Materials (Basel).* **2016**, *9*, p. 1-14.

327. Lin, Z.-A.; Zheng, J.-N.; Lin, F.; Zhang, L.; Cai, Z.; Chen, G.-N. Synthesis of magnetic nanoparticles with immobilized aminophenylboronic acid for selective capture of glycoproteins. *J. Mater. Chem.* **2011**, *21*, p. 518–524.

328. Liu, L.; Deng, Q.-F.; Ma, T.-Y.; Lin, X.-Z.; Hou, X.-X.; Liu, Y.-P.; Yuan, Z.-Y. Ordered mesoporous carbons: citric acid-catalyzed synthesis, nitrogen doping and CO2 capture. *J. Mater. Chem.* **2011**, *21*, p. 16001-16009.